RECENT ADVANCES IN SOLAR-DRIVEN THERMOCHEMICAL FUEL PRODUCTION AND THERMAL ENERGY STORAGE

EDITED BY: Alfonso J. Carrillo, Alicia Bayon, Juan M. Coronado and Emanuela Mastronardo

PUBLISHED IN: Frontiers in Energy Research and Frontiers in Materials

frontiers Research Topics

ISSN 1664-8714
ISBN 978-2-88976-033-6
DOI 10.3389/978-2-88976-033-6

About Frontiers

Frontiers is more than just an open-access publisher of scholarly articles: it is a pioneering approach to the world of academia, radically improving the way scholarly research is managed. The grand vision of Frontiers is a world where all people have an equal opportunity to seek, share and generate knowledge. Frontiers provides immediate and permanent online open access to all its publications, but this alone is not enough to realize our grand goals.

Frontiers Journal Series

The Frontiers Journal Series is a multi-tier and interdisciplinary set of open-access, online journals, promising a paradigm shift from the current review, selection and dissemination processes in academic publishing. All Frontiers journals are driven by researchers for researchers; therefore, they constitute a service to the scholarly community. At the same time, the Frontiers Journal Series operates on a revolutionary invention, the tiered publishing system, initially addressing specific communities of scholars, and gradually climbing up to broader public understanding, thus serving the interests of the lay society, too.

Dedication to Quality

Each Frontiers article is a landmark of the highest quality, thanks to genuinely collaborative interactions between authors and review editors, who include some of the world's best academicians. Research must be certified by peers before entering a stream of knowledge that may eventually reach the public - and shape society; therefore, Frontiers only applies the most rigorous and unbiased reviews.
Frontiers revolutionizes research publishing by freely delivering the most outstanding research, evaluated with no bias from both the academic and social point of view. By applying the most advanced information technologies, Frontiers is catapulting scholarly publishing into a new generation.

What are Frontiers Research Topics?

Frontiers Research Topics are very popular trademarks of the Frontiers Journals Series: they are collections of at least ten articles, all centered on a particular subject. With their unique mix of varied contributions from Original Research to Review Articles, Frontiers Research Topics unify the most influential researchers, the latest key findings and historical advances in a hot research area! Find out more on how to host your own Frontiers Research Topic or contribute to one as an author by contacting the Frontiers Editorial Office: frontiersin.org/about/contact

RECENT ADVANCES IN SOLAR-DRIVEN THERMOCHEMICAL FUEL PRODUCTION AND THERMAL ENERGY STORAGE

Topic Editors:
Alfonso J. Carrillo, Institute of Chemical Technology, Spanish National Research Council (CSIC), Spain
Alicia Bayon, Arizona State University, United States
Juan M. Coronado, Institute of Catalysis and Petrochemistry, Spanish National Research Council (CSIC), Spain
Emanuela Mastronardo, University of Messina, Italy

Citation: Carrillo, A. J., Bayon, A., Coronado, J. M., Mastronardo, E., eds. (2022). Recent Advances in Solar-driven Thermochemical Fuel Production and Thermal Energy Storage. Lausanne: Frontiers Media SA. doi: 10.3389/978-2-88976-033-6

Table of Contents

frontiers | Frontiers in Energy Research

EDITORIAL
published: 06 April 2022
doi: 10.3389/fenrg.2022.885894

Editorial: Recent Advances in Solar-Driven Thermochemical Fuel Production and Thermal Energy Storage

Alfonso J. Carrillo[1]*, *Alicia Bayon*[2]*, *Juan M. Coronado*[3]* and *Emanuela Mastronardo*[4]*

[1]Instituto de Tecnología Química (Universitat Politècnica de València—CSIC), Valencia, Spain, [2]School for Engineering of Matter, Transport and Energy, Arizona State University, Tempe, AZ, United States, [3]Instituto de Catálisis y Petroleoquímica, CSIC, Madrid, Spain, [4]Engineering Department, University of Messina, Messina, Italy

Keywords: concentrated solar power, thermal energy storage, solar fuels, thermochemical cycles, hydrogen production

Editorial on the Research Topic

Recent Advances in Solar-Driven Thermochemical Fuel Production and Thermal Energy Storage

OPEN ACCESS

Edited and reviewed by:
Michael Folsom Toney, University of Colorado Boulder, United States

***Correspondence:**
Alfonso J. Carrillo
alcardel@itq.upv.es
Alicia Bayon
abayonsa@asu.edu
Juan M. Coronado
jm.coronado@csic.es
Emanuela Mastronardo
emanuela.mastronardo@unime.it

Specialty section:
This article was submitted to Solar Energy, a section of the journal Frontiers in Energy Research

Received: *28 February 2022*
Accepted: *21 March 2022*
Published: *06 April 2022*

Citation:
Carrillo AJ, Bayon A, Coronado JM and Mastronardo E (2022) Editorial: Recent Advances in Solar-Driven Thermochemical Fuel Production and Thermal Energy Storage. Front. Energy Res. 10:885894. doi: 10.3389/fenrg.2022.885894

Renewable energies are the core of the transition to a decarbonized and more sustainable energy sector. Among them, solar energy shows great potential since 430 EJ per hour of sunlight energy hit the Earth, which is about the annual world energy consumption (Lewis and Nocera, 2006). However, solar energy radiation is not equally distributed along the planet surface and it suffers from an inherent intermittence problem. Therefore, development of efficient and cost-effective energy storage technologies is fundamental for the implementation of solar energy worldwide. In this respect, concentrated solar power (CSP) plants incorporate thermal energy storage (TES) units that allows for a round-the-clock electricity production and are radically cheaper than other storage solutions such as batteries (Carrillo et al., 2019; Bayon et al., 2021). In addition, the high temperatures achieved in concentrated solar thermal (CST) plants based on cavity receiver, with heliostat field or dish concentrators, can be used to drive the thermal reduction of metal oxides than can be subsequently re-oxidized with steam and/or CO_2 producing H_2 or syngas, respectively. These renewable fuels can be used for industry and transportation or as precursors for liquid fuels or chemicals.

This Research Topic focuses on the recent advances both in thermal energy storage and in thermochemical cycles for hydrogen production. The published contributions cover several key aspects for the progress of these technologies, e.g., storage media and reactors development, computational tools for the discovery of new materials and techno-economic assessment of thermochemical energy storage (TCS) units. Regarding thermal energy storage, both latent and thermochemical technologies have been addressed. Gokon et al. reported on the use of copper-germanium alloys as phase-change materials (PCMs) for high-temperature latent heat storage. These PCM alloys, with varying the Cu-Ge ratio, showed chemical compatibility with alumina or SiC containers, albeit not with stainless steel or Inconel tanks. The authors assessed the thermophysical properties of these alloys which showed reversible phase transitions for 20 cycles, with a latent heat at 644°C of 232.8 kJ kg^{-1}.

In the case of thermochemical energy storage, contributions covered both carbonate and redox-based systems, which are amongst the most promising. Regarding the former, Fedunik-Hofman et al. found that by supporting CaO on $Ca_3Al_2O_6$ and Dy_2O_3, it was possible to overcome the multicycle deactivation caused by sintering of $CaCO_3$/CaO particles. These novel materials exhibit an exothermic heat exchange of 582.2 kJ kg^{-1}, retaining a carbonation capacity of 82.7% over the course of 40 calcination-carbonation cycles.

Wild et al. developed a reactor combining sensible and thermochemical heat storage. The thermochemical unit was based on carbonation/calcination reactions, using a tubular packed bed of CaO:MgO in a 58:42 wt%. The materials were tested in different particle conformations over 80 consecutive cycles. Agglomerates exhibited higher energy storage density (866 kJ kg^{-1}) than granules (450 kJ kg^{-1}). However, the latter were more stable over cycling. These results validated previous heat and mass models performed by the authors, proving the feasibility of this modular reactor design.

An important piece of experimental research on materials for high temperature thermochemical reactions encompasses the use of electric furnaces in which a fast response for heating and cooling is required. In this regard, Gao et al. developed a low-cost radiant heater that could replace more expensive options, such as infrared furnaces. Their design could achieve temperatures above 1,500°C, with heating/cooling rates of 400°C min^{-1}. Tests of more than 10,000 cycles and 350 h of operation confirmed the robustness of this device.

TCS based on reduction/oxidation reactions of metal oxides was also addressed in this special issue. Miller et al. report on the use of $CaMnO_{3-\delta}$ perovskite oxides for high temperature energy storage. The authors analyzed the partial replacement of Ca and Mn in the perovskite formula by using a plethora of metal cations. The results indicated that $CaAl_{0.2}Mn_{0.8}O_{3-\delta}$ and $CaTi_{0.2}Mn_{0.8}O_{3-\delta}$ were the most promising materials, being the former the preferred choice in terms of cost.

Two more contributions concerning techno-economic assessments of redox-based TCS were published. Buck et al. analyzed three redox systems in a CSP plant with a particle receiver, namely, Co_3O_4/CoO, $(Mn_{0.75}Fe_{0.25})_3O_4/(Mn_{0.75}Fe_{0.25})_2O_3$ and the $Ca_{0.9}Sr_{0.1}MnO_{3-\delta}$ perovskite compositions. The cobalt-based oxide requires lower storage mass and volume. However, its elevated cost makes this choice not economically appealing. In this sense, the perovskite-based system, which presents a lower price due the use of abundant elements, is an attractive option for further development.

Gorman et al. evaluated a CSP plant exploiting an air Brayton cycle for energy dispatch and using $CaAl_{0.2}Mn_{0.8}O_{3-\delta}$ as TCS storage media. Their results indicated an increase in the plant capacity factor when using the redox-based energy storage system. In addition, their model predicted an LCOE of 5.98 ¢ kWh_e^{-1}, for a plant with 12 h of storage, which is very close to the U.S. Department of Energy 2030 target of 5.00 ¢ kWh_e^{-1}, illustrating the promise of redox-based TCS.

Two works were devoted to the production of hydrogen via thermochemical cycles at high temperatures. Boretti et al. contributed with a perspective on the production of green hydrogen using a beam-down concentrator coupled with a TES unit. The authors proposed the use of the three-step sulfur-iodine cycling scheme for hydrogen production.

Finally, Park et al. reported the discovery of a new redox oxide with promising properties for 2-step thermochemical hydrogen production. By using computational methods, the authors found that $Gd_{0.5}La_{0.5}Co_{0.5}Fe_{0.5}O_3$ could have remarkable potential for water splitting. Experiments confirmed the ability of this perovskite oxide to produce hydrogen. Namely, after reduction in inert gas at 1,350°C, the material produced 101 μmol g^{-1} and 141 μmol g^{-1} of hydrogen, when the water splitting reaction was performed at temperatures of 850 and 1,000°C, respectively. This work shows the importance of computational assisted discovery of new class of oxides for solar-driven thermochemical cycles for hydrogen production and it could be extended to thermochemical heat storage materials.

We would like to thank all the authors and reviewers for their high quality contribution to this Research Topic. This Special Issue has covered a broad spectrum of relevant aspects that are key to continue with the development of these technologies, including computational discovery of new materials, reactor development and techno-economic assessments that validate the feasibility of these sustainable technologies.

AUTHOR CONTRIBUTIONS

AC prepared the editorial, AB, JC and EM provided feedback and revised the draft.

ACKNOWLEDGMENTS

AC thanks the support of a fellowship from "la Caixa" Foundation (ID 100010434). The fellowship code is LCF/BQ/PI20/11760015. JC acknowledge financial support from ACES 2030 (P2018/EMT-4319) from "Comunidad de Madrid" and European Structural Funds.

REFERENCES

Bayon, A., Carrillo, A. J., Mastronardo, E., and Coronado, J. M. (2021). "Thermochemical Heat Storage at High Temperature," in *Adv. Chem. Eng.* Editor W. Lipiński. 1st ed. (Elsevier), 247–295. doi:10.1016/bs.ache.2021.10.004

Carrillo, A. J., González-Aguilar, J., Romero, M., and Coronado, J. M. (2019). Solar Energy on Demand: A Review on High Temperature Thermochemical Heat Storage Systems and Materials. *Chem. Rev.* 119, 4777–4816. doi:10.1021/acs.chemrev.8b00315

Lewis, N. S., and Nocera, D. G. (2006). Powering the Planet: Chemical Challenges in Solar Energy Utilization. *Proc. Natl. Acad. Sci. U.S.A.* 103, 15729–15735. doi:10.1073/pnas.0603395103

Conflict of Interest: The authors declare that the research was conducted in the absence of any commercial or financial relationships that could be construed as a potential conflict of interest.

Publisher's Note: All claims expressed in this article are solely those of the authors and do not necessarily represent those of their affiliated organizations, or those of the publisher, the editors and the reviewers. Any product that may be evaluated in this article, or claim that may be made by its manufacturer, is not guaranteed or endorsed by the publisher.

frontiers in Energy Research

ORIGINAL RESEARCH
published: 21 April 2021
doi: 10.3389/fenrg.2021.652203

Low-Cost Radiant Heater for Rapid Response, High-Temperature Heating

Xiang Gao[1], Matt von Boecklin[2], Ivan Ermanoski[1,3] and Ellen B. Stechel[1,4]*

[1] ASU LightWorks®, Arizona State University, Tempe, AZ, United States, [2] Francis College of Engineering, University of Massachusetts Lowell, Lowell, MA, United States, [3] School of Sustainability, Arizona State University, Tempe, AZ, United States, [4] School of Molecular Sciences, Arizona State University, Tempe, AZ, United States

High-temperature processing has an irreplaceable role in many research and industrial applications. Despite remarkable development spanning over a century, the pursuit of even higher thermal flux density and more rapid thermal transients has not slowed down. As part of the ongoing energy evolution, many industrial applications are transitioning from direct combustion of fossil fuels as primary energy sources to increasing electrification, capable of adapting to renewable power grids. Thus, there is an emerging need for electrical heaters that can replace burners and supply the heat demand, especially at the highest temperatures. In this study, we report on a radiant heater design that can achieve cyclic heating/cooling rates of up to 400 K min^{-1} and a temperature range in excess of 1,800 K, comparable to those of commercial infrared gold image furnaces, at high surface and volumetric power densities. The heater consists of a modular unit of incandescent tungsten filament and is enclosed in an evacuated ceramic envelope, chemically inert, tolerant of thermal shock, and impervious to gasses. The material and manufacture cost of such heaters, which is estimated at ∼$0.05/W, is less than 0.03% of that for infrared gold image furnaces, which is at >$2/W. Tests of more than 10,000 demanding cycles (high temperature and high heating/cooling rate) over 350 h of total operational time and in different temperature ranges confirm the robust performance of radiant heater prototypes. The design is widely applicable to high-temperature reactor and furnace designs. In thermochemistry research and practice, these radiant heaters could offer multiple benefits compared to solar simulators, lasers, infrared gold furnaces, ceramic heaters, or direct concentration of solar input.

Keywords: high temperature, renewable energy, radiant electric heater, cost-effective, rapid response, thermochemistry

OPEN ACCESS

Edited by:
Juan M. Coronado, Institute of Catalysis and Petrochemistry (ICP), Spain

Reviewed by:
Nathan Siegel, Bucknell University, United States
Alessandro Gallo, Universidad Carlos III de Madrid, Spain

****Correspondence:***
Ivan Ermanoski
ivan.ermanoski@asu.edu

Specialty section:
This article was submitted to Process and Energy Systems Engineering, a section of the journal Frontiers in Energy Research

Received: *12 January 2021*
Accepted: *17 March 2021*
Published: *21 April 2021*

Citation:
Gao X, von Boecklin M, Ermanoski I and Stechel EB (2021) Low-Cost Radiant Heater for Rapid Response, High-Temperature Heating. Front. Energy Res. 9:652203. doi: 10.3389/fenrg.2021.652203

INTRODUCTION

High-temperature processing is essential for the functioning of human society, including the production of most of the materials in use today, such as cement and lime manufacture, brick and ceramic manufacture, most metal processing, glass making, etc., These processes generally require combustion of fossil fuels as the primary heat supply (Jenkins and Mullinger, 2008). In many such

processes, it is difficult to ensure efficient use of fuel energy (The Rebound Effect: An Assessment of the Evidence for Economy-Wide Energy Savings from Improved Energy Efficiency | UKERC | The UK Energy Research Centre, n.d.). With the primary energy supply of the world moving toward renewables, high-temperature electric heating can potentially substitute fossil fuel combustion in industrial processes (Van Geem et al., 2019). To be a viable substitute, heaters will need to be economical (acceptable cost) and offer competitive performance characteristics, such as power density, achievable temperature, maintenance, and durability with fast ramp up/down rates. Conventional high-temperature electrical heaters (>1,750 K surface temperature), mostly based on *SiC* (He et al., 2014) or $MoSi_2$ (He et al., 2018), have the disadvantage of slow heating/cooling rates (3–10 K min^{-1}). In addition, due to increase in volatility with decrease in pressure, the maximum allowable temperature of *SiC* and $MoSi_2$ also decreases, limiting their usage for high-temperature, sub-ambient pressure applications. *SiC* and $MoSi_2$ are also costly (∼$1/W) and achieve low power density, especially at the upper end of their operating temperature ranges (Jenkins and Mullinger, 2008). Many heaters also use tungsten in quartz enclosures. However, due to the low maximum allowable temperature of quartz, these heaters generally cannot operate beyond 1,450 K, significantly undermining the heating capability of tungsten filaments. Hence, there is value in developing advanced high-temperature heaters that are cost-effective and can respond rapidly to the intermittent "ups" and "downs" of renewable energy.

In this study, we report of a novel radiant heater design capable of achieving high temperatures, high power densities, and outstanding ramp rates. To describe it briefly, the heater consists of a refractory ceramic envelope and an internal tungsten or similar refractory metal filament as the active heating element. The ceramic envelope is chemically inert, impermeable to gases, and transparent in the infrared (IR) region of the electromagnetic spectrum (Kim et al., 2009). The IR transparency of the envelope allows direct radiative coupling between the filament and the heated materials without substantial direct radiative heating of the envelope, ensuring high heat transfer rates. The design enables direct radiative coupling between the heater and its working environment instead of wall-mediated indirect heating.

The radiant heater is compact (i.e., has high-power density), uses non-hazardous materials, and is economical to manufacture. As noted, the application space for high-temperature heaters is broad. We frame our discussion of heater performance in relation to thermochemical water and CO_2 splitting—one of the most demanding applications in terms of temperature and heating/cooling rates.

EXPERIMENT

Figure 1 shows a simplified schematic of the radiant heater prototype. Two key heater components are a tungsten coil filament and a thin-wall alumina envelope. Low-cost techniques widely established in incandescent lighting can be used for manufacturing the tungsten filaments. They are appealing resistive heating elements, as they are capable of generating sustained temperatures of up to 2,800 K without significant material loss due to sublimation (MacIsaac et al., 1999). Our experiments used a filament wire with Ø0.254–0.4318 mm (Midwest Tungsten Service, Willowbrook, IL, United States, 99.95% purity, sag free), densely coiled around stainless steel mandrels. The outer diameter of freestanding filaments (OD_f) ranges from 3 to 4 mm. To ensure a uniform and reproducible power density in the experiments, each filament had 100 active coils and was L_f = 50 mm long in the mounted position, longer than the "as-wound" length, to ensure that neighboring coils do not touch. The optically translucent alumina envelope (Coorstek, Golden, CO, United States, 99.8% purity) had a temperature rating of up to 2,173 K, a nominal OD_t = 6.35 mm and wall thickness w_t = 0.785 mm. Based on known alumina properties (Harris et al., 2017) and tungsten emissivity (De Vos, 1954; Larrabee, 1959), we expected good infrared transmittance through these alumina envelopes (75–85% at the emission peak of ∼1.4 μm), to enable direct and effective radiative heating from the filament. The high infrared transmittance of the designed heater also ensured a radiation-dominant heat transfer mechanism to the surrounding environment. A thermocouple could measure the temperature of the environment, which would be the same as an emissivity-corrected temperature measurement derived from an optical/IR pyrometry device (Tank and Dietl, 1990; Urbas et al., 2004). The intention of the thin envelope wall was to minimize temperature differences between the inner and outer surface, and therefore limit thermally induced stresses. Additionally, the non-porous envelopes can maintain an ultra-high vacuum (UHV) working environment and essentially eliminate filament oxidation.

Filaments were attached to the envelope ends by support wires. During the development and prototyping phase, we typically capped one envelope end and connected the other to the UHV test stand. The free (capped) end was unconstrained, to permit thermal expansion and minimize temperature-induced stresses. Note, however, that as the prototype matures, we can seal both ends of the envelope and make standalone heaters free from external vacuum pumping. We sealed all metal-ceramic connections using a KL–5 Vacuum Leak Sealant (Kurt J. Lesker, Jefferson Hills, PA, United States). **Figure 2** shows the schematic setup. A programmable 80 V/6.5 A DC power supply (3663A, Array Electronic Co., Ltd, Nanjing, Jiangsu, China) provided the heating power for a single heater. Characterization of the temperature measurement around the heater used K- and S-type thermocouples (TC Direct, Hillside, IL, United States). Because of the substantial emissivity difference between K- and S-type thermocouples ($\varepsilon_K \sim 0.6–0.8$, $\varepsilon_S \sim 0.1–0.2$) (Bradley and Entwistle, 1961; Roberts et al., 2011; Hindasageri et al., 2013) and the radiation-dominated heat transfer, we conducted cross-comparison temperature measurements under identical heater and insulation conditions. These showed differences of no more than 1 K, well within our margin of experimental error. Depending on the purpose of a given experiment, the heater hot zone is bare, wrapped in a high-T alumina fiber blanket, or insulated in a firebrick cavity. We repeated the cavity temperature distribution experiment with bare S-type and

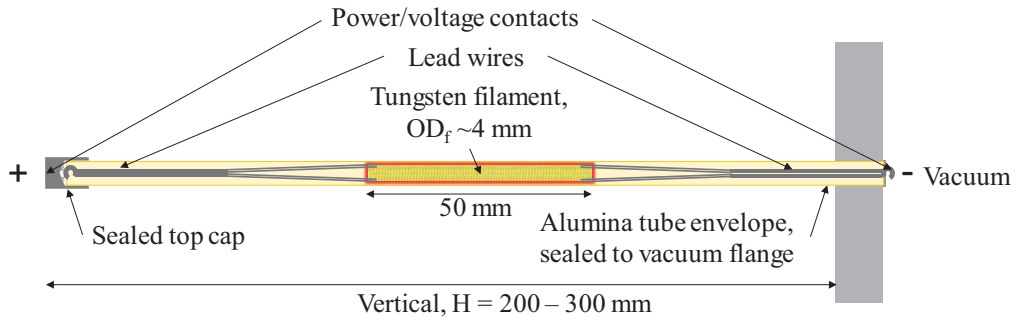

FIGURE 1 | Schematic of the prototype heater unit. The filament is 50 mm long in the mounted position with 100 active coils. The heater dimensions closely resemble that of a pencil.

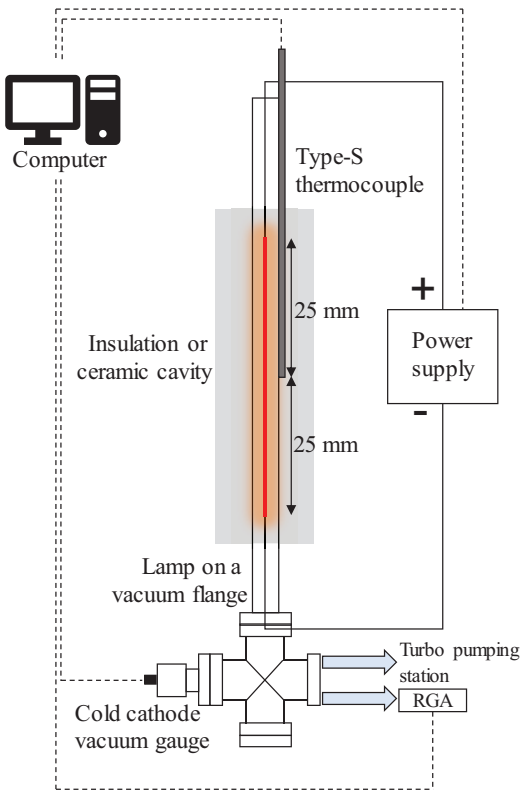

FIGURE 2 | Schematic of the heater experimental test stand. The thermocouple tip is positioned next to the center of the hot zone.

alumina-protected B-type thermocouples. The results are nearly identical, within 1 K of errors.

A turbo pumping station (HiCube 80 Eco, Pfeiffer Vacuum, Nashua, NH, United States) maintained a UHV environment ($p < 2{\cdot}10^{-6}$ Pa), measured with a cold cathode ionization gauge (CCG–525, Duniway Stockroom Corp., Fremont, CA, United States). A residual gas analyzer (RGA200, Stanford Research Systems, Sunnyvale, CA, United States), connected to the test stand, enabled gas analysis, leak checking, and monitoring of the partial pressures of the oxidizing gases, particularly O_2 and H_2O. Routine baking of the vacuum system to 393–423 K following every exposure to the atmosphere minimized filament deterioration from high-T oxidation by residual H_2O.

The **Supplementary Material** contains additional results of the heater performance, including temperature profiles of a single heater at 350–400 K min^{-1} heating/cooling rates for over 2,000 cycles, filament current response with respect to instant power shifts between 15 and 145.5 W, a heater reaching a steady temperature of 1,835 K, and the cavity temperature response with a single heater under steadily increasing (up to 190 W) and cyclic (58.5 and 190 W) power outputs.

RESULTS AND DISCUSSION

High Temperature and Rapid Response Tests

Guided by the needs of a myriad of processes, including thermochemical cycles, one of the design goals of the heater is the ability to cycle rapidly in temperature. We evaluated this attribute of the heater in detail by placing a S-type thermocouple in immediate proximity to the alumina envelope, in the center of the hot zone. Additionally, to minimize external thermal inertia influence on the measurements, we used a lightweight (i.e., low heat capacity) alumina-insulating blanket and wrapped it around the hot zone and the thermocouple.

Figure 3 shows the temperature measurements of the thermocouple when the heater (using a Ø0.254 mm filament) was subject to a campaign of cyclic power input of 22.5 W (30 s) and 84 W (30 s). After more than ~2,000 continuous cycles, the heater exhibited a consistent rapid response, achieving a heating/cooling rate of 350–400 K min^{-1} in the range between 1,365 and 1,570 K. For further details, **Supplementary Figure 1** shows several temperature profiles during distinct stages of the campaign. These results confirm the expected low thermal inertia of the heater and its ability to rapidly modulate power and temperature as a primary heater source. Equally importantly, the off-the-shelf thin-wall tubular geometry, operating with one unconstrained end, demonstrated excellent resilience with respect to thermal cycling. Of note is that thinner wall tubes (0.5 mm) from a different manufacturer (Kyocera, Kyoto, Japan)

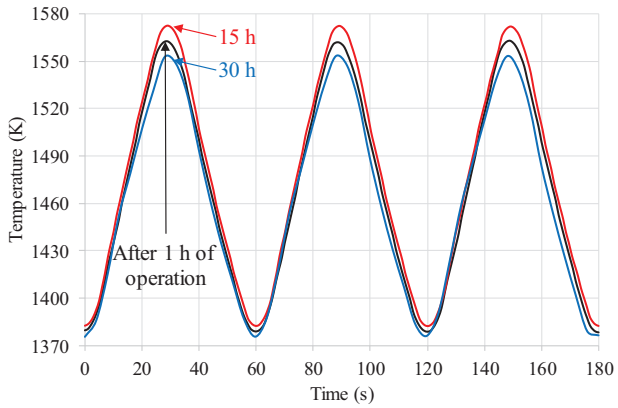

FIGURE 3 | Temperature profiles of a single heater (Ø 0.254 mm) at 350 K min^{-1} rapid heating/cooling rate, over 2,000 cycles (30 s heating and 30 s cooling per cycle). Representative 3 cycles after 1 h (black), 15 h (red) and 30 h (blue) of operation.

are also able to maintain UHV and are resilient to cycling, giving confidence that the design is sound when used with alumina tubes from other reputable sources.

To extend the temperature range and to evaluate the cycling response, especially in a region relevant for the thermal reduction reaction temperature of 1,723 K in two-step thermochemical water and CO_2 splitting (U.S. Department of Energy, n.d.), we further conducted a 4-day campaign with 6–8 h per day of cycling time at a peak temperatures of 1,723 K. **Figure 4** shows the cumulative cycling profiles with the daily initial heating and final cooling steps truncated. **Figure 4A** shows the overall temperature consistency of over 700 cycles for a total uptime of over 23.3 h. The heater was able to perform 2-min cyclic swings between 1,523 and 1,723 K, and again demonstrated consistent temperature profiles at a heating/cooling rate of ∼200 K min^{-1} (**Figure 4B**). The heating/cooling rate at this temperature range is on par with that of state-of-the-art infrared gold image furnaces (Advance Riko, Kanagawa, Japan, 200–500 K min^{-1} in thermal cycling tests), in a much less costly heater package (Hackenberger and Speyer, 1994).

Another measure of heater response is the filament temperature, which can be estimated from its resistivity (**Supplementary Figure 2**). During instant power shifts between 15 and 145.5 W every 20 s, the filament current (I_{fil}) rise/fall time, corresponding to 90% of the difference between the initial and final I_{fil} value, is ∼2.25 s. The I_{fil} change rate (1 A/s) corresponds to a temperature change rate of ∼500 K s^{-1}. In this context, heating/cooling rates measured by external thermocouples could be considered a significant underestimate of the heater response itself. Of note is that the ramp rate of the heaters is on par with those of solar simulators, with the benefit of using cost-effective, well-characterized, and widely available materials without the need for an optical aperture—a major advantage in terms of re-radiation losses and cavity design simplicity.

The maximum steady-state temperature measured with a Ø0.254 mm and L = 50 mm filament was ∼1,835 K, limited by the S-type thermocouple, and was achieved at a power input of 90 W (**Supplementary Figure 3**). This temperature is sufficient even for demanding high-temperature processes such as thermochemical H_2O/CO_2 splitting reactions (Kodama, 2003; Steinfeld, 2005). We can routinely reach lower temperatures than those presented here. Nevertheless, such temperatures are well within reach of resistance wire heaters, and thus we focused on the higher temperatures.

High Power and High-Power Density Tests

To evaluate the capability of the heater to deliver higher power and to scale up the heated volume, we fabricated a cavity test stand, which is illustrated in **Figure 5**. The cavity models a working environment of a high-temperature process using the heaters as the core heating component. The cavities used high temperature (up to 1,800 K) insulating firebrick and were 76 mm long and 35 mm in diameter, with sufficient space for multiple heaters. Placing the thermocouple ∼5 mm from

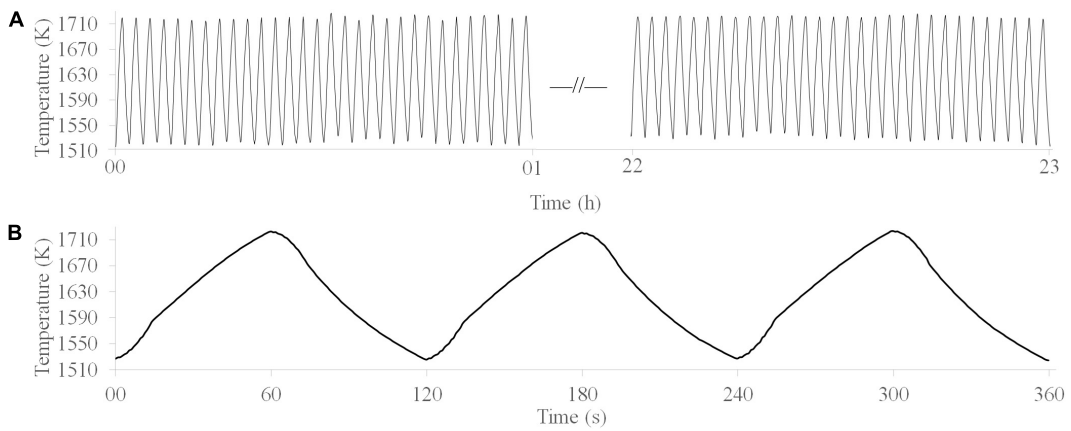

FIGURE 4 | High-temperature cycling performance of a single heater (Ø 0.254 mm) between 1,523 and 1,723 K. **(A)** Extended temperature profiles of 700 cycles over 23.3 h of continuous operation (1 min heating and 1 min cooling per cycle). **(B)** Representative temperature profiles of 3 cycles after ∼10 h of operation.

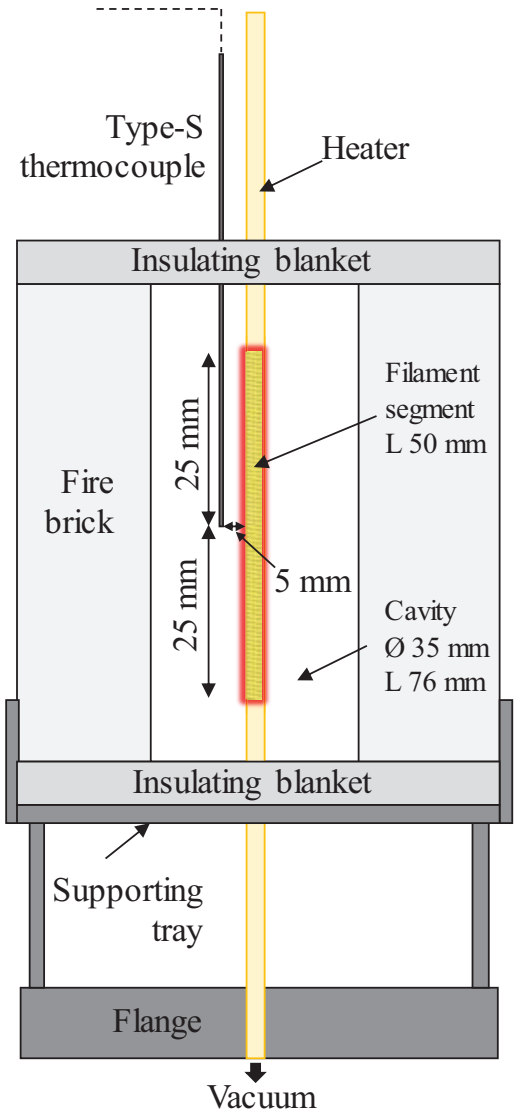

FIGURE 5 | Setup for the volumetric heating capability. The thermocouple tip is positioned in-plane to the central hot zone, 5 mm away from the envelope wall.

the inner cavity wall, in plane with the centers of the 50-mm lengthwise filament heated zones, facilitates measurement of the temperature resulting from the coupling of the radiation from the heaters and the re-radiation from the cavity.

Throughout the development of the heaters, maximizing power output per heater while minimizing stress on the filaments, and especially on the envelopes, and therefore minimizing failures, has been an ongoing goal. The filaments described in the previous section are able to achieve a linear power density of $\prod \sim 30\ \mathrm{W\ cm^{-1}}$, but only when operating at an estimated temperature of ∼2,700 K, i.e., much higher than the rated temperature of the alumina envelope. The filaments also required maximization of the coil diameter (to maximize the filament length), which left minimal clearance (<0.3 mm) from the envelope wall. We identified high temperatures and small clearances as a key risk factor for localized heating and consequent envelope failures. To mitigate this failure, we modified the initial design and increased the wire diameter to Ø0.3048 mm, permitting a decrease in coil diameter to $OD_f \sim 3.2$ mm and an increase in wall clearance (0.7 mm) to evaluate at higher power.

The above changes allowed an increased power output to over 180 W, twice that of the Ø0.254 mm filament. Simply put, the improvement allowed the heater to reach higher power density under milder conditions. **Supplementary Figure 4** shows the temperature response in the cavity with a single heater with the increased Ø0.3048 mm filament, reaching a cavity temperature of ∼1,159 K. We further characterized the cyclic temperature response inside the cavity by continuously operating a single heater between 58.5 (1 min) and 190 W (1 min) for over 70 h. **Supplementary Figure 5** shows the temperature profile of the middle 10 h (30–40 h). The heating/cooling rate inside the cavity shows a consistent ∼130 K $\mathrm{min^{-1}}$. The maximum (∼1,080 K) and minimum (∼950 K) temperatures per cycle consistently show a negligible variation (±3 K).

The above results motivate the potential of using multiple heaters inside the cavity to boost temperature output at a lower current density per heater. **Figures 6A,B** show a three-heater setup. The modularity of the heaters enables scale-up by adding units inside the same cavity without significant modification. **Figure 6C** shows the cavity temperature response with respect to mild current increase of 0.25 A/heater every 5 min. The cavity reaches a temperature of 1,700 K, suitable for the reduction temperature in two-step redox-active metal–oxide thermochemical H_2O/CO_2 splitting, at a current of 4.25 A/heater and <70% of the heater power (∼375 W total or ∼125 W per heater).

Using multiple heaters also enables greater temperature uniformity in the cavity by creating a partial surround radiation bath. **Figure 7** shows the characterization of the temperature distribution inside the three-heater cavity, which confirms this effect. The distribution results from an interpolation of 15 temperature points spanning across the central vertical plane, measured by a bare-tip S-type thermocouple. The thermocouple tip was moved sequentially to each point, and the temperature was recorded upon reaching equilibrium. The experiment was re-evaluated with a B type thermocouple in an alumina protective tube, which showed near-identical results within 1 K. With a steady-state central maximum of 1,777 K, a minimum of ∼1,500 K (15.6% lower) occurs near the lower side on the cavity wall. Restricting convection between the cavity and the ambient environment through the top and bottom openings should further reduce the temperature non-uniformity.

The three-heater test provides another key result: a surround reactor cavity geometry where the interior is uniformly and radiatively coupled to the heater filaments may leave significant room to decrease the filament temperature by duplication of a few heaters and yet achieve high cavity temperatures, addressing the main heater limitation, namely, the envelope temperature rating. To achieve the best application-specific performance, it is necessary to optimize the filament wire diameters in conjunction with application specifics, such that the filament temperature,

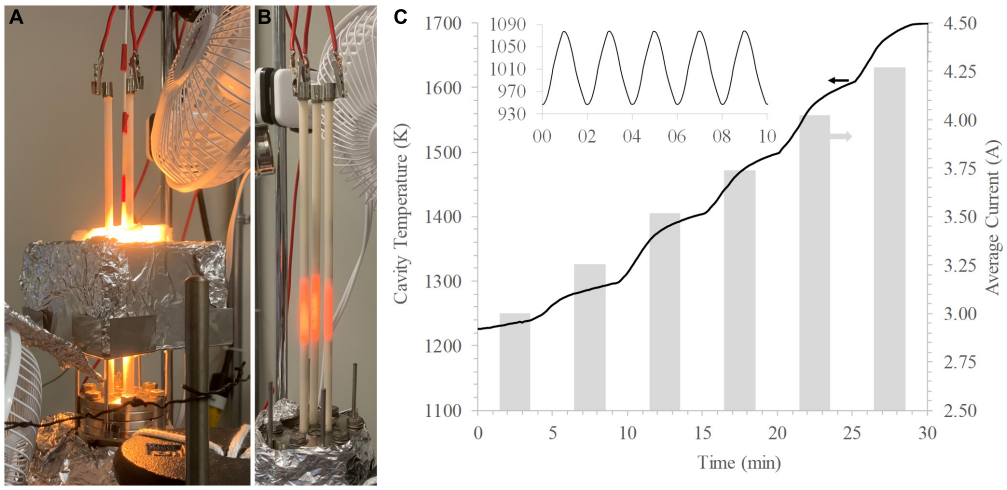

FIGURE 6 | (A) Three heaters (Ø 0.3048 mm) operating inside a firebrick cavity. **(B)** Direct view of the three heaters. **(C)** Temperature inside the cavity reaching 1,700 K at a current of 4.25 A/heater with three heaters. **(C)** Insert: Fast heating cooling (~130 K min^{-1}) with a single heater in the same setup.

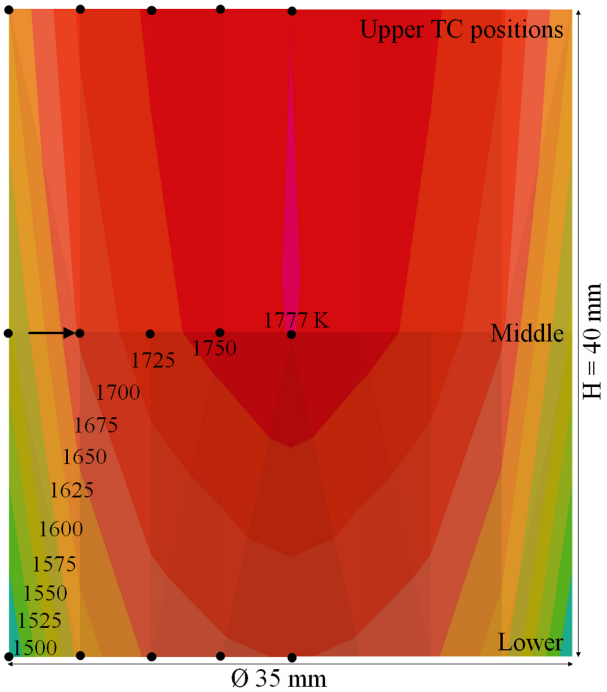

FIGURE 7 | Temperature distribution measured by a single thermocouple inside the firebrick cavity with 3 heaters (Ø 0.381 mm) and total power of 386.8 W. The dots indicate the 15 temperature points where the bare thermocouple tip was positioned. The arrow indicates the orientation of the thermocouple with respect to a particular point.

under the desired operating conditions, does not exceed the envelope temperature rating (2,150 K in the case of alumina but higher for other suitable ceramics). In this study, the envelope temperature rating was used as the maximum working temperature of the filament. Thus, the optimal wire diameter was determined based on the resistivity as a function of temperature, a fundamental and well-characterized relationship for tungsten.

It is worth noting that even the smaller OD_f filaments fill most of the envelope ID. Furthermore, with the thickest wires used in our experiments and considering dense coils, no "gaps" in the filaments exist when observed from the side. These geometrical details make it possible to create a surround geometry using a small number of concentric heater layers, in which all radial lines of sight terminate at a filament. Coupled with the fast filament response time, such geometries offer the possibility of achieving at a low cost cavity temperature changes of several hundred K s^{-1} for materials (such as redox active metal oxide materials) placed in the cavity.

Due to the characteristics of tungsten filaments, the heaters can provide reliable output even under imperfect power conditions, such as voltage spikes and frequency fluctuations, making them compatible with a wide range of power supply units. Moreover, our experimental experience and the simplicity of the design suggest that the cost to manufacture the heaters can be as little as $0.05/W, at scale.

CONCLUSION

The radiant heater fulfills the design principle of utilizing low-cost manufacturing techniques and materials while generating substantial heat output in compact and modular units. Consistent performance of generating high-T (>1,800 K) and rapid response (up to 400 K min^{-1}) with respect to modulated power inputs provides a compelling demonstration of the design principle. Simply assembling multiple identical units achieved our objective of volumetric high-density heating, which paves the way for easy scale-up and adaptation into emerging applications, such as thermochemical processes, and offers fast-response high-temperature heating solutions. Due to their inherent robustness, the heaters can use inexpensive power supplies and/or operate

in environments with imperfectly conditioned power input. Heaters using renewable electricity will be particularly attractive in sustainable (e.g., thermochemical) production of chemicals and energy carriers, such as syngas, light olefins, ammonia, methanol, and aromatics. The low manufacturing and operating cost of the heaters can enable low-cost production of chemical commodities. In research and practice, these radiant heaters could offer multiple benefits compared to solar simulators, lasers, infrared gold furnaces, or ceramic heaters.

DATA AVAILABILITY STATEMENT

The original contributions presented in the study are included in the article/**Supplementary Material**, further inquiries can be directed to the corresponding author/s.

AUTHOR CONTRIBUTIONS

XG and IE conducted the core design of the heaters and experiments. ES assisted in the design of the heaters. XG fabricated/characterized the heaters, collected/interpreted data from the experiments, and prepared the manuscript. MB assisted in fabrication/characterization of the heaters and data collection/interpretation. XG, IE, and ES revised the manuscript. IE and ES supervised and funded this work. All authors contributed to the article and approved the submitted version.

FUNDING

This study was based on work supported by the U.S. Department of Energy under Award No. DE–EE0008991.

ACKNOWLEDGMENTS

We wish to acknowledge the team and institutions involved in this work: Arizona State University, Oregon State University, Siemens Corporate Technology, Sandia National Laboratories, and Southwest Research Institute. The assistance in heater fabrication by Brandon Palafox and design by Ryan Milcarek is gratefully acknowledged.

SUPPLEMENTARY MATERIAL

The Supplementary Material for this article can be found online at: https://www.frontiersin.org/articles/10.3389/fenrg.2021.652203/full#supplementary-material

Supplementary Figure 1 | Temperature profiles of a single heater (Ø0.254 mm) at 350–400 K min^{-1} rapid heating/cooling rate, over 2,000 test cycles (30 s heating and 30 s cooling per cycle). **(A)** The first 250 cycles of the campaign. **(B)** The middle 200 cycles of the campaign. **(C)** The 350 cycles near the end of the campaign.

Supplementary Figure 2 | Filament current response (I_{fil}) of a single heater (Ø0.3048 mm) inside the cavity when cycling between 15 (1.93 A) and 145.5 W (4.55 A) power outputs every 20 s. Note the two I_{fil} transient regimes: a fast one (2–3 s) corresponding to filament heating/cooling, and a slower one (∼20 s) corresponding to heating/cooling of the internal lead wires.

Supplementary Figure 3 | (A) A heater (Ø0.254 mm) reaching a steady temperature of 1,835 K at a power input of approximately 90 W. **(B)** The thermocouple is located next to the ceramic envelope wall, secured by alumina insulation.

Supplementary Figure 4 | Cavity temperature response with a single heater (Ø0.3048 mm) reaching 190 W (5 A) power output.

Supplementary Figure 5 | Cavity temperature response with a single lamp heater (Ø0.3048 mm) when cycling between 58.5 (3.25 A) and 190 W (5 A) power outputs.

REFERENCES

Bradley, D., and Entwistle, A. G. (1961). Determination of the emissivity, for total radiation, of small diameter platinum-10% rhodium wires in the temperature range 600-1450∼C. *Br. J. Appl. Phys.* 12, 708–711. doi: 10.1088/0508-3443/12/12/328

De Vos, J. C. (1954). A new determination of the emissivity of tungsten ribbon. *Physica* 20, 690–714. doi: 10.1016/S0031-8914(54)80182-0

Hackenberger, W. S., and Speyer, R. F. (1994). A fast-firing shrinkage rate controlled dilatometer using an infrared image furnace. *Rev. Sci. Instrum.* 65, 701–706. doi: 10.1063/1.1145088

Harris, D. C., Johnson, L. F., Cambrea, L. R., Baldwin, L., Baronowski, M., Zelmon, D. E., et al. (2017). Refractive index of infrared-transparent polycrystalline alumina. *Opt. Eng.* 56:077103. doi: 10.1117/1.OE.56.7.077103

He, R., Fang, D., Wang, P., Zhang, X., and Zhang, R. (2014). Electrical properties of ZrB2-SiC ceramics with potential for heating element applications. *Ceram. Int.* 40, 9549–9553. doi: 10.1016/j.ceramint.2014.02.029

He, R., Tong, Z., Zhang, K., and Fang, D. (2018). Mechanical and electrical properties of MoSi2-based ceramics with various ZrB2-20 Vol% SiC as additives for ultra high temperature heating element. *Ceram. Int.* 44, 1041–1045. doi: 10.1016/j.ceramint.2017.10.043

Hindasageri, V., Vedula, R. P., and Prabhu, S. V. (2013). Thermocouple error correction for measuring the flame temperature with determination of emissivity and heat transfer coefficient. *Rev. Sci. Instrum.* 84:24902. doi: 10.1063/1.4790471

Jenkins, B., and Mullinger, P. (2008). *Industrial and Process Furnaces*. Oxford: Butterworth-Heinemann.

Kim, B. N., Hiraga, K., Morita, K., Yoshida, H., Miyazaki, T., and Kagawa, Y. (2009). Microstructure and optical properties of transparent alumina. *Acta Mater.* 57, 1319–1326. doi: 10.1016/j.actamat.2008.11.010

Kodama, T. (2003). High-temperature solar chemistry for converting solar heat to chemical fuels. *Prog. Energy Combust. Sci.* 29, 567–597. doi: 10.1016/S0360-1285(03)00059-5

Larrabee, R. D. (1959). Spectral emissivity of tungsten†. *J. Opt. Soc. Am.* 49, 619–625. doi: 10.1364/JOSA.49.000619

MacIsaac, D., Kanner, G., and Anderson, G. (1999). Basic physics of the incandescent lamp (Lightbulb). *Phys. Teach.* 37, 520–525. doi: 10.1119/1.880392

Roberts, I. L., Coney, J. E. R., and Gibbs, B. M. (2011). Estimation of radiation losses from sheathed thermocouples. *Appl. Therm. Eng.* 31, 2262–2270. doi: 10.1016/j.applthermaleng.2011.03.020

Steinfeld, A. (2005). Solar thermochemical production of hydrogen—-a review. *Sol. Energy* 78, 603–615. doi: 10.1016/j.solener.2003.12.012

Tank, V., and Dietl, H. (1990). Multispectral infrared pyrometer for temperature measurement with automatic correction of the influence of emissivity. *Infrared Phys.* 30, 331–342. doi: 10.1016/0020-0891(90)90049-2

The Rebound Effect: An Assessment of the Evidence for Economy-Wide Energy Savings from Improved Energy Efficiency | UKERC | The UK Energy Research Centre. (n.d.) Available online at: https://ukerc.ac.uk/publications/the-rebound-effect-an-assessment-of-the-evidence-for-economy-wide-energy-savings-from-improved-energy-efficiency/ (accessed April 9, 2021).

U.S. Department of Energy (n. d.). *Hydrogen and Fuel Cell Technologies Office Multi-Year Research, Development, and Demonstration Plan | Department of Energy*. Available online at: https://www.energy.gov/eere/fuelcells/downloads/hydrogen-and-fuel-cell-technologies-office-multi-year-research-development (accessed March 3, 2021)

Urbas, J., Parker, W. J., and Luebbers, G. E. (2004). Surface temperature measurements on burning materials using an infrared pyrometer: accounting for emissivity and reflection of external radiation. *Fire Mater.* 28, 33–53. doi: 10.1002/fam.844

Van Geem, K. M., Galvita, V. V., and Marin, G. B. (2019). Making chemicals with electricity. *Science* 364, 734–735. doi: 10.1126/science.aax5179

Conflict of Interest: A U.S. provisional patent application for this invention entitled "High-Temperature Heater Lamp" has been filed on Dec 9, 2019 with a Serial No. 62/945,835.

frontiers in Energy Research

OPINION
published: 14 May 2021
doi: 10.3389/fenrg.2021.666191

Hydrogen Production by Solar Thermochemical Water-Splitting Cycle via a Beam Down Concentrator

Alberto Boretti[1,2]*, *Jamal Nayfeh*[2] *and Ayman Al-Maaitah*[3]

[1] Deanship of Research, Prince Mohammad Bin Fahd University, Al Khobar, Saudi Arabia, [2] College of Engineering, Prince Mohammad Bin Fahd University, Al Khobar, Saudi Arabia, [3] Wahaj Investment L.L.C., Dubai, United Arab Emirates

Keywords: concentrated solar energy, thermochemical water splitting cycles, hydrogen, thermal energy storage, S-I cycle

INTRODUCTION

About 95% of the hydrogen presently produced is from natural gas and coal, and the remaining 5% is generated as a by-product from the production of chlorine through electrolysis[1]. In the hydrogen economy (Crabtree et al., 2004; Penner, 2006; Marbán and Valdés-Solís, 2007), hydrogen is produced entirely from renewable energy. The easiest approach to advance renewable energy production is through solar photovoltaic and electrolysis, a pathway of high technology readiness level (TRL) suffering, however, from two downfalls. First of all, electricity is already an energy carrier, and transformation with a penalty into another energy carrier, hydrogen, is, in principle, flawed. The second problem is that the efficiency of commercial solar panels is relatively low. The cadmium telluride (CdTe) thin-film solar cells have a solar energy conversion efficiency of 17%. Production of hydrogen using the current best processes for water electrolysis has an efficiency of ∼70%. As here explained, the concentrated solar energy may be used to produce hydrogen using thermochemical water-splitting cycles at much global higher efficiency (fuel energy to incident sun energy). This research and development (R&D) effort is, therefore, undertaken to increase the TRL of this approach as a viable and economical option.

THERMOCHEMICAL WATER-SPLITTING CYCLES

Solar thermochemical water-splitting cycles (TWSCs) use high-temperature solar heat to drive a series of reactions producing hydrogen with oxygen as a welcomed by-product (Safari and Dincer, 2020). The chemicals used are recycled, creating a closed-loop process utilizing only water as feedstock, plus solar heat. The simplest TWSC is a two-step process. The metal oxide redox reactions include one endothermic reaction and one exothermic reaction. The metal oxide is transformed first into a reduced-valence metal oxide plus oxygen.

$$MO_{ox} \rightarrow MO_{red} + ½O_2 \quad (1)$$

The reduced-valence metal oxide then reacts with H_2O producing H_2, oxygen, and the initial metal oxide.

$$MO_{red} + H_2O \rightarrow MO_{ox} + H_2 \quad (2)$$

[1] www.irena.org/-/media/Files/IRENA/Agency/Publication/2019/Sep/IRENA_Hydrogen_2019.pdf.

Edited by:
Emanuela Mastronardo, University of Messina, Italy

Reviewed by:
Francesco Rovense, Rey Juan Carlos University, Spain

***Correspondence:**
Alberto Boretti
deanshipofresearch@pmu.edu.sa

Specialty section:
This article was submitted to Solar Energy, a section of the journal Frontiers in Energy Research

Received: *09 February 2021*
Accepted: *10 March 2021*
Published: *14 May 2021*

Citation:
Boretti A, Nayfeh J and Al-Maaitah A (2021) Hydrogen Production by Solar Thermochemical Water-Splitting Cycle via a Beam Down Concentrator. Front. Energy Res. 9:666191. doi: 10.3389/fenrg.2021.666191

The metal oxide is, thus, recycled. These cycles require temperatures well above 1,500°C. A TWSC with more than two steps has been designed to deliver better performances at lower temperatures. The general electric sulfur–iodine (S-I) TWSC is the most renowned three-step TWSC (Schultz, 2003; Bhosale et al., 2019). It is made up of two endothermic steps and one intermediate exothermic step.

$$H_2SO_4 \rightarrow SO_2 + H_2O + \tfrac{1}{2}O_2 \quad (3)$$

$$I_2 + SO_2 + 2H_2O \rightarrow 2HI + H_2SO_4 \quad (4)$$

$$2HI \rightarrow I_2 + H_2 \quad (5)$$

The intermediate step is exothermic, the other two endothermic. Sink et al. (2009) suggests 850–900°C for the endothermic reaction (3), 400–500°C for the endothermic reaction (5), and 100°C for the exothermic reaction (4). While even lower temperatures have been proposed (Russ, 2009), the efficiency of the cycle increases by increasing the temperature of the reaction (3). It is η∼52% at a temperature of 900°C, and η∼60% at a temperature of 1,000°C (Schultz, 2003). As a downfall, the environment is, however, corrosive on the reactor side, and the supply of high-temperature solar heat is also challenging. This cycle has been extensively studied (Norman et al., 1982; Anzieu et al., 2006; Vitart et al., 2006; Zhou et al., 2007; Cerri et al., 2010; Zhang et al., 2010; Liberatore et al., 2012; Park et al., 2019), with technological advances still needed. Opposite to direct solar thermochemical water splitting into an integrated receiver/reactor (Chueh et al., 2010) presently featuring a very low TRL, the TRL of the indirect solar thermochemical hydrogen production is medium.

AYMAN SOLAR CONCENTRATOR

While the cycle was originally developed for nuclear heat, it is the use of solar heat that may revive the technology, thanks to improvements in solar concentrators' technologies, and the formulation of higher-temperature molten salts/liquid metal heat transfer fluids (HTF)/heat storage fluids (HSF). Thermal energy storage (TES) is mandatory for the dispatchability of electricity and continuous thermochemical hydrogen production.

To obtain such high temperatures, point-focusing solar concentrators should be used. Until recently, only two types of point solar concentrators are known and investigated. The first type is the parabolic dish, which can reach very high concentration ratios reaching very high temperatures at the focal point. The optical efficiency of the parabolic dish is high. Values from 78 to 89% were already achieved in the 1990s (Stine and Diver, 1994). A more recent study reported a 95% efficiency (Lovegrove et al., 2011). However, there are two disadvantages of the parabolic dish. The first is that its focal point is moving in space as the dish tracks the sun from sunrise to sunset. As such, the high-pressure and high-temperature HTF has to go through flexible pipes or rotary swivel joints to the storage tank, which is not practical at temperatures around 1,000°C. Also, high-temperature thermal storage of energy harvested from the parabolic dish is not practical. Moreover, the solid cross-sectional area of the parabolic dish results in high wind load on its structure pausing structural limitation on its size. Practically, no commercial parabolic dish with a diameter of more than 10 m is on the market. The other known point concentrator is the heliostat field and solar tower technology. Although this technology has a fixed focal point at the top of the tower, it has very low optical efficiency due to its heliostat tracking and reflecting concept. The beam-down variant with a fixed focal point at the ground is not any better. In theory, the optical efficiency is between 40 and 60%, even if some special design has delivered up to 63.9% efficiency (Wang et al., 2019), but in practice, it is even considerably less due to imperfect reflection over large distances. Moreover, the commercially available types can only reach temperatures below 600°C due to inaccuracies in the concentration procedures (receiver outlet temperature 565°C in Gemasolar, Ivanpah, and Crescent Dunes[2]). However, recently, Heliogen[3] has utilized artificial intelligence (AI) technology to increase the concentration accuracy allowing temperatures up to 1,000°C to be reached at the receiver. Nonetheless, the technology still has low optical efficiency and is quite expensive as it is still in the R&D phase.

Recently, Al-Maaitah (2017, 2019) has developed a high flux solar concentrator with a lower focal point fixed to the ground composed of nested conical reflective rings resulting in high solar concentrations and temperatures well above 1,000°C (Al-Maaita, 2020[4]). Since the focal point is fixed on the ground, then the high-temperature and high-pressure HTF can easily be conveyed through solid inexpensive pipes to the storage tank sitting at the ground underneath the receiver or next to it. A 10 m in diameter concentrator was built and tested in Masdar Institute Solar Platform in Abu Dhabi (UAE) where temperatures exceeding 1,000°C have been reached at the fixed focal point even at low DNI (Al-Maaita, 2020; see text footnote 4). One spherical or cylindrical receiver is used to heat HTF to the levels needed for the TWSC. The commercial name given to this concentrator is ASC (Ayman Solar Concentrator). The optical efficiency of the ASC is high and reaches 91% in practice, while it is 100% theoretically like the parabolic dish. Since the wind flows through its conical rings, the wind load of the ASC is about 10% that of the parabolic dish of the same dimensions. A 15-m ASC is designed and can be easily deployed, and a 25-m ASC is under design consideration. The system is modular, and many units can combine their inputs to a fixed storage tank to have a large storage capacity.

ASC WITH THERMAL ENERGY STORAGE AND THERMOCHEMICAL WATER-SPLITTING CYCLES

Between the different HTFs being considered, one receiving attention is $MgCl_2$-KCl (Ding et al., 2018; Polimeni et al.,

[2] solarpaces.nrel.gov/by-technology/power-tower.

[3] heliogen.com.

[4] www.cmimarseille.org/menacspkip/wp-content/uploads/2018/09/8.B.-Wahaj-Invest-Ayman-Al-Maaitah.pdf.

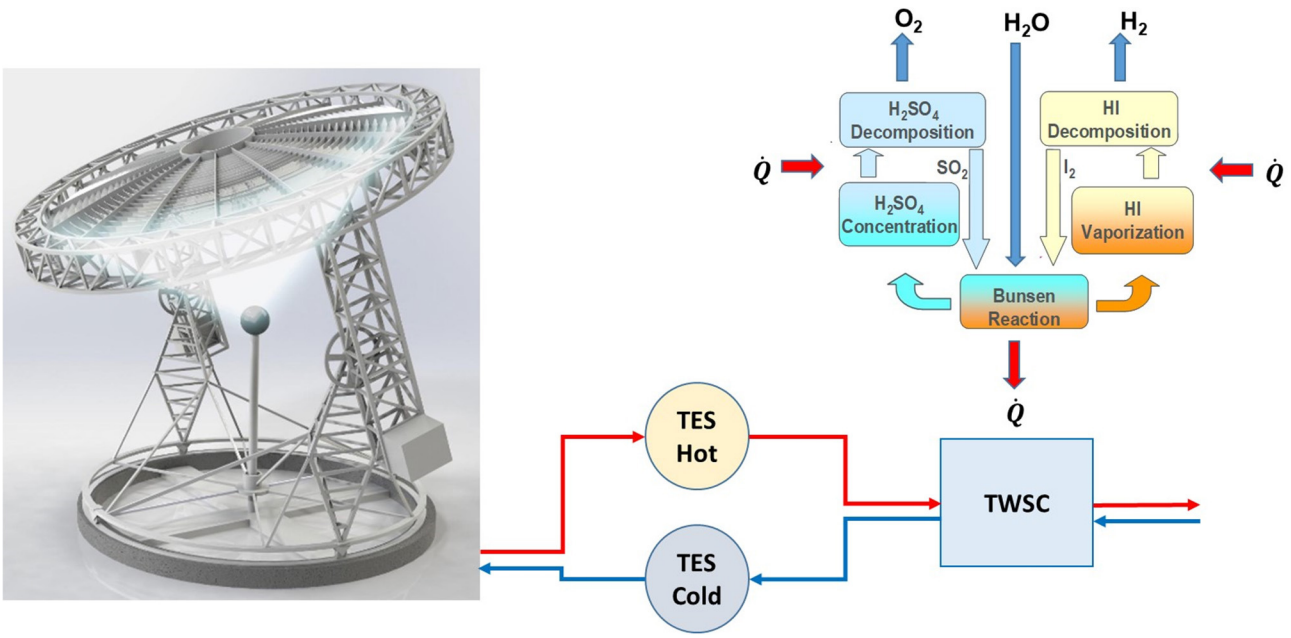

FIGURE 1 | Scheme of the upstream Ayman Solar Concentrator (ASC) with thermal energy storage (TES), plus the downstream thermochemical water-splitting cycle (TWSC).

2018; Xu et al., 2018; Kurley et al., 2019; Peng, 2019; Vidal and Klammer, 2019; Wu et al., 2019; Fernández and Cabeza, 2020a,b,c). $MgCl_2$-KCl is 37.5% $MgCl_2$ and 62.5% KCl. It can be used between 426°C and 1,412°C. Within this range of temperatures, c_p varies between 0.989 and 1.092 kJ kg^{-1} K^{-1}, ρ between 1,668.5 and 1,124.3 kg m^{-3}, μ between $5.73 \cdot 10^{-3}$ and $8.57 \cdot 10^{-3}$ Pa s, λ between 0.46 and 0.36 W m^{-1} K^{-1}, and h between 421,391 and 1,542,352 J kg^{-1}. $\rho \cdot c_p$ varies between 1,650.5 and 1,228.1 $\rho \cdot c_p$ kJ m^{-3} K^{-1}.

The sulfur-iodine (S-I) TWSC (i.e. Ross, 2009) is adopted. Other metal oxide three steps are investigated (Charvin et al., 2007; Bhosale, 2020).

The opportunity of using TLC components upstream of the TWSC section and synergy between applications (basically the same design of concentrator and storage applies for the production of electricity or hydrogen) reduce the total cost of R&D, more intense on the TWSC side. Efficiency and durability of reactant materials, and efficient and robust reactor designs compatible with high temperatures and corrosive environments are major challenges.

Figure 1 presents a scheme of the upstream ASC with TES, plus the downstream TWSC. The metallic lenses focus the solar energy on the point receiver. The cold HFT from the cold TES reservoir passes through the receiver to reach the hot TES reservoir. The hot HTF then supplies the thermal energy needed by the TWSC. While the design of the ASC and TES is relatively simple, the design of the TWSC is much more complicated, requiring multiple different reactor sections and heat exchangers. The waste heat may also be recovered.

The ASC has a much better collection efficiency compared with a field of heliostat and a tower receiver [91% (Al-Maaita, 2020; see text footnote 4) compared with, only in special cases, 63.9% (Wang et al., 2019)]. Storage can be done at high temperatures (1,100°C within easy reach). Importantly, it is much less costly to have a demonstration pilot plant than in a concentrated solar power, solar tower, and plant (Boretti et al., 2019). Moreover, the ASC is being developed anyway for high-temperature solar heat production, and thermal energy storage, coupled to continuous electricity production through high-temperature power cycles.

Opposite to the direct solar thermochemical water splitting into an integrated receiver/reactor (Chueh et al., 2010), the proposed solution permits a much more complex, but less challenging, chemical plant, not subjected to thermal transients, receiving heat and not direct solar energy, and without the extremely tight space constraints making the catalytic chemical processes hard to progress.

DISCUSSION AND CONCLUSIONS

Green hydrogen is booming, and the preferred technology is solar photovoltaic plus electrolysis[5]. The projected cost is 1.5 US$ per kg of H_2 by 2050. By using about the same solar concentrator and collector, plus TES, of high temperature concentrated solar power to feed a TWSC, there is the opportunity to achieve even better costs of 1–1.5 US$ per kg and much earlier. Kayfeci et al. (2019) suggests a cost of 2.17–2.63 US$ per kg of H_2 from nuclear thermolysis. Novel solar concentrators may produce thermal energy at a cost less than the cost of nuclear thermal energy. This

[5]hydrogencouncil.com/wp-content/uploads/2021/02/Hydrogen-Insights-2021-Report.pdf.

cost is competitive with the current steam reforming of methane without CO2 capture and storage (Boretti, 2020).

ASC with TES may deliver solar heat continuously at temperatures up to 1,100°C. TWSC three steps, originally developed for nuclear hydrogen production, may return popular for solar thermal.

Synergies with power generation are beneficial. The upstream section of solar energy collection and storage is unaltered. The downstream section is specialized for electricity production, hydrogen production, or other high-temperature thermal processes. The three-step S-I already was developed up to a medium-high technology readiness level (TRL) (Boretti, 2021) when the interest in nuclear hydrogen dropped following the Fukushima Daiichi nuclear accident of 2011. By assuming the development of a high-temperature solar concentrator and collector, plus TES will progress independently for power generation, the only research and development effort is the one needed to further optimize the TWSC.

AUTHOR CONTRIBUTIONS

AB: conceptualization. AB, JN, and AA-M: writing—original draft preparation and writing—review and editing. AA-M and AB: visualization. All authors have read and agreed to the published version of the manuscript.

REFERENCES

Al-Maaita, A. A. (2020). "Design and demonstration of a 10-meter metallic reflector-based fresnel lens, with lower focal point fixed to the ground," in *Proceedings of the 26th SolarPACES Conference, Sept. 28-October 2nd, 2020*. Available online: cms2020.solarpaces-conference.org/file/display_attachment/ab37be5b91c0133a162b848b87bcc27?filename=Ayman+Al-Maaitah+-+Paper.pdf (accessed February 01, 2021).

Al-Maaitah, A. A. (2017). *Method and Apparatus for Tracking and Concentrating Electromagnetic Waves Coming From a Moving Source to a Fixed Focal Point*. U.S. Patent No. 9,772,121B1, Alexandria, VA: United States Patent and Trademark Office (USPTO).

Al-Maaitah, A. A. (2019). *Systemfor Collecting Radiant Energy with a Non-Imaging Solar Concentrator*. U.S. Patent No. US 10,436,182B2, Alexandria, VA: United States Patent and Trademark Office (USPTO).

Anzieu, P., Carles, P., Duigou, A. L., Vitart, X., and Lemort, F. (2006). The sulphur–iodine and other thermochemical process studies at CEA. *Int. J. Nuclear Hydrog. Product. Appl.* 1, 144–153. doi: 10.1504/IJNHPA.2006.011248

Bhosale, R. R. (2020). A novel three-step GeO_2/GeO thermochemical water splitting cycle for solar hydrogen production. *Int. J. Hydrog. Energy* 45, 5816–5828. doi: 10.1016/j.ijhydene.2019.05.190

Bhosale, R. R., Takalkar, G., Sutar, Kumar, A., AlMomani, F., and Khraisheh, M. (2019). A decade of ceria based solar thermochemical H_2O/CO_2 splitting cycle. *Int. J. Hydrog. Energy* 44, 34–60. doi: 10.1016/j.ijhydene.2018.04.080

Boretti, A. (2020). Perspectives of production of hydrogen for export from wind and solar energy, natural gas, and coal in Australia. *Int. J. Hydrogen Energy* 47, 3899–3904.

Boretti, A. (2021). Technology readiness level of solar thermochemical splitting cycles. *ACS Energy Lett*. 6, 1170–1174. doi: 10.1021/acsenergylett.1c00181

Boretti, A., Castelletto, S., and Al-Zubaidy, S. (2019). Concentrating solar power tower technology: present status and outlook. *Nonl. Eng.* 8, 10–31. doi: 10.1515/nleng-2017-0171

Cerri, G., Salvini, C., Corgnale, C., Giovannelli, A., Manzano, D. D. L., Martinez, A. O., et al. (2010). Sulfur–Iodine plant for large scale hydrogen production by nuclear power. *Int. J. Hydrog. Energy* 35, 4002–4014. doi: 10.1016/j.ijhydene.2010.01.066

Charvin, P., Abanades, S., Lemort, F., and Flamant, G. (2007). Hydrogen production by three-step solar thermochemical cycles using hydroxides and metal oxide systems. *Energy Fuels* 21, 2919–2928. doi: 10.1021/ef0701485

Chueh, W. C., Falter, C., Abbott, M., Scipio, D., Furler, P., Haile, S. M., et al. (2010). High-flux solar-driven thermochemical dissociation of CO_2 and H_2O using nonstoichiometric ceria. *Science* 330, 1797–1801. doi: 10.1126/science.1197834

Crabtree, G. W., Dresselhaus, M. S., and Buchanan, M. V. (2004). The hydrogen economy. *Phys. Today* 57, 39–44. doi: 10.1063/1.1878333

Ding, W., Bonk, A., and Bauer, T. (2018). Corrosion behavior of metallic alloys in molten chloride salts for thermal energy storage in concentrated solar power plants: a review. *Front. Chem. Sci. Eng.* 12, 564–576. doi: 10.1007/s11705-018-1720-0

Fernández, A. G., and Cabeza, L. F. (2020a). Corrosion evaluation of eutectic chloride molten salt for new generation of CSP plants. Part 1: thermal treatment assessment. *J. Energy Storage* 27, 101125. doi: 10.1016/j.est.2019.101125

Fernández, A. G., and Cabeza, L. F. (2020b). Corrosion evaluation of eutectic chloride molten salt for new generation of CSP plants. Part 2: materials screening performance. *J Energy Storage* 29:101381. doi: 10.1016/j.est.2020.101381

Fernández, A. G., and Cabeza, L. F. (2020c). Cathodic protection using aluminum metal in chloride molten salts as thermal energy storage material in concentrating solar power plants. *Appl. Sci.* 10:3724. doi: 10.3390/app10113724

Kayfeci, M., Keçebaş, A., and Bayat, M. (2019). "Hydrogen production," in *Solar Hydrogen Production* (Cambridge, MA: Academic Press), 45–83. doi: 10.1016/B978-0-12-814853-2.00003-5

Kurley, J. M., Halstenberg, W., McAlister, A., Raiman, S., Dai, S., and Mayes, R. T. (2019). Enabling chloride salts for thermal energy storage: implications of salt purity. *RSC Adv.* 9, 25602–25608. doi: 10.1039/C9RA03133B

Liberatore, R., Lanchi, M., Caputo, G., Felici, C., Giaconia, A., Sau, S., et al. (2012). Hydrogen production by flue gas through sulfur–iodine thermochemical process: economic and energy evaluation. *Int. J. Hydrog. Energy* 37, 8939–8953. doi: 10.1016/j.ijhydene.2012.02.163

Lovegrove, K., Burgess, G., and Pye, J. (2011). A new 500 m2 paraboloidal dish solar concentrator. *Solar Energy* 85, 620–626. doi: 10.1016/j.solener.2010.01.009

Marbán, G., and Valdés-Solís, T. (2007). Towards the hydrogen economy? *Int. J. Hydrog. Energy* 32, 1625–1637. doi: 10.1016/j.ijhydene.2006.12.017

Norman, J. H., Mysels, K. J., Sharp, R., and Williamson, D. (1982). Studies of the sulfur-iodine thermochemical water-splitting cycle. *Int. J. Hydrog. Energy* 7, 545–556. doi: 10.1016/0360-3199(82)90035-0

Park, J., Lee, S. Y., and Lee, I. B. (2019). Study of alternative reactor–separator network in bunsen process of sulfur-iodine cycle for hydrogen production. *J. Chem. Eng. Jap.* 52, 638–649. doi: 10.1252/jcej.18we078

Peng, Y. (2019). *High-Temperature Corrosion Study of Alloys in Molten $MgCl_2$-KCl Eutectic Salt*. Tuscaloosa, AL: The University of Alabama.

Penner, S. S. (2006). Steps toward the hydrogen economy. *Energy* 31, 33–43. doi: 10.1016/j.energy.2004.04.060

Polimeni, S., Binotti, M., Moretti, L., and Manzolini, G. (2018). Comparison of sodium and KCl-$MgCl_2$ as heat transfer fluids in CSP solar tower with sCO_2 power cycles. *Sol Energy* 162, 510–524. doi: 10.1016/j.solener.2018.01.046

Russ, B. (2009). *Sulfur Iodine Process Summary for the Hydrogen Technology Down-Selection.* Process Performance Package [No. INL/EXT-12-25772]. Idaho Falls, ID: Idaho National Laboratory [INL].

Safari, F., and Dincer, I. (2020). A review and comparative evaluation of thermochemical water splitting cycles for hydrogen production. *Energy Convers. Manage.* 205:112182. doi: 10.1016/j.enconman.2019.112182

Schultz, K. (2003). *Thermochemical Production of Hydrogen from Solar and Nuclear Energy*. Presentation to the Stanford Global Climate and Energy Project. Available online at: web.stanford.edu/group/gcep/pdfs/hydrogen_workshop/Schultz.pdf (accessed February 01, 2021).

Sink, C., Sakaba, N., Yvon, P., Shin, Y. J., Dominguez, M. T., and Suppiah, S. (2009). "For the very high temperature reactor system," in *GIF Symposium* (Paris), 109.

Stine, W. B., and Diver, R. B. (1994). *A Compendium of Solar Dish/Stirling Technology. SAND-93-7026.* Albuquerque, NM: Sandia National Laboratories. doi: 10.2172/10130410

Vidal, J. C., and Klammer, N. (2019). "Molten chloride technology pathway to meet the US DOE sunshot initiative with Gen3 CSP," in *AIP Conference Proceedings, Vol. 2126* (Melville, NY: AIP Publishing LLC). doi: 10.1063/1.5117601

Vitart, X., Le Duigou, A., and Carles, P. (2006). Hydrogen production using the sulfur–iodine cycle coupled to a VHTR: an overview. *Energy Conv. Manage.* 47, 2740–2747. doi: 10.1016/j.enconman.2006.02.010

Wang, W. Q., Qiu, Y., Li, M. J., Cao, F., and Liu, Z. B. (2019). Optical efficiency improvement of solar power tower by employing and optimizing novel fin-like receivers. *Energy Convers. Manage.* 184, 219–234. doi: 10.1016/j.enconman.2018.12.029

Wu, F., Roy, S., Ivanov, A. S., Gill, S. K., Topsakal, M., Dooryhee, E., et al. (2019). Elucidating ionic correlations beyond simple charge alternation in molten $MgCl_2$-KCl mixtures. *J. Phys. Chem. Lett.* 10, 7603–7610. doi: 10.1021/acs.jpclett.9b02845

Xu, X., Wang, X., Li, Li, Y., Hao, Q., Xiao, B., Elsentriecy, H., et al. (2018). Experimental test of properties of KCl–$MgCl_2$ eutectic molten salt for heat transfer and thermal storage fluid in concentrated solar power systems. *J. Sol. Energy Eng.* 140:051011. doi: 10.1115/1.4040065

Zhang, P., Chen, S. Z., Wang, L. J., Yao, T. Y., and Xu, J. M. (2010). Study on a lab-scale hydrogen production by closed cycle thermo-chemical iodine–sulfur process. *Int. J. Hydrog. Energy* 35, 10166–10172. doi: 10.1016/j.ijhydene.2010.07.150

Zhou, J., Zhang, Y., Wang, Z., Yang, W., Zhou, Z., Liu, J., et al. (2007). Thermal efficiency evaluation of open-loop SI thermochemical cycle for the production of hydrogen, sulfuric acid and electric power. *Int. J. Hydrog. Energy* 32, 567–575. doi: 10.1016/j.ijhydene.2006.06.043

Conflict of Interest: AA-M is one of the owners of the company Wahaj Investment L.L.C.

The remaining authors declare that the research was conducted in the absence of any commercial or financial relationships that could be construed as a potential conflict of interest.

frontiers in Materials

ORIGINAL RESEARCH
published: 31 May 2021
doi: 10.3389/fmats.2021.670638

Dysprosium Oxide-Supported CaO for Thermochemical Energy Storage

Larissa Fedunik-Hofman[1,2], Alicia Bayon[2], Xiang Gao[3], Antonio Tricoli[3] and Scott W. Donne[1]**

[1] Discipline of Chemistry, The University of Newcastle, Callaghan, NSW, Australia, [2] CSIRO Energy, Newcastle, NSW, Australia, [3] College of Engineering and Computer Science, Australian National University, Canberra, ACT, Australia

A novel CaO-based material supported with $Ca_3Al_2O_6$ and Dy_2O_3 was found to show excellent performance as a thermochemical energy storage material for use in solar thermal power plants. It retains a carbonation conversion capacity of 82.7% for a period of 40 cycles, as well as exothermic heats of reaction of 582.2 kJ kg^{-1}, up to seven times greater than other materials found in the literature. The improved performance was attributed to the greater prevention of sintering and retention of high surface area by the addition of two inert supports: $Ca_3Al_2O_6$ and Dy_2O_3. Long-term effectiveness of the novel material was also evaluated by using a sintering model. It retains an energy storage utilization of 6.2 kg kWh^{-1} after 30 years of cycling, while commercial limestone would require 81 tons kWh^{-1} equivalent. Limestone requires replacement every six thermal cycles, making it impractical for real thermochemical energy storage implementation. The extra cost associated with the addition of supports in this CaO-based material is justified by the long-term durability, which would imply a reduction in the overall capital and operational expenditure of the plant.

Keywords: thermochemical energy storage, calcium looping, solar energy, concentrated solar thermal, Thermogravimetric analysis (TGA), differential scanning calorimetry

OPEN ACCESS

Edited by:
Vardan Galstyan, University of Brescia, Italy

Reviewed by:
Roberto Gonzalez Rodriguez, Texas Christian University, United States
Jong Hoon Joo, Chungbuk National University, South Korea

***Correspondence:**
Alicia Bayon
abayonsa@asu.edu
Scott W. Donne
scott.donne@newcastle.edu.au

Specialty section:
This article was submitted to Energy Materials, a section of the journal Frontiers in Materials

Received: *10 March 2021*
Accepted: *12 April 2021*
Published: *31 May 2021*

Citation:
Fedunik-Hofman L, Bayon A, Gao X, Tricoli A and Donne SW (2021) Dysprosium Oxide-Supported CaO for Thermochemical Energy Storage. Front. Mater. 8:670638. doi: 10.3389/fmats.2021.670638

INTRODUCTION

Renewable energy generation and storage systems are a key strategy in order to reduce CO_2 emissions and limit global warming (Greenblatt et al., 2017). CO_2 capture technologies are essential for transitioning into novel renewable energy-based society while still obtaining an economic return on the current infrastructure. However, CO_2 capture itself is not enough to solve the emissions problem. CO_2 capture technologies could be coupled with CO_2 storage, which solves in part the problem of taking carbon emissions out of the atmosphere. Thus, if instead of storing CO_2 we can utilize it effectively for other purposes, then there is a benefit (not only cost) on the carbon emissions. Nowadays, CO_2 is widely use in food industry for conservation. However, this CO_2 is not reused it in a way that it is easily storable and utilize.

Commercial concentrated solar power (CSP) plants employ sensible heat storage, and various candidate solar salts and other storage media have been explored (Gil et al., 2010; Liu M. et al., 2016). However, CSP plants require a higher levelized cost of electricity than other renewable alternatives, limiting deployment of these technologies (Starke et al., 2018; Awan et al., 2019). One of the main alternatives for cost reduction is replacing the low- efficiency subcritical Rankine cycle with the highly efficient supercritical CO_2 Brayton power cycle. Specifically, this power cycle has been demonstrated to achieve solar to electricity efficiencies as high as 55% when operating at

temperatures around 700°C (Calle et al., 2018). However, there are no commercially established energy storage systems for power cycles operating at such high temperatures. A promising alternative is the use of thermochemical energy storage (TCES) (André et al., 2016; Prieto et al., 2016; André and Abanades, 2018). The gas-solid reactions involved in TCES have high energy storage densities, making the process suitable for long-term energy storage (Bayon et al., 2018). Of all TCES technologies under investigation currently, carbonate looping has been found to have the greatest potential in the range of temperatures suitable for supercritical CO_2 Brayton cycles (Bayon et al., 2018).

The carbonate looping cycle based on $CaCO_3$ has been well researched for both TCES storage (Chacartegui et al., 2016; Prieto et al., 2016; Benitez-Guerrero et al., 2017, 2018; Ortiz et al., 2018a,b); and CO_2 capture technologies (Grasa et al., 2008; Erans et al., 2018). The calcination reaction is endothermic and can be driven by concentrated solar energy, as shown in Eq. (1), where ΔH_r is the reaction enthalpy (kJ mol^{-1}). The reaction products, CaO and CO_2, are stored separately. The reverse carbonation reaction recombines the calcination products in a separate reactor, releasing heat to be transferred to the gas turbine (Edwards and Materić, 2012); i.e.,

$$CaCO_3(s) \leftrightarrow CaO(s) + CO_2(g)\ (\Delta H_r(25^\circ C) = 178\ kJ\ mol^{-1}) \quad (1)$$

One of the major challenges associated with carbonate looping is the declining conversion efficiency of the carbonation reaction with ongoing thermal cycling. According to Grasa et al. (2008) carbonation conversion decreases dramatically during the first 20 cycles to a reversible conversion of about 8%. This results in a large proportion of inactive CaO cycling through the carbonate looping system, which leads to increased capital and operating costs (Edwards and Materić, 2012). At high calcination temperatures (>850°C), the decrease in the extent of conversion has been mainly attributed to the sintering of CaO grains (Benitez-Guerrero et al., 2017). The driving force for sintering is the reduction of surface energy of the grains caused by decreasing their surface area or increasing their grain size (Stone, 1960). Reducing the surface area reduces CaO reactivity by decreasing the amount of active sites available for the carbonation reaction (Liu W. et al., 2016), leading to longer CO_2 diffusion pathways.

High sintering resistance is related to the refractory nature of a material. Tammann temperature provides an indication for a material's susceptibility to sintering (Aihara et al., 2001). The correlation between Tammann (T_T) and melting temperatures (Tm) is described by the following relationship:

$$T_T = 0.5T_m \quad (2)$$

Hence, supporting materials with melting points higher than that of $CaCO_3$ (such as Dy_2O_3) will theoretically impart sintering-resistant properties to the sorbent (Liu et al., 2012b).

The onset of sintering is influenced by other factors in addition to the material's Tammann temperature, such as particle size and morphology, including the extent of porosity. For a discussion of the role of supports from a morphological perspective, see section "Characterization Results."

In order to improve carbonation efficiency and hence cyclability, the use of synthetic CaO-based materials synthesized with sintering-resistant inert supports is well documented (for CO_2 capture applications) (Liu et al., 2012b). A variety of materials have been investigated, such as $CaTiO_3$ (Liu et al., 2012b), Al_2O_3 (Broda et al., 2012), Y_2O_3 (Derevschikov et al., 2011), SiO_2 (Li et al., 2014; Sanchez-Jimenez et al., 2014), and oxides of Si, Co, Ti, Cr, Ce, and Zr (Lu et al., 2009). Synthesis processes usually involve dispersing CaO in a stable, solid matrix made up of the inert material, acting to preserve the available active surface layer of CaO and preventing loss of conversion with cycling (Li et al., 2005). Some of the most extensively investigated supports include aluminium-containing materials such as calcium aluminates, which form different polymorphs depending on the preparation method; e.g., mayenite ($Ca_{12}Al_{14}O_{33}$) (Li et al., 2005; Liu et al., 2012a), $Ca_9Al_6O_{18}$ (Zhou et al., 2012, 2013; Radfarnia and Sayari, 2015), or $Ca_3Al_2O_6$ (Angeli et al., 2014; Li et al., 2015; Sun et al., 2016; Wang et al., 2018). These supports have been found to be highly effective at stabilizing CaO, particularly when $Ca_3Al_2O_6$ is prepared using nitrate precursors (Zhou et al., 2012; Azimi et al., 2019). There is less research on the use of active supports as dopants for CaO-based sorbents. Active supports which have been examined include MgO (both dolomites and synthetically doped sorbents) (Albrecht et al., 2008; Liu et al., 2012a; Ping et al., 2016) and Li_2SO_4 (Lu and Wu, 2016).

Recently, lanthanides have become an attractive group of materials for use as supports. Several lanthanides have been tested as supports for CaO for CO_2 capture technologies, both active (able to absorb CO_2) (Cotton et al., 1999) and inactive (Luo et al., 2010). A CaO/La_2O_3 material produced using sol-gel combustion synthesis displayed good performance for 20 cycles under both inert gas and 100% CO_2 atmosphere (Luo et al., 2010). A CaO/La_2O_3 composite was also synthesized by Albrecht et al. (2008) using a hydrothermal process with nitrate precursors, limestone and tetrahydrofuran as a solvent. Materials containing small amounts of La_2O_3 showed a higher absorption capacity through 30 cycles than untreated limestone. However, this benefit was not retained with longer term cycling, with CO_2 capture capacity comparable to that of untreated limestone after 80 cycles (Albrecht et al., 2008).

Hu et al. (2015) incorporated Nd_2O_3 into CaO particles by wet mixing for CO_2 capture purposes. Improved durability and higher carbonation conversion were observed (67% after 100 cycles at a calcination temperature of 900°C), which was attributed to the prevention of sintering (Hu et al., 2015). Although the authors describe Nd_2O_3 as an inert solid sorbent, it is actually an effective CO_2 sorbent (Perry, 2015). Taking this into account and noting the drop off in conversion capacity at more severe calcination conditions, it is likely that the improved carbonation conversion is also due to the CO_2 uptake of Nd_2O_3 compared to inactive supports such as calcium aluminate. Hu et al. (2016) also supported CaO with Yb_2O_3, which achieved modest sintering-resistance (17% carbonation conversion after 50 cycles when tested under severe calcination conditions, a 9.5% improvement compared to CaO). However, the use of Pr_6O_{11} as

a support for CaO was unsuccessful, which was attributed to its very high molecular weight (Hu et al., 2016).

To address the challenge of finding a material that exhibits durability with thermal cycling under TCES conditions (high calcination temperature and 100% CO_2 atmosphere), this work proposed the use of Dy_2O_3 as a support to CaO. It is envisaged that the use of Dy_2O_3 will be beneficial due to its high melting temperature (∼2340°C), which predicts high sintering resistance (Liu et al., 2012b). This is supported by the improved performance of lanthanide-supported CaO in the literature (Luo et al., 2010; Hu et al., 2015, 2016).

The inert support mayenite ($Ca_{12}Al_{14}O_{32}$) has been consistently shown to prevent sintering, despite possessing a comparatively low Tammann temperature (Li et al., 2005; Liu et al., 2012a). This work also proposes a combination of Dy_2O_3 and $Ca_3Al_2O_6$ which obtains exceptional sintering resistance, improving the durability of CaO as compared with other explored supports with smaller amount of inactive material. A further long-term performance analysis reveals that the use of Dy_2O_3 and $Ca_3Al_2O_6$ could also be feasible compared with other TCES materials, as no replacement of the storage material is required during the typical lifetime of a CSP plant (commonly 30 years) (Liu M. et al., 2016).

EXPERIMENTAL

Materials Preparation

Pechini-synthesized CaO (denoted as P-CaO or P-$CaCO_3$ in its carbonate form) was prepared using the Pechini method, following the steps described in the literature (Jana et al., 2010). The reagents utilized were $Ca(NO_3)_2$ (Sigma-Aldrich; 99.0% purity), $Al(NO_3)_3$ (Sigma-Aldrich; 99.0% purity), dysprosium(III) nitrate hydrate ($Dy(NO_3)_3.xH_2O$); (Sigma-Aldrich; 99.9% purity), citric acid (CA; $C_6H_8O_7$; Sigma-Aldrich; 99.5% purity) and ethylene glycol (EG; $HOCH_2CH_2OH$; Sigma-Aldrich; 99.8% purity). The quantities of the reagents used are shown in **Table 1** as well as the nomenclature of the synthesized products. A precursor with a CA molar ratio of 1:5 and a CA to EG ratio of 3:2 were utilized.

Approximately 0.3 mol (57.4 g) of CA was added to 100 mL of distilled water (Milli-Q) and stirred at 70°C until dissolved totally. The metal precursors $Ca(NO_3)_2$ (11.8 g) and $Dy(NO_3)_3$ (1.3 g) were then added to the solution, which was stirred for 3 h before the temperature was increased to 90°C. EG (10 mL) was added and the resulting solution was further stirred at the same temperature to remove the excess solvent until the solution became a viscous resin. The obtained resin was subsequently dried in an oven at 180°C for 5 h. The sample was then ground with an agate mortar to achieve fine particles and then calcined in a tube furnace. The furnace was programmed to 400°C for 2 h, before heating to 900°C at a ramp speed of 10°C min^{-1}, holding for 4 h and cooling to ambient temperature at 10°C min^{-1}. After calcination, the sample was ground again to ensure very fine particles were obtained.

To produce a material supported with both dysprosium oxide and calcium aluminate, the stoichiometry of the reaction of Al_2O_3 and CaO at high temperatures was analyzed. Several studies describe the production of the calcium aluminate known as mayenite; i.e.,

$$7Al_2O_3 + 12CaO \rightarrow Ca_{12}Al_{14}O_{33} \quad (3)$$

At temperatures greater than 850°C, mayenite can react with excess CaO to form tricalcium aluminate (Peng et al., 2015); i.e.,

$$Ca_{12}Al_{14}O_{33} + 9CaO \rightarrow 7Ca_3A_{12}O_6 \quad (4)$$

The stoichiometry of these reactions were used to estimate the amount of inert support in the material, and the amount of active CO_2 sorbent was determined based on the percentage of calcination conversion compared to the theoretical mass loss of 43.97% for $CaCO_3$ (see **Table 1**). It was assumed that there would be no reaction between the $Al(NO_3)_3$ and the $Dy(NO_3)_3$. For comparative purposes, materials composed only of Dy_2O_3, CaO, and CaO supported with calcium aluminate were also prepared (see **Table 1**).

TABLE 1 | Quantities of reagents used and characteristics of resulting powder samples.

Name	Precursor composition	CA (g)	EG (mL)	$Ca(NO_3)_2$ (g)	$Dy(NO_3)_3$ (g)	$Al(NO_3)_3$ (g)	CaO Yield (%)
P-Dy_2O_3	$Dy(NO_3)_3$	6.4	1.3	–	4.67	–	0
P-CaO	$Ca(NO_3)_2$	48.0	9.2	11.8	–	–	100
P-CaO-Al20	80 mol% $Ca(NO_3)_2$ 20 mol% $Al(NO_3)_3$	34.6	7.5	7.6	–	3.0	65
P-CaDy20	93 mol% $Ca(NO_3)_2$ 7 mol% $Dy(NO_3)_3$	51.6	10.0	11.8	1.3	–	88
P-CaDy-Al5	88.84 mol% $Ca(NO_3)_2$ 6.64 mol% $Dy(NO_3)_3$ 5 mol% $Al(NO_3)_3$	54.4	10.5	11.8	1.3	1.1	85
P-CaDy-Al10	83.71 mol% $Ca(NO_3)_2$ 6.29 mol% $Dy(NO_3)_3$ 10 mol% $Al(NO_3)_3$	57.4	11.1	11.8	1.3	2.2	81
P-CaDy-Al20	74.41 mol% $Ca(NO_3)_2$ 5.59 mol% $Dy(NO_3)_3$ 20 mol% $Al(NO_3)_3$	64.6	12.5	11.8	1.3	5.0	62

Material Characterization

Powder X-ray diffraction (XRD) analysis was performed using CuK_α radiation ($K_{\alpha 1}$ = 1.540598 Å; $K_{\alpha 2}$ = 1.544426 Å) at a scanning rate of 2.5° min^{-1} (step size = 0.026°, time per step = 0.31 s) over the 2θ range 15–70°. Diffraction patterns were analyzed with Joint Committee on Powder Diffraction Standards (JCPDS). Crystallite sizes were obtained using the Scherrer calculator function in PANalytical X'Pert HighScore software (Degen et al., 2014). The crystallite sizes were calculated using the peak at 37.4° (the most intense peak at 29° was not evaluated due to an overlap with the peak of Dy_2O_3) using:

$$d = \frac{0.89\lambda}{B\cos(\theta)} \quad (5)$$

where d is the mean crystallite diameter (Å), λ is the X-ray wavelength (Å), 0.89 is the shape factor for CaO, and B is the full width half maximum (FWHM) of the CaO diffraction peak (rad), taking into account instrumental peak broadening.

BET surface area, pore volume and pore size distribution were determined by N_2 adsorption-desorption analysis using a Micromeritics TriStar II 3020 surface area analyzer. All samples were degassed under vacuum for 4 h at 120°C prior to the measurement. Surface area was determined by applying the multipoint BET method, and isotherms were typically analyzed over the relative pressure range of 0.05–0.30. Pore volume and pore size distribution were determined using the BJH adsorption method.

SEM images were recorded by using a Zeiss Sigma VP FESEM. Samples were carbon coated before analysis. Energy dispersive spectroscopy (EDS) mapping was carried out using a Bruker light element SSD EDS detector. TEM images were recorded using a JEOL JEM-1200EXII TEM with STEM and EDS system. Samples were suspended in acetone, sonicated and dispersed on copper grids prior to analysis.

Calcination-Carbonation Cycling Analysis

The extent of conversion with cycling was monitored by thermogravimetric analysis (TGA) using a SETSYS Evolution 1750 TGA-DSC from SETARAM Instrumentation. Testing conditions varied based on calcination atmosphere (N_2/CO_2) and carbonation atmosphere (mixture of CO_2 and N_2/100% CO_2) (cf., **Table 2**). Experiments in the literature are typically carried out with calcination in N_2 and carbonation under a mixed atmosphere, so these conditions were replicated for comparative purposes. However, a CO_2 atmosphere is potentially more favorable, as using pure CO_2 as the reactor unit atmosphere avoids the need for multiple gas storage, separation and purification units, lowering costs and preventing compression losses (Schaube et al., 2011).

In a typical experiment under 100% CO_2, 18 mg of powder sample was placed into a 100 μL alumina crucible and subjected to 40 cycles of heating to 1000°C and subsequent cooling to 850°C (10°C min^{-1} heating rate), where the sample was held isothermally for 30 min to allow for carbonation. A constant CO_2 gas flow of 20 mL min^{-1} was utilized. Experiments such as these with calcination temperatures greater than 900°C are described as "severe" conditions. For an experiment with N_2 as the calcination atmosphere (described as "mild" calcination conditions), the sample was heated to 800°C, held isothermally for 10 min and then cooled to 650°C. The reacting gas was switched to a mixture of 75% v/v N_2 and 25% CO_2 and held isothermally for 30 min to allow for carbonation. The gas was then switched back to N_2 and cycling continued for 40 cycles.

TABLE 2 | Testing conditions and selected results for synthesized materials.

Sample	Calcination			Carbonation							References
	Temperature	Atmosphere	Time	Temperature	Pco2	Time	X(t) (% at cycle)				
	(°C)		(min)	(°C)	(% v/v)	(min)	1	20	40	100	
Severe Conditions											
P-CaDy20-CO_2	1000	CO_2	None	850	100	30	94.9	51.6	31.6		This work
P-CaDy-A120-CO_2	1000	CO_2	None	850	100	30	91.1	84.6	82.7		This work
P-CaDy-A110-CO_2	1000	CO_2	None	850	100	30	90.2	82.1	63.3		This work
P-CaDy-A15-CO_2	1000	CO_2	None	850	100	30	95.0	67.6			This work
P-CaO-A120-CO_2	1000	CO_2	None	850	100	30	88.8	80.2	72.8		This work
CalOLa-950	950	CO_2	10	650	25	15	85.5	36.0			Luo et al., 2010
Ca70Nd-1000	1000	N_2	5	650	15	15	99.1	48.9	29.1	15.1	Hu et al., 2015
Mild Conditions											
P-CaDy-A120-N2	800	N_2	10	650	25	30	100.0	87.5	76.0		This work
Ca70Nd-800	800	N_2	5	650	15	15	99.2	98.7	97.9	91.6	Hu et al., 2015
CalOYb-800	800	N_2	5	650	30	25	75.0	64.8			Hu et al., 2016
CalOLa-850	850	N_2	10	650	25	15	65.2	43.1			Luo et al., 2010
Ca70Nd-900	900	N_2	5	650	15	15	99.2	98.7	86.4	66.9	Hu et al., 2015
CalOYb-900	900	N_2	5	650	15	25	50.1	36.2	17.1		Hu et al., 2016

The carbonation conversion of CaO to $CaCO_3$ was calculated using:

$$X(t) = \left(\frac{m(t) - m_i}{X.m_{x=1}}\right)\left(\frac{M_{caco_3}}{M_{caco_3} - M_{cao}}\right) \quad (6)$$

where X(t) is the carbonation conversion extent as a function of time, m(t) is the mass of the sample (g) after time t (min) at the carbonation temperature or under the carbonation atmosphere (t = 30 min), m_i is the initial mass of the sample before carbonation (g), x is the active mass fraction of CaO, $m_{X\ =\ 1}$ is the theoretical mass of the sample in grams after 100% carbonation conversion (g; 43.97% mass gain) and M is the molar mass (g mol^{-1}).

As a means of comparing synthetic materials with different proportions of active material, effective carbonation conversion was calculated. The effective carbonation conversion, $X(t)_{eff}$, takes into account the inert portion of the material and was calculated as follows:

$$X(t)_{eff} = x.X(t) = \left(\frac{m(t) - m_i}{m_{x=1}}\right)\left(\frac{M_{caco_3}}{M_{caco_3} - M_{cao}}\right) \quad (7)$$

For ease of reference, X(t) refers to the "original (carbonation) conversion" and $X(t)_{eff}$ as "effective (carbonation) conversion" and a comparison of both properties is detailed in the results.

Differential scanning calorimetry was used to determine endothermic and exothermic heats of reaction. Cycling experiments under severe experimental conditions were used to obtain heats of reaction. SETARAM post-processing analysis software was used to integrate the heat flow peaks using the Bezier integration function.

Sintering Model

It has been noted that the practical use of modified synthetic TCES materials will depend on their economic performance, and the impact of inert supports on cost performance has yet to be evaluated in many studies (Valverde, 2013). Prices of inert supports are much higher than natural limestone (Qin et al., 2014), so the improvement in performance of the synthetic TCES materials must be quantified to justify their additional cost. The deactivation of the natural limestone occurs rapidly, which will require a replacement of the materials after a small number of thermal cycles (Grasa and Abanades, 2006). Deactivation of natural limestone was evaluated from cycling experiments performed by Sarrión et al. (2018) using limestone under realistic TCES conditions.

To determine the deactivation of the material with long-term cycling (i.e., assuming the same material is used during the whole lifetime of a CSP plant), the sintering model described by Grasa and Abanades (2006) was used to determine the carbonation conversion (X(N)) after N cycles. The decay trend could be correlated using the parameters deactivation constant (k), residual conversion (X_r) and N; i.e.,

$$X(N) = X_r + \frac{1}{\frac{1}{1-X_r} + KN} \quad (8)$$

This was used to model loss in conversion for P-CaO and P-CaDy-Al20 (see section "Feasibility Study" and **Table 1** for sample composition). The parameters k and X_r were determined using least squares regression. When this model proved unsuitable for modeling sintering over the first 40 cycles (as in the case of P-CaO-Al20 and limestone, referred to as Comm-$CaCO_3$), a semi-empirical model from Valverde et al. (2017) was used to determine the number of sorbent replacements required over the whole life of a CSP plant [assumed to be 30 years (Steinhagen and Nitsch, 2005)]; i.e.,

$$X(N) = X_r + \frac{X_1}{K(N-1) + \left(1 - \frac{X_r}{X_1}\right)^{-1}} \quad (9)$$

where X_1 is the carbonation conversion after the first cycle. In this model it is assumed that the material will be charged and discharged once a day and therefore the number of cycles is identical to the number of days of operation. For reference, it is assumed than replacement will be made when the conversion falls below 20%.

The mass specific storage utilization (kg kWh^{-1}) was evaluated using the experimentally determined exothermic heat of reaction of the candidate materials. To determine the required amount of material over the plant lifetime ($\mu_{Storage}$), the storage utilization after 30 years was obtained by dividing the number of material replacements ($R_{30\ years}$) by the heat storage capacity after 40 cycles as per:

$$\mu_{Storage} = \frac{R_{30\ years}}{\Delta H_r} \quad (10)$$

RESULTS AND DISCUSSION

Thermal Cycling and Initial Characterization

Table 2 sets out the experimental conditions and cycling results of synthesized oxides from this work and experiments from published literature. In order to examine the TCES potential, calcination and carbonation conversions were recorded up to 40 cycles (see **Table 2**). The thermal cycling results under two distinct experimental conditions, severe calcination and mild calcination, are discussed in sections "Cycling Under Severe Calcination Conditions" and "Cycling Under Mild Calcination Conditions," respectively.

As-synthesized materials were first characterized by XRD, as shown in **Figure 1**. In addition to peaks of Dy_2O_3, CaO and $Ca_3Al_2O_6$, the Dy-supported materials show peaks of calcium oxide minerals such as portlandite ($Ca(OH)_2$) and vaterite (a polymorph of $CaCO_3$). This indicates that these substances are not completely decomposed during the initial calcination process. Another possibility is that these compounds are formed due to materials reacting with atmospheric moisture and CO_2 post-calcination. Scans taken after cycling (**Figure 2**) indicate that both portlandite and vaterite decompose during the calcination process, while calcite ($CaCO_3$) forms during carbonation. Dysprosium carbonate was not detected in the scan, which shows that the dysprosium oxide does not undergo cycling to dysprosium carbonate.

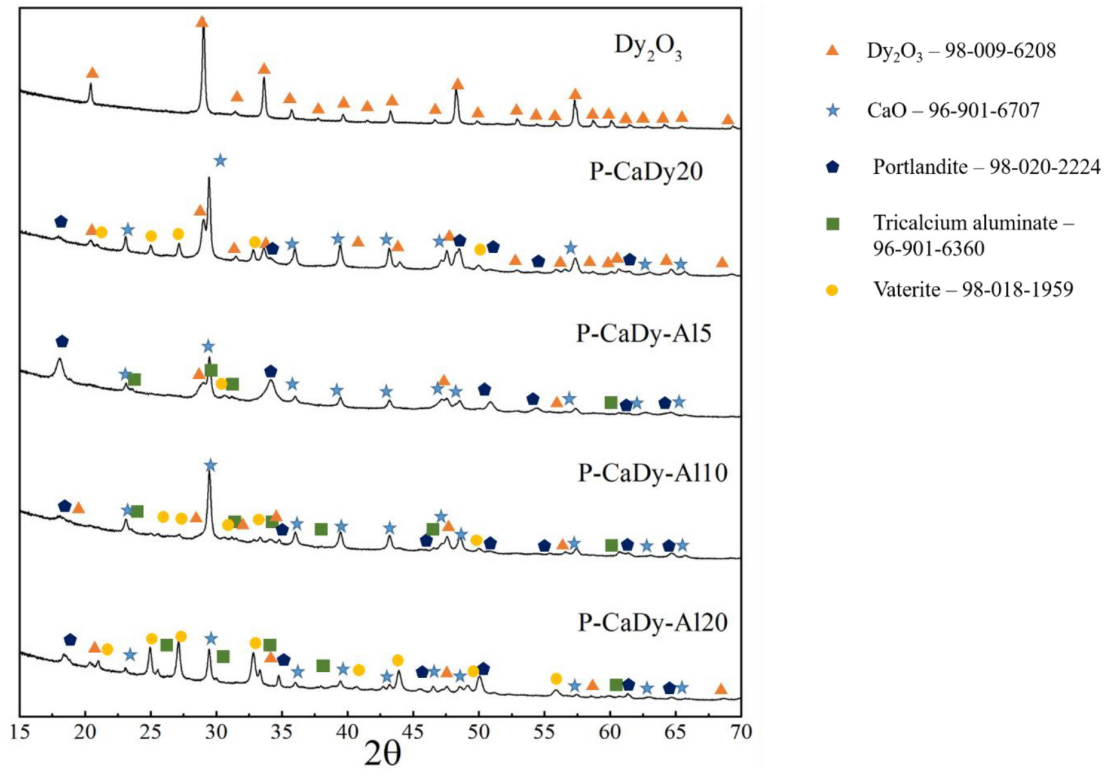

FIGURE 1 | XRD patterns of the as-synthesized materials.

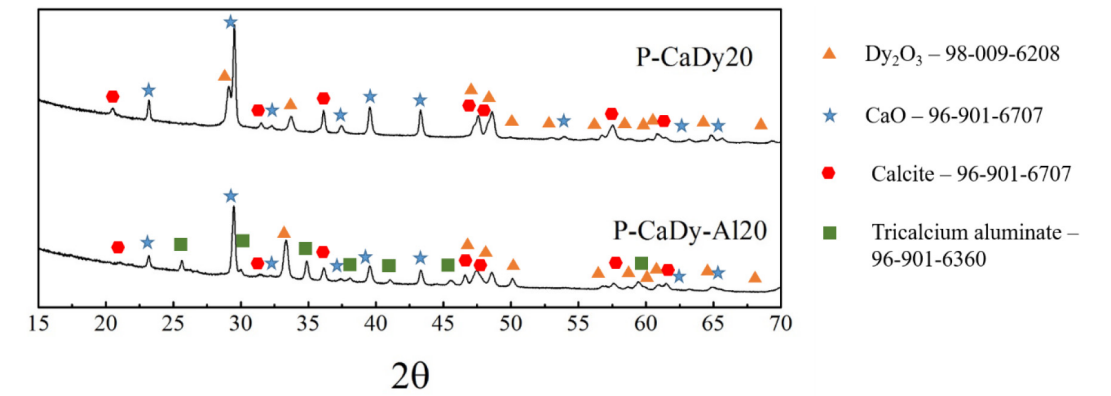

FIGURE 2 | XRD patterns of selected materials post TGA cycling.

Cycling Under Severe Calcination Conditions

To evaluate the TCES potential, the materials are cycled under severe calcination conditions (100% CO_2, cycling between 1000 and 850°C). The selected conditions, original conversion and reaction times are gathered in **Table 2**. The evolution with cycling of original and effective conversion are plotted in **Figures 3A,B**, respectively. The literature materials selected for comparison are Ca10La-950 (10% La_2O_3, calcined to 950°C) and Ca70Nd-1000 (70% Nd_2O_3, calcined to 1000°C).

When comparing the original conversion (**Figure 3A** and **Table 2**), it can be observed that the P-CaDy20-CO_2 suffers from a loss of conversion from 94.9% in the first cycle to 51.6% in cycle 20. It is important to note that this material has been synthesized without the addition of $Ca_3Al_2O_6$. When $Ca_3Al_2O_6$ is added, the material stability with cycling improves considerably. Addition of 5, 10 or 20% of the Al precursor results in an increase in conversion of 67.6, 82.1, and 84.6%, respectively, after 20 cycles. The latter two materials were cycled for a longer period, with the result that the material with a larger amount

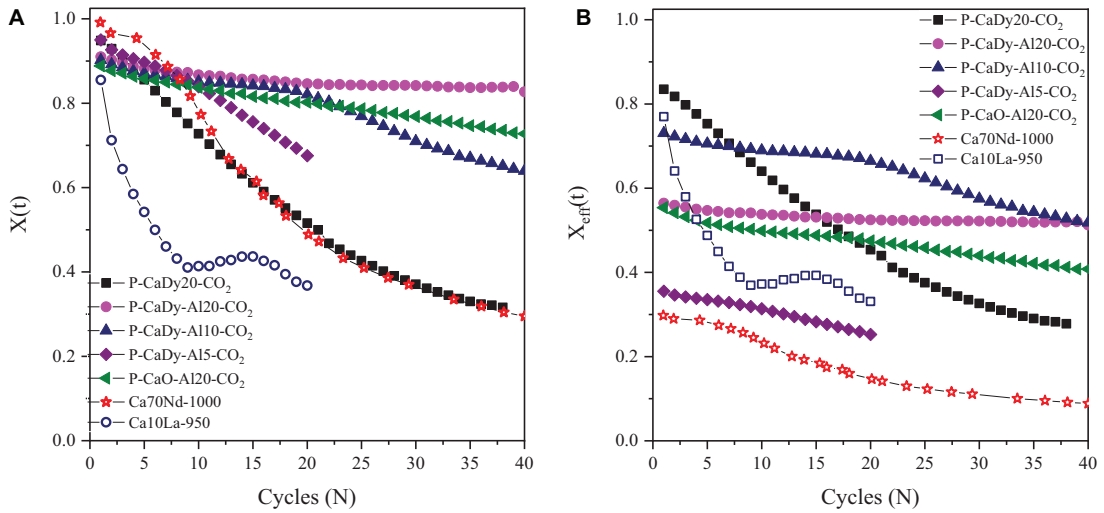

FIGURE 3 | Carbonation conversion compared to literature results – severe calcination conditions, **(A)** original carbonation conversion and **(B)** effective carbonation conversion. Empty symbols are literature.

of $Ca_3Al_2O_6$ (P-CaDy-Al20-CO_2) achieves the best stability in this study. This material also achieves the lowest decline in carbonation conversion with thermal cycling, with a decrease of only 8.3% after 40 cycles. The incorporation of Dy_2O_3 was further evaluated by comparing P-CaDy-Al20-CO_2 with P-CaO-Al20-CO_2 (synthesized without the Dy_2O_3 support). The latter shows a loss of conversion from 88.8% in the first cycle to 72.8% in cycle 40, although loss of conversion capacity is less extreme than the material synthesized with only Dy_2O_3 (P-CaDy20-CO_2). The stability of the synthesized materials can be classified in the following order:

> P-CaDy-Al20-CO_2 > P-CaO-Al20-CO_2 > P-CaDy-Al10-CO_2 > P-CaDy20-CO_2.

The materials selected for comparison from literature have the following Ca70Nd-1000 (70% Nd_2O_3, calcined to 1000°C) and Ca10La-950 (10% La_2O_3, calcined to 950°C) (see **Table 2**). The carbonation conversion achieved by P-CaDy20-CO_2 is higher at 20 and 40 cycles (15.6% and 2.7% higher than Ca10La-950 and Ca70Nd-1000, respectively). It is also necessary to highlight that the amount of inert support contained in Ca70Nd-1000 is much larger as compared to P-CaDy20-CO_2, and the latter slightly improved the carbonation conversion. When CaO was combined with both Dy_2O_3 and $Ca_3Al_2O_6$ (in P-CaDy-Al20-CO_2) the conversion is 48.6% and 35.7% higher after 20 cycles as compared to Ca10La-950 and Ca70Nd-1000, even though P-CaDy-Al20-CO_2 is calcined under more severe calcination conditions (higher temperature or CO_2 concentration). These results reveal that firstly, the use of Dy_2O_3 improves the stability of CaO, as compared with the supports La_2O_3 and Nb_2O_3, and secondly, that the extra addition of $Ca_3Al_2O_6$ significantly contributes to an increase in stability with cycle number.

To study the effect of the mass fraction of inert supports, the effective carbonation conversion is shown in **Figure 3B**. After 40 cycles P-CaDy-Al10-CO_2 and P-CaDy-Al20-CO_2 outperform all the materials in this study, as well as in the literature references. When 10% aluminium precursor is added (P-CaDy-Al10-CO_2), the effective carbonation conversion drops from 66.5% in cycle 20 to 51.8% in cycle 40, and the slope of the conversion decay indicates that the carbonation conversion is not yet stabilized after 40 cycles. However, the addition of 20% aluminium precursor (P-CaDy-Al20-CO_2) helps to maintain the effective carbonation conversion from 56.4% in cycle 1 to 51.3% in cycle 40. The best performing material P-CaDy-Al20-CO_2 has stabilized after 40 cycles with 82.7% original and 51.3% effective conversion capacities (see **Figures 3A,B**, respectively). In comparison, the Nd_2O_3 and La_2O_3 supported materials from the literature show much lower effective carbonation conversions after 40 cycles. Comparing effective carbonation conversion gives a more realistic picture of material performance, particularly in the case of Ca70Nd-1000, which contains 70% inert material. Additionally, only the Ca10La-950 is tested under 100% CO_2, while Ca70Nd-1000 is calcined under a N_2 atmosphere (see **Table 2**). Testing under pure CO_2 displaces the reaction equilibrium point to higher temperatures and is known to accelerate sintering and loss of conversion (Stanmore and Gilot, 2005). Therefore, the higher carbonation conversions of the materials in this work are particularly noteworthy, considering that the experimental conditions are more severe than those in the literature. Good performance under 100% CO_2 is also highly relevant to TCES, as these more realistically represent reactor conditions (Schaube et al., 2011).

Cycling Under Mild Calcination Conditions

To further evaluate the materials and compare with literature, the synthesized material which performed best under severe conditions (P-CaDy-Al20; cf., section "Cycling Under Severe Calcination Conditions") was tested under mild calcination conditions (100% N_2 calcination, 75:25 N_2:CO_2 carbonation, cycling between 800 and 650°C). As for section "Cycling Under

Severe Calcination Conditions," the selected conditions, original conversion and reaction times are gathered in **Table 2**, while original and effective carbonation conversion are plotted in **Figures 4A,B**, respectively. The literature materials selected for comparison are Ca70Nd-800/900 (70% Nd_2O_3, calcined to 800/900°C), Ca10Yb-800/900 (10% Yb_2O_3, calcined to 800/900°C), and Ca10La-850 (10% La_2O_3, calcined to 850°C).

When examining the original conversion (**Figure 4A**) it can be observed that the P-CaDy-Al20-N_2 achieves ~100% carbonation conversion in the first cycle, dropping to 76% in cycle 40. Taking into account the fraction of inert support (**Figure 4B**), P-CaDy-Al20-N_2 achieves 62% carbonation conversion in the first cycle, and this drops to 55% carbonation conversion in cycle 40.

Compared to P-CaDy-Al20-CO_2 (**Figures 3A,B**) the carbonation conversion of P-CaDy-Al20-N_2 is initially greater, but this drops off with cycling and the material does not reach stable conversion after 40 cycles (**Figures 4A,B**). This could be due to the phenomenon of "self-reactivation" under CO_2 as compared to calcination under N_2 (Manovic and Anthony, 2005). It is well known that calcining CaO under 100% CO_2 displaces the reaction point to higher temperatures, and is known to accelerate sintering and loss of conversion (Stanmore and Gilot, 2005). Thermal cycling causes the development of a hard inward skeleton of low porosity, less reactive CaO, surrounded by a softer layer of reactive, porous CaO. This hard skeleton is hypothesized to keep the pore structure stable during cycling while the external soft skeleton is regenerated in each re-carbonation (Manovic and Anthony, 2005). The residual CO_2 uptake capacity was determined by the CaO skeleton structure, which is heavily influenced by the calcination temperature (Kierzkowska et al., 2013). Manovic and Anthony found that pre-treatment of limestone to temperatures greater than 1000°C increased residual conversion (Manovic and Anthony, 2005), which is reflected in this study.

P-CaDy-Al20-N_2 was then compared with materials from literature experiments. As shown in **Figure 4A**, P-CaDy-Al20-N_2 outperforms the La_2O_3 and Yb_2O_3 supported materials, but falls short of the Nd_2O_3 supported material. When considering effective carbonation conversion (**Figure 4B**), P-CaDy-Al20-N_2 clearly outperforms the Nd_2O_3-supported sample, which is predominantly composed of inert material (70%). It also outperforms the La_2O_3 supported material and is predicted to outperform the Yb_2O_3-supported material, which shows poor stability. P-CaDy-Al20 is therefore seen to perform well and exhibit high performance under both mild and severe experimental conditions. Its performance is best under 100% CO_2, conditions which are most relevant for TCES.

Characterization Results

Table 3 presents the crystallite sizes of the synthesized materials obtained using the Scherrer equation. Crystallite sizes range from 58 to 90 nm in the materials in their as-synthesized state. Using XRD results, similar crystallite sizes were initially obtained for P-CaDy20 and the supported material P-CaDy-Al20 (87 and 83 nm, respectively). However, a significant difference in the crystallite sizes is calculated after 40 calcination and carbonation cycles. Average crystallite size increases to 201 nm for P-CaDy20, while P-CaDy-Al20 reaches 128 nm after 40 cycles, which reflects its resistance to sintering.

Table 4 shows the results of BET and pore size analysis for the materials, as synthesized and after 40 cycles of calcination and carbonation cycling. Measurements show that supporting CaO with Dy_2O_3 results in a significant improvement in the retention of surface area. P-CaDy-Al20-c shows a reduction of surface area of only 3.4 $m^2\ g^{-1}$, as compared to P-CaO, which has almost negligible surface area after 40 cycles.

SEM images (**Figure 5**) show that the synthesized materials P-CaDy20 and P-CaDy-Al20 display a porous structure, indicative of high surface area. The morphology of Dy_2O_3 is seen to be more jagged. In **Figures 5a,b** it can be seen that the P-CaDy20 sinters significantly after 20 cycles. **Figure 5b** shows that the material clumps together, losing its fluffy, porous nature and develops rounded particle edges. However, with the

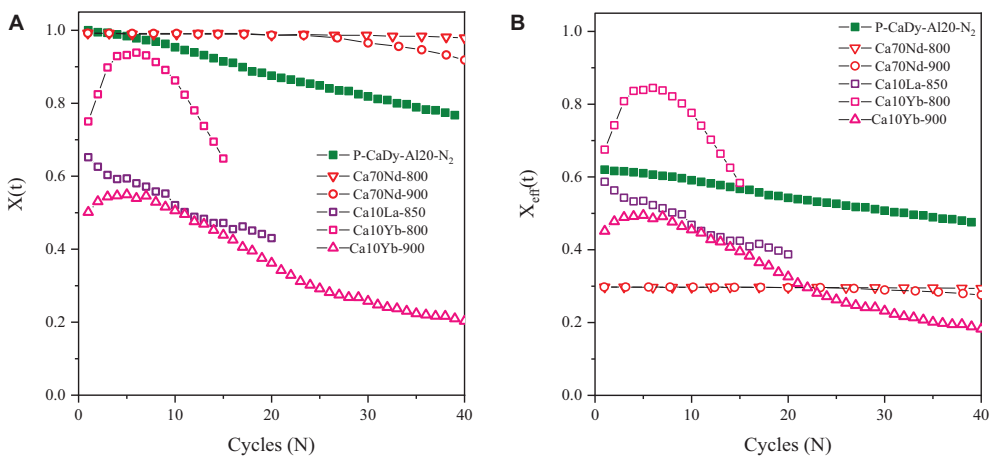

FIGURE 4 | Carbonation conversion compared to literature results – mild calcination conditions, **(A)** original carbonation conversion and **(B)** effective carbonation conversion. Empty symbols are literature.

TABLE 3 | Heat of reactions for TCES materials in this work and literature.

Material	Heat of reaction (kJ kg^{-1}; cycle)		References
	Endothermic	Exothermic	
P-CaO	413.8 (40)	229.5 (40)	This work
P-CaO-Al20	678.0 (40)	462.8 (40)	This work
P-CaDy-Al20	689.8 (40)	582.2 (40)	This work
$CaCO_3$ (limestone)	81.2 (40)*	NA	Sarrión et al., 2018
Co_3O_4	600.8 (1)	495.57 (1)	Carrillo et al., 2014
BaO_2	77 (1)	NA	Fahim and Ford, 1983
CuO	811** (0)	NA	Alonso et al., 2015
Mn_2O_3	161.8 (1)	79.3 (1)	Carrillo et al., 2014
$(Mn_{0.1}Fe_{0.9})_2O_3$	178.0 (1)	111.0 (1)	Carrillo et al., 2015
$(Mn_{0.33}Fe_{0.67})_2O_3$	199.60 (1)	177.8 (10)	Al-Shankiti et al., 2019; Hamidi et al., 2019
$(Co_{0.867}Fe_{0.133})_3O_4$	433.3 (1)	414.9 (1)	Block et al., 2014
$(Co_{0.99}Mn_{0.01})_3O_4$	490.8 (1)	424.8 (1)	Carrillo et al., 2014

**Value obtained from HSC Chemistry 8 ® and deactivation model.*
NA, not available.
***Denotes value has been obtained from database and not experimentally.*

TABLE 4 | Crystallite sizes of synthesized sorbents (as synthesized, at 30°C).

Material	Crystallite size (nm)
P-Dy_2O_3	108
P-CaDy20	70.8
P-CaDy-Al5	90.3
P-CaDy-Al10	57.8
P-CaDy-Al20	79.0

addition of an alumina support in P-CaDy-Al20, less sintering is evident (**Figures 5c,d**). The TEM images show the increased porosity of P-CaDy-Al20 (**Figures 6d–f**) compared to P-CaDy20 (**Figures 6a–c**). Note the dark regions in these figures which indicate the presence of Dy_2O_3.

Figure 7 displays EDS mapping for the as-synthesized materials, unsupported (P-CaDy20; **Figures 7A,C**) and supported (P-CaDy-Al20; **Figures 7B,D**). **Figure 7A** shows that the elements of P-CaDy20 are unevenly distributed across the material, particularly dysprosium. However, **Figure 7B** shows a much more thorough homogeneous distribution. In particular, the red dysprosium is barely visible due to complete overlap with the green calcium, which reflects the even dispersion of Dy_2O_3 across the CaO. Particle growth after cycling can be compared between the supported and unsupported materials. **Figure 7C** shows that P-CaDy20 exhibits significant particle growth after 40 cycles, while P-CaDy-Al20 resists sintering (**Figure 7D**).

Theories on how inert supports act to prevent sintering include the grain boundary "pinning effect" and the effect of densification. Adhesion of the support particle to the grain boundary was postulated to exert a pinning effect and hence provide a drag force to oppose grain growth (Li et al., 2013). Only the support particles on the grain boundaries will exert a pinning force. In this way, the support particles act as a "metal skeleton" – spacers to separate the CaO/$CaCO_3$ particles (Hu et al., 2015). Alternatively, inert spacers are suggested to suppress densification and loss of micro- or meso-porosity during repeated calcinations (Zhao et al., 2014). As $CaCO_3$ has a lower density than CaO, this leads to pore closure of unreacted CaO and increased diffusional resistance of CO_2. If CaO is supported with

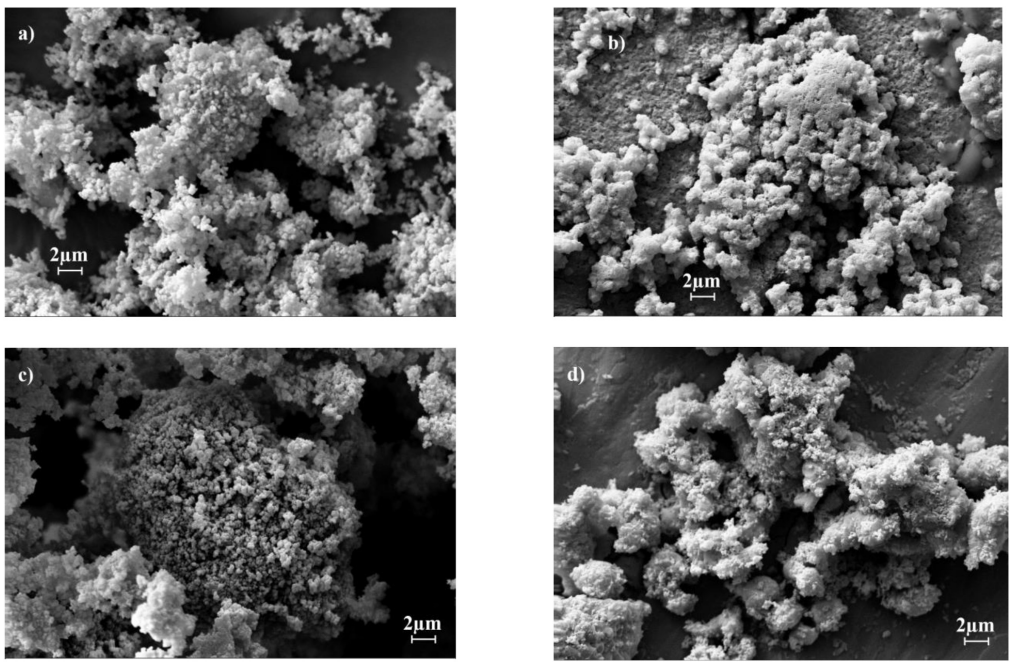

FIGURE 5 | SEM images for **(a)** P-CaDy20 as synthesized, **(b)** after 20 cycles, **(c)** P-CaDy-Al20 as synthesized, **(d)** after 20 cycles.

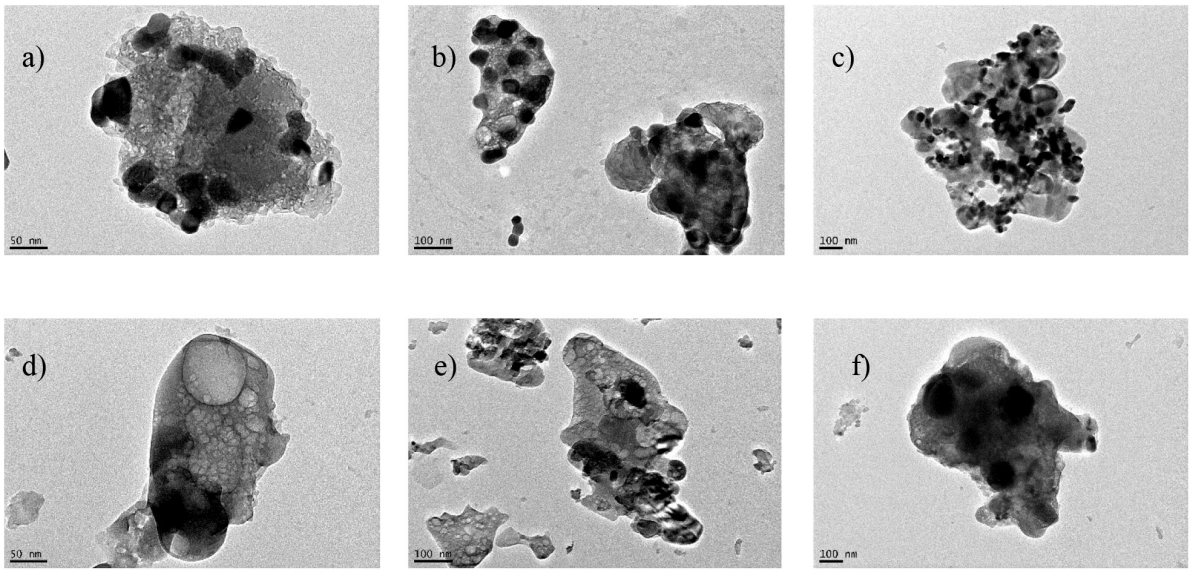

FIGURE 6 | TEM images for **(a)** and **(b)** P-CaDy20 as synthesized, **(c)** after 20 cycles, **(d)** and **(e)** PCaDy-Al20 as synthesized, **(f)** after 20 cycles.

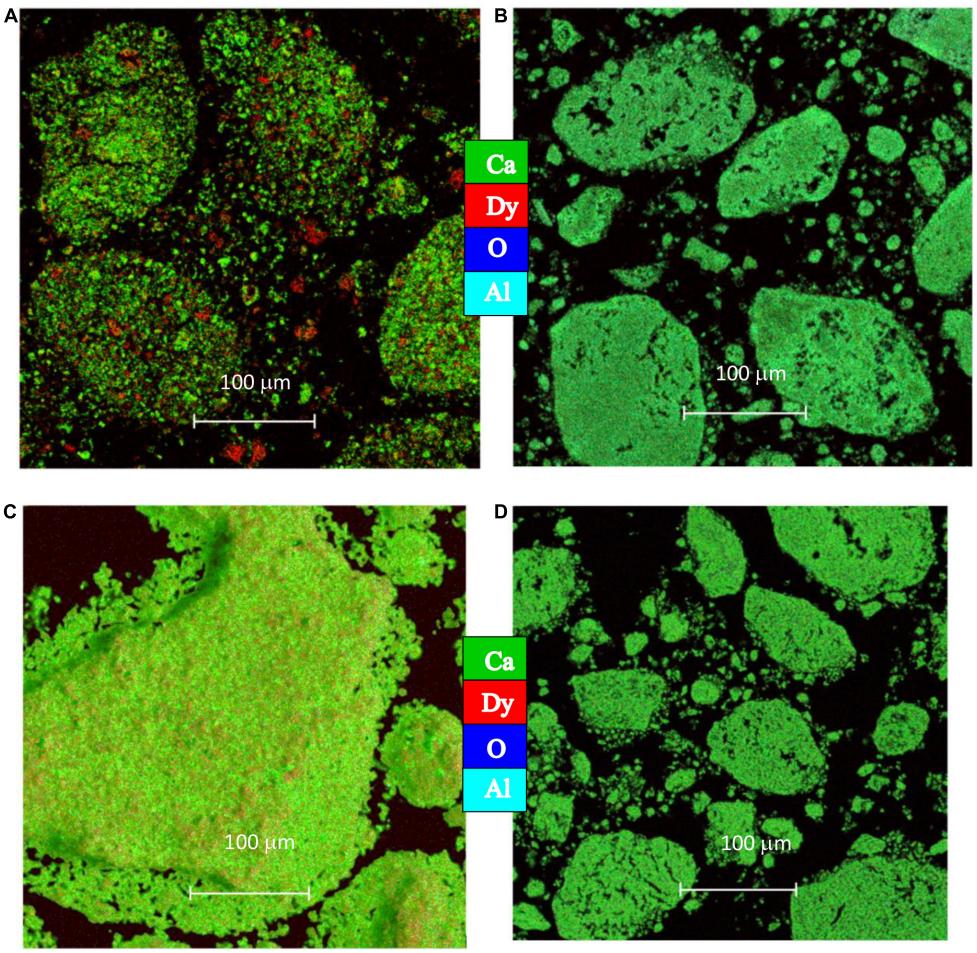

FIGURE 7 | EDS mapping for **(A)** P-CaDy20 as synthesized **(B)** P-CaDy-Al20 as synthesized, **(C)** PCaDy20 after 40 cycles **(D)** P-CaDy-Al20 after 40 cycles.

TABLE 5 | BET and BJH analysis results, as synthesized and after 40 cycles.

Material	BET surface area ($m^2\ g^{-1}$)	BJH cumulative pore volume ($cm^3\ g^{-1}$)	BJH average pore width (nm)
P-CaO	11.2	0.079	22.3
P-CaO-c	0.6	–	–
P-CaO-Al20	6.7	0.042	25.1
P-CaDy20	8.2	0.052	23.8
P-CaDy20-c	4.1	0.011	10.1
P-CaDy-Al20	13.4	0.12	41.5
P-CaDy-Al20-c	10.1	0.044	19.2

an inert support with unchanging volume, sorbent expansion during carbonation will be decreased, keeping pores open for CO_2 diffusion through the product layer (Jing et al., 2017).

Both explanations can potentially explain the improved performance of P-CaDy-Al20. TEM imaging reveals greater pore volume in P-CaDy-Al20 compared to P-CaDy20 (**Figures 6d–f**), which is also retained after cycling. EDS mapping also shows evidence of the mitigation of sintering in P-CaDy-Al20 as opposed to P-CaDy20 (**Figure 7**). The light blue aluminate domains throughout the material and around the grain boundaries could be indicative of the "pinning" effect of calcium aluminate.

Heat Storage Capacity and Comparison With Other TCES Materials

The heat storage capacities of the synthesized materials were evaluated using DSC analysis during thermal cycling and compared with experimental data from literature (see **Table 5**). **Figure 8** shows the variation of heat storage capacity with cycling, with **Figure 8A** showing that stable readings were obtained for P-CaDy-Al20. While the heat storage capacity of P-CaO-Al20 is initially higher due to the slightly higher amount of active CaO in P-CaO-Al20 (cf., **Table 1**), P-CaDy-Al20 exhibits a greater stability measured with cycling for both endothermic and exothermic processes (cf., **Figure 3**). After 40 cycles, the heat storage capacity of P-CaDy-Al20 is 25% greater than P-CaO-Al20 without Dy_2O_3. The greater exothermic heat flows in P-CaDy-Al20 are due to enhanced stability and are linked directly to enhanced carbonation conversion with cycling (cf., **Figure 3**). Cycling of pure Dy_2O_3 ascertained that the material does not act as a CO_2 sorbent, and without the inert support calcium aluminate (as in P-CaDy20; cf., **Figure 8B**), the material is unstable. However, the synergistic combination of Dy_2O_3 and $Ca_3Al_2O_6$ as inert supports achieves excellent results.

Table 5 compares the experimental results to heat storage capacities of other materials in published literature except for CuO (Alonso et al., 2015) and commercial $CaCO_3$, for which the values have been obtained using thermochemical data. P-CaDy-Al20 and P-CaO-Al20 achieve the highest heat of reaction values, even after 40 reaction cycles. Pure $CaCO_3$ has a calcination heat of reaction of 1624.6 kJ kg^{-1} [according to simulations performed using HSC Chemistry 8 ® (Roine, 2018)], but this is predicted to drop to 81 kJ kg^{-1} after 40 cycles, taking into account loss of reactivity using a sintering model (see section "Sintering Model"). As compared with other well-investigated thermochemical systems, such as Co_3O_4/CoO (Carrillo et al., 2014), BaO (Fahim and Ford, 1983), CuO (Alonso et al., 2015), Mn_2O_3/Mn_3O_4 (Carrillo et al., 2014), $(Mn_{0.1}Fe_{0.9})_2O_3$ (Carrillo et al., 2015), the spinel $(Mn_{0.33}Fe_{0.67})_2O_3$ (Al-Shankiti et al., 2019; Hamidi et al., 2019), $(Co_{0.867}Fe_{0.133})_3O_4$ (Block et al., 2014), and $(Co_{0.99}Mn_{0.01})_3O_4$ (Carrillo et al., 2014), P-CaDy-Al20 has the largest exothermic heat storage capacity after a longer cycling period. After 40 cycles, this heat of reaction (582.2 kJ kg^{-1}) is 3.3 times greater than $(Mn_{0.33}Fe_{0.67})_2O_3$ (Hamidi et al., 2019), 18% higher than the well-known Co_3O_4/CoO redox pair (Carrillo et al., 2014) and 7.3 times higher than Mn_2O_3/Mn_3O_4 (Carrillo et al., 2014). Therefore, it can be concluded that

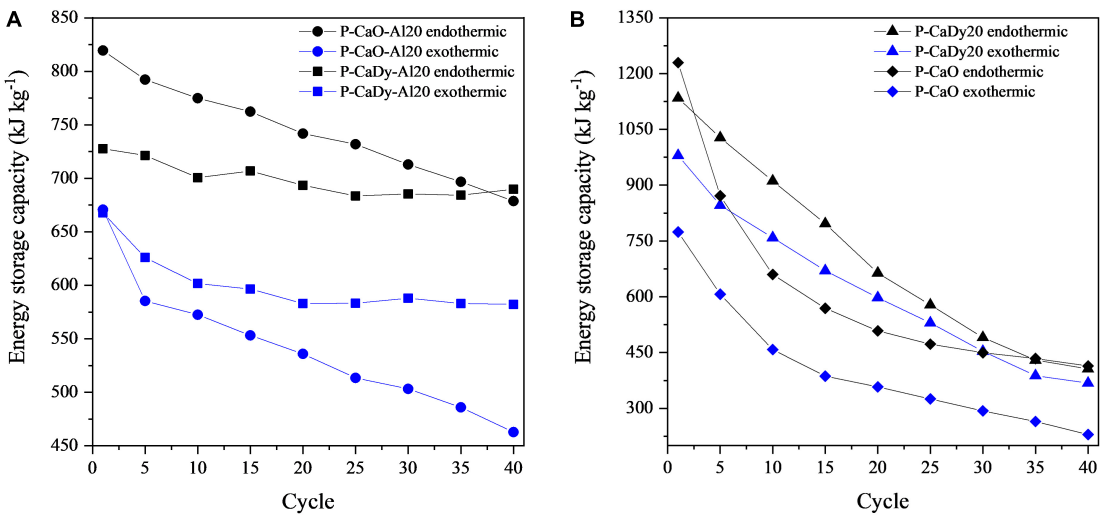

FIGURE 8 | (A) Endothermic and exothermic heat flows for supported and **(B)** weight loss of supported materials under CO_2.

the materials P-CaDy-Al20 and P-CaO-Al20 have the best performance so far found in literature for this type of small laboratory scale analysis. Further work should be perfomed at reactor level to compare the materials in this work with reactor-scale tests in published literature (Tescari et al., 2013).

Feasibility Study

Figures 9A,B show the application of sintering models to the first 40 carbonation cycles of experimental data (cf., sections "Material Characterization" and "Calcination-Carbonation Cycling Analysis"). Using the sintering model with the greatest accuracy (**Table 6**), the long-term performance of selected synthesized materials was modeled (**Figure 9C**).

A feasibility assessment of the selected synthesized materials and commercial $CaCO_3$ is presented in **Table 6**. The indicated sintering models were used to determine the number of cycles for carbonation conversion to fall below 20%. This cut-off has been suggested as the minimum carbonation conversion capacity to allow for optimum plant efficiency using a pressurized fluidized bed combustor as the carbonator (Prieto et al., 2016). If carbonation conversion drops below this capacity, it will need to be replaced with fresh material.

The sintering models determine that residual carbonation conversion does not drop below 20% for P-CaDy-Al20, even after 30 years of continuous cycling, whereas unsupported P-CaO would need to be replaced after seven cycles and Comm-$CaCO_3$ would need to be replaced every six cycles. This would incur

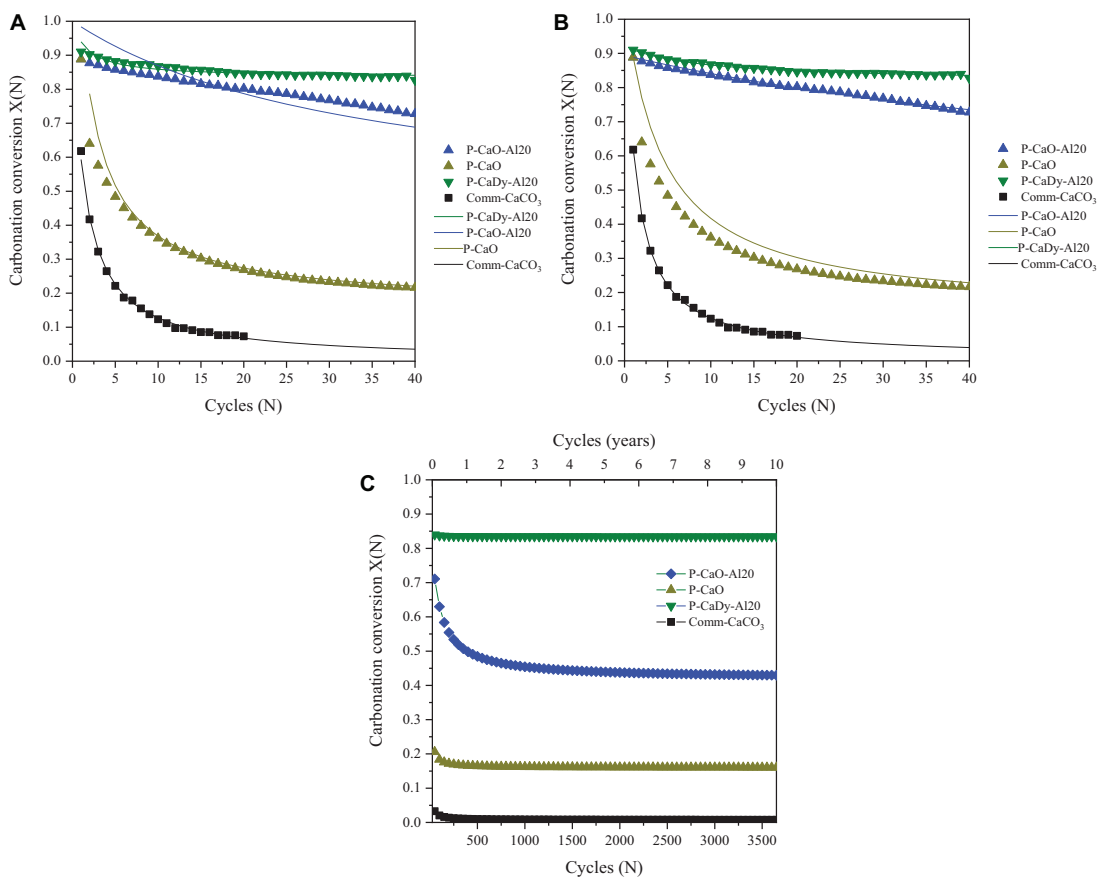

FIGURE 9 | Sintering model compared to experimental data using **(A)** deactivation sintering model (Luo et al., 2010) and **(B)** semi-empirical model (Hu et al., 2016), with **(C)** long-term CaO-based sorbent performance using best fitting sintering models.

TABLE 6 | Feasibility assessment of selected candidate materials.

Material	Sintering model	Cycles to drop below 20% conversion (days)	Number of sorbent replacements needed after 30 years of cycling	μStorage after 40 cycles (kg kWh^{-1})	μStorage after 30 years of cycling assuming 1 cycle per day (kg kWh^{-1})
P-CaO	[53]	7	1564	15.7	24533
P-CaO-Al20	[55]	58	189	7.78	1470
P-CaDy-Al20	[53]	Infinite	None (1)	6.18	6.18
Comm-$CaCO_3$	[55]	6	1825	44.3	80911

additional operation and maintenance costs on top of the cost required to replace the material.

When evaluating the mass specific storage utilization ($\mu_{Storage}$) after 40 charge and discharge cycles, the best performing materials are P-CaDy-Al20 and P-CaO-Al20, with storage densities of 6.2 and 7.8 kg kWh^{-1}, respectively. When considering the amount of material required after replacement over the CSP plant lifetime, the improved storage utilization of P-CaDy-Al20 is even more apparent. After 30 years, it is expected to retain a storage utilization (μstorage) as low as 6.2 kg kWh^{-1}, compared to 81 tons kWh^{-1} for commercial $CaCO_3$ (**Table 6**). This is due to its superior stability and extremely high residual carbonation conversion. These results justify the additional cost of inert supports for the synthesized material P-CaDy-Al20 and indicate its suitability for large-scale energy storage applications.

CONCLUSION

A CaO-based material supported with $Ca_3Al_2O_6$ and Dy_2O_3 shows excellent energy sorption cycling under a CO_2 atmosphere. The main benefits are due to its retention of high surface area compared to CaO and the addition of anti-sintering properties, even under an atmosphere which accelerates sintering. A conversion capacity of 82.7% is retained after 40 cycles under severe calcination conditions while other materials in the literature show high deactivation. The retention of conversion capacity is not the only feature that makes the material promising for TCES. A further feasibility study found that the exothermic heat of reaction obtained (582.2 kJ kg^{-1}) is up to seven times higher than other TCES systems (like Mn_2O_3/Mn_3O_4 redox cycle). In addition, a sintering model was applied to evaluate the specific storage utilization. In this study it was found that 6.2 kg kWh^{-1} is required for the CaO supported with $Ca_3Al_2O_6$ and Dy_2O_3, while for commercial limestone 81 tons kWh^{-1} will be needed over 30 years (a common CSP plant life). This is because the conversion capacity of commercial limestone drops below 20% after six thermal cycles (or 6 days assuming one cycle per day) and this implies the need for 1825 replacements over a common CSP plant life. This initial feasibility study shows that despite the additional cost of the supports, their addition is beneficial for the stable and long-term performance of the storage system.

DATA AVAILABILITY STATEMENT

The raw data supporting the conclusions of this article will be made available by the authors, without undue reservation.

AUTHOR CONTRIBUTIONS

LF-H, AB, and SD contributed to conception and design of the study. AB and SD obtained funding for the research. LF-H and XG performed the experiments. AT, AB, and SD supervised the experimental results. All authors contributed to the writing the manuscript, manuscript revision, read, and approved the submitted version.

FUNDING

This research was performed as part of the Australian Solar Thermal Research Initiative (ASTRI), a project supported by the Australian Government, through the Australian Renewable Energy Agency (ARENA).

REFERENCES

Aihara, M., Nagai, T., Matsushita, J., Negishi, Y., and Ohya, H., (2001). Development of porous solid reactant for thermal-energy storage and temperature upgrade using carbonation/decarbonation reaction. *Appl. Energy* 2001, 225–238. doi: 10.1016/s0306-2619(00)00072-6

Albrecht, K. O., Wagenbach, K. S., Satrio, J. A., Shanks B. H., and Wheelock, T. D. (2008). Development of a CaO-Based CO2 Sorbent with Improved Cyclic Stability. *Industr. Eng. Chem. Res.* 47, 7841–7848. doi: 10.1021/ie8007743

Alonso, E., Rabago, C. P., Licurgo, J., Fuentealba, E., and Estrada, C. A. (2015). First experimental studies of solar redox reactions of copper oxides for thermochemical energy storage. *Sol Energy* 115, 297–305. doi: 10.1016/j.solener.2015.03.005

Al-Shankiti, I. A., Ehrhart, B. D., Ward, B. J., Bayon, A., Wallace, M. A., Bader, R., et al., (2019). Particle design and oxidation kinetics of iron-manganese oxide redox materials for thermochemical energy storage. *Sol. Energy* 183, 17–29. doi: 10.1016/j.solener.2019.02.071

André, L., Abanades S., and Flamant, S. (2016). Screening of thermochemical systems based on solid-gas reversible reactions for high temperature solar thermal energy storage. *Renew. Sustain. Energy Rev* 64, 703–715. doi: 10.1016/j.rser.2016.06.043

André, L., and Abanades, S. (2018). Investigation of metal oxides, mixed oxides, perovskites and alkaline earth carbonates/hydroxides as suitable candidate materials for high-temperature thermochemical energy storage using reversible solid-gas reactions. *Mater. Today Energy* 10, 48–61. doi: 10.1016/j.mtener.2018.08.007

Angeli, S. D., Martavaltzi C. S. and Lemonidou, A. A. (2014). Development of a novel-synthesized Ca-based CO2 sorbent for multicycle operation: parametric study of sorption. *Fuel* 127, 62–69. doi: 10.1016/j.fuel.2013.10.046

Awan, AB., Zubair, M., Praveen, R. P., and Bhatti, A. R. (2019). Design and comparative analysis of photovoltaic and parabolic trough based CSP plants. *Sol. Energy* 183, 551–565. doi: 10.1016/j.solener.2019.03.037

Azimi, B., Tahmasebpoor, M., Sanchez-Jimenez, P. E., Perejon, A., and Valverde, J. M. (2019). Multicycle CO2 capture activity and fluidizability of Al-based synthesized CaO sorbents. *Chem. Eng. J.* 358, 679–690. doi: 10.1016/j.cej.2018.10.061

Bayon, A., Bader, R., Jafarian, M., Fedunik-Hofman, L., Sun, Y., Hinkley, J., et al. (2018). Techno-economic assessment of solid-gas thermochemical energy storage systems for solar thermal power applications. *Energy* 149, 473–484. doi: 10.1016/j.energy.2017.11.084

Benitez-Guerrero, M., Sarrion, B., Perejon, A., Sanchez-Jimenez, P. E., and Perez-Maqueda, L. A., and Valverde, J. M. (2017). Large-scale high-temperature solar energy storage using natural minerals. *Sol. Energy Mater. Sol. Cells* 168, 14–21. doi: 10.1016/j.solmat.2017.04.013

Benitez-Guerrero, M., Valverde, J. M., Perejon, A., Sanchez-Jimenez, P. E., and Perez-Maqueda, L. A., (2018). Low-cost Ca-based composites synthesized by biotemplate method for thermochemical energy storage of concentrated solar power. *Appl. Energy* 210, 108–116. doi: 10.1016/j.apenergy.2017.10.109

Block, T., Knoblauch, N., and Schmücker, M. (2014). The cobalt-oxide/iron-oxide binary system for use as high temperature thermochemical energy storage material. *Thermochim. Acta* 577, 25–32. doi: 10.1016/j.tca.2013.11.025

Broda, M., Kierzkowska, A. M., and Müller, C. R. (2012). Influence of the Calcination and Carbonation Conditions on the CO2 Uptake of Synthetic Ca-Based CO2 Sorbents. *Environ. Sci. Technol* 46, 10849–10856. doi: 10.1021/es302757e

Calle, A. D. L., Bayon A., and Too, Y. C. S. (2018). Impact of ambient temperature on supercritical CO2 recompression Brayton cycle in arid locations: finding the optimal design conditions. *Energy* 153, 1016–1027. doi: 10.1016/j.energy.2018.04.019

Carrillo, A. J., David Serrano, P., Pizarro, P., and Coronado, J. M. (2015). Improving the Thermochemical Energy Storage Performance of the Mn2O3/Mn3O4 Redox Couple by the Incorporation of Iron. *ChemSusChem*. 8, 1947–1954. doi: 10.1002/cssc.201500148

Carrillo, A. J., Moya, J., Sandoval, A. B., Jana, P., O'Shea, V. A. D. L. P., Romero, M., et al., (2014). Thermochemical energy storage at high temperature via redox cycles of Mn and Co oxides: pure oxides versus mixed ones. *Sol. Energy Mater. Sol. Cells* 123, 47–57. doi: 10.1016/j.solmat.2013.12.018

Chacartegui, R., Alovisio, A., Ortiz, C., Valverde, J. M., Verda, V., and Becerra, J. A., (2016). Thermochemical energy storage of concentrated solar power by integration of the calcium looping process and a CO2 power cycle. *Appl. Energy* 173, 589–605. doi: 10.1016/j.apenergy.2016.04.053

Cotton, F. A., Wilkinson, G., Murillo, C. A., and Bochmann, M. (1999). *Advanced Inorganic Chemistry*. 6th ed. New York: Wiley-Interscience.

Degen, T., Sadki, M., Bron, E., König, U., and Nénert, G. (2014). HighScore Plus, in *Powder Diffraction* United Kingdom: Malvern Panalytical Instrumentation compan

Derevschikov, V. S., Lysikov A. I., and Okunev, A. G. (2011). High Temperature CaO/Y2O3 Carbon Dioxide Absorbent with Enhanced Stability for Sorption-Enhanced Reforming Applications. *Industr. Eng. Chem. Res.* 50, 12741–12749. doi: 10.1021/ie2015334

Edwards, S., and Materić, V. (2012). Calcium looping in solar power generation plants. *Sol. Energy* 86, 2494–2503. doi: 10.1016/j.solener.2012.05.019

Erans, M., Jeremias, M., Zheng, L., Joseph Y. G., Blamey, J., Manovic, V., et al., (2018). Pilot testing of enhanced sorbents for calcium looping with cement production. Applied Energy, 225, 392–401. doi: 10.1016/j.apenergy.2018.05.039

Fahim M. A. and Ford, J. D. (1983). Energy storage using the BaO2-BaO reaction cycle. *The Chem. Eng. J*. 1983. 27, 21–28. doi: 10.1016/0300-9467(83)80042-2

Gil, A., Medrano, M., Martorell, I., Lázaro, A., Dolado, P., Zalba, B. et al. (2010). State of the art on high temperature thermal energy storage for power generation. Part 1—Concepts, materials and modellization. *Renew. Sustain. Energy Rev.* 14, 31–55. doi: 10.1016/j.rser.2009.07.035

Grasa, G. S., Abanades, J. C., Alonso, M., and González, B. (2008). Reactivity of highly cycled particles of CaO in a carbonation/calcination loop. *Chem. Eng. J.* 137, 5615–5667.

Grasa, G. S., and Abanades, J. C. (2006). CO2 Capture Capacity of CaO in Long Series of Carbonation/Calcination Cycles. *Industr. Eng. Chem. Res* 45, 8846–8851. doi: 10.1021/ie0606946

Greenblatt, H. B., Brown, N. R., Slaybaugh, R., Wilks, T., Stewart, E., and McCoy, S. T. (2017). The Future of Low-Carbon Electricity. *Ann. Rev Environ. Resour.* 42, 289–316.

Hamidi, M., Bayon, A., Wheeler, V. M., Kreider, P., Wallace, M. A., Tsuzuki, T., et al., (2019). Reduction kinetics for large spherical 2:1 iron–manganese oxide redox materials for thermochemical energy storage. *Chem. Eng. Sci.* 201, 74–81. doi: 10.1016/j.ces.2019.02.012

Hu, Y. C., Liu, W. Q., Sun, J., Li, M. K., Yang, X. W., Zhang, Y., et al., (2015). Incorporation of CaO into novel Nd2O3 inert solid support for high temperature CO2 capture. *Chem. Eng. J.* 273, 333–343. doi: 10.1016/j.cej.2015.03.074

Hu, Y., Liu, W., Sun, J., Yang, X., Zhou, Z., Zhang Y., et al., (2016). High Temperature CO2 Capture on Novel Yb2O3-Supported CaO-Based Sorbents. *Energy Fuels* 30, 6606–6613. doi: 10.1021/acs.energyfuels.6b01185

Jana, P., O'Shea, V. A. D. L. P., Coronado, J. M., and Serrano, D. P. (2010). Cobalt based catalysts prepared by Pechini method for CO2-free hydrogen production by methane decomposition. *Int. J. Hydrogen Energy* 35, 10285–10294. doi: 10.1016/j.ijhydene.2010.07.125

Jing, J., Li, T., Zhang, X., Wang, S., Feng, J., Turmel, W. A., et al., (2017). Enhanced CO2 sorption performance of CaO/Ca3Al2O6 sorbents and its sintering-resistance mechanism. *Appl. Energy* 199, 225–233. doi: 10.1016/j.apenergy.2017.03.131

Kierzkowska, A. M., Pacciani, R., and Müller, C. R. (2013). CaO-based CO2 sorbents: from fundamentals to the development of new, highly effective materials. *ChemSusChem*. 6, 1130–1148. doi: 10.1002/cssc.201300178

Li, C., Wu U. -T and Lin, H. -P., (2014). Cyclic performance of CaCO3@mSiO2 for CO2 capture in a calcium looping cycle. *J. Mater. Chem. A* 2, 8252–8257. doi: 10.1039/c4ta00516c

Li, Y., Shi, L., Liu, C., He, Z., Wu, S. (2015). Studies on CO2 uptake by CaO/Ca3Al2O6 sorbent in calcium looping cycles. *J. Therm. Anal. Calorim*, 120, 1519–1528. doi: 10.1007/s10973-015-4480-9

Li, Z. -S., Cai, N. -S., Huang Y. -Y., and Han, H. J. (2005). Synthesis, experimental studies, and analysis of a new calcium-based carbon dioxide absorbent. *Energy Fuels* 19, 1447–1452.

Li, Z., Liu Y., and Cai, N. (2013). Understanding the effect of inert support on the reactivity stabilization for synthetic calcium based sorbents. *Chem. Eng. Sci.* 89, 235–243. doi: 10.1016/j.ces.2012.12.006

Liu, M., Tay, N. H. S., Bell, S., Belusko, M., Jacob, R., Will, G., et al. (2016). Review on concentrating solar power plants and new developments in high temperature thermal energy storage technologies. *Renew Sustain. Energy Rev.* 53, 1411–1432. doi: 10.1016/j.rser.2015.09.026

Liu, W., An, H., Qin, C., Yin, J., Wang, G., Feng, B., et al., (2012b). Performance enhancement of calcium oxide sorbents for cyclic CO2 capture: a review. *Energy Fuels* 26, 2751–2767. doi: 10.1021/ef300220x

Liu, W., González, B., Dunstan, M. T., Sultan, D. S., Pavan, A., Ling, C. D., et al., (2016). Structural evolution in synthetic, Ca-based sorbents for carbon capture. *Chemical Eng. Science* 139, 15–26. doi: 10.1016/j.ces.2015.09.016

Liu, W., Dennis, J. S., Sultan, D. S., Redfern, S. A. T., and Scott, S. A. (2012a)An investigation of the kinetics of CO2 uptake by a synthetic calcium based sorbent. *Chem. Eng. Sci.*, 69, 644–658. doi: 10.1016/j.ces.2011.11.036

Lu S., and Wu, S., (2016). Calcination–carbonation durability of nano CaCO3 doped with Li2SO4. *Chem. Eng. J.* 294, 22–29. doi: 10.1016/j.cej.2016.02.100

Lu, H., Khan, A., Pratsinis S. E. and Smirniotis, P. G. (2009). Flame-Made Durable Doped-CaO Nanosorbents for CO2 Capture. *Energy Fuels* 23, 1093–1100. doi: 10.1021/ef8007882

Luo, C., Zheng, Y., Ding, N., Wu, Q., Bian G., and Zheng, C. (2010). Development and Performance of CaO/La2O3 Sorbents during Calcium Looping Cycles for CO2 Capture. *Industr. Eng. Chem. Res.* 49, 11778–11784.

Manovic, V., and Anthony, E. J., (2005). Thermal Activation of CaO-Based Sorbent and Self-Reactivation during CO2 Capture Looping Cycles. *Environ. Sci. Technol.* 42, 4170–4174. doi: 10.1021/es800152s

Ortiz, C., Romano, M. C., Valverde, J. M., Binotti, M., and Chacartegui, R., (2018a). Process integration of Calcium-Looping thermochemical energy storage system in concentrating solar power plants. *Energy* 155, 535–551. doi: 10.1016/j.energy.2018.04.180

Ortiz, C., Valverde, J. M., Chacartegui R., and Perez-Maqueda, L. A. (2018b). Carbonation of Limestone Derived CaO for Thermochemical Energy Storage: from Kinetics to Process Integration in Concentrating Solar Plants. *ACS Sustain. Chem. Eng.* 6, 6404–6417. doi: 10.1021/acssuschemeng.8b00199

Peng, W., Xu, Z., Luo, C., and Zhao, H. (2015). Tailor-Made Core–Shell CaO/TiO2–Al2O3 Architecture as a High-Capacity and Long-Life CO2 Sorbent. *Environ. Sci. Technol* 49, 8237–8245. doi: 10.1021/acs.est.5b01415

Perry, D. L. (2015). *Handbook of Inorganic Compounds*. CRC Press. United States.

Ping, H., Wang Y. and Wu, S. (2016). Preparation of MgO-coated nano CaO using adsorption phase reaction technique for CO2 sorption. *RSC Adv.* 6, 41239–41246. doi: 10.1039/c6ra05452h

Prieto, C., Cooper, P., Fernández, A. I., Cabeza, L. F. (2016). Review of technology: thermochemical energy storage for concentrated solar power plants. *Renew. Sustain. Energy Rev.* 60, 909–929. doi: 10.1016/j.rser.2015.12.364

Qin, C., Du, H., Liu, L., Yin J., and Feng, B. (2014). CO2 Capture Performance and Attrition Property of CaO-Based Pellets Manufactured from Organometallic Calcium Precursors by Extrusion. *Energy Fuels* 28, 329–339. doi: 10.1021/ef4012609

Radfarnia H. R. and Sayari, A. (2015). A highly efficient CaO-based CO2 sorbent prepared by a citrate-assisted sol-gel technique. *Chem. Eng. J.* 262, 913–920. doi: 10.1016/j.cej.2014.09.074

Roine, Q. A., (2018). HSC Chemistry 8 0. Outotec, Pori

Sanchez-Jimenez, P. E., Perez-Maqueda, L. A. and Valverde, J. M., (2014). Nanosilica supported CaO: a regenerable and mechanically hard CO2 sorbent at Ca-looping conditions. *Appl. Energy* 118, 92–99. doi: 10.1016/j.apenergy.2013.12.024

Sarrión, B., Perejón, A., Sánchez-Jiménez, P. E., Pérez-Maqueda, L. A., and Valverde, J. M. (2018). Role of calcium looping conditions on the performance of natural and synthetic Ca-based materials for energy storage. *J. CO2 Util.* 28, 374–384. doi: 10.1016/j.jcou.2018.10.018

Schaube, F., Wörner A., and Tamme, R., (2011). High temperature thermochemical heat storage for concentrated solar power using gas–solid reactions. *J. Sol. Energy Eng.* 133, 31006.

Stanmore, B. R., and Gilot, P., (2005). Review: calcination and carbonation of limestone during thermal cycling for CO2 sequestration. *Fuel Proce. Technol.* 86, 1707–1743. doi: 10.1016/j.fuproc.2005.01.023

Starke, A. R., Cardemil, J. M., Escobar, R., and Colle, S. (2018). Multi-objective optimization of hybrid CSP+PV system using genetic algorithm. *Energy* 147, 490–503. doi: 10.1016/j.energy.2017.12.116

Steinhagen, H. M., and Nitsch, J. (2005). The Contribution of Renewable Energies to a Sustainable Energy Economy. *Process Safety Environ. Prot.*, 83, 285–297. doi: 10.1205/psep.05084

Stone, F. S. (1960). Reactivity of Solids. in 4th International Symposium on the Reactivity of Solids. Amsterdam: Elsevier. doi: 10.1016/0168-7336(88)80069-x

Sun, J., Liu, W., Li, M., Yang, X., Wang, W., Hu, Y., et al., (2016). Mechanical Modification of Naturally Occurring Limestone for High-Temperature CO2 Capture. *Energy Fuels* 8, 6597–6605. doi: 10.1021/acs.energyfuels.6b01131

Tescari, S., Neises, M., de Oliveira, L., Sattler, C., and Neveu, P. (2013). Thermal model for the optimization of a solar rotary kiln to be used as high temperature thermochemical reactor. *Sol. Energy* 95, 279–289. doi: 10.1016/j.solener.2013.06.021

Valverde, J. M. (2013). Ca-based synthetic materials with enhanced CO2 capture efficiency. *J. Mater. Chem. A* 1, 447–468. doi: 10.1039/c2ta00096b

Valverde, J. S., -López, M. B., Perejón, A., Sánchez-Jiménez P. E., and Pérez-Maqueda, L. A. (2017). Effect of Thermal Pretreatment and Nanosilica Addition on Limestone Performance at Calcium-Looping Conditions for Thermochemical Energy Storage of Concentrated Solar Power. *Energy Fuels* 31, 4226–4236. doi: 10.1021/acs.energyfuels.6b03364

Wang, N., Feng, Y., Liu, L., and Guo, X. (2018). Effects of preparation methods on the structure and property of Al-stabilized CaO-based sorbents for CO2 capture. *Fuel Process. Technol.* 173, 276–284. doi: 10.1016/j.fuproc.2018.02.005

Zhao, M., Shi, J., Zhong, X., Tian, S., Blamey, J., Jiang J., et al., (2014). A novel calcium looping absorbent incorporated with polymorphic spacers for hydrogen production and CO2 capture. *Energy Environ. Sci.* 7, 3291–3295. doi: 10.1039/c4ee01281j

Zhou, Z., Qi, Y., Xie, M., Cheng, Z., and Yuan, W. (2012). Synthesis of CaO-based sorbents through incorporation of alumina/aluminate and their CO2 capture performance. *Chem. Eng. Sci.* 74, 172–180. doi: 10.1016/j.ces.2012.02.042

Zhou, Z., Xu, P., Xie, M., Cheng, Z., and Yuan, W. (2013)Modeling of the carbonation kinetics of a synthetic CaO-based sorbent. *Chemical Engineering Science*, 95, 283–290. doi: 10.1016/j.ces.2013.03.047

Conflict of Interest: The authors declare that the research was conducted in the absence of any commercial or financial relationships that could be construed as a potential conflict of interest.

NOMENCLATURE

ΔH_r, Reaction enthalpy, kJ mol^{-1};
k, Deactivation constant, min^{-1};
M, Molar mass, g mol^{-1};
m_i, Initial sample mass, g;
m(t), Sample mass after t min of carbonation, g;
$m_{X=1}$, Theoretical sample mass after 100% conversion, g;
T, Temperature, K;
X(N), Carbonation conversion after N cycles;
X_r, Residual carbonation conversion;
X(t), Carbonation conversion after t time;
$X(t)_{Eff}$, Effective carbonation conversion (considering inert support) after t time;
$\mu_{Storage}$, Gravimetric energy storage utilization, kg kWh^{-1}.

frontiers in Energy Research

ORIGINAL RESEARCH
published: 08 June 2021
doi: 10.3389/fenrg.2021.696213

Phase Change Material of Copper–Germanium Alloy as Solar Latent Heat Storage at High Temperatures

Nobuyuki Gokon[1], Chew Shun Jie[2], Yuya Nakano[2], Shogo Okazaki[2], Tatsuya Kodama[1], Tsuyoshi Hatamachi[1] and Selvan Bellan[1]*

[1]Dep. of Chemistry and Chemical Engineering, Faculty of Engineering, Niigata University, Niigata, Japan, [2]Graduate School of Science and Technology, Niigata University, Niigata, Japan

A copper–germanium alloy (Cu–Ge alloy) was examined as a phase change material, at temperatures exceeding 600°C, for latent heat storage in solar thermal applications. First, the thermo-physical properties of the Cu–Ge alloy were examined using differential scanning calorimetry, thermomechanical analysis, and laser flash analysis. Second, to evaluate the thermal response and reliability of the Cu–Ge alloy, the cyclic properties of thermal charge/discharge were examined under various thermal conditions. The alloys obtained after the tests were examined for their chemical compatibility with the stainless steel container using an electron probe micro analyzer. The elemental distribution of each Cu–Ge alloy was evaluated using cyclic performance tests. Finally, the chemical compatibility of the Cu–Ge alloy was evaluated using a high-temperature test with candidate materials of a phase change material container vessel [stainless steel (SUS310S), Inconel625, silicon carbide (SiC), and alumina (Al2O3)]. The Cu–Ge alloy exhibited significant potential as a latent heat storage material in next-generation solar thermal power plants because it demonstrates various advantages, including a superior storage capacity at a temperature of 644°C, temperature coherence to the phase diagram, a quick thermal response, satisfactory cyclic behavior of charge/discharge modes, a thermodynamically stable metallographic structure, and non-reactivity with container ceramic materials (SiC and Al2O3).

Keywords: phase change material, thermal storage system, latent heat, copper-germanium alloy, concentrated solar power

OPEN ACCESS

Edited by:
Alfonso J. Carrillo, Instituto de Tecnología Química (ITQ), Spain

Reviewed by:
María Orfila, Rey Juan Carlos University, Spain
Richard Murdey, Kyoto University, Japan
Anastasia Stamatiou, Lucerne University of Applied Sciences and Arts, Switzerland

****Correspondence:***
Nobuyuki Gokon
ngokon@eng.niigata-u.ac.jp

Specialty section:
This article was submitted to Solar Energy, a section of the journal Frontiers in Energy Research

Received: *16 April 2021*
Accepted: *19 May 2021*
Published: *08 June 2021*

Citation:
Gokon N, Jie CS, Nakano Y, Okazaki S, Kodama T, Hatamachi T and Bellan S (2021) Phase Change Material of Copper–Germanium Alloy as Solar Latent Heat Storage at High Temperatures. Front. Energy Res. 9:696213. doi: 10.3389/fenrg.2021.696213

INTRODUCTION

Renewable energy sources are attractive alternatives to fossil fuels because of their promising social, environmental, and economic benefits. The Sustainable Development Scenario of the International Energy Agency (IEA) outlook 2020 predicted that CO_2 emissions will fall to less than 27 billion tonnes in 2030, and low-carbon electricity will account for almost two-thirds of the world's total electricity generation (International Energy Agency (IEA), 2020). Solar energy is one of the most environmentally friendly energy sources, and the milestones for solar energy exploitation are energy capture, energy conversion, and energy storage. Solar energy can be harnessed in two different ways, namely, photovoltaic cells and thermal conversion systems (Goswami, 2015).

Concentrating solar power technologies (CSPs) convert sunlight into thermal power, which is traditionally used as a heat source for power generation by thermodynamic cycles (Islam et al., 2018). CSP technology has the advantage of higher utilization efficiency of solar energy, extension of the energy operating period from day to night, or from sunny to cloudy weather due to the capability to store energy in the thermal storage system and use it when required (Cohen, 2008; Skumanich, 2010; Stoffel et al., 2010). In accordance with relevant physicochemical mechanisms, the working principles of thermal energy storage (TES) are typically classified into three types: sensible heat storage, latent heat storage, and thermochemical heat storage (Gil et al., 2010; Pelay et al., 2017).

Molten salts are excellent for use in liquid sensible TES and as heat transfer fluids (HTFs) because of their thermal stability at high (generally over 500°C) temperatures. They are commonly utilized in modern central tower CSP technology (Kuravi et al., 2013). One of these molten salts, solar salt (60 wt% $NaNO_3$-40 wt % KNO_3), has proven successful even for TES in the GWh-scale at an operating temperature range of 290–560°C. In current CSP technologies, the highest temperature of the heat source is largely restricted by the thermal decomposition temperature of the HTF (Xu et al., 2018). In addition, corrosion by molten salts of the pipe material and storage tank is an important factor requiring improvement. To increase solar-to-power efficiency in current CSP plants, coating technology (Agüero et al., 2019) allowing the control of moderate corrosion degradation, using low-cost steel instead of expensive Ni-base alloys, and enhancing the thermal stability limit of solar salt to 600°C or above temperature (Bonk et al., 2019) by controlling the salt chemistry of corrosive species have been extensively studied. The high-temperature limit of the molten salt directly affects the volumetric thermal storage capacity and efficiency of the coupled thermodynamic cycle. Thus, HTFs with high thermal durability at high temperatures are required for next-generation CSP.

The cost of CSP in 2018, with an average levelized cost of electricity (LCOE) of 0.185 USD/kWh (IRENA, 2018), remain uncompetitive with other renewable energy technologies (wind and solar PV). However, next-generation CSP tower technologies are expected to significantly lower this figure to 0.08–0.11 USD/kWh by 2025 (IRENA, 2016), mainly because the utilization of high temperature (>700°C) receivers will unlock the possibility of improving power block efficiency. The Generation three Concentrating Solar Power (Gen3CSP) program was initiated by the Department of Energy (DOE) to improve commercial viability (Mehos et al., 2017). The Gen3CSP liquid pathway (G3LP) project of the three technology tracks is being developed to increase the operating temperature of CSP plants using liquid heat transfer and storage fluids to 700°C to increase plant efficiencies and reduce the LCOE. One option includes a liquid sodium receiver to collect concentrated thermal energy, a 3-part or ternary mixture of chloride molten salts to store heat, and a supercritical carbon dioxide (sCO_2) Brayton cycle to convert it to electricity (Carlson et al., 2020).

Several latent heat storage (LHS) systems using phase change materials (PCMs), between solid and liquid phases, have been identified in molten salts and metals. Molten-salts have been utilized as potential PCMs for TES in CSP applications (Medrano et al., 2010; Kotzé et al., 2013). Most salt-based PCMs suffer from a series of drawbacks, including low thermal conductivity, being highly corrosive in the liquid phase at high temperature, and large volume changes during the phase change (Zhang et al., 2016). Metallic-based PCMs exhibit a rapid thermal response and high operating power owing to their high thermal conductivity, which leads to a decrease in the plant startup time and considerable latent storage capacity owing to the high density of the solid phase, in comparison to salt-based PCMs. In addition, high thermo-mechanical durability and reliability are beneficial for alleviating rapid thermal shocks caused by solar fluctuations and radiation transients (Risueño et al., 2017). These significant features make metallic-based PCMs promising candidates for LHS applications in current and next-generation CSP.

Birchenall and Reichmann (Birchenall and Riechman, 1980), and Farakas and Birchenall (Farkas and Birchenall, 1985) initially reported the possibility of metallic PCMs storing thermal energy by the enthalpy of fusion in binary and ternary eutectic mixtures. Most studies on TES in CSP applications have focused on low melting temperatures of T < 400°C, including Al–Mg–Zn (Khare et al., 2012), Mg–Zn (Blanco-Rodríguez et al., 2014; Rodríguez-Aseguinolaza et al., 2014), Al–Mg–Zn (Sun et al., 2007), Zn–Sn (Adinberg et al., 2010), Zn–Al–Mg (Risueño et al., 2017), Zn–Al (Risueño et al., 2017), Zn–Mg (Risueño et al., 2017), and Al–Sn (Sugo et al., 2013) systems. The potential TESs of metallic PCMs at an upper melting temperature of 600°C, which corresponds to a current central tower CSP using solar salt as the HTF and liquid sensible heat storage include Al–Mg–Zn (Farkas and Birchenall, 1985), Mg–Cu–Zn (Farkas and Birchenall, 1985), Mg–Bi (Fang et al., 2016), Al–Cu (Zhao et al., 2017), Al–Cu–Si (Farkas and Birchenall, 1985), Cu–Mg (El Karim et al., 2019), Al–Si (Wang et al., 2015) systems. The most promising TESs of metallic PCMs that allow their combination with next-generation CSP using liquid heat transfer and storage fluids up to 800°C include Fe–Mg (Sugo et al., 2013), Cu–Si (Gokon et al., 2016), Fe–Ge (Gokon et al., 2020), Zn–Cu–Mg (Farkas and Birchenall, 1985), Cu–Zn–Si (Farkas and Birchenall, 1985), Cu–Si–Mg (Farkas and Birchenall, 1985) systems.

One of the favorable features of metallic PCMs is a small volume change during the phase change. Recently, Si-containing alloys have been increasingly investigated as potential PCMs for TES in CSP applications. Eutectic compositions of 87.2% Al–12.2%Si and hyper-eutectic mixture containing more Si have great heat storage characteristics in the range 550–700°C (Gokon et al., 2015; Nomura et al., 2015; Wang et al., 2015; Fukahori et al., 2016; Wei et al., 2016). The eutectic composition is preferred as the PCM because of its thermal stability, based on the phase diagram operating within a narrow temperature range.

From the literature review and previous research on metallic PCMs in our laboratory, the Cu–Ge binary system was chosen as a metallic PCM for TES in CSP applications in this study. Si and Ge elements belong to the carbon group in the periodic table, in which the Cu–Ge alloy has a eutectic mixture containing Ge contents that may lead to a small volume change during the phase change. In addition, data available for thermo-physical properties of the Cu–Ge alloy is limited (Zhai et al., 2012). Similarly, there

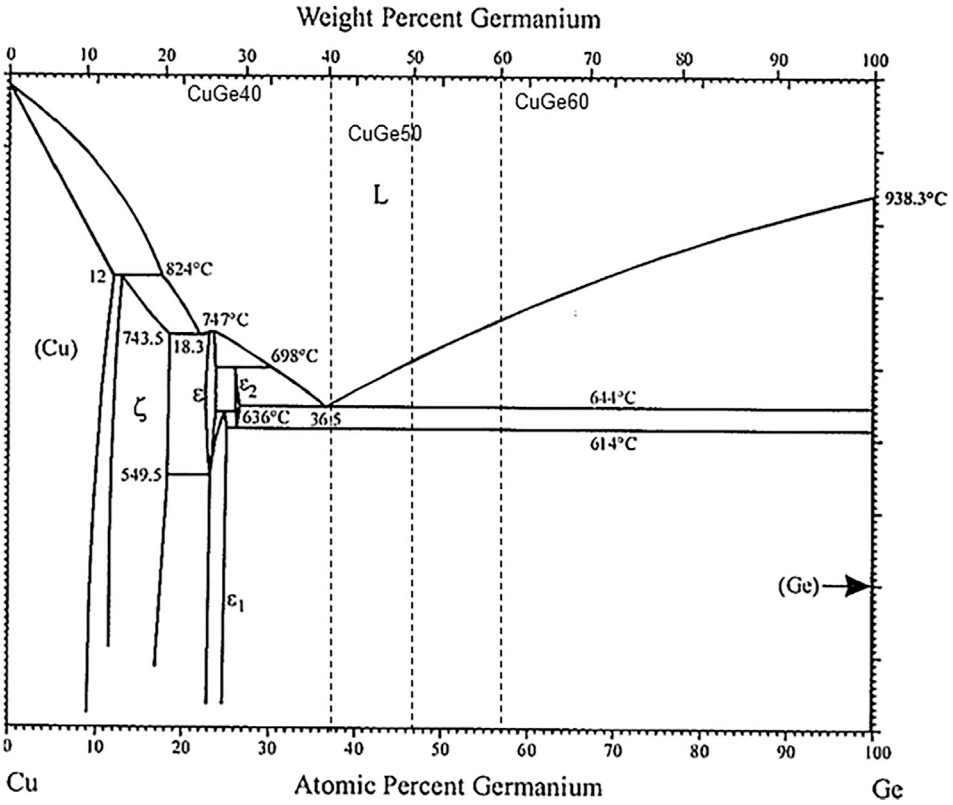

FIGURE 1 | Binary phase diagram of Copper and Germanium (Okamoto, 2010).

remains a dearth of information on the expected thermal response and consistence with the phase diagram based on the thermodynamic equilibrium, and favorable eutectic and liquefaction temperatures for TES in the net-generation CSP. Thus, eutectic and hypereutectic compositions of Cu–Ge alloys with liquefaction temperatures to 800 °C are the focus of this study.

In this study, Cu–Ge alloys with different compositions were examined as promising metallic PCMs. The chemical composition, crystal structure, and lattice parameters of the formed phases were investigated by X-ray diffraction (XRD) and Rietveld analysis. The thermophysical properties of the Cu–Ge alloys, including melting temperature, specific heat capacity, volume change, density, thermal diffusivity/conductivity, and latent heat, were determined to evaluate the potential of Cu–Ge alloys as a metallic PCM for TES in next-generation CSP applications. Furthermore, the thermal response and conformity of the thermal charge/discharge of the Cu–Ge alloys were studied and compared to the phase diagram based on thermodynamic equilibrium. Finally, chemical compatibility between the Cu and Ge alloy and candidate materials of the PCM container was tested and evaluated to identify potential construction materials for PCM container/capsulation.

EXPERIMENTAL PROCEDURE AND ANALYSES

Cu–Ge Alloy as a Phase Change Material

Eutectic and hypereutectic Cu–Ge alloys were selected to ensure a small volume change during phase change, liquefaction temperatures up to 800°C, and high thermal storage capacity because of the excess Ge content. Generally, most alloys expand thermally with increasing temperature. However, Ge may thermally shrink at the eutectic temperature owing to the nature of the abnormal liquid when the phase changes from solid to liquid. In terms of volume change and latent heat storage, this indicates that excess Ge can alleviate the thermal stress of the PCM container/capsulation during the solid–liquid phase transition in the charge–discharge mode; the excess Ge can contribute to enhancing the latent heat in a narrow temperature range. Hence, the potential of the Cu–Ge alloy was examined as a PCM thermal storage material.

Figure 1 shows the phase diagram of the Cu–Ge alloy. A phase diagram has been previously reported for binary alloys (Okamoto, 2010). Based on the storage temperature to 800°C, the present study selected eutectic (60 wt% Cu–40 wt% Ge, CuGe40) and hypereutectic (50 wt% Cu–50 wt% Ge, CuGe50) (40 wt% Cu–60 wt% Ge, CuGe60) mixtures of the Cu–Ge alloy.

The eutectic mixture corresponded to the CuGe40 = ε_2 phase + (Ge) and behaved in a reversible solid/liquid phase change at T = 644°C, and a solid/solid phase change between the ε_2 and ε_1 phases at T = 614°C. The hypereutectic alloys of CuGe50 and CuGe60 corresponded to a mixture of eutectic mixture and excess Ge solid, CuGe50, and CuGe60 = eutectic mixture + (Ge), and acted in a manner similar to the eutectic mixture at T = 644 °C. Subsequently, they continued to melting/solidification (latent heat storage) of the primary crystal (Ge) and sensible heat storage of liquid and solid phases to liquefaction temperatures of T = 644–765°C. Thus, the eutectic and hypereutectic Cu–Ge alloys exhibit a high latent heat capacity across the range of 614–765°C.

From the viewpoint of volume change during phase change, a hypereutectic Cu–Ge alloy contains more Ge compared to that of the eutectic composition, thereby indicating that the volume change of the PCM can be controlled at the phase change (solid/liquid phase). The possibility of volume change by varying the chemical composition of the Cu–Ge alloy was also investigated in this study.

Preparation

The Cu–Ge alloys were synthesized from reagents (high-purity materials, KOJUNDO CHEMICAL LABORATORY CO, LTD.) in a laboratory. A fine powder of copper (purity 99.9%, 180 μm) and germanium (4N, 300 μm) were weighed and mixed in an alumina boat. The alumina boat containing the powders was heated at 1,400°C for 2 h in an Ar stream of 1 dm^3/min at a normal state to prevent oxidation during the alloying process, and to melt the powder and form ingots of Cu–Ge alloy. The ingots of Cu–Ge alloy were subjected to homogeneous heat treatment at 800–900°C under vacuum. The ingot was cut into pellets (diameter <25 mm and thickness <10 mm) and chemically washed and cleaned to remove oil and dust from the surface. The identification of the solid phase and structural characterization of the Cu–Ge alloy were carried out by X-ray diffraction (XRD) (D2Phaser, Burker) using CuKα radiation (λ = 0.15418 nm) (30 kV-10 mA) at room temperature. The specimens for XRD measurement were prepared by utilizing a mounting press on phenolic resin to encapsulate the alloy and adding a layer of carbon conductive filler. The surface of the alloy was polished using SiC paper and then mounted on a specimen holder ring. Diffraction data were collected in the angular range corresponding to $10^\circ < 2\theta < 80^\circ$ with a 0.02° step size and a 1-s step interval. The crystalline phases were identified by comparison with standard reference patterns (Inorganic Crystal Structure Database, ICSD) (ICSD, 2020) and the Crystallography Open Database (COD). The lattice cell parameters of the refined structures of the synthesized solid phase were evaluated via Rietveld refinement of the structure models by using the pattern fitting method of the FullProf package.

Thermo-Physical Properties at High Temperatures

There is a paucity of studies on the values of the specific heat (C_p) based on the temperature and thermophysical properties of the Cu–Ge alloy. The phase transition temperatures and enthalpy of fusion for Cu–Ge alloys with a wide range of chemical compositions have been examined (Zhai et al., 2012). In this study, the melting, solidification, and eutectic temperatures, enthalpies, and specific heat capacity of the alloys were measured using differential scanning calorimetry [DSC, NETZSCH DSC 404 F3 Pegasus® manufactured by NETZSCH Co. Ltd., temperature resolution of $\pm 0.0025 \times |t|$ °C)] under an Ar flow of 100 ml/min with a heating and cooling rate of 10°C/min between room temperature and 900°C. Heating/cooling cycles in DSC were repeated three times under an Ar stream. From these measurements, the temperature dependence of sensible heat was estimated using the measured C_p values of the Cu–Ge alloy via DSC.

The thermal volume change of the Cu–Ge alloys was measured via thermomechanical analysis (TMA, NETZSCH 4000 SE, temperature resolution of ±0.5°C). To measure the thermal expansion/shrinkage when the phase changes between solid and liquid phases at high temperature, we designed and customized a sample holder to put the sample in the TMA equipment. The sample holder comprised a hollow cylinder (inner diameter of 6.5 mm, outer diameter, 10.5 mm, length, 22 mm) and pistons (diameter, 6.4 mm, length, 8 mm). A test sample of the Cu–Ge alloy (diameter, 6.2 mm, length, 7.5 mm) was prepared in a laboratory. The test sample was placed in the customized sample holder (inner diameter of 6.5 mm, length, 22 mm), and the test unit was placed in the TMA equipment. The coefficient of thermal expansion/shrinkage based on the temperatures and phase change between solid and liquid phases at specific temperatures was monitored under an N_2 flow of 100 ml/min with a heating and cooling rate of 5°C/min. The density of the Cu–Ge alloys was measured at 25°C using the Archimedes method. The temperature dependence of the density of the Cu–Ge alloys was determined using TMA data.

Thermal diffusivity of the Cu–Ge alloys was measured using a NETZSCH LFA-467HT hyper flash analyzer. The test sample (diameter of 10 mm and thickness of 1.14 mm) was prepared in a laboratory. The test sample was placed in a sapphire container, and the test unit was placed in the LFA equipment. Thermal diffusivity measurements were performed with Xe flashlight (pulse width 600 μs, five shots) at 250 V in an Ar stream at 20–900°C to avoid oxidation of the test sample. The thermal conductivities of the Cu–Ge alloys were calculated using these data.

Thermal Response Tests of Cyclic Charge/Discharge Modes

The thermal response of the charge/discharge modes was tested for the eutectic Cu–Ge alloy (60 wt% Cu-40 wt%Ge) as follows: The experimental arrangement for the thermal response tests is shown in **Figure 2**. A stainless-steel (SUS310S) test container (length, 200 mm; inner and outer diameters, 93.6 and 101.6 mm, respectively), was used for the thermal charge/discharge performance tests. The PCM container (length, 35 mm; inner diameter, 30 mm, and thickness, 10 mm) was composed of graphitic carbon in vacuum, and stainless steel (SUS 310S) in

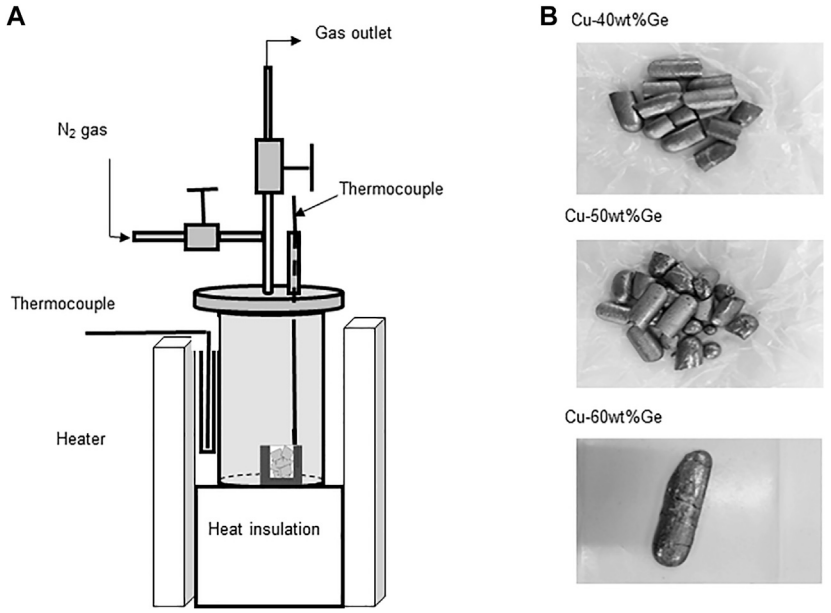

FIGURE 2 | Experimental set-up for the thermal response tests of cyclic charge/discharge modes: **(A)** test vessel and PCM container and **(B)** Cu–Ge alloy PCMs.

an air-flow atmosphere and was placed inside the test container. The Cu–Ge alloy was packed into a PCM container. 60 g of the eutectic Cu–Ge alloy was loaded into the PCM container (**Figure 2B**). For the charge mode, the electric heater was controlled at a constant heating rate of 4–6°C/min (1-9 cycles) and 8–12°C/min (10–20 cycles), to a temperature of 850°C, exceeding the eutectic temperature, based on the chemical composition of the Cu–Ge alloy. The temperature variation of the test container with an endothermic phase change was measured under a controlled heating rate. The temperature was maintained for 60 min to homogenize the melt alloy. Subsequently, the test container was subjected to the discharge mode. For discharge, the electric heater was controlled at different cooling rates, ranging within 4–6°C/min (1–9 cycles) and 4–10°C/min (10–20 cycles), to a temperature of 250°C. Temperature variation of the test container with an exothermic phase change was measured under a controlled cooling rate. The charge and discharge modes for the Cu–Ge alloy were repeated in a vacuum and air atmosphere to evaluate the temperature conformity and repeatability of the phase diagram and the effects on the reproducibility of both modes under different atmospheres and heating/cooling rates. The thermal responses were evaluated during heating and cooling (dT/dt vs. time). The PCM temperature was measured relative to time using a type K thermocouple (temperature resolution of $\pm 0.0075 \times |t|$ °C), which was directly inserted into the crucible inside the test container.

After the thermal response tests, the oxidation state, metallographic structure, and extent of elemental distribution of the Cu–Ge alloy were observed and evaluated. Each element in the Cu–Ge alloy was analyzed using an electron probe microanalyzer (EPMA, Shimadzu EPMA-1610) equipped with a wavelength dispersive X-ray spectrometer (WDS, relative error of <1%) operating at an acceleration voltage of 15 kV, beam current of 200 mA, beam size of 1 μm, step size of 0.5 μm, and sampling time of 0.1 s. The samples for the microstructural analyses were prepared via mechanical grinding and polishing using resin bonded diamond grinding discs (Struers, MD-Piano 1,200, 2,000, and 4,000) to obtain a mirror-like finish prior to EPMA analysis. The chemical compositions of the oxidized outer layer and non-oxidized inner layer were quantitatively measured using EPMA analysis. The average chemical compositions of the oxidized and non-oxidized layers were estimated to evaluate the variation in chemical composition via oxidation.

Chemical Compatibility Test Between the Cu–Ge Alloy and Candidate Materials of Phase Change Materials Container

A chemical compatibility test between the Cu–Ge alloy and candidate materials of the PCM container at high temperature was performed. Stainless steel (SUS 310S, rod-shape), alumina (tube-shape), Inconel625 (rod-shape) and silicon carbide (SiC, powder) were selected as candidate materials. A piece of the Cu–Ge alloy (10 g) was placed together with a PCM container candidate material into a round-bottom-shaped tanman tube (alumina 99.99%, inner diameter of 8 mm and length 25 mm) and heated in vacuum at 800°C for 2 h to pre-melt the Cu–Ge alloy in contact with the candidate materials. A test vessel (length, 120 mm; height, 60 mm) made of stainless steel was used to hold the tanman tube. The tanman tubes were vertically arranged in a test vessel (length, 120 mm; height, 60 mm) within a glovebox maintained in an Ar atmosphere to avoid oxygen contamination, which was then bolted and sealed using an elastic airtight packing (O-ring) made from copper. The test vessel was heated for 720 h at 800°C in a muffle

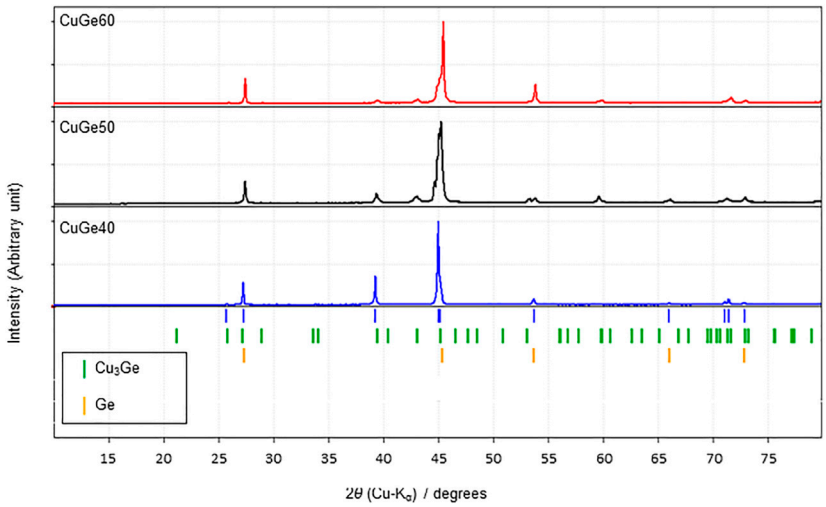

FIGURE 3 | XRD patterns of synthesized CuGe40, CuGe50, and CuGe60 alloys.

furnace. After the heat treatment, the tanman tubes were removed from the test vessel and cut parallel to the horizontal axis. A piece of test sample was embedded in epoxy resin to observe and evaluate the cross section of the alloy and candidate material of the PCM container. To evaluate the chemical compatibility and the extent of element distribution of the alloy, each of the constituent elements contained in the alloy and the candidate materials were analyzed using an electron probe microanalyzer (EPMA, Shimadzu EPMA-1610) equipped with a wavelength dispersive X-ray spectrometer operating at an acceleration voltage of 15 kV, a beam current of 200 mA, beam size of 2 μm, step size of 2 μm, and sampling time of 30 ms. The samples for the EPMA analysis were mechanically ground and polished using resin bonded diamond grinding discs (Struers, MD-Piano 1,200, 2,000, and 4,000) to obtain a mirror-like finish before EPMA analysis.

RESULTS AND DISCUSSION

X-Ray Diffraction Analysis of Synthesized Cu–Ge Alloy

Figure 3 shows XRD patterns of the synthesized CuGe40, CuGe50, and CuGe60 alloys at room temperature in the 2θ range. Blue vertical bars below the XRD pattern indicate the peak positions of the Cu–Ge alloys. The peak positions were compared with XRD data of some phases obtained from the ICSD and COD standard databases, and the phases were identified. A series of peaks, denoted by green vertical bars below the XRD patterns, correspond to the Cu_3Ge phase (ICSD-86007). The Cu_3Ge phase was equivalent to ε_1 phase at room temperature and high-temperature stable ε_2 phase in the phase diagram (**Figure 1**). Neither phases are line compounds, but small chemical composition range (solid-solution). The other series of peaks, denoted by orange vertical bars below the XRD patterns, correspond to the Ge phase (COD-96–900–8568). The phase was equivalent to Ge solid-solution phase in the phase diagram (**Figure 1**) and observed for all Cu–Ge alloys at room temperature. Other peaks were not observed in the pattern. All diffraction peaks were assigned as ε_1 phase and Ge solid-solution phases, and lattice cell parameters of solid phases were evaluated via Rietveld refinement of the structure models and the results are listed in **Table 1**. All peaks assigned by ε_1 phase were identified as an orthorhombic unit cell [space group P m n m (59)] while those specified by Ge solid-solution phase were determined as a cubic unit cell [space group F d −3 m (227)]. The lattice parameters for Ge solid-solution phase were very close to that [a = 5.657 (3) Å] obtained from the database. The lattice parameters for ε_1 phase were identified and compared to those (a = 5.272 Å, b = 4.204 Å, c = 4.578 Å). Small deviations for all Cu–Ge alloys were observed. This is because of solid-solution with a very narrow gap of chemical composition. The results indicated that the alloys were successfully synthesized without impurities as per the phase diagram of the Cu–Ge alloy (Okamoto, 2010).

Thermo-Physical Properties of Cu–Ge Alloy at High Temperatures

The temperature dependence of specific heat capacities, C_p, and thermal expansion/contraction fraction, α, at high temperatures have not been reported to-date. In the present study, the thermophysical properties were measured and reported for all alloys in the temperature range 100–900°C. The C_p data were utilized to estimate the sensible heat and evaluate the thermal storage performance. **Figure 4A** shows specific heat capacity and (b) volume change as a function of temperature for all the alloys. The approximation formula of the solid phase was estimated from the secondary fitting of the

TABLE 1 | Solid phases, space grope, crystal system, and lattice parameters of refined structured of Cu–Ge alloys.

Material	Solid phase	Space group	Crystal system	Lattice parameters		
				a (Å)	b (Å)	c (Å)
CuGe40 (eutectic alloy)	e1(epsilon one) phase (Cu3Ge)	P m n m (59)	Orthorhombic	5.276 (9)	4.213 (2)	4.581 (2)
	Ge solid-solution, (Ge)	F d –3 m (227)	Cubic	5.660 (5)	5.660 (5)	5.660 (5)
CuGe50 (Hypereutectic alloy)	e1(epsilon one) phase (Cu3Ge)	P m n m (59)	Orthorhombic	5.307 (3)	4.219 (0)	4.591 (4)
	Ge solid-solution, (Ge)	F d –3 m (227)	Cubic	5.668 (8)	5.668 (8)	5.668 (8)
CuGe60 (Hypereutectic alloy)	e1(epsilon one) phase (Cu3Ge)	P m n m (59)	Orthorhombic	5.276 (9)	4.213 (1)	4.581 (3)
	Ge solid-solution, (Ge)	F d –3 m (227)	Cubic	5.660 (5)	5.660 (5)	5.660 (5)

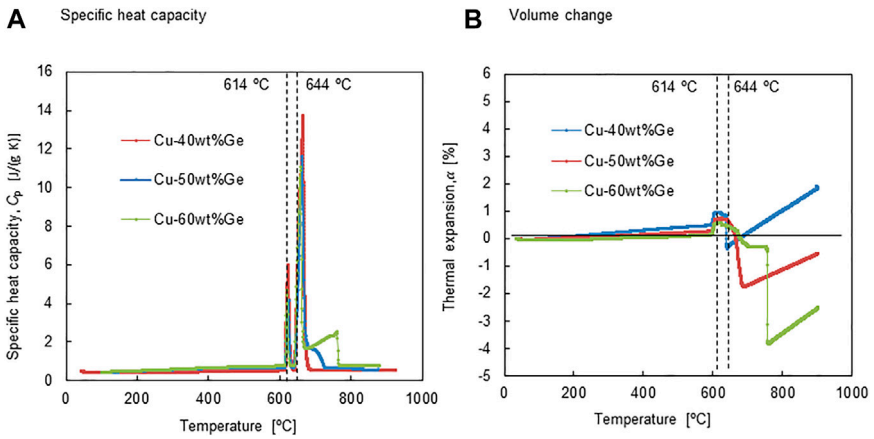

FIGURE 4 | (A) specific heat capacity and **(B)** volume change as a function of temperature for all the alloys.

measured C_p values, while that of the liquid phase was calculated from the linear fit to obtain a C_p-T correlation in the following forms:

CuGe40 alloy:

Solid phase

$$\boldsymbol{C_p} = 3.43 \times 10^{-7}\boldsymbol{T}^2 - 8.58 \times 10^{-5}\boldsymbol{T} + 4.37 \times 10^{-1} \ (100 - 600°\boldsymbol{C}) \quad (1)$$

Liquid phase

$$\boldsymbol{C_p} = 0.5223 + 6.794 \times 10^{-6}(\boldsymbol{T} - 700) \ (700 - 920°\boldsymbol{C}) \quad (2)$$

CuGe50 alloy:

Solid phase

$$\boldsymbol{C_p} = 1.02 \times 10^{-6}\boldsymbol{T}^2 + 1.28 \times 10^{-3}\boldsymbol{T} + 2.84 \times 10^{-1} \ (100 - 600°\boldsymbol{C}) \quad (3)$$

Liquid phase

$$\boldsymbol{C_p} = 0.6840 + 7.536 \times 10^{-4}(\boldsymbol{T} - 730) \ (730 - 875°\boldsymbol{C}) \quad (4)$$

CuGe60 alloy:

Solid phase

$$\boldsymbol{C_p} = 3.69 \times 10^{-7}\boldsymbol{T}^2 + 9.34 \times 10^{-4}\boldsymbol{T} + 3.35 \times 10^{-1} \ (100 - 600°\boldsymbol{C}) \quad (5)$$

Liquid phase

$$\boldsymbol{C_p} = 0.7960 + 5.444 \times 10^{-4}(\boldsymbol{T} - 780) \ (780 - 880°\boldsymbol{C}) \quad (6)$$

where C_p has units J/(g°C), and T is in °C. The results shown in **Figure 4** were the third dataset, when the experiments were repeated three times. The standard deviations were as follows: 2.16×10^{-3} @500°C and 4.00×10^{-3} @800°C for CuGe40, 4.47×10^{-3} @500°C, and 4.90×10^{-3} @800°C for CuGe50, 4.97×10^{-3} @500°C and 8.87×10^{-3} @800°C for CuGe60. The coefficients of determination for **Eqs 1**, **3**, **5** were $R^2 = 0.998$, 0.996, and 0.998, respectively. All equations for the solid phase exhibited a large positive slope for the C_p-T correlation. However, all equations for the liquid phase exhibited a very weak slope of the C_p-T correlation. These results suggest that the heat capacity of the Cu-Ge eutectic and hypereutectic alloys has a weak temperature dependency in the liquid state. The coefficients of determination for **Eqs 2**, **4**, **6** were $R^2 = 0.884$, 0.872, and 0.667, respectively. The values for R^2 were smaller for the liquid phase than for the solid phase. Thus, **Eqs 2**, **4**, **6** should be applicable in the assigned temperature range. The measured C_p for both phases were utilized to estimate the sensible heat of the solid and liquid phases.

Figure 4B shows the temperature dependence of the linear thermal expansion/contraction α for all alloys. The standard deviations were as follows: 8.12×10^{-2} @500°C and 5.95×10^{-2} @800°C for CuGe40, 3.15×10^{-2} @500°C, and 7.68×10^{-2} @800°C for CuGe50, 7.52×10^{-3} @500°C, and 5.59×10^{-2} @800°C for CuGe60. The fraction of thermal expansion/

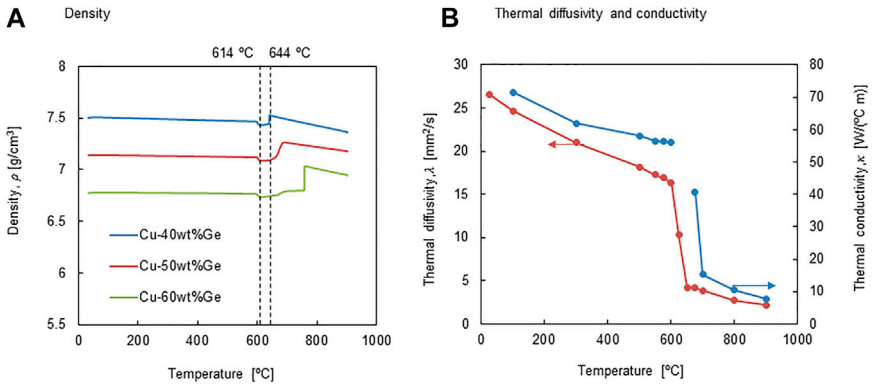

FIGURE 5 | (A) density and **(B)** thermal diffusivity and conductivity as a function of temperature.

contraction was measured as a standard point at 25°C. The slope of the solid phase at ~ 600°C is positive for all alloys, and the degree of thermal expansion was reduced with increasing Ge content. The values of thermal expansion at 600°C were 0.47% for CuGe40, 0.25% for CuGe50, and 0.13% for CuGe60. These results suggest that the Ge solid-solution phase has a small expansion coefficient compared to the ε_1 phase in the solid state. At T = 614°C, all alloys expanded to 0.93% for CuGe40, 0.72% for CuGe50, and 0.54% for CuGe60. This is due to the solid phase transition from the ε_1 to ε_2 phase at this temperature. Subsequently, CuGe40 apparently shrank to 0.36% at a eutectic temperature of T = 644°C. This result suggests that the Ge solid-solution phase has a negative coefficient of thermal expansion when the solid phase melted. For CuGe50, a thermal shrinkage of −1.68% was observed at a liquefaction temperature of T = 705°C. A thermal shrinkage of −3.79% was apparent at a liquefaction temperature of T = 765°C for CuGe60. Thermal shrinkage increased with increasing Ge content, which indicates that the Ge solid-solution phase shrinks upon melting at T = 644–765°C. Finally, all the alloys exhibited increasing thermal expansion over the liquefaction temperatures. These results indicate that the liquid phase thermally expanded with increasing temperature. The thermal expansion for all alloys is capable of controlling to +1.85 to −2.55% based on the chemical composition at T = 900°C.

Figure 5A shows the temperature dependence of the apparent density of the CuGe alloys. The apparent density was calculated using the third dataset of thermal expansion/contraction. The apparent density of all alloys at 25°C was measured using Archimedes' principle and estimated from the volume change data at various temperatures (**Figure 4B**). The apparent density of CuGe40 was in the range $\rho = 7.50 - 7.45\ g/cm^3$ for the solid phase at T = 25–600°C (**Figure 5A**). When the ε_1 phase transformed to the ε_2 phase at T = 614°C, the apparent density decreased slightly. Subsequently, density increased owing to melting of the eutectic mixture at T = 644°C. The density was $\rho = 7.37\ g/cm^3$ for the liquid phase at T = 900°C. The rate of density change for CuGe40 was estimated to be 1.73% between T = 25–900 °C. For CuGe50, the apparent density ranged between 7.11 and 7.14 g/cm^3 for the solid phase at T = 25–600°C. In the case of the CuGe60, the apparent density ranged between 6.76 and 6.78 g/cm^3 for the solid phase at T = 25–600°C. Owing to the hypereutectic mixture, the density increased to a liquefaction temperature of T = 705°C for CuGe50 and a liquefaction temperature of T = 765°C for CuGe60. The rates of density change for CuGe50 and 60 were estimated to be +0.56 and +2.66% between T = 25–900°C, respectively. The results of very small density changes as a function of temperature indicate that the PCM is capable of loading rate over 95% when the PCM alloys are packed into a thermal storage container filled in a storage tank/capsule. Thus, the thermal storage capacity per storage volume can be enhanced by using PCM alloys.

In theory, the density of liquid metal at high temperatures can be described by a linear equation, as demonstrated by Cailletet and Mathias (Cailletet and Mathias, 1886). Thus, the measured density data were fitted to the following linear equations:

CuGe40 alloy:

$$\boldsymbol{\rho} = -6.129 \times 10^{-4}\boldsymbol{T} + 7.918,\ \boldsymbol{R}^2 = 0.9997\ \text{at T} = 650 - 900°\text{C} \quad (7)$$

CuGe50 alloy:

$$\boldsymbol{\rho} = -4.085 \times 10^{-4}\boldsymbol{T} + 7.548,\ \boldsymbol{R}^2 = 0.9997\ \text{at T} = 700 - 900°\text{C} \quad (8)$$

CuGe60 alloy:

$$\boldsymbol{\rho} = -6.156 \times 10^{-4}\boldsymbol{T} + 7.503,\ \boldsymbol{R}^2 = 0.9999\ \text{at T} = 760 - 900°\text{C} \quad (9)$$

where temperature T is in °C.

Figure 5B shows the temperature dependence of thermal diffusivity, λ and conductivity κ for the CuGe40 alloy. The standard deviations of the measured thermal diffusivity were 1.26×10^{-2} @500°C and 1.50×10^{-1} @800°C for CuGe40. The values of thermal diffusivity decreased with increasing temperature in the solid phase at temperatures of 25–600°C and decreased to approximately 25% of the original value in the liquid phase at temperatures of 675–900°C when the alloy melted. Thermal diffusivity, λ, is a material-specific property that

characterizes self-diffuse thermal energy; this value represents how quickly the material responds to temperature changes. Thermal conductivity, κ, is defined as the amount of energy transferred as heat that flows through the mass in response to a temperature gradient. Thus, the thermal conductivity, κ, was calculated from values of density ρ, specific heat capacity, C_p, and thermal diffusivity λ according to **Eq. 10**.

$$\kappa = \rho \times C_p \times \lambda \tag{10}$$

The temperature dependence of the calculated thermal conductivity is shown in **Figure 5B**. The thermal conductivity at a low-temperature ($T < 100$°C) for the solid phase of CuGe40 was higher than that for pure germanium (59.9 W/(°C m) @27°C) (AIST, 2019) and much lower than that of pure copper (386 W/(°C m) @ 27°C) (AIST, 2019) and comparable to that at high temperatures (500–600 °C). A main reason for this is the coexistence of the ε_1 phase and the Ge solid-solution phase. This result indicates that the ε_1 phase is more thermally conductive than the Ge solid-solution phase at low temperatures, thereby leading to an increase in the thermal conductivity of the solid mixture. In addition, the solid mixture forms a periodic lamella microstructure, as seen in *Chemical Compatibility Test at High-Temperate*, which appears in the eutectic mixture of the ε_1 and Ge solid-solution phases and involves a homogeneous nucleation-growth process. At high temperatures (700–900°C), the thermal conductivity of 15–8 W/(°C m) in a liquid mixture was much lower than that in a solid mixture. The trend of relatively low thermal conductivity in the liquid phase has been observed in other alloys (Blanco-Rodríguez et al., 2014; Risueño et al., 2017).

The following equations give the fitted second-order polynomial for these properties in the liquid phase:

$$\boldsymbol{\lambda} = 2.59 \times 10^{-5}\boldsymbol{T}^2 - 4.98 \times 10^{-2}\boldsymbol{T} + 2.60 \times 10^{1}, \quad \boldsymbol{R}^2 = 0.999 \text{ at T} = 650 - 900\text{°C} \tag{11}$$

$$\boldsymbol{\kappa} = 1.08 \times 10^{-4}\boldsymbol{T}^2 - 2.11 \times 10^{-1}\boldsymbol{T} + 1.10 \times 10^{2}, \quad \boldsymbol{R}^2 = 0.999 \text{ at T} = 650 - 900\text{°C} \tag{12}$$

Thermal Storage Performance

Third-generation (Gen3) CSP technology has a new target for the temperatures of HTF ($T > 700$°C) to ensure higher energy efficiency using supercritical CO_2 thermal cycles. Chloride eutectic molten salts are suitable for meeting some important thermophysical properties, including: 1) a melting point that is as low as possible; 2) a boiling point at least 800°C or above; 3) thermophysical properties that are acceptable for convective heat transfer and thermal storage; 4) low corrosion to metal pipes and containers at high temperatures; and 5) low cost. The University of Arizona selected and tested binary eutectic KCl/$MgCl_2$ molten salt that can be used as HTF and sensible thermal storage for next-generation CSP plants (Xu et al., 2018). Researchers at the National Renewable Energy Laboratory (NREL) of the United States reported a new ternary eutectic chloride salt comprising $MgCl_2$-KCl-NaCl as a third third-generation high-temperature HTF and TES in the community of Gen3-CSP (Zhao and Vidal, 2020). In the present study, thermophysical properties of binary and ternary chloride molten salts were compared to the Cu–Ge alloys on the basis of assumption that the molten salts was used as PCMs.

The latent heat storage capacities and dependence of the specific heat, C_p, in the range 100–800°C were measured for all alloys, and the sensible heat was estimated to evaluate the thermal storage performance (**Figure 4A**). **Figure 6** shows (a) heat storage density per unit weight and (b) thermal storage capacity per unit volume for the Cu–Ge alloys. The measured C_p for the solid and liquid phases were utilized to estimate the sensible heat capacities of the solid and liquid phases, respectively. The sensible heat capacity of the solid phase increased with temperature in the range 100–614°C (**Figure 6A**). In addition, the slope increased with increasing Ge content in the Cu–Ge alloys. The average specific heat capacity of Cu [0.386 J/(g °C)] is higher than that of Ge [0.310 J/(g °C)] in the temperature range 0–100°C (Kinzoku data book, 2018). Thus, these results indicate that the specific heat capacity of Ge has a relatively strong sensitivity at high temperatures. Small discontinuous changes are the sum of sensible heat and latent heat released/stored in the solid/solid phase transition ($\varepsilon_1 \Leftrightarrow \varepsilon_2$ phase) at a temperature of 614°C. The latent heat were estimated as 41.8, 27.3, and 23.2 kJ/kg for CuGe40, CuGe50, and CuGe60, respectively. The value of latent heat for CuGe40 was estimated by reference data (28.4 kJ/kg) (Zhai et al., 2012). Strong discontinuous changes are the sum of sensible heat and latent heat released/stored in the solid/liquid phase transition (eutectic mixture of ε_2 + (Ge) ⇔ liquid phase) at a temperature of 644 °C. The latent heat were estimated as 232.8, 198.2, and 163.5 kJ/kg for CuGe40, CuGe50, and CuGe60, respectively. The value of latent heat for CuGe40 is comparable to reference data (169.7 kJ/kg) (Zhai et al., 2012). Additionally, the heat storage density of CuGe50 increased in the temperature range 644–705°C owing to the latent heat from the primary Ge and sensible heat from the eutectic mixture, while the heat storage density of CuGe60 is enhanced in the temperature range 644–765°C. Beyond the liquefaction temperature, which depends on chemical composition, the sensible heat from the liquid phase contributes to increases in the heat storage density of the Cu–Ge alloys. An advantage of the hypereutectic chemical composition (CuGe50 and CuGe60) is that it reinforces the total storage at high temperatures over the eutectic temperature. An advantage of the eutectic mixture (CuGe40) is that it behaves like a simple substance performing solid/liquid phase transition at a constant temperature.

The thermophysical properties of the Cu–Ge alloys were compared with those of the binary chloride molten salt (**Table 2**). The heat storage densities per unit weight for the Cu–Ge alloys were compared to those of the binary chloride molten salt (Xu et al., 2018), and are plotted in **Figure 6B**. For the ternary molten salt, the values of C_p in the solid state have not been previously reported (Zhao, 2020); thus, the data were not plotted. The accumulated storage density at 700°C was greater for the chloride molten salt than for all alloys (**Figure 6A**). In addition, the liquid phase of the molten salt has a larger storage capacity compared to all alloys. It is very promising as an HTF and liquid TES in next-generation CSP technologies. However, the accumulated sensible heat capacities of solid phase for all alloys was higher than that of the chloride molten salts

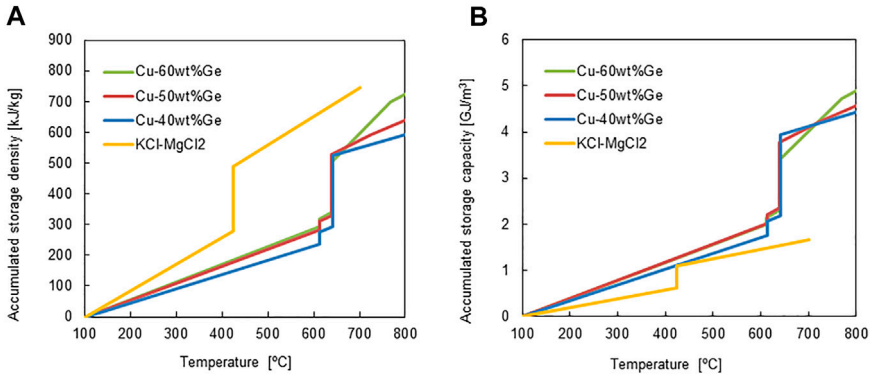

FIGURE 6 | (A) accumulated thermal storage density and **(B)** accumulated thermal storage capacity for all the alloys and chloride molten salt.

TABLE 2 | Comparison of thermophysical properties for CuGe alloys and molten salts in a liquid phase.

	Melting point [°C]	Density [g/cm3]	Heat capacity [J/(g K)]	Thermal expansion [%]	Thermal conductivity [W/(K m)]	Thermal storage density [kJ/kg]	References
CuGe40	644	7.49@700°C	0.525@ 700°C	+0.21 (25–700°C)	15.0@700°C	232.8@644°C	In this work
CuGe50	705[a]	7.25@710°C	0.676@ 730°C	−1.60 (25–710°C)	–	198.2@ 644°C	In this work
CuGe60	765[a]	7.03@770°C	0.798@ 770°C	−3.73 (25–770°C)	–	163.5@644°C	In this work
KCl/MgCl2 (Mole: 68%:32%)	424	1.514@ 700°C	1.013@ 700°C	+24.5 (25–700°C)	0.442@700°C	207.0 (heat of fusion)	[10]
MgCl2/KCl/NaCl (Mole:37.5%:40.9%: 21.6%) (wt:45.3%:38.7%:16.0%)	401	1.563@ 700°C	0.954@ 700°C	+42.7% (25–700°C)	0.415@700°C	248.3 (heat of fusion)	[48]

[a]*Liquefaction temperature.*

(**Figure 6B**) due to the high density of the alloys (molten salt of 1.89 g/cm^3 (extrapolation value at 25°C); Cu–Ge alloys of 6.77–7.50 g/cm^3 (25°C). The latent heat capacities of all alloys at the eutectic temperature were also superior to those of chloride molten salts. In addition, all alloys exhibited a high thermal conductivity in the solid/liquid phases and little density change at the solid/liquid transition. These results indicate the potential of all alloys as PCMs, based on the limitations of the usable volume in an LTES system. In the ongoing Gen3 liquid pathway project, two options are considered suitable for reaching high temperatures: 1) direct heating of a chloride molten salt; and 2) indirect heating via liquid sodium and an associated sodium–salt heat exchanger (Energy Efficiency and Renewable Energy, 2021). Both options use a two-tank system comprising a hot tank and cold tank for chloride molten salt storage. To reduce the storage cost of constituent materials for large quantities of thermal energy storage, 1-tank thermocline system, which is a storage mixture of low-cost sensible material (for example, rock) and latent PCM filler (for example, capsulated alloy), may be a promising technology in view of the limitations of the useable volume for TES. The volumetric capacity of heat storage is a key parameter for next-generation CSP technologies.

Thermal Response Tests of Cyclic Charge/Discharge Modes

When the alloys are installed as latent heat storage (PCM) into the TES of a CSP plant, the alloy is subjected to numerous day–night cycles, and the evaluation of repeatability and compatibility is necessary. In the present study, short-term reliability (repeatability of the charge/discharge performance and compatibility with the PCM container) was initially evaluated via 20 cycle tests using a few dozen Gram samples (**Figure 7**). From a thermodynamic viewpoint, CuGe40 must behave reproducibly based on the phase diagram (**Figure 1**) during the thermal response test if it does not chemically react with the container and stream gas. From a kinetics viewpoint, for the phase transition between solid and liquid phases, it is desirable that charge/discharge responds quickly at the eutectic temperature assigned in the phase diagram.

Figure 7 shows dT/dt vs. the PCM temperature T for the CuGe40 in an air stream and a vacuum. The thermal response is influenced by heating/cooling rates, heat transfer, gas stream in the PCM container, and container material. Thus, the main purpose is to examine thermal response and repeatability of the CuGe40 placed in a crucible in an air stream. The crucible was made of SUS304 stainless steel with excellent thermal

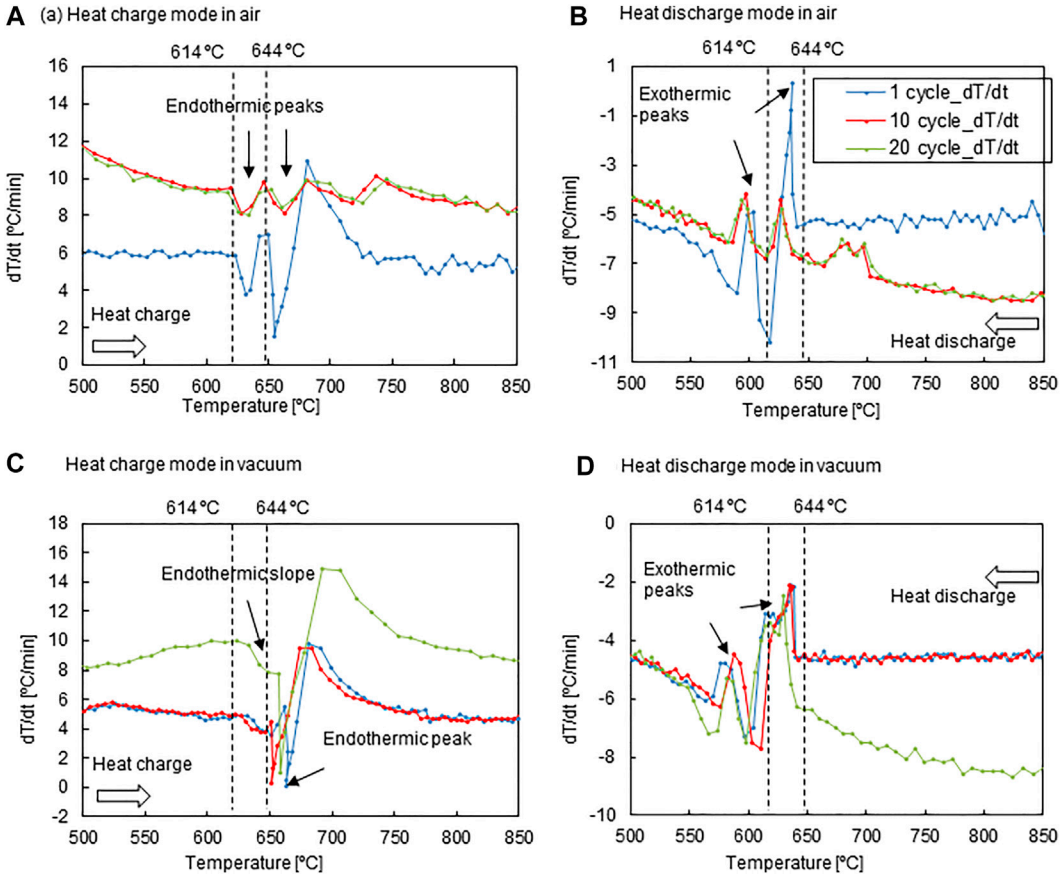

FIGURE 7 | d*T*/d*t* variations of the PCM temperature for the CuGe40 alloy in an air stream during the **(A)** heat-charge mode and **(B)** dis-charge mode, and in a vacuum during the **(C)** heat-charge mode and **(D)** heat-discharge mode.

conductivity and oxygen resistance. To examine the impact of oxygen in the gas stream on the charge/discharge performance, the test was performed using ambient air. In addition, tests in vacuum were conducted to compare the impact of thermal conduction and radiation without convective heat transfer from the external heater into the PCM. Strong endothermic peaks for all cycles were observed immediately after, at temperatures of 614 and 644°C during the heat charge mode (**Figure 7A**). The peak temperatures were in agreement with the $\varepsilon_1 \Leftrightarrow \varepsilon_2$ phase transition (614°C) and eutectic (644°C) temperatures of the CuGe40 alloy in the phase diagram (**Figure 1**). The endothermic peak was largest during the first cycle and relative to small during the 2nd–20th cycles. These results indicate that the surface of the CuGe40 alloy was oxidized by the air stream during the first cycle, but the internal fraction of the alloy functioned as a PCM throughout the 2nd–20th cycles. In addition, the charge performance for the CuGe40 alloy after the oxidation were obtained with high repeatability in static (constant) heating mode. A large peak was observed for all cycles at 681°C given the termination of the latent heat storage. It was caused via rapid heating of the CuGe40 alloy, which retained relatively low temperatures due to the absorption of latent heat, compared to the heater temperature, which automatically increased at a constant rate. The variation in the d*T*/d*t* profile in the charge mode indicated that the latent heat storage of the CuGe40 alloy under different heating rates was maintained, with good conformity to the phase diagram, with no deterioration of performance in the PCM container.

During heat discharge, a strong peak consistently appeared at 644°C, and a strong peak appeared at 614°C (**Figure 7B**). The exothermic behaviors for all cycles corresponded to the solidification of the eutectic mixture from the melting alloy and the solid/solid phase transition ($\varepsilon_1 \Leftrightarrow \varepsilon_2$). As observed during heat charge mode (**Figure 7A**), the peak intensity of the two exothermic peaks was larger for the first cycle than for the 2nd–20th cycles. In addition, the exothermic peaks for the 2nd–20th cycles were shifted to lower temperatures. The discharge performance for the CuGe40 alloy was observed with good repeatability during the 2nd–20th cycles. These results indicate that an oxidation layer formed on the surface of the CuGe40 alloy caused a late response of exothermic heat discharge during the 2nd–20th cycles. The charge or discharge of latent heat from a eutectic mixture and solid/solid phase transition occurs under quasi-thermodynamic equilibrium conditions at a fixed atmospheric pressure (**Figures 7A,B**). Thus, the experimental results for the d*T*/d*t* profiles indicated

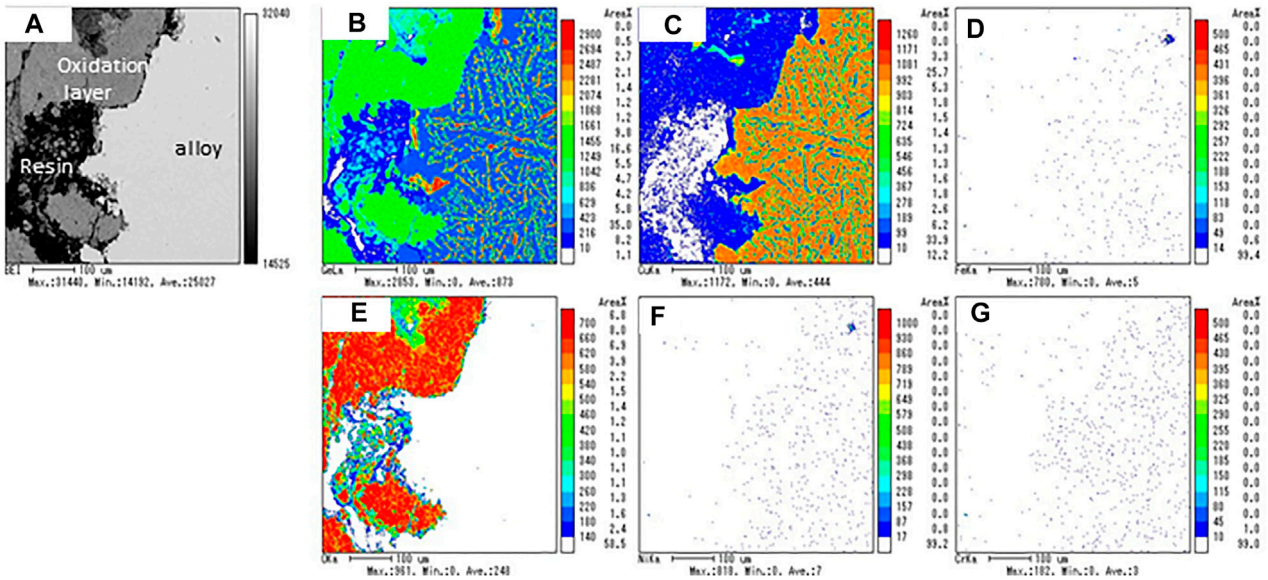

FIGURE 8 | (A) Backscattered electron image (BEI) micrograph and elemental mapping images of **(B)** Ge, **(C)** Cu, **(D)** Fe, **(E)** O, **(F)** Ni, and **(G)** Cr for the sample obtained after the thermal response test in an air stream.

that the melting or solidification of the eutectic mixture and the solid/solid phase transition consistently occurred under different cooling rates, without supercooling.

Figure 7C shows the d*T*/d*t* profiles plotted relative to the PCM temperature measured under vacuum. The cyclic thermal response was examined using a PCM container composed of graphitic carbon. Additionally, heat charging was imposed at heating rates of 5–6°C/min for the first ten cycles, but at 8–10°C/min for the remaining ten cycles. The thermal response of the CuGe40 alloy in a vacuum is governed by thermal conduction and radiation from the heater into the alloy. An endothermic very weak peak due to solid/solid phase transition for all cycles was observed at an onset temperature of 633°C (**Figure 7C**), and the peak temperature was shifted to a higher temperature when in an air stream (**Figure 7A**). Similarly, a strong endothermic peak, due to the melting of the eutectic mixture, was observed at temperatures of 651–663°C. This is because of deficient and inhomogeneous heat transfer without convection in a vacuum. The endothermic behavior in the d*T*/d*t* profiles was almost the same for different heating rates. The repeatability of charge performance under vacuum during the 2nd-20th cycles was inferior to in the air stream.

During heat-discharge (**Figure 7D**), the cooling rate was set to 4–5°C/min for the initial ten cycles and dynamically changed between 6 and 9°C/min for the remaining ten cycles. A very strong exothermic peak, due to the solidification of the eutectic mixture from the melting alloy, was observed for all cycles, with an onset temperature of 644°C. However, an exothermic peak due to the solid-state phase transition appeared at an onset temperature of 610–598°C. The reason for this fluctuation is the cooling process in vacuum, which is governed by the limited heat transfer. Thus, the heat stored in the alloy was not quickly released into the atmosphere. This leads to a delay and fluctuation (poor repeatability) in the onset temperature of the exothermic process. The impact on the cooling rate was not clearly observed during discharge under vacuum. The thermal response of the exothermic peaks was consistently observed under fluctuating onset and termination temperatures for the solid-state phase transition and solidification of the eutectic mixture for all cycles. The CuGe alloy behaved consistently, based on the thermodynamic equilibrium in a gas stream and quickly responded under the limited heat transfer without the effect of alloy oxidation in vacuum.

To evaluate the effect of oxidation during the thermal response test in an air stream, and chemical compatibility between the stainless steel vessel and CuGe50 alloy (sample), the microscopic distribution of the sample and vessel elements was examined after the test. **Figure 8** shows the backscattered electron image (BEI) micrograph of the cross-sectional surface of the sample and elemental mapping images of Ge, Cu, Fe, O, Ni, and Cr. These analytical elements were selected from the main constituents of the sample and the vessel. The BEI image consists of a light gray area (right side of the image), a dark gray area (upper-left side of the image), and a black area (lower left side of the image). The black area corresponds to the epoxy resin used to mount the sample. The light gray area represents the internal microstructure of the alloy without oxidation, while the dark gray area is an oxidation layer in which the alloy was externally covered. The BEI image indicates that an oxidation layer was formed on the surface of the alloy during the heat charge-discharge process in air. In the mapping images of the Ge element, the green region is widely spread in the oxidation layer (dark gray area) in the BEI image. In addition, a number of red, yellow and green microscopic spots and needles (Ge solid solution, aggregation of coarsened particles) and a blue region (mainly the ε_1 phase) characteristic of a metallographic eutectic structure, were observed in the internal microstructure of the alloy. These results indicate that the ε_1 phase and Ge solid solution were homogeneously distributed in the eutectic mixture of the alloy.

TABLE 3 | EPMA analysis of chemical composition for the oxidized outer layer and the internal microstructure of the alloy.

Outer layer (oxidation)	Cu [wt%]	Ge [wt%]	O [wt%]	Inner layer (alloy)	Cu [wt%]	Ge [wt%]
#1	4.6	68.2	27.2	#1	58.6	41.4
#2	6.2	66.5	27.3	#2	74.9	25.1
#3	10.1	58.8	30.9	#3	52.0	48.0
#4	4.2	65.8	30.0	#4	62.0	38.0
#5	1.9	66.2	31.8	#5	72.6	27.4
Average	5.4	65.1	29.5	Average	64.0	36.0

The blue region of the Ge mapping image corresponds to the brown region of Cu mapping. A number of reddish-brown spots and yellowish-brown areas surrounding the reddish-brown spots appeared in the Cu mapping. Because the reddish spots have a relatively higher Cu content than the yellowish area, the authors consider that the brown region of the Cu mapping is composed of two phases: the reddish spots correspond to the thermodynamically stable ε_1 phase (76.9 %–72.9%Cu) (Okamoto, 2010) and the yellowish area corresponds to the high-temperature stable ε_2 phase (73.95–73.5 at%Cu) (Okamoto, 2010) with slightly lower Cu contents than the ε_1 phase. The ε_2 phase at room temperature can be changed into the ε_1 phase, leading to an increase in the latent heat via the solid-state phase transition.

As seen in the O mapping image, the internal microstructure of the alloy was observed with no oxidation; the formation of the oxidation layer was observed in the dark gray area of the BEI image. The thickness of the oxidation layer was in the range of 100–200 mm (**Figure 8A**). The chemical composition of the alloy and oxidation layers were quantified by randomly selecting five points by EPMA analysis (**Table 3**). The average weight ratio of $Ge_{65.1}Cu_{5.4}O_{29.5}$ for the oxidation layer corresponded to a solid mixture of GeO_2/CuO (or Cu_2O) = 10/1, and that of $Cu_{64}Ge_{36}$ for the alloy corresponded to a solid mixture of hypoeutectic chemical composition (67 at%Cu-33 at %Ge). These results indicate that Ge was preferentially oxidized compared to Cu in the CuGe50 alloy, resulting in compositional deviation of the alloy. The chemical composition and thickness of the oxidation layer may impact on charge/discharge storage performance and thermal response. The thermal response of the PCM lowered by the formation of the oxidation layer as far as appears in **Figures 7A,B**. In order to quantitatively estimate the impacts on storage performance under the oxidation layer, a numerical simulation of the PCM covered the oxidation layer and comparison with the experiments are required in some future works.

As seen in the mapping images (**Figure 8**) of the Fe, Ni, and Cr elements, the internal region of the alloy and the oxidation layer did not chemically react with the stainless steel container under the test conditions. These results indicate that the container (SUS310S) can be used as a PCM container in an air stream during charge-discharge modes.

Chemical Compatibility Test at High-Temperate

To use the alloy as a PCM in a thermal storage system, the alloy should be encapsulated by a material having an excellent thermal conductivity, high-temperature resistance, and corrosion resistance at high temperatures. Consequently, the chemical compatibility between the alloys and candidate container materials was tested at high temperatures. The chemical compatibility between the alloys (CuGe40, CuGe50, and CuGe60) and the candidate materials (stainless steel (SUS 310S), alumina, Inconel625, and silicon carbide (SiC)) was examined and evaluated by cross-reactivity at high temperature using EPMA analysis. **Figure 9** shows the results of the EPMA analysis for a combination of SUS 310S/CuGe50. A light gray area of Cu-rich and Ge-poor contents, and dark gray areas of Ge, Fe, Ni, and Cr-rich contents, were observed in the backscattered electron image (BEI) micrograph (**Figure 9A**). In addition, the high Ni content region was locally distributed in the Cu-rich alloy. A black region observed on the left side of the image corresponded to the epoxy resin used to mount the sample. No oxidation of either area appeared in the mapping image of the O element (**Figure 9G**), which supports the compatibility test without the oxidation effect. These results show that corrosion of the stainless steel into the CuGe50 alloy occurred at high temperatures and SUS310S stainless steel was not chemically compatible with the studied alloy.

Figure 10 shows the results of EPMA analyses for a combination of Inconel625/CuGe40. A vertical array of voids appeared at the center of the BEI image (**Figure 10A**). This was due to the initial bonded interface of Inconel625/CuGe40, or Kirkendall voids, which generally are an accumulation of atomic vacancies generated by the imbalance in the interdiffusion on the bonded interface. The observation area of the BET image was classified as deep dark gray of Ni-rich content, dark gray area of Cu-rich and Ge-poor contents, and light gray areas of Cr, Ge, and Mo-rich contents. These results show that the Cu and Ge atoms of the alloy diffused into the Inconel layer, and Ni atoms diffused into the CuGe alloy at high-temperatures. Thus, Inconel625 is chemically bonded with the CuGe40 alloy during the test, which is not chemically compatible with the combination at high-temperatures.

Figure 11 shows the results of the EPMA analyses for a combination of alumina/CuGe60/SUS 310S, that is, the chemical compatibility between the tanman-tube crucible made from alumina (purity of 99.99%) and CuGe60/SUS 310S. No dissolution of Al and O from alumina was found in the Cu-rich and Ge, Fe, Ni, and Cr-rich alloys. These results demonstrated that alumina is fully compatible with CuGe60 alloy in a closed inert atmosphere at high temperatures.

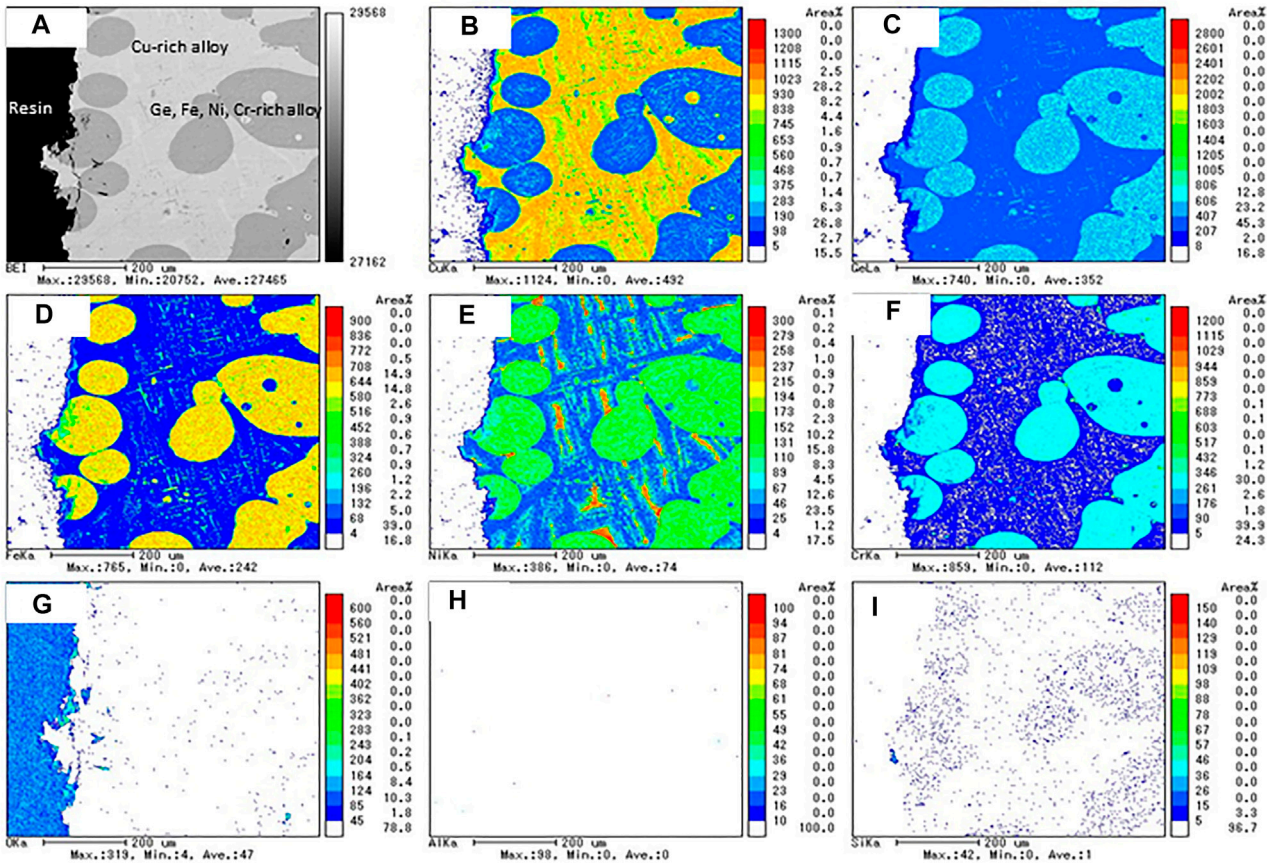

FIGURE 9 | The results of the EPMA analysis for the chemical compatibility test of SUS 310S/CuGe50. **(A)** BEI image, **(B)** Cu, **(C)** Ge, **(D)** Fe, **(E)** Ni, **(F)** Cr, **(G)** O, **(H)** Al, and **(I)** Si mapping images.

Figure 12 shows the results of the EPMA analysis for a combination of CuGe50/SiC heated in a tanman-tube crucible. The BEI image demonstrates an interface, where the SiC powder is on the left side and CuGe50 alloy is on the right is clearly observed in the cross-section of the surface of the CuGe alloy and SiC. In addition, Si and C were distributed on the left side without interdiffusion, while Cu and Ge were distributed on the right, without spreading on the other side. After the test, the combined material was easily removed from the tanman crucible. Therefore, no chemical corrosion occurred for the combination of CuGe50/SiC. These results demonstrated that SiC has good compatibility with the chosen alloy and crucible under an inert atmosphere.

SUMMARY

Eutectic and hypereutectic Cu–Ge alloys were studied as promising metallic PCMs, with liquefaction temperatures to 800°C, for next-generation CSP applications at temperatures exceeding 600°C. The thermophysical properties of the Cu–Ge alloy, including the melting temperature, specific heat capacity, volume change, density, thermal diffusivity/conductivity, and latent heat were examined to evaluate the potential of the Cu–Ge alloy as a metallic PCM for TES. Furthermore, the thermal response and consistency of the thermal charge/discharge of the Cu–Ge alloy were studied and compared to the phase diagram, based on thermodynamic equilibrium. Finally, chemical compatibility between the Cu and Ge alloy and candidate materials of the PCM container was tested and evaluated to identify potential construction materials for PCM container/encapsulation.

The specific heat capacities of all the alloys have not previously been reported. The specific heat capacity as a function of temperature was successfully formulated for solid and liquid states, and the measured values for both phases were utilized to estimate the sensible heat of the solid and liquid phases. The temperature dependence of the volume change was measured for all alloys. The volume of the alloys increased owing to the solid phase transition from the ε_1 to ε_2 phase at a temperature of 614°C, and decreased at a eutectic temperature of $T = 644$°C. The extent of thermal shrinkage increased with increasing Ge content, which means that the Ge solid-solution phase shrinks during melting at $T = 644$–765°C. The temperature dependence of apparent density of the CuGe alloys was measured for the solid and liquid phases. The apparent density discontinuously decreased owing to the

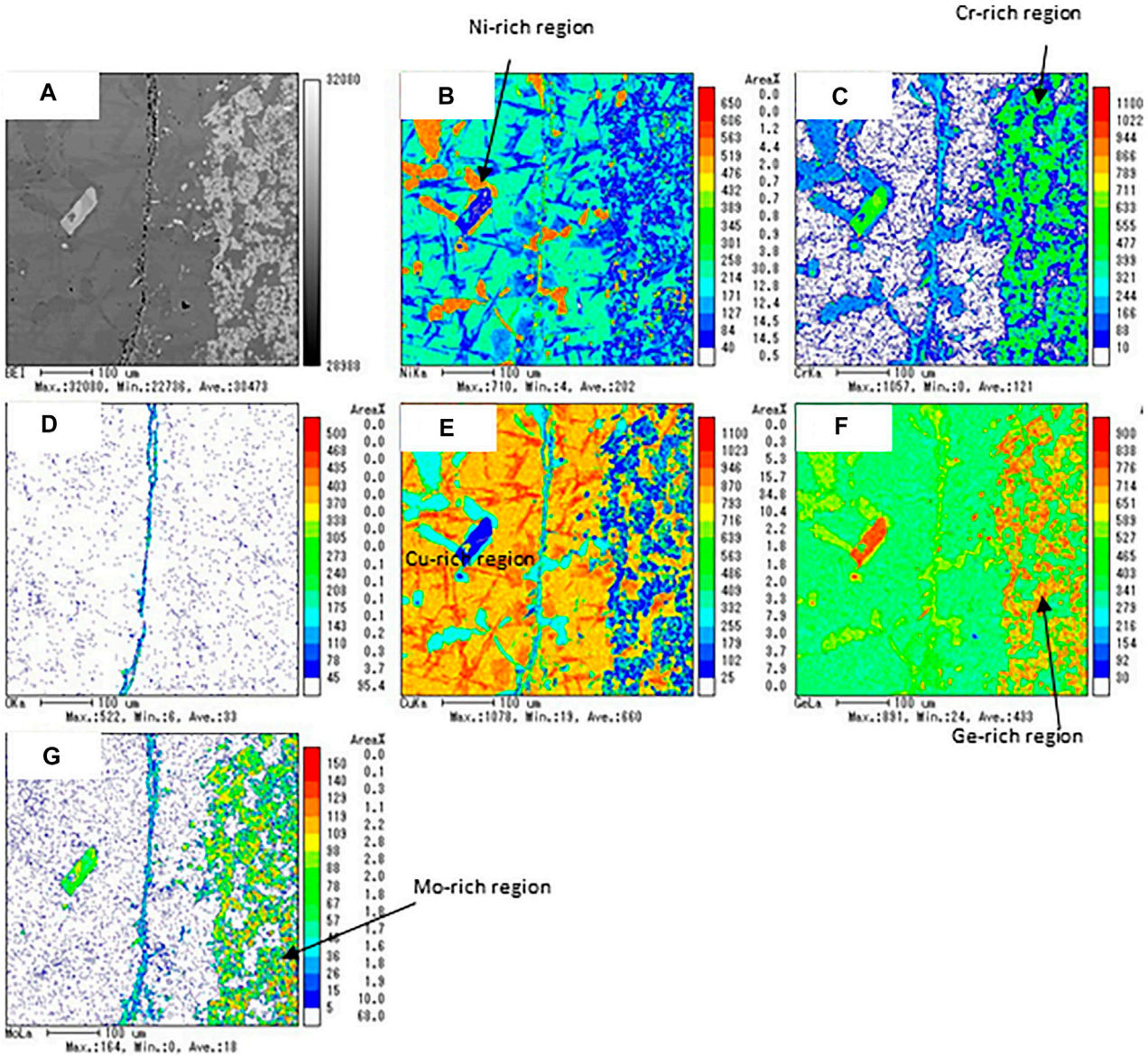

FIGURE 10 | The results of the EPMA analysis for the chemical compatibility test of Inconel625/CuGe40. **(A)** BEI image, **(B)** Ni, **(C)** Cr, **(D)** O, **(E)** Cu, **(F)** Ge, and **(G)** Mo mapping images.

solid phase transition from the ε_1 to ε_2 phase at 614°C, and discontinuously increased owing to the melting of the eutectic mixture at T = 644°C. For the hypereutectic mixture of CuGe50 and CuGe60, density increased to the liquefaction temperatures. The results of very small density changes as a function of temperature indicate that the PCM is capable of loading rate over 95% when the PCM alloys are packed into a thermal storage container filled in a storage tank/capsule. The temperature dependence of the thermal diffusivity and conductivity of the CuGe40 alloy for the solid and liquid phases was estimated and formulated. The thermal conductivity at a low-temperature (T < 100°C) for the solid phase of the CuGe40 alloy was higher than that for pure Ge, much lower than that for pure Cu, and comparable to that at high temperatures (500–600°C). At high temperatures (700–900°C), the thermal conductivity in the liquid mixture was much lower than that in the solid mixture. The trend of relatively low thermal conductivity in the liquid phase was in good agreement with that of the other alloys.

The latent heat storage densities, capacities, and sensible heat were estimated to evaluate the thermal storage performance in the temperature range 100–800°C. The sensible heat of the solid phase increased with temperature in the range 100–614°C. In addition, the slope increased with increased Ge content in the Cu–Ge alloys. Thus, these results indicate that the specific heat capacity of Ge has a relatively strong sensitivity at high temperatures. Small discontinuous changes corresponded to the latent heat released/

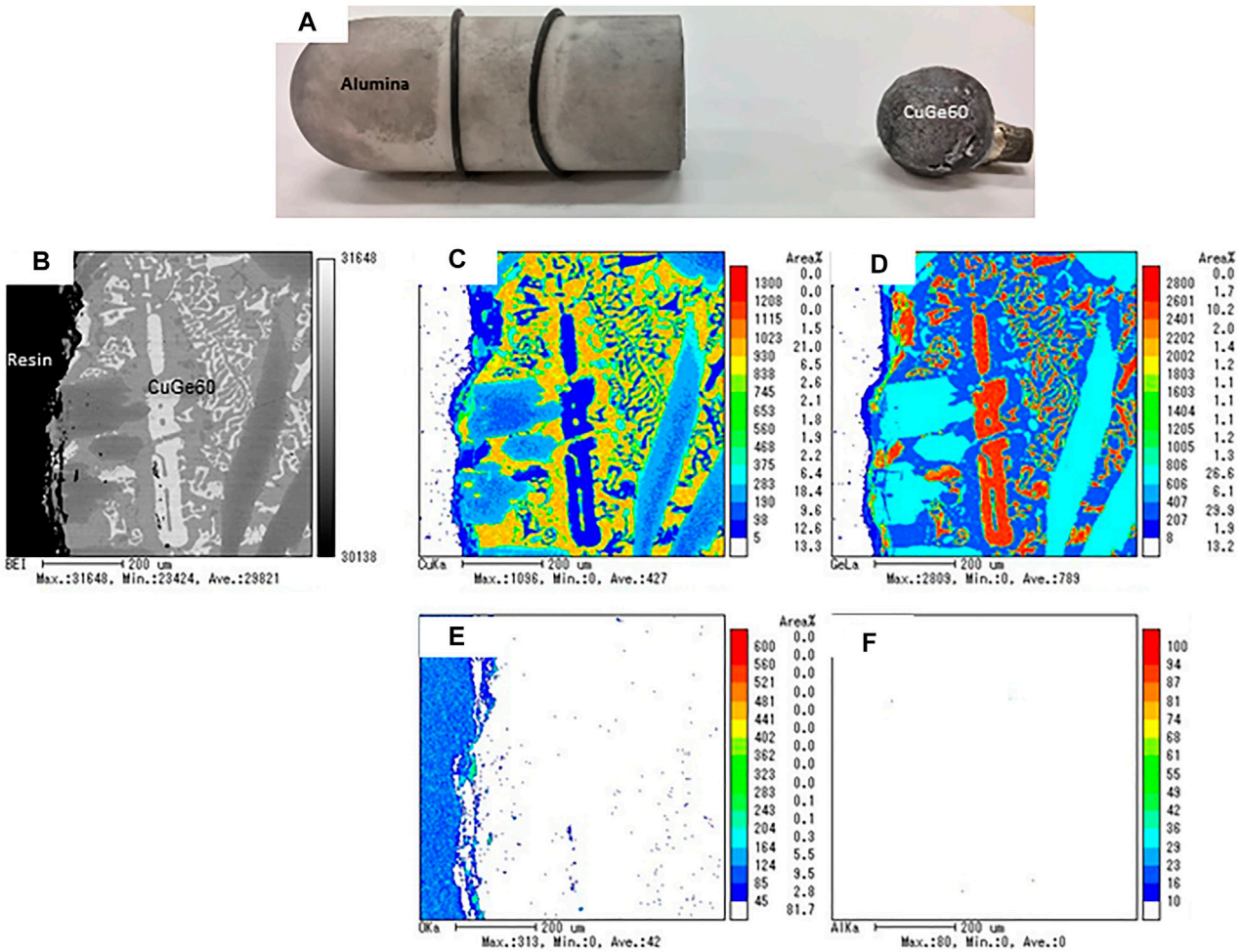

FIGURE 11 | The results of the EPMA analysis for the chemical compatibility test of alumina/CuGe60. **(A)** photograph of alumina tube and test sample, **(B)** BEI image, **(C)** Cu, **(D)** Ge, **(E)** O, and **(F)** Al mapping images.

stored in solid/solid phase transition ($\varepsilon_1 \Leftrightarrow \varepsilon_2$ phase) at a temperature of 614°C, while large discontinuous changes corresponded to latent heat released/stored in solid/liquid phase transition (eutectic mixture of ε_2 + (Ge) ⇔ liquid phase) at 644°C. A value of the latent heat at 614 °C was estimated to be 41.8, 27.3 and 23.2 kJ/kg for CuGe40, CuGe50, and CuGe60, respectively. The latent heat at 644°C was estimated to be 232.8, 198.2, and 163.5 kJ/kg for CuGe40, CuGe50, and CuGe60, respectively. Additionally, the heat storage density of CuGe50 increased in the temperature range of 644–705°C because of the latent heat from the primary Ge and sensible heat from the eutectic mixture, while the heat storage density of CuGe60 was enhanced in the range 644–765°C. An advantage of the hypereutectic chemical composition (CuGe50 and CuGe60) is that it reinforces the total storage at high temperatures over the eutectic temperature. An advantage of the eutectic mixture (CuGe40) is that it behaves like a simple substance performing solid/liquid phase transition at a constant temperature.

The short-term reliability (repeatability of the charge/discharge performance and compatibility with the PCM container) and thermal response of CuGe40 were evaluated via 20 cycle tests in an air stream and vacuum. Strong endothermic/exothermic peaks for all cycles were observed immediately after, at 614 and 644°C during the heat charge/discharge modes in the air stream. The peak temperatures were in good agreement with the $\varepsilon_1 \Leftrightarrow \varepsilon_2$ phase transition (614°C) and eutectic (644°C) temperatures. The endothermic peak was largest for the first cycle and remained the same for the remaining cycles. Variations in the dT/dt profile in charge/discharge modes indicated that the latent heat storage/release of the CuGe40 alloy under different heating/cooling rates was consistently reproduced and conformed to the phase diagram without deterioration of performance in the PCM container. During the vacuum test, an endothermic very weak peak, due to solid/solid phase transitions for all cycles, was shifted to a high temperature in the air stream. Similarly, a strong endothermic peak due to the melting of the eutectic mixture moved to temperatures of 651–663°C. This A behavior of endothermic peaks may have arisen because of deficient and inhomogeneous heat transfer without convection in a vacuum. During heat-discharge in vacuum, the

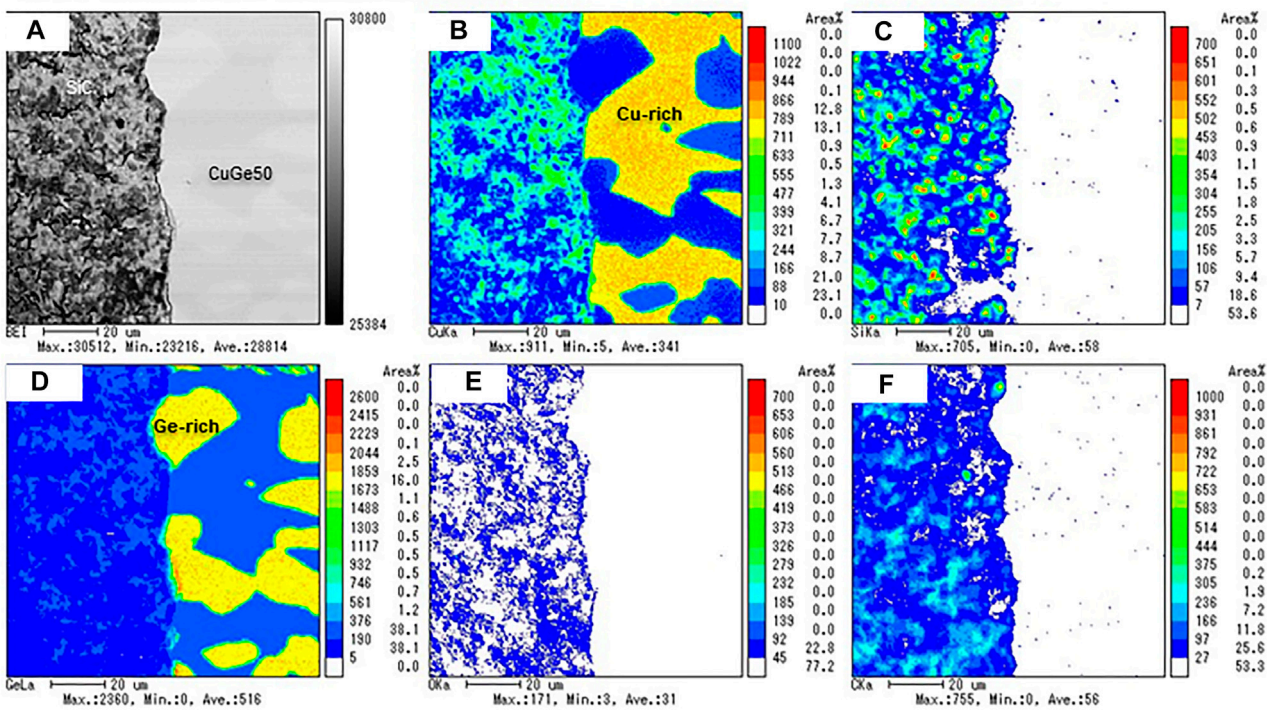

FIGURE 12 | The results of the EPMA analysis for the chemical compatibility test of CuGe50/SiC. **(A)** BEI image, **(B)** Cu, **(C)** Si, **(D)** Ge, **(E)** O, and **(F)** C mapping images.

exothermic peak temperature due to the solid-state phase transition fluctuated, with an onset temperature of 598–610°C. the reason of peak fluctuation for the fluctuation may have been the cooling process in vacuum, which is governed by the limited heat transfer. Thus the heat stored in the alloy was not quickly released into the atmosphere. These results indicated that the CuGe alloy behaved consistently, based on thermodynamic equilibrium in a gas stream, and responded under the limited heat transfer without the effect of alloy oxidation under vacuum.

The chemical compatibility between the CuGe alloys (CuGe40, CuGe50, and CuGe60) and candidate container materials (stainless steel (SUS 310S), alumina, Inconel625, and silicon carbide (SiC)) was tested at high temperatures and evaluated by EPMA analysis. For SUS 310S and Inconel625, corrosion and chemically bonded with the CuGe alloys at high temperatures was observed. Thus, there materials were not chemically compatible with the studied alloy. However, For a combination of SUS 310S/CuGe50, corrosion of the stainless steel into the CuGe50 alloy at high temperatures was observed and the SUS310S stainless steel was not chemically compatible with the studied alloy. For a combination of Inconel625/CuGe40, Cu. and Ge atoms of the alloy diffused into the Inconel layer, and Ni atoms diffused into the CuGe alloy at high temperatures. Thus, Inconel625 was chemically bonded with the CuGe40 alloy during the test and therefore this combination was not chemically compatible at high temperatures. For a combination of alumina/CuGe60/SUS 310S, no dissolution of Al and O from alumina was found in any area of the alloy. Alumina was therefore fully compatible with the CuGe60 alloy in a closed inert atmosphere at high temperatures. Finally, for a combination of CuGe50/SiC heated in the tanman-tube crucible, the sample was easily removed from the tanman crucible after the test. Therefore, no chemical corrosion occurred for the combination of CuGe50/SiC. The results demonstrate that SiC has good compatibility with the chosen alloy and crucible under an inert atmosphere.

Some merits of CuGe alloy relative to chloride molten salt in CSP technologies are 1) quick thermal response due to superior thermal conductivity, 2) no corrosive properties at elevated temperatures to alumina and SiC used as an insulated liner/capsulation material in vessels or tanks, 3) very small volume change at solid/liquid phase change leading to high loading amount in the PCM capsule, 4) high thermal-reliability without thermal decomposition. Their properties are suitable to alleviate thermal shocks, solar fluctuations, and radiation transients. However, the demerits of CuGe alloy are 1) low oxidation-resistance at elevated temperatures, 2) low chemical compatibility with stainless steel and Inconel alloys used in vessels or tanks. Based on the experimental results above, eutectic and hypereutectic CuGe alloys are satisfactory and acceptable for use as latent heat storage materials exposed to high temperatures in next-generation CSP plants.

DATA AVAILABILITY STATEMENT

The original contributions presented in the study are included in the article/Supplementary Material, further inquiries can be directed to the corresponding author.

AUTHOR CONTRIBUTIONS

NG contributed to perform conceptualization, methodology, validation, software, formal analysis, writing–original draft, writing–review and editing, visualization, supervision, project administration, funding acquisition; CSJ, YN, and SO contributed to conduct formal analysis, investigation, visualization; TK contributed to provide software and resource; TH contributed to investigation, and funding acquisition; SB contributed to provide resource.

FUNDING

This research was partially supported by the Ministry of Education, Culture, Sports, Science and Technology, Grant-in-Aid for Scientific Research (B), JSPS KAKENHI (grant number 19H02658) and Grant-in-Aid for Scientific Research (C), JSPS KAKENHI (grant number 20K05398).

ACKNOWLEDGMENTS

The authors gratefully acknowledge technical staff (Katsutoshi Iwafune) for supporting the XRD measurement and technical staff (Masayoshi Kobayashi, and Ayako Ikarashi) for supporting the EPMA measurement at Niigata University.

REFERENCES

Adinberg, R., Zvegilsky, D., and Epstein, M. (2010). Heat Transfer Efficient thermal Energy Storage for Steam Generation. *Energ. Convers. Management* 51 (1), 9–15. doi:10.1016/j.enconman.2009.08.006

Agüero, A., Audigié, P., and Rodríguez, S. (2019). *10,000 H of Corrosion Testing on Molten Salt of IN617 and Uncoated and Aluminide Coated Ferritic Steels at 580°C. Solar PACES proceedings*. Melville, NY: AIP Publishing LLC, 150002. doi:10.1063/5.0028930

Aist (2019). Thermophysical Properties Database System. Availble at:https://tpds.db.aist.go.jp/ (Accessed March 20, 2021).

Birchenall, C. E., and Riechman, A. F. (1980). Heat Storage in Eutectic Alloys. *Mta* 11 (8), 1415–1420. doi:10.1007/bf02653497

Blanco-Rodríguez, P., Rodríguez-Aseguinolaza, J., Risue~no, E., and Tello, M. (2014). Thermophysical Characterization of Mg–51%Zn Eutectic Metal alloy: A Phase Change Material for thermal Energy Storage in Direct Steam Generation Applications. *Energy* 72 (1), 414–420.

Bonk, A., Braun, M., Hanke, A., Sötz, V. A., and Bauer, T. (2019). *Enhancing the thermal Stability of Solar Salt up to 600°C in Extended Lab-Scale Experiments. SolarPACES proceedings*. Melville, NY: AIP Publishing LLC.

Cailletet, L., and Mathias, E. (1886). Recherches sur les densités des gaz liquéfiés et de leurs vapeurs saturées. *J. Phys. Theor. Appl.* 5, 549–564. doi:10.1051/jphystap:018860050054900

Carlson, M., Alvarez, F., and Dorsey, D. (2020). *200 MWth and 1 MWth Chloride Salt to Supercritical Carbon Dioxide Heat Exchanger and Test Integration Designs. SolarPACES proceedings*. Melville, NY: AIP Publishing LLC. doi:10.1115/es2020-1675

Cohen, G. (2008). "Nevada Solar One Update," in *Proceedings of the Third Concentrated Solar Power Summit US*.

El Karim, Y., Grosu, Y., Faik, A., and Lbibb, R. (2019). Investigation of Magnesium-Copper Eutectic Alloys with High thermal Conductivity as a New PCM for Latent Heat thermal Energy Storage at Intermediate-High Temperature. *J. Energ. Storage* 26, 100974. doi:10.1016/j.est.2019.100974

Energy Efficiency and Renewable Energy (2021). *Generation 3 Concentrating Solar Power Systems (Gen3 CSP)*. Washington, DC: Solar Energy Technologies Office, 20585. Available at:https://www.energy.gov/eere/solar/generation-3-concentrating-solar-power-systems-gen3-csp (Accessed March 20, 2021).

Fang, D., Sun, Z., Li, Y., and Cheng, X. (2016). Preparation, Microstructure and thermal Properties of MgBi Alloys as Phase Change Materials for thermal Energy Storage. *Appl. Therm. Eng.* 92, 187–193. doi:10.1016/j.applthermaleng.2015.09.090

Farkas, D., and Birchenall, C. E. (1985). New Eutectic Alloys and Their Heats of Transformation. *Metall. Mat Trans. A.* 16, 323–328. doi:10.1007/bf02814330

Fukahori, R., Nomura, T., Zhu, C., Sheng, N., Okinaka, N., and Akiyama, T. (2016). Thermal Analysis of Al-Si Alloys as High-Temperature Phase-Change Material and Their Corrosion Properties with Ceramic Materials. *Appl. Energ.* 163, 1–8. doi:10.1016/j.apenergy.2015.10.164

Gil, A., Medrano, M., Martorell, I., Lázaro, A., Dolado, P., Zalba, B., et al. (2010). State of the Art on High Temperature thermal Energy Storage for Power Generation. Part 1-Concepts, Materials and Modellization. *Renew. Sustainable Energ. Rev.* 14, 31–55. doi:10.1016/j.rser.2009.07.035

Gokon, N., Jie, C. S., Nakano, Y., Kodama, T., Bellan, S., and Cho, H. (2020). Thermal Charge/discharge Performance of Iron-Germanium Alloys as Phase Change Materials for Solar Latent Heat Storage at High Temperatures. *J. Energ. Storage* 30, 101420. doi:10.1016/j.est.2020.101420

Gokon, N., Nakamura, S., Yamaguchi, T., and Kodama, T. (2015). Cyclic Properties of thermal Storage/discharge for Al-Si alloy in Vacuum for Solar Thermochemical Fuel Production. *Energ. Proced.* 69, 1759–1769. doi:10.1016/j.egypro.2015.03.145

Gokon, N., Yamaguchi, T., and Kodama, T. (2016). Cyclic thermal Storage/discharge Performances of a Hypereutectic Cu-Si alloy under Vacuum for Solar Thermochemical Process. *Energy* 113, 1099–1108. doi:10.1016/j.energy.2016.07.005

Goswami, D. Y. (2015). *Principles of Solar Engineering*. 3rd Edn. Boca Raton: CRC Press, 822. doi:10.1201/b18119

ICSD (2020). *Inorganic Crystal Structure Database (ICSD)*. Available at: https://icsd.products.fiz-karlsruhe.de/.

International Energy Agency (IEA) (2020). World Energy Outlook. Available at: https://www.iea.org/reports/world-energy-outlook-2020. (Accessed March 20, 2021).

IRENA (2018). *Renewable Power Generation Costs in*. Available at: https://www.irena.org/-/media/Files/IRENA/Agency/Publication/2019/May/IRENA_Renewable-Power-Generations-Costs-in-2018.pdf.

IRENA (2016). *The Power to Change: Solar and Wind Cost Reduction Potential to 2025*. Available at: https://www.irena.org/publications/2016/Jun/The-Power-to-Change-Solar-and-Wind-Cost-Reduction-Potential-to-2025.

Islam, M. T., Huda, N., Abdullah, A. B., and Saidur, R. (2018). A Comprehensive Review of State-Of-The-Art Concentrating Solar Power (CSP) Technologies: Current Status and Research Trends. *Renew. Sustain. Energ. Rev.* 91, 987–1018. doi:10.1016/j.rser.2018.04.097

Khare, S., Dell'Amico, M., Knight, C., and McGarry, S. (2012). Selection of Materials for High Temperature Latent Heat Energy Storage. *Solar Energ. Mater. Solar Cell* 107, 20–27. doi:10.1016/j.solmat.2012.07.020

Kinzoku data book (2018). *The Japan Institute of Metals and Materials*. 4th Edn. Tokyo, Japan: MARUZEN-YUSHODO Company, Limited.

Kotzé, J. P., von Backström, T. W., and Erens, P. J. (2013). High Temperature thermal Energy Storage Utilizing Metallic Phase Change Materials and Metallic Heat Transfer Fluids. *J. Sol. Energ. Eng. Tran. ASME* 135, 035001. doi:10.1115/1.4023485

Kuravi, S., Trahan, J., Goswami, D. Y., Rahman, M. M., and Stefanakos, E. K. (2013). Thermal Energy Storage Technologies and Systems for Concentrating

Solar Power Plants. *Prog. Energ. combustion Sci.* 39, 285–319. doi:10.1016/j.pecs.2013.02.001

Medrano, M., Gil, A., Martorell, I., Potau, X., and Cabeza, L. F. (2010). State of the Art on High-Temperature thermal Energy Storage for Power Generation. Part 2-Case Studies. *Renew. Sustainable Energ. Rev.* 14, 56–72. doi:10.1016/j.rser.2009.07.036

Mehos, M., Turchi, C., Vidal, J., Wagner, M., Ma, Z., Ho, C., et al. (2017). *Concentrating Solar Power Gen3 Demonstration Roadmap, Nrel/Tp-5500-67464*, 140. Available at: https://www.osti.gov/biblio/1338899-concentrating-solar-power-gen3-demonstration-roadmap.

Nomura, T., Zhu, C., Sheng, N., Saito, G., and Akiyama, T. (2015). Microencapsulation of Metal-Based Phase Change Material for High-Temperature Thermal Energy Storage. *Sci. Rep.* 5, 9117. doi:10.1038/srep09117

Okamoto, H. (2010). *Phase Diagrams for Binary Alloys*. Materials Park, OH: ASM International.

Pelay, U., Luo, L., Fan, Y., Stitou, D., and Rood, M. (2017). Thermal Energy Storage Systems for Concentrated Solar Power Plants. *Renew. Sustainable Energ. Rev.* 79, 82–100. doi:10.1016/j.rser.2017.03.139

Risueño, E., Faik, A., Gil, A., Rodríguez-Aseguinolaza, J., Tello, M., and D'Aguanno, B. (2017). Zinc-rich Eutectic Alloys for High Energy Density Latent Heat Storage Applications. *J. Alloys Compounds* 705, 714–721. doi:10.1016/j.jallcom.2017.02.173

Rodríguez-Aseguinolaza, J., Blanco-Rodríguez, P., Risueño, E., Tello, M. J., and Doppiu, S. (2014). Thermodynamic Study of the Eutectic Mg49-Zn51 alloy Used for thermal Energy Storage. *J. Therm. Anal. Calorim.* 117, 93–99. doi:10.1007/s10973-014-3639-0

Skumanich, A. (2010). CSP: Developments in Heat Transfer and Storage Materials. *Renew. Energ. Focus* 11 (5), 40–43. doi:10.1016/s1755-0084(10)70115-0

Stoffel, T., Renne, D., Myers, D., Wilcox, S., Sengupta, M., George, R., et al. (2010). *Concentrating Solar Power- Best Practices Handbook for the Collection and Use of Solar Resource Data (CSP)*. NREL/TP-550-47465. Golden, CO: National Renewable Energy Lab. (NREL). . Available at: https://www.osti.gov/biblio/989017-bvKldG/. doi:10.2172/989017

Sugo, H., Kisi, E., and Cuskelly, D. (2013). Miscibility gap Alloys with Inverse Microstructures and High thermal Conductivity for High Energy Density thermal Storage Applications. *Appl. Therm. Eng.* 51, 1345–1350. doi:10.1016/j.applthermaleng.2012.11.029

Sun, J. Q., Zhang, R. Y., Liu, Z. P., and Lu, G. H. (2007). Thermal Reliability Test of Al-34%Mg-6%Zn alloy as Latent Heat Storage Material and Corrosion of Metal with Respect to thermal Cycling. *Energ. Convers. Management* 48 (2), 619–624.

Wang, Z., Wang, H., Li, X., Wang, D., Zhang, Q., Chen, G., et al. (2015). Aluminum and Silicon Based Phase Change Materials for High Capacity thermal Energy Storage. *Appl. Therm. Eng.* 89, 204–208. doi:10.1016/j.applthermaleng.2015.05.037

Wei, G., Huang, P., Xu, C., Liu, D., Ju, X., Du, X., et al. (2016). Thermophysical Property Measurements and thermal Energy Storage Capacity Analysis of Aluminum Alloys. *Solar Energy* 137, 66–72. doi:10.1016/j.solener.2016.07.054

Xu, X., Wang, X., Li, P., Li, Y., Hao, Q., Xiao, B., et al. (2018). Experimental Test of Properties of KCl-MgCl2 Eutectic Molten Salt for Heat Transfer and Thermal Storage Fluid in Concentrated Solar Power Systems. *J. Solar Energ. Eng.* 140, 1051011. doi:10.1115/1.4040065

Zhai, W., Geng, D. L., Wang, W. L., and Wei, B. (2012). A Calorimetric Study of Thermodynamic Properties for Binary Cu-Ge Alloys. *J. alloys Compd.* 535, 70–77. doi:10.1016/j.jallcom.2012.04.091

Zhang, H., Baeyens, J., Cáceres, G., Degrève, J., and Lv, Y. (2016). Thermal Energy Storage: Recent Developments and Practical Aspects. *Prog. Energ. Combustion Sci.* 53, 1–40. doi:10.1016/j.pecs.2015.10.003

Zhao, J., Yuan, Y., and Cui, F. (2017). Relationship between the Cu Content and thermal Properties of Al-Cu Alloys for Latent Heat Energy Storage. *J. Therm. Anal. Calorim.* 129, 109–115. doi:10.1007/s10973-017-6153-3

Zhao, Y. (2020). *Molten Chloride Thermophysical Properties, Chemical Optimization, and Purification*. Nrel/Tp-5500-78047. Golden, CO: National Renewable Energy Lab. (NREL), 1–82. doi:10.2172/1734652

Zhao, Y., and Vidal, J. (2020). Potential Scalability of a Cost-Effective Purification Method for MgCl2-Containing Salts for Next-Generation Concentrating Solar Power Technologies. *Solar Energ. Mater. Solar Cell* 215, 110663. doi:10.1016/j.solmat.2020.110663

Conflict of Interest: The authors declare that the research was conducted in the absence of any commercial or financial relationships that could be construed as a potential conflict of interest.

frontiers in Energy Research

ORIGINAL RESEARCH
published: 12 July 2021
doi: 10.3389/fenrg.2021.694248

Techno-Economic Analysis of Candidate Oxide Materials for Thermochemical Storage in Concentrating Solar Power Systems

Reiner Buck[1]*, *Christos Agrafiotis*[2], *Stefania Tescari*[2], *Nicole Neumann*[2] and *Martin Schmücker*[3]

[1]German Aerospace Center (DLR), Institute of Solar Research, Stuttgart, Germany, [2]German Aerospace Center (DLR), Institute of Future Fuels, Köln, Germany, [3]HRW University of Applied Sciences, Mülheim/Ruhr, Germany

The thermal storage capability is an important asset of state-of-the-art concentrating solar power plants. The use of thermochemical materials, such as redox oxides, for hybrid sensible/thermochemical storage in solar power plants offers the potential for higher specific volume and mass storage capacity and as a consequence reduced levelized cost of electricity making such plants more competitive. For the techno-economic system analysis, three candidate redox materials were analyzed for their cost reduction potential: cobalt-based, manganese–iron–based, and perovskite-based oxide materials. As a reference process the use of inert commercial bauxite particles (sensible-only storage) was considered. A solar thermal power plant with a nominal power of 125 MW_e and a storage capacity of 12 h was assumed for the analysis. For each storage material a plant layout was made, taking the specific thermophysical properties of the material into account. Based on this layout a particle break-even cost for the specific material was determined, at which levelized cost of electricity parity is achieved with the reference system. Cost factors mainly influenced by the material selection are storage cost and steam generator cost. The particle transport system cost has only a minor impact. The results show differences in the characteristics of the materials, for example, regarding the impact on storage size and cost and the steam generator cost. Regarding the economic potential of the candidate redox materials, the perovskite-based particles promise to have advantages, as they might be produced from inexpensive raw materials.

Keywords: solar power, thermochemical energy storage, particles, redox reaction, techno-economic optimization

OPEN ACCESS

Edited by:
Juan M. Coronado, Institute of Catalysis and Petrochemistry, Spain

Reviewed by:
Alfonso Chinnici, University of Adelaide, Australia
George Karagiannakis, Centre for Research and Technology Hellas, Greece

***Correspondence:**
Reiner Buck
reiner.buck@dlr.de

Specialty section:
This article was submitted to Solar Energy, a section of the journal Frontiers in Energy Research

Received: *12 April 2021*
Accepted: *07 June 2021*
Published: *12 July 2021*

Citation:
Buck R, Agrafiotis C, Tescari S, Neumann N and Schmücker M (2021) Techno-Economic Analysis of Candidate Oxide Materials for Thermochemical Storage in Concentrating Solar Power Systems. Front. Energy Res. 9:694248. doi: 10.3389/fenrg.2021.694248

INTRODUCTION

The use of thermochemical energy storage (TCS) materials, such as redox pair oxides, for hybrid sensible/thermochemical storage in concentrated solar power (CSP) plants (Wong, 2011) can potentially reduce the levelized cost of electricity (LCOE) and make such plants more competitive. The basic operation concept is that a large part of the heat supplied from solar concentration facilities to a solar receiver is employed to drive the endothermic reduction of the oxidized state of an oxide (the one with the higher valence of the cation metal) to the reduced one. The heat stored in the reduced oxide can be recovered at will, as the enthalpy of the reverse exothermic oxidation reaction, and used for electricity generation during off-sun operation. In

contrast to other TCS schemes (e.g., carbonation/decarbonation or hydration/dehydration), both reactions can be performed in principle under direct contact of the oxide with air, waived thus of the need for an additional heat exchanger as well as of handling other-than-air gases like carbon dioxide or steam. The same feature renders them compatible with the quest for development of higher efficiency CSP plants operating via air-Brayton gas turbine power cycles instead of the currently employed Rankine steam one, since the input in a gas turbine is an air stream of high pressure and temperature (Schrader et al., 2015). This high-temperature air stream could be achieved by exploiting the enthalpy of sufficiently exothermic air-oxide oxidation reactions between air and the oxide instead of utilizing a gas combustor burning fossil fuels.

The ideas for eventual implementation of these redox oxide–based TCS concepts in commercial, utility-scale CSP plants capitalize on approaches for sensible-only high-temperature storage in ceramic media (Khare et al., 2013) already industrially practiced or currently under consideration and investigation. In this context, the concepts proposed so far for the integration of such systems in CSP plants can be categorized in two broad concepts depending on whether the solid oxide, in addition to its role as the storage medium, is also employed as the solar energy harvesting medium and consequently as the heat transfer fluid (HTF) or not.

The first concept utilizes moving particle streams as a combined HTF/storage medium, which stems from recent approaches considering inexpensive, chemically inert, refractory ceramic particles as alternative heat transfer and extremely high temperature storage (T > 1,000°C) media for CSP plants (Siegel et al., 2015). Oxide particle streams in their oxidized state are transported to the top of a solar tower where they are thermally reduced in a solar particle receiver. This receiver can be, for example, a rotary kiln (Neises et al., 2012), a fluidized or spouted bed type (Flamant et al., 2013; Ma et al., 2014), a gravity-led inclined "sliding-bed" type (Schrader et al., 2020), or a centrifugal receiver recently introduced and developed by DLR (Wu et al., 2014). The reduced particles are stored in a hot particle storage tank and subsequently fed to an oxidation reactor for power generation when and where needed. At the end of this step they are oxidized, stored in a cold particle storage tank, and then recirculated back to the solar receiver for a new cycle.

Alternatively, in a second approach, a different heat transfer fluid—and in the particular case of oxides, air is the obvious choice—heated in the solar receiver can indirectly heat a non-moving oxide storage medium in the form of either particle bed or monolithic structures like honeycombs/bricks reducing it during on-sun operation. During off-sun operation "cold" air is introduced and flows through the volume of the solid storage medium, oxidizes it, and consequently is heated by the oxidation reaction enthalpy to the levels required for its introduction to the power block. Again, this approach stems from commercial high temperature regenerative storage systems, for example, the so-called Cowper stove used with blast furnaces that consist of a stacked firebrick storage medium (Tamme et al., 1991) as well as with similar sensible heat storage units employed in air-operated solar thermal power plants, like the one of DLR at Jülich, Germany (Zunft et al., 2014).

Both approaches essentially target to convert a chemically inert, sensible-only storage ceramic medium (particle, granule, honeycomb, or brick) to a hybrid sensible/TCS one by introducing chemical reaction functionality (with oxygen) in it in the same volume. Hence, such hybrid sensible/TC systems using oxide-gas reactions have the potential of greatly shrinking the size of storage subsystems/tanks. This becomes especially relevant for longer storage durations, where the combination of CSP and thermal storage may be most competitive with regards to LCOE, for example, in comparison to PV and battery storage (Schöniger et al., 2021).

DLR is investigating both approaches in conjunction with issues on the material composition itself. On the materials' side, potential candidate of redox pair oxides that can be thermally reduced in the temperature range of interest without requiring very low oxygen partial pressures, that is, in direct contact with atmospheric air includes BaO_2/BaO, Co_3O_4/CoO, Mn_2O_3/Mn_3O_4, CuO/Cu_2O, and Fe_2O_3/Fe_3O_4 (Wong, 2011) as well as their mixed compositions (Block and Schmücker, 2016). Among them, extensive work has been performed on the Co_3O_4/CoO system due to its very high energy density (ΔH of the reaction in kJ/kg of solid oxide), stoichiometric and fully reversible reaction, and excellent long-term cyclic stable performance. Thus, along the second approach above pursued in project RESTRUCTURE, the concept evolved to a 74 kWh_{th} hybrid sensible-TCS unit encompassing 88 kg of Co_3O_4 coated on cordierite honeycombs that has clearly manifested recordable substantial temperature effects due to chemical reactions and is the largest oxide TCS system developed and experimentally validated so far (Tescari et al., 2017). However, cobalt is mined in areas of the world generally acknowledged for mismanagement, environmental degradation, and adverse impacts to public health and therefore on the way to a low-carbon economy and ethical and societal issues advocate for its eventual elimination from such energy-related technologies (including electric energy storage in batteries). Thus, research is focused on alternative systems based on inexpensive, non-critical, abundant, and environmentally safe materials such as Ca^-, Mn^-, and Fe^- based redox oxides, despite their lower energy storage density compared to Co_3O_4.

In the RedoxStorE project a CSP system utilizing particles as HTF and storage material is investigated. In this context particle-based options for such a system were analyzed and the relevant components were further developed. Experimental work focused on the development of suitable particles (Wokon et al., 2017a; Wokon et al., 2017b; Preisner et al., 2018), high temperature particle receivers for the thermal reduction of these particles (Tescari et al., 2020), and a particles-to-air heat exchanger for thermochemical oxidation of the reduced particles and heat recovery (Preisner and Linder, 2020). According to the rationale above, manganese–iron–based redox particles were investigated experimentally in detail, as an example of earth-abundant, environmental-friendly, and inexpensive thermochemical particles (Wokon et al., 2017a; Wokon et al., 2017b). In parallel, such kinds of solar particle receivers based on perovskites have been proposed in the United States, within the so-called PROMOTES project (Miller et al., 2016). This concept

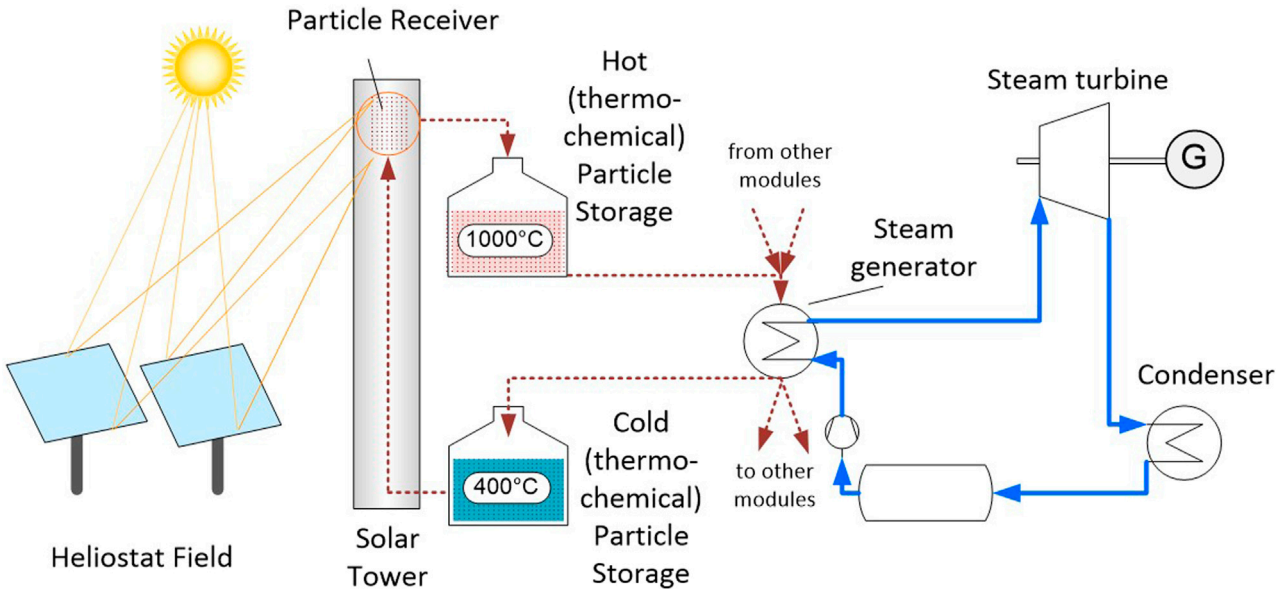

FIGURE 1 | Scheme of the particle-based solar thermal power system (power cycle simplified).

foresees a controlled atmosphere solar receiver chamber where the oxides at their oxidized state are thermally reduced under low oxygen partial pressure (slight or higher vacuum or under inert gas flow) and a reoxidation reactor, wherein the reduced particles react with pressurized air on-demand (Babiniec et al., 2016) in the context of coupling the process to an air-Brayton gas turbine cycle, as already discussed. In the latter design, the air is preheated by the compression stage, with no further preheating from other sources.

In parallel to more fundamental materials–composition screening studies and demonstration of effective reactor/heat exchanger concepts, there is a need to illustrate how the various components can be materialized in storage modules effectively incorporated in the operation of a full CSP plant. The large-scale adoption of oxide-based TCS in such real CSP plants will depend on the one hand on whether such materials can be produced cost-effectively at large-scale, but, most crucially, on whether such concepts can eventually compete with current industrial scale sensible–only storage ones, generally implemented with inexpensive systems, to justify the introduced plant complexity. Hence, the present work is targeted to such a comparative techno-economic system analysis, considering three candidate redox materials for their cost reduction potential: cobalt-based, manganese-based, and perovskite-based oxide materials. As a reference process, the use of inert commercial bauxite particles as sensible-only storage medium was considered. The paper presents the results of this techno-economic analysis.

A first assessment of the same or similar materials was performed in a study by Buck et al., (2020) using simplified cost assumptions. In this study, new compositions for the manganese-based and perovskite material are assessed. In addition, further refinement on some cost assumptions like the ground transportation cost was introduced. The cost for heliostats and bauxite particles was also revised to be in accordance with the US-DoE next generation CSP "Gen3" (Mehos et al., 2017) system analysis assumptions.

SYSTEM DESCRIPTION

The study investigates a solar power plant with different storage materials. The concentrating solar power (CSP) plant has a nominal power of 125 MW_e and includes thermal storage with a capacity of 12 h. The solar subsystem consists of a multi-tower configuration with 14 identical solar tower modules, feeding hot particles to a common high-efficiency steam cycle for power production. **Figure 1** shows a scheme of the system under consideration.

An advanced subcritical steam power cycle with reheat and multiple preheating stages is assumed, as described in (Buck and Giuliano, 2019). In the steam generator, high pressure steam is heated from 261 to 620°C; in the reheat section, the intermediate pressure steam is reheated from 426 to 620°C. For this steam process, a net cycle efficiency of 43% is calculated. Using this efficiency, a thermal input power of 291 MW_{th} is required from the solar subsystem for nominal load operation. For the layout and costing study the steam generator is considered as a single heat exchanger, that is, the primary (high pressure) heater and the (intermediate pressure) reheater are not considered separately.

The multi-tower concept is selected since the considered receiver technology, the centrifugal particle receiver CentRec® developed by DLR (Ebert et al., 2016; Ebert et al., 2018), has inherent size limitations due to its rotating drum design. As of now, a receiver limit of 50 MW_{th} per receiver is assumed. This size corresponds to an outer drum diameter of about 7.5 m and an

aperture diameter of about 5.4 m, a size which seems to be feasible based on knowledge about existing industrial rotary kiln and milling units. In total 14 solar tower modules are assumed, with each of the modules consisting of a receiver with a design point (DP) power of 50 MW_{th}, a tower, a heliostat field, and a thermal storage composed of two storage containments integrated into the tower structure (hot storage above cold storage). The total thermal system power of all modules is 700 MW_{th} at DP conditions. With the power cycle demand of 291 MW_{th} this represents a solar multiple of 2.4.

The upper particle temperature in the process is assumed as 1,000°C. This represents the temperatures of the receiver exit, the hot particle storage, and the steam generator particle inlet. For the lower temperature, representing steam generator particle outlet, cold particle storage, and receiver inlet conditions, a value of 400°C is set. This temperature range includes the reduction temperatures of all three thermochemical oxides under study. The comparison implies that the same open-air centrifugal receiver will be employed for the thermal reduction of the thermochemical oxide particles, and therefore this reduction will take place under air atmosphere. Just like the chemically inert particles, the thermochemical ones are stored in a hot and a cold storage bin after their reduction and oxidation, respectively. The thermochemical characteristics of the particles were considered by approximated total enthalpy values at the high and low operation temperature points in the cycle.

PERFORMANCE AND COST ASSUMPTIONS

The layout of the solar subsystem (heliostat field, tower, and receiver) is not affected by the material selection for the thermochemical particles, meaning fix cost for these components. Cost factors influenced by material selection are the storage cost, the steam generator cost, and the particle transport system cost. System performance is hardly affected by the material selection, only the effect of changed particle mass flow has a small impact on annual energy yield, due to changes in parasitic power. Based on the total system cost and annual electricity generation, the LCOE is calculated. All cost data is given in Euro (€).

Performance and cost assumptions are selected in many aspects similar to the assumptions given in the Gen3 road map (Mehos et al., 2017) and related documents.

Plant Site

For the present analysis, a site near Daggett (California, United States) is considered. The site is located at a latitude of 34.85°north and a longitude of 116.79°west. The altitude of the site is 588 m above sea level. The annual direct normal irradiance (DNI) is reported as 2,791.4 kWh/m^2a.

Steam Power Cycle

As a steam power cycle a high efficiency power block with 620°C/125 bar live steam conditions is assumed (Buck and Giuliano, 2019). The power block is rated at 125 MW_e with a net efficiency of 43%. For the cost analysis, the power cycle and the steam generator are treated as separate items, since the cost of the latter is influenced by the operating temperature conditions while the power cycle cost is not. For the cost of the power cycle without steam generator a fixed specific cost of $C_{sp,pc}$ = 700 €/kW_e is assumed. This results in a power cycle cost C_{pc} of 87.5 Mio €.

Steam Generator

The operating conditions in the steam generator change when thermochemical particles are used, compared to the situation with sensible-only heating. When chemically active particles are used the reaction keeps the temperature level higher in the steam generator, while transferring the chemically stored heat.

A moving bed particle heat exchanger is foreseen for the steam generator of the power cycle. In this heat exchanger type, the solid particles are moving slowly across the heat exchanger tubes, driven by gravity [6]. The mass flow is controlled by variable gate valves at the cold exit of the heat exchanger. The required heat transfer area of this heat exchanger is calculated as follows:

$$A_{HX,0} = \frac{P_{el}/\eta_{pc}}{h_{SG} \cdot \Delta T_{log}}. \quad (1)$$

In a study by Baumann and Zunft (2014), convective heat transfer coefficients up to 240 W/m^2K were measured for a tube bundle type heat exchanger with particle inlet temperatures ranging from 355 to 470°C. Since the particle heat exchanger for the steam power cycle is operated at much higher temperatures, radiative heat transfer will improve the overall heat transfer significantly. Therefore, a constant heat transfer coefficient h_{SG} of 300 W/m^2K is assumed. The mean logarithmic temperature difference ΔT_{log} for a heat exchanger in countercurrent flow configuration is calculated based on the solid particle temperature selection and the power cycle temperature levels. The water/steam temperatures in the steam generator are 261°C for the preheated water inlet and 620°C for the steam outlet.

The steam generator material temperatures are mainly defined by the steam conditions, as the highest heat transfer resistance will be between particles and tube material, that is, the tube material temperatures will be relatively close to the steam temperatures and quite independent of particle temperatures. Thus, the heat exchanger cost is assumed to be only a function of the required heat transfer area.

For thermochemical storage materials typically a higher temperature level is maintained in the steam generator, driven by the oxidation reaction that occurs while the material passes through the steam generator. Therefore, a higher driving temperature difference occurs in the heat exchanger regions where the reaction occurs. This effect is considered in the analysis by modifying the initially calculated heat exchanger area as follows:

$$A_{HX} = \frac{A_{HX,0}}{R_{tc}}. \quad (2)$$

The ratio R_{tc} is calculated from the particle specific heat capacity and the reaction enthalpy ΔH, as follows:

$$R_{tc} = \frac{\left(c_{p,part} \cdot \Delta T + \Delta H\right)}{c_{p,part} \cdot \Delta T}. \quad (3)$$

Results for R_{tc} are given in "Results and Discussion." This simplified approach is taken since the characteristics of a heat exchanger for chemically active heat transfer materials is quite complex. In reality, factors like reaction kinetics and air stream requirements (blower, recuperator, and additional heat losses) limit the benefit of the redox reactions on heat transfer. The above reduction of the required heat exchanger area is considered quite positive for the thermochemical systems. A more realistic representation for the heat exchanger performance needs a detailed understanding and modeling of the heat exchanger and the reaction characteristics of the particles while passing through the heat exchanger. This is beyond the scope of the current study.

For the cost of the steam generator a correlation was derived using the MATCHE data base [Matches Equipment Cost, 2018] assuming Inconel 625 as tube material. With a correction factor, the high pressure of the steam system, a translation from 2014 cost into actual cost, and after converting from $ to € this resulted in the following correlation (Buck et al., 2020):

$$C_{HX} = 128122 \cdot A_{HX}^{0.66}. \quad (4)$$

Heliostat Field

The heliostat field is composed of a large number of heliostats. Each heliostat is tracked in two axes and has a rectangular shape with 12.84 m width and 9.45 m height, covered with 4 × 7 facets of 3.21 m width and 1.35 m height. This results in a net reflective area of 121.34 m^2. A total beam error of 3.8 mrad is used for the Gaussian approximation of the beam reflected from the mirrors (as used in the HFLCAL optimization), representing the sunshape and a combined heliostat slope and tracking error of about 1.4 mrad. An effective reflectivity of 88% is assumed, accounting for the mirror reflectivity and an average dirt coverage of the mirrors. A specific cost $C_{sp,f}$ of 71 €/m^2 installed heliostat field is used, as prescribed by the Gen3 cost assumptions, taking the heliostat cost and the land preparation cost into account (Gonzalez-Portillovet al., 2021).

Tower

A tower is required to locate the solar receiver at a suitable height above the heliostat field. The tower height H_t is dominated by the heliostat field and receiver configuration, and is optimized together with other parameters. The cost of the tower is assumed (Weinrebe et al., 2014) as follows:

$$C_t = 1767767 \cdot e^{6.931E-3 \cdot H_t}. \quad (5)$$

The tower includes the two integrated storage tanks, the tower wall structure serves also as the outer wall of the tanks.

Particle Receiver

The receiver technology for the multi-tower concept is based on the centrifugal particle receiver technology CentRec® (Ebert et al., 2016), currently under development at DLR. The receiver uses the direct absorption principle, meaning that the dark particles are irradiated directly by the concentrated solar radiation and get heated from the absorbed radiation. A first demonstration receiver with about 2.5 MW_{th} peak power was installed at the DLR solar tower test facility in Jülich, Germany. Nearly 70 h of solar testing was carried out so far, and average particle outlet temperatures up to 965°C were achieved (Ebert et al., 2018). The receiver considered in this study has a circular aperture facing north at a certain tilt angle. The area A_{ap} of the circular aperture and the tilt angle are determined during the solar system optimization. A simplified receiver model is considered, with the absorbed power $P_{r,abs}$ defined as a function of intercepted power $P_{r,int}$ and receiver exit temperature $T_{r,ex}$ by following equation:

$$P_{r,abs} = \alpha \cdot P_{r,int} - \varepsilon\sigma A_{ap} T_{r,ex}^4 - h A_{ap} \left(T_{r,ex} - T_{amb}\right). \quad (6)$$

For the CentRec® receiver, the effective values are set: solar absorptivity α = 0.95, emissivity ε = 0.9, and convective heat transfer coefficient h = 30 W/m^2K. Ambient temperature T_{amb} is set to 300 K (27°C). These parameters were found to be a good fit to more detailed simulation results from finite element models.

Important to note is that the receiver has an open aperture, that is, the particle heating takes place at ambient air conditions. This is relevant for the perovskite material where the reaction enthalpy is strongly dependent on oxygen partial pressure.

Particle Transport System

The multi-tower system needs particle transportation in two ways: lifting the 400°C particles up to the receiver inlet ("vertical" particle transport) and transporting the particles between the solar tower modules and the central power station ("ground" particle transport).

When sufficient solar power is available for the receiver, the 400°C particles are lifted up to the receiver for heating. The heated particles are then flowing by gravitation to the hot storage. When the power block is operated, particles are charged from the hot storage into insulated transportation containers and then transported to the central unit. After being cooled down in the steam generator of the central power block, the colder particles are transported back in insulated containers to the solar tower modules and are either lifted up to the receiver (when enough solar power is available) or lifted to the inlet of the cold storage container. When more solar power is available than the power cycle actually uses, the hot storage fills up while the cold storage is emptied.

Vertical Particle Transport

A mine hoist system is foreseen for the vertical particle transport. Repole and Jeter (2016) have made a conceptual design for a hoist for a solar demonstration system with a thermal capacity of 60 MW_{th}. Since the selected solar tower module size is close to this capacity, this mine hoist design was taken as base value for the calculation of the cost for the specific configuration. Scaling factors are applied for conditions differing from the original design values. The used correlation for the lift cost in € is (after currency conversion from $ to €) as follows:

$$C_{tr} = 425000 \cdot \left\{1 + k_T\left(\frac{T_l - T_{l,0}}{T_{l,0}}\right)\right\} \cdot \left\{1 + k_m\left(\frac{\dot{m} - \dot{m}_0}{\dot{m}_0}\right)\right\} \cdot \left\{1 + k_H\left(\frac{H_l - H_{l,0}}{H_{l,0}}\right)\right\}. \quad (7)$$

The scaling factors are selected as $k_T = 0.1$ (for temperature dependency), $k_m = 0.65$ (for mass flow dependency), and $k_H = 0.6$ (for lift height dependency). The relevant mass flow is for design point conditions. For the particle lifting, parasitics are calculated considering a 80% efficient vertical lift system. The determined power consumption, which is different for each material, is subtracted from the produced annual electricity.

Ground Particle Transport

For transportation between the solar tower modules and the central power station a number of trucks are foreseen, each transporting insulated containers. To avoid severe thermal cycling of the high temperature containers, one container type is for hot and another type for cold particles, that is, a truck always transports a container set consisting of a hot and a cold container. On the way from an external module to the central module the hot container is charged, and on the way back the cold container is charged. Standard 20 feet ISO containers are assumed for particle ground transport. For such containers a lot of handling equipment is available. The containers are equipped with a 30 cm internal insulation (different type for hot and cold particle containers). With a filling level of 90% an active storage volume of 14.9 m^3 is available per container. The energy content transported by the containers is then defined by the particle mass in this volume and the enthalpy difference between hot and cold particles. With the given temperature difference, the energy content depends on the type of particles used in the system. For a hot particle container, a cost of 90,000 $ is assumed, for a cold particle container 60,000 $, with the difference stemming from the different insulation type according to the temperature level. The cost of a container set is then $C_{containerset}$ = 150,000 $.

A truck can serve one or multiple modules, depending on the required mass flow. Mass flow per truck cycle is defined by the container's energy content, the path length, and the loading/unloading time. The trucks are continuously operated whenever the power cycle is producing electricity, for example, also during night time. As the paths between the solar tower modules and the central power block are clearly defined, fully autonomous trucks are foreseen. Such truck systems are known as automated guided vehicles (AGV); commercial solutions are available. The cost of each truck is assumed as C_{truck} = 100,000 $. In addition to the truck and container cost, for each tower a container loading system was accounted for, with cost of $C_{loading}$ = 50,000 $ per tower. The number of trucks to provide the required mass flow is calculated from the total path length and the timing conditions. The total ground transport cost is calculated as follows:

$$C_{transport} = C_{truck} \cdot n_{truck} + C_{containerset} \cdot n_{truck} + C_{loading} \cdot n_{mod}. \quad (8)$$

The number of trucks and container sets varies depending on the material properties. Additional thermal losses of 2% are assumed for the particle lifting and ground transportation, reducing the annual yield by this amount. This loss is associated with the thermal losses of the containers and the losses due to filling/emptying procedures. Estimates on the ground transport power consumption showed that this is negligible.

Thermal Storage System

For the solar tower system, a thermal storage time of 12 h full load operation is assumed, resulting in a total thermal storage capacity E_{st} of 3.49 GWh. This storage capacity is evenly distributed over all solar tower modules, leading to a module storage capacity of 249 MWh. The hot and cold storage containments are installed inside the tower, using the tower walls as containment walls. An inner insulation prevents the concrete tower walls from overheating.

Thermal losses in the storage system are assumed as 2% of the total energy provided by the receiver. The total particle inventory per module depends on the selected particle material and is calculated as follows:

$$m_{st} = \frac{E_{st}}{n_{mod} \cdot \Delta h_{total}}. \quad (9)$$

The total enthalpy difference Δh_{total} is the sum of the reaction enthalpy and the sensible heat between upper and lower temperature of the particles.

For the total particle mass another 5% of this particle mass is added to account for particles contained in components other than the storage, for example, the transportation containers. Mass loss during the plant lifetime is not taken into account here. The cost of the total particle inventory C_{part} is then calculated from the specific particle $C_{sp,part}$ cost as follows:

$$C_{part} = 1.05 \cdot m_{st} \cdot n_{mod} \cdot C_{sp,part}. \quad (10)$$

The cost of the storage containment C_{stc} is calculated from the surface area A_{stc} of the containment. A cylindrical containment with a height-to-diameter ratio of 1.6 is assumed. From the particle inventory, m_{st}, the volume of the containment is calculated, accounting for a useable filling level of 80%. With the derived diameter and height data the outer surface area is calculated. A temperature-dependent area-specific insulation cost $C_{A,sp,is}$ [€/m^2] is calculated as follows:

$$C_{A,sp,is}(T_{st}) = 2000 \cdot \left(1 + 0.3 \cdot \frac{(T_{st} - 600)}{400}\right). \quad (11)$$

The total storage containment cost for all modules is the sum of the cost of the hot and cold storage containments, as given below:

$$C_{stc} = \left\{A_{stc} \cdot C_{A,sp,is}(T_{r,ex}) + A_{stc} \cdot C_{A,sp,is}(T_{r,in})\right\} \cdot n_{mod}. \quad (12)$$

The total cost of the storage system C_{st} is then obtained as the sum of C_{part} and C_{stc}.

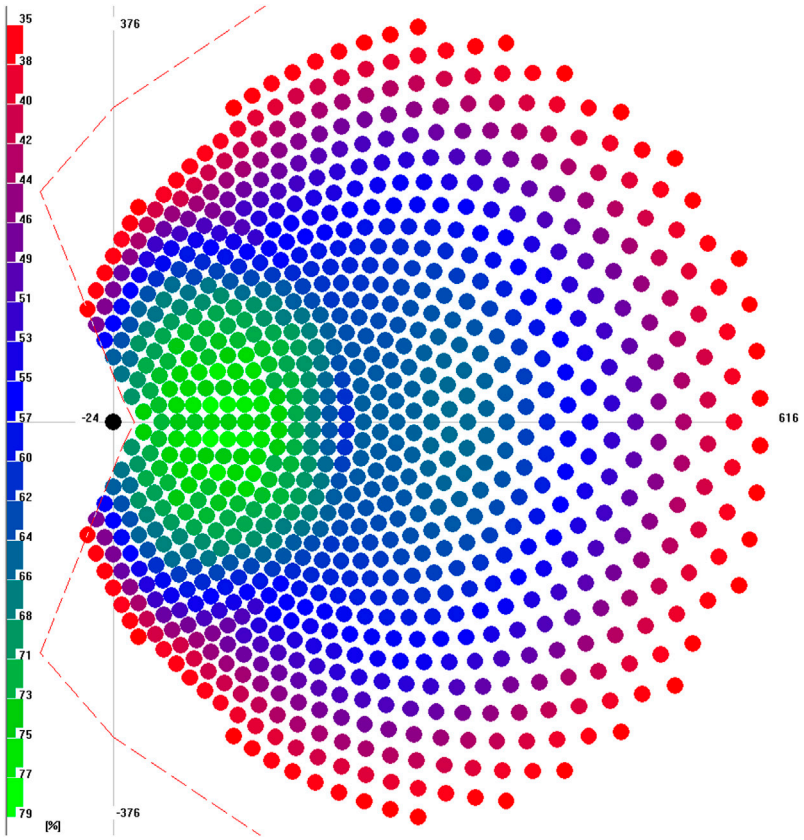

FIGURE 2 | Field configuration of a solar tower module.

LCOE Evaluation

The levelized cost of electricity (LCOE) is selected as the evaluation criteria. The total capital expenditure (CAPEX) is the sum of all module cost plus the cost of the central power block (steam generator and power cycle). Contingencies of 20% are added to the total CAPEX. Annual operational expenditures (OPEX) are assumed as 2% of the CAPEX. The annual electric power production $E_{el,annual}$ is obtained from the HFLCAL layout calculation, based on the annual thermal energy harvested at the selected site. The LCOE is then calculated using a simplified annuity approach as follows:

$$LCOE = \frac{CAPEX\, f_{annuity} + OPEX}{E_{el,annual}}. \tag{13}$$

The annuity factor $f_{annuity}$ is based on interest rate and the depreciation period. With an interest rate of 7% and a depreciation period of 25a an annuity factor $f_{annuity}$ of 8.58% is obtained. Whenever costs are given in $, they are converted to € with an exchange rate of 1 € = 1.1851 $ (March 09, 2021).

System Layout

For the given fixed temperature range and power requirement, the heliostat field layout and the number of heliostats were optimized using the simulation tool HFLCAL (Schwarzbözl et al., 2009). A radially staggered field layout is selected. As a result, the field layout, the number of heliostats, and total heliostat field area are obtained together with the tower height and the receiver aperture diameter and the tilt angle. The field, receiver, and tower layout are done for the reference system with bauxite particles, and these components are kept the same for the cases with thermochemically active particles. The resulting field layout for a single module is shown in **Figure 2**. In total 869 heliostats are required to obtain 50 MW_{th} design point power from the receiver. Further layout results are as follows:

- receiver diameter: 5.9 m
- receiver tilt angle (vs. horizontal): 34°
- receiver aperture center height: 111.7 m
- total tower height: 118.7 m (for shadowing calculations)

For the cases with redox materials the following components are adapted:

- storage (variation of size)
- particle inventory (mass)
- heat exchanger (variation of heat exchange area)
- transport system (variation of mass flow)

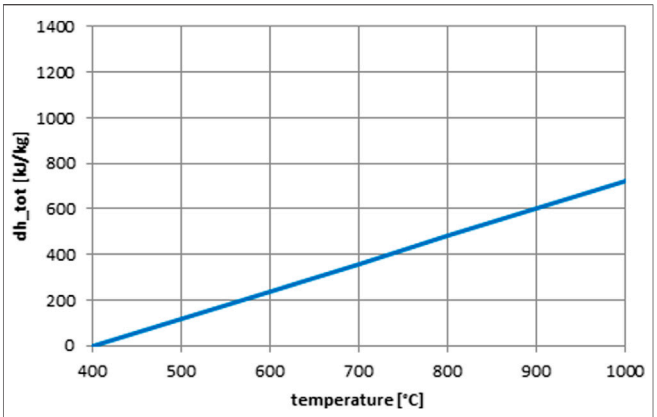

FIGURE 3 | Enthalpy data for bauxite material (as reference).

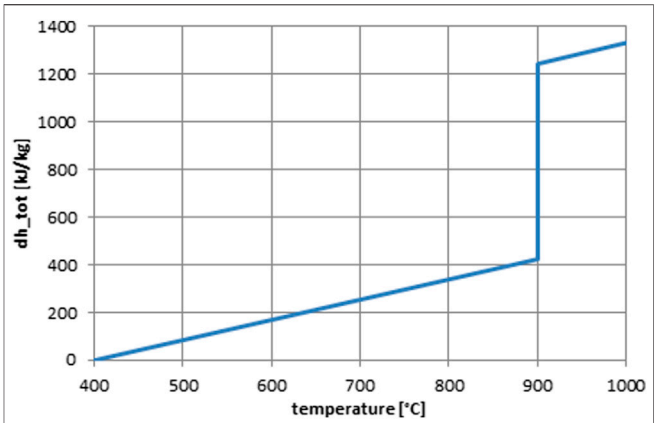

FIGURE 4 | Enthalpy data for cobalt-based redox material.

CASE DESCRIPTIONS

The evaluated cases differ by the selected particle material. The following cases are considered:

- bauxite particles (inert particles, reference case)
- cobalt oxide–based redox particles
- manganese/iron oxide–based redox particles
- calcium–manganese–based perovskite redox particles

For the thermochemical particles, the following simplifying assumptions are made:

- chemical reactions are assumed to be not limited by reaction kinetics
- the reaction is proceeding from 0 to 100% within the used temperature range of the particles, and vice versa
- as the thermophysical properties of the redox materials change with the reaction, the values for density and specific heat capacity were approximated by constant average values.
- additional equipment for the reaction process is not considered (e. g. air system for the steam generator)

Since the cost of the selected particles at large quantities is only known for the bauxite material, the comparison between materials is done by the particle break-even cost. This cost is the specific particle cost at which the same LCOE is achieved as in the reference case with bauxite. For each material this break-even cost is determined and discussed.

Bauxite Material

As the reference case, the use of bauxite particles as sensible–only storage medium, as currently proposed by several research teams, is included. Bauxite particles are produced in huge quantities, for example, for use in fracking or casting processes. A heat capacity of $c_{p,part}$ = 1200 J/kgK (Siegel et al., 2014) and a particle bulk density of ρ_{part} = 2000 kg/m³ are assumed. For comparison with the curves for the thermochemical materials, the enthalpy curve for bauxite with the above properties is shown in **Figure 3**. A specific particle cost of $C_{sp,part}$ = 1 $/kg is assumed, based on quotations for proppants.

Cobalt-Based Redox Material

For the cobalt-based redox materials, the following reaction is considered:

$$3\,CoO + \frac{1}{2}\,O_2 \leftrightarrow Co_3O_4. \tag{14}$$

The reaction enthalpy is 844 kJ/kg, and the idealized reaction equilibrium temperature is at 900°C (Block and Schmücker, 2016). **Figure 4** shows the idealized enthalpy curve as function of temperature.

Manganese–Iron–Based Redox Material

For the manganese–based redox materials, the following reaction is considered:

$$2\,(Mn_{0.75}Fe_{0.25})_3O_4 + \frac{1}{2}\,O_2 \leftrightarrow 3\,(Mn_{0.75}Fe_{0.25})_2O_3. \tag{15}$$

The advantage of this system vs. the pure manganese oxide redox pair Mn_3O_4/Mn_2O_3 examined in our previous work (Buck

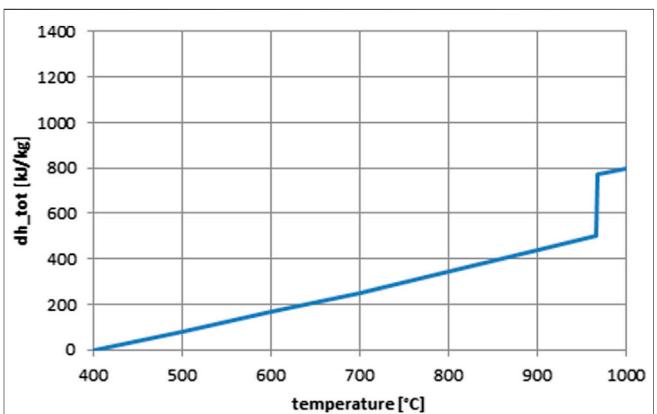

FIGURE 5 | Enthalpy data for manganese–iron–based redox material.

et al., 2020) is that the latter shows a hysteresis between reduction and oxidation, that is, oxidation takes place at about 800°C and reduction happens at about 1,000°C. On the contrary, in the mixed Mn–Fe composition this hysteresis is mitigated (Carrillo et al., 2015), and if the reduced oxide is cooled down slowly enough it can be almost eliminated, so that reduction and oxidation can take place at temperatures very close to each other (Agrafiotis et al., 2015). Hence, a single fixed reaction temperature of 967°C is used in the analysis presented here. The reaction enthalpy of this system is 271 kJ/kg (Preisner et al., 2020). **Figure 5** shows the simplified enthalpy curve as function of temperature used in the system analysis.

Perovskite-Based Redox Material

For the perovskite-based redox materials, the situation is more complex. The Co_3O_4/CoO and $(Mn_{0.75}Fe_{0.25})_3O_4/(Mn_{0.75}Fe_{0.25})_2O_3$ systems considered so far belong to the class of so-called stoichiometric (or phase change) redox oxides (Bulfin et al., 2017a). In such materials, all the cations of the multivalent metal are transformed from the higher to the lower oxidation state during reduction upon heating and vice versa during oxidation upon cooling, at distinct, reduction/oxidation equilibrium temperatures where "abrupt" oxygen release/uptake takes place in a stoichiometric proportion accompanied by the respective weight loss/gain and endothermal/exothermal effects (**Figures 4**, **5**). On the contrary, perovskites–mixed oxides with multivalent cations of the type ABO_3–belong to the class of the so-called non-stoichiometric (or partial reduction or oxygen vacancy) ones. In the materials of this category, the reduction product does not contain all the reducible metal cations at their lower valence state but only a smaller percentage of them. Oxygen is allowed to move through and leave the lattice through the formation of oxygen vacancies without causing phase transformations that induce crystal structure disruption. Substantial fractions of vacancies can be sustained on the oxide ion sites to enable stoichiometries $ABO_{3-\delta}$. Therefore, such materials react via the following scheme, where the extent of partial reduction δ depends on temperature and oxygen partial pressure and is usually much smaller than 1, as given below:

$$ABO_{3-\delta} + \frac{\delta}{2} O_2 \leftrightarrow ABO_3. \quad (16)$$

Furthermore, the oxide reduction reaction has an equilibrium partial pressure of oxygen that changes with temperature. Therefore, upon heating under an initial oxygen partial pressure (e.g., 0.21 bar in the case of air at ambient pressure), the reduction of these materials does not take place at a specific distinct equilibrium temperature but within a wide temperature range: as soon as the onset temperature of this reduction is crossed upon heating, the materials release oxygen in a continuous, quasi-linear mode during further heating. The phenomenon is reversible during cooling/oxidation. The extent of reduction/oxidation and the consequent weight change as well as enthalpy effects depend on the particular temperature and partial pressure of oxygen reached. That is exactly the rationale behind performing the reduction of these materials under very low oxygen partial pressures and their subsequent oxidation under high (oxygen partial) pressures, mentioned in the Introduction section, so that the enthalpy effects recovered during oxidation can be higher than the ones needed during reduction (of course, this scheme has the additional energy penalty of providing the necessary low oxygen partial pressure).

However, in this framework, the reduction/oxidation reaction enthalpies are also absorbed/released in a similar gradual matter with increasing/decreasing temperature. Therefore—unless any other exothermic/endothermic phenomena like for example, relevant to phase transformations take place, which is sometimes the case—the respective enthalpy–temperature plot for these materials will not be characterized by a vertical "step" at the reduction onset temperature like these of the cobalt and manganese–iron oxides in **Figures 4**, **5**, but it should rather be conceived as a continuous "quasi-linear" enhancement of the material's sensible heat capacity that augments the overall amount of energy stored (sensible + thermochemical) beyond this onset temperature (e.g., Albrecht et al., 2016). The magnitude of this "enhancement" as already argued, depends naturally on the material's composition and the actual reduction procedure followed. In this respect, in the quest for materials with higher reducibility, many literature studies follow an approach based on thermodynamic modeling of the extent of reduction δ for a specific material composition as a function of temperature and oxygen partial pressure, complemented by thermogravimetric analysis/differential scanning calorimetry (TGA/DSC) experiments to determine equilibrium values, that either through the van't Hoff (Mastronardo et al., 2020) or through point defects (oxygen vacancies) equilibrium approach (Bulfin et al., 2017b; Albrecht et al., 2018), produce P-T-δ relationships as charts of isothermal or isobaric or "iso-δ" curves. Parametric studies with respect to the kind and the quantity of the dopant elements can then identify optimal material compositions and respective conditions for a given (or maximum possible) reduction extent, δ. Following the relevant work in redox-oxide–based thermochemical water splitting, the first targeted perovskite families were lanthanum manganites, $LaMnO_3$ (LM) doped with strontium, cobalt, and iron (Babiniec et al., 2015). However, more recent studies seem to converge to that calcium manganite; $CaMnO_3$ (CM)-based perovskites are more promising in thermochemical storage applications, on the one hand due to their more suitable thermodynamic properties and on the other hand due to the lower cost and higher earth-abundance of the constituent elements (Bulfin et al., 2017b; Jackson et al., 2019; Babiniec et al., 2016; Babiniec et al., 2020, Mastronardo et al., 2020).

In the vast majority of these thermodynamic studies, even though the temperature range span corresponds to that to be encountered in a solar thermal power tower plant (i.e., from 400–500°C up to 1,100–1,300°C), the respective pressure range usually spans very low oxygen partial pressures (from 0.21 down to 10^{-2} or 10^{-4} atm). Hence, the calculated reduction enthalpies presumably to be recovered through oxidation cited therein, usually correspond to an extent of δ achievable only under very low oxygen partial pressures. The same holds true for many "perovskite

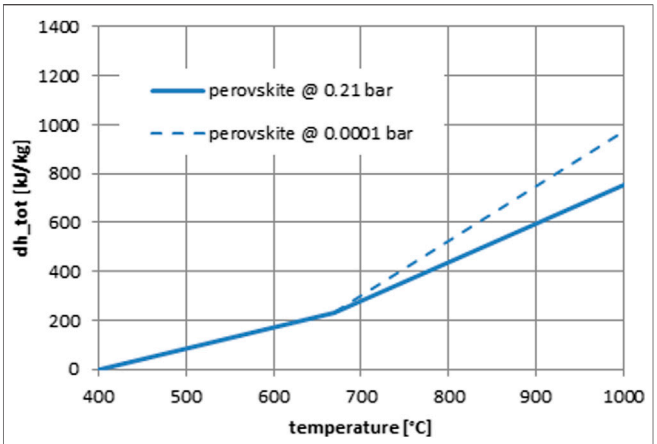

FIGURE 6 | Enthalpy data for perovskite redox material.

materials screening" small-scale experimental studies aimed at quantifying these parameters, that is, weight loss, δ, and reduction enthalpy as a function of operating temperature and oxygen partial pressure, usually through TGA/DSC mentioned above: reduction is performed under reduced oxygen partial pressure, equilibrium is achieved, and then reoxidation is implemented via a stream of much higher oxygen partial pressure.

In our case, for an objective comparison among plants operating under the same boundary conditions, like for example, an open-air particle receiver, data for the reduction of perovskites under ambient air atmosphere has to be employed. For a first comparison among the systems considered in this study, we selected the widely studied for TCS applications material composition $CaMnO_3$ and the very relevant to that doped with a small amount of strontium $Ca_{0.9}Sr_{0.1}MnO_{3-\delta}$. The specific heat capacity of this compound is known and the thermodynamically calculated enthalpy of reduction had the reduction taken place at an oxygen partial pressure of 0.0001 bar and a final temperature of 1,000°C which can be considered as an upper practical limit with today's technology, has been calculated as 455 kJ/kg (Imponenti et al., 2017). Furthermore, the temperature at which the material starts to release oxygen upon heating under air is around 670 °C (Agrafiotis et al., 2019), and a reduction enthalpy under air has been reported as 240 kJ/kg in a recent study (Yilmaz et al., 2021). Based on this data, **Figure 6** shows the respective enthalpy curves for the two cases, reduction under low oxygen partial pressure and under air, as function of temperature. The fit function for the latter case has been used in the system analysis.

Since the extend of reduction δ, depends on the temperature and partial oxygen pressure, under the conditions considered, that is, reduction temperature of 1,000°C, δ varies between 0.34 and 0.09 for an oxygen partial pressure ranging between 10^{-55} and 1 (as can be read from the isothermal curves on a δ vs. P chart like the ones mentioned above, and in the study by Imponenti et al. (2017). For the particular case selected in the present study for oxidation with air, δ = 0.13.

RESULTS AND DISCUSSION

Table 1 summarizes the relevant properties of the considered materials and the consequences for the storage system. The data is based on the total storage capacity of 3.490 GWh, excess particle material is not included here, only the values for a fully charged storage are given.

The bulk density of the cobalt and perovskite oxide materials was calculated from the pure material density from the study by Jackson et al. (2019) assuming a packing density of 64%.

From the thermophysical data point of view, the cobalt-based material is clearly advantageous. This material leads to significantly reduced storage mass and quite small storage volume. For the manganese–iron–based material, the additional reaction enthalpy is largely offset by the low specific heat capacity and bulk density, so in the end the storage mass is only slightly less than the bauxite reference, and storage volume is even higher. The perovskite material shows about 5% advantage for mass and about 34% advantage for volume, compared to bauxite.

The results of the analysis show that some redox materials can significantly reduce the required storage mass and volume, while others lead only to a marginal improvement. More important than these effects is the impact on LCOE which is affected by the particle cost and other material-dependent cost factors. As no reliable cost information is currently available for mass-produced thermochemically active particles, the particle break-even cost is evaluated for each material.

The system cost consists of fixed and material-dependent contributions. Fixed cost items of the solar power plant are as follows:

- heliostat field: 104.8 M€ (12,166 heliostats)
- tower: 56.35 M€
- receiver: 26.75 M€
- power cycle excl. steam generator: 87.5 M€

Material-dependent contributions are listed in **Table 2**, together with the particle break-even cost to achieve the same LCOE as the reference case.

It should be noted here that a high particle break-even cost is an advantage, meaning that high material cost is allowable while still achieving the same LCOE as the reference system. In consequence, the particle inventory cost can be relatively high in this case since it is based on the high particle break-even cost.

The main findings from the results are as follows:

- for cobalt-based materials: storage mass and storage volume are significantly reduced, as well as the size of the steam generator. This results in reductions in steam generator and the storage containment cost. For breakeven the specific particle cost can be about 6x higher than for bauxite materials, significantly increasing the particle inventory cost. However, it is expected that cobalt-based materials are even more expensive than the break-even cost, making this material unattractive.

TABLE 1 | Comparison of thermophysical properties of considered materials (values from: [a][Jackson et al., 2019], [b][Wokon et al., 2017b], [c][Imponenti et al., 2017], [d][Yilmaz et al., 2021], [e][Preisner et al., 2018]).

		Bauxite	Cobalt	Manganese-iron	Perovskite
Avg. specific heat capacity	[kJ/kgK]	1.2	0.86[a]	0.88[a]	0.86[a]
sensible heat 400–1,000°C	[kJ/kg]	720	516	528	516
Reaction enthalpy	[kJ/kg]	0	844[a]	271[b]	240[d] (P_{O2} = 0.21 bar) 455[c] (P_{O2} = 0.0001 bar)
Total enthalpy difference	[kJ/kg]	779	1,360	799	756 (P_{O2} = 0.21 bar)
Volumetric enthalpy difference	[MJ/m³]	1,558	5,318	1,230	2,192
Ratio R_{tc} (**Eq. 3**)	[-]	1.00	2.64	1.51	1.47
Bulk density	[kg/m³]	2000	3910[a]	1539[b]	2899[a]
storage mass	[t]	17,442	9,234	15,717	16,611
storage volume	[m³]	10,902	2,951	12,765	7,162

TABLE 2 | Cost contributions and the particle break-even cost of considered materials.

		Bauxite	Cobalt	Manganese-iron	Perovskite
LCOE	[€/MWh]	64.9	64.9	64.9	64.9
Total system cost	[M€]	435.5	436.5	435.7	435.6
Steam generator area	[m²]	4,044	1,534	2,672	2,760
Steam generator cost	[M€]	31.9	16.84	24.29	24.82
Particle inventory cost	[M€]	15.45	52.99	19.55	31.35
Particle inventory cost share		3.5%	12.1%	4.5%	7.2%
storage containment cost	[M€]	28.87	12,08	32.07	21.82
specific storage cost	[€/kWh]	12.7	18.7	14.8	15.2
Particle lift cost	[M€]	5.99	4.58	5.70	5.85
Particle ground transport cost	[M€]	5.23	1.86	6.08	3.76
Particle break-even cost	[€/kg]	0.844	5.465	1.184	1.798

- for manganese–iron–based materials: storage volume and total storage cost are increased while steam generator cost is decreased. The particle break-even cost is about 1.4x higher than that for bauxite materials.
- for perovskite materials: storage volume and the storage containment cost are reduced as well as the steam generator cost. The particle inventory cost is increased with the particle break-even cost that is about 2.1x higher than that for bauxite materials.
- changes in the transportation cost have only a minor impact on the system cost and LCOE.

Since several aspects of the redox systems are not well known yet, the analysis is based on several simplifications that need to be validated by future work. The evaluation is considered optimistic for the following reasons:

- reaction kinetics are neglected in the analysis. The effects of reaction kinetics will reduce the benefit from thermochemically active particles in two ways:
  - o larger steam generators will be required than assumed in the above analysis, the cost of the steam generator will increase.
  - o the reaction extent might be lower than equilibrium conditions
- additional plant equipment required for the reactive system is not considered (air loop, recuperator, and blower); these components will also introduce additional parasitic power consumption and thermal losses from the hot air stream.

In that sense, the determined particle break-even cost is considered as an indication for particle selection. Only those particle materials that can be mass-produced at cost lower than the break-even cost should be further considered. Using cost assumptions for the raw materials, especially the perovskite materials seem to be promising candidates for future work.

CONCLUSION

In the techno-economic system analysis three candidate redox materials were analyzed for their cost reduction potential: cobalt-based, manganese–iron–based, and perovskite-based oxide materials. These cases were compared to a reference process using inert bauxite particles (sensible-only storage). A solar thermal power plant, consisting of 14 identical solar tower modules with a central power block, with a nominal power of 125 MW_e and a storage capacity of 12 h was considered for the analysis. For each storage material a plant layout was made, taking the specific aspects of the material into account: density, reaction enthalpy, and heat capacity. Simplifying assumptions were made for the impact of temperature stabilization in the heat exchanger, due to the ongoing chemical reaction. For each of the redox material options a particle break-even cost was determined, leading to the same LCOE than with bauxite particles. Cost

factors mainly influenced by the material selection are the storage cost and the steam generator cost. The particle transport system cost has only a minor impact. The results show differences in the characteristics of the materials, with significant reduction on storage size and steam generator cost for example for the cobalt-based particles. However, not all redox materials have advantages regarding storage size, as for example for the manganese–iron–based particles the storage size is even increased due to the combination of thermophysical properties with low specific heat capacity. Regarding the economic potential of the candidate redox materials the perovskite particles seem to have advantages, as they can be in principle produced from inexpensive raw materials. It is therefore recommended to focus future research and development work on this material class.

For the impact of the thermochemically active particles the study uses assumptions that might be too optimistic, for example, neglecting reaction kinetics and the estimated reduction of the heat exchanger area. Detailed heat exchanger design and modeling is required to improve the accuracy of predictions.

DATA AVAILABILITY STATEMENT

The raw data supporting the conclusion of this article will be made available by the authors, without undue reservation.

AUTHOR CONTRIBUTIONS

Conceptualization, RB; methodology, RB; software, RB; validation, RB, material investigation, ST, CA, NN, and MS; writing—original draft preparation, RB, CA; writing—review and editing, ST, NN, CA, and MS; visualization, RB; project administration, ST.

FUNDING

This research was made using institutional funding from DLR. Part of the work concerning the perovskite systems was supported by the European Commission through the project "Perovskites as 'oxygen-carriers' in solar-powered redox processes for synthetic fuels production and energy storage (PERFECTION)" in the framework of the EU-ERANETMED2-72-379 Call.

ACKNOWLEDGMENTS

The authors acknowledge the support of Gregory Jackson (Colorado School of Mines, Golden, CO/United States) for providing thermophysical data for the perovskite material. The content of this manuscript has been presented in part at the SolarPACES Conference 2019 (Buck and Giuliano, 2019).

REFERENCES

Agrafiotis, C., Pein, M., Giasafaki, D., Tescari, S., Roeb, M., and Sattler, C. (2019). Redox Oxides-Based Solar Thermochemistry and its Materialization to Reactor/Heat Exchanger Concepts for Efficient Solar Energy Harvesting, Transformation and Storage. *ASME. J. Sol. Energ. Eng.* 141 (2), 021010. doi:10.1115/1.4042226

Agrafiotis, C., Tescari, S., Roeb, M., Schmücker, M., and Sattler, C. (2015). Exploitation of Thermochemical Cycles Based on Solid Oxide Redox Systems for Thermochemical Storage of Solar Heat. Part 3: Cobalt Oxide Monolithic Porous Structures as Integrated Thermochemical Reactors/heat Exchangers. *Solar Energy* 114, 459–475. doi:10.1016/j.solener.2014.12.037

Albrecht, K. J., Jackson, G. S., and Braun, R. J. (2018). Evaluating Thermodynamic Performance Limits of Thermochemical Energy Storage Subsystems Using Reactive Perovskite Oxide Particles for Concentrating Solar Power. *Solar Energy* 167, 179–193. doi:10.1016/j.solener.2018.03.078

Albrecht, K. J., Jackson, G. S., and Braun, R. J. (2016). Thermodynamically Consistent Modeling of Redox-Stable Perovskite Oxides for Thermochemical Energy Conversion and Storage. *Appl. Energ.* 165, 285–296. doi:10.1016/j.apenergy.2015.11.098

Babiniec, S. M., Ambrosini, A., Coker, E. N., and Miller, J. E. (2020). Redox-active Oxide Materials for thermal Energy Storage. US patent US2020/0048106 A1.

Babiniec, S. M., Coker, E. N., Miller, J. E., and Ambrosini, A. (2015). Investigation of La Sr1−Co M1−O3− (M = Mn, Fe) Perovskite Materials as Thermochemical Energy Storage media. *Solar Energy* 118, 451–459. doi:10.1016/j.solener.2015.05.040

Babiniec, S. M., Miller, J. E., Ambrosini, A., Stechel, E. B., Coker, E. N., Loutzenhiser, P. G., et al. (2016). Considerations for the Design of a High-Temperature Particle Reoxidation Reactor for Extraction of Heat in Thermochemical Energy Storage Systems. Proceedings of the ASME 10th International Conference on Energy Sustainability ES2016, Charlotte, North Carolina, ES2016–59646. June 26–30, 2016. doi:10.1115/es2016-59646

Baumann, T., and Zunft, S. (2014). *Eurotherm Seminar #99–Advances in Thermal Energy Storage* 28. Lleida, Spain. 978 84 697 0467 7. 05.-30.05.2014. Experimental Investigation on a Moving Bed Heat Exchanger Used for Discharge of a Particle-Based TES for CSP.

Block, T., and Schmücker, M. (2016). Metal Oxides for Thermochemical Energy Storage: A Comparison of Several Metal Oxide Systems. *Solar Energy* 126, 195–207. doi:10.1016/j.solener.2015.12.032

Buck, R., and Giuliano, S. (2019). Solar Tower System Temperature Range Optimization for Reduced LCOE. *AIP Conf. Proc.* 2126, 030010. doi:10.1063/1.5117522

Buck, R., Tescari, S., Schmücker, M., Preisner, N., and Agrafiotis, C. (2020). Techno-Economic Analysis of Thermochemical Storage for CSP Systems. *AIP Conf. Proc.* 2303, 200002. doi:10.1063/5.0028904

Bulfin, B., Vieten, J., Agrafiotis, C., Roeb, M., and Sattler, C. (2017a). Applications and Limitations of Two Step Metal Oxide Thermochemical Redox Cycles; a Review. *J. Mater. Chem. A.* 5, 18951–18966. doi:10.1039/c7ta05025a

Bulfin, B., Vieten, J., Starr, D. E., Azarpira, A., Zachäus, C., Hävecker, M., et al. (2017b). Redox Chemistry of CaMnO3 and Ca0.8Sr0.2MnO3 Oxygen Storage Perovskites. *J. Mater. Chem. A.* 5 (17), 7912–7919. doi:10.1039/c7ta00822h

Carrillo, A. J., Serrano, D. P., Pizarro, P., and Coronado, J. M. (2015). Improving the Thermochemical Energy Storage Performance of the Mn2O3/Mn3O4 Redox Couple by the Incorporation of Iron. *ChemSusChem* 8, 1947–1954.

Ebert, M., Amsbeck, L., Jensch, A., Hertel, J., Rheinländer, J., Trebing, D., et al. (2016). Upscaling, Manufacturing and Test of a Centrifugal Particle Receiver. PowerEnergy2016-59252, Proc. ASME Energy Sustainability Conference 26, 30. June 2016, Charlotte, United States.

Ebert, M., Amsbeck, L., Rheinländer, J., Schlögl-Knothe, B., Schmitz, S., Sibum, M., et al. (2019). Operational Experience of a Centrifugal Particle Receiver Prototype. *AIP Conf. Proc.* 2126, 030018. doi:10.1063/1.5117530

Flamant, G., Gauthier, D., Benoit, H., Sans, J.-L., Garcia, R., Boissière, B., et al. (2013). Dense Suspension of Solid Particles as a New Heat Transfer Fluid for Concentrated Solar thermal Plants: On-Sun Proof of Concept. *Chem. Eng. Sci.* 102, 567–576. doi:10.1016/j.ces.2013.08.051

González-Portillo, L. F., Albrecht, K., and Ho, C. K. (2021). Techno-Economic Optimization of CSP Plants with Free-Falling Particle Receivers. *Entropy* 23, 76. doi:10.3390/e23010076

Imponenti, L., Albrecht, K. J., Wands, J. W., Sanders, M. D., and Jackson, G. S. (2017). Thermochemical Energy Storage in Strontium-Doped Calcium Manganites for Concentrating Solar Power Applications. *Solar Energy* 151, 1–13. doi:10.1016/j.solener.2017.05.010

Jackson, G. S., Imponenti, L., Albrecht, K. J., Miller, D. C., and Braun, R. J. (2019). Inert and Reactive Oxide Particles for High-Temperature thermal Energy Capture and Storage for Concentrating Solar Power. *ASME J. Sol. Energ. Eng.* 141 (2), 021016. doi:10.1115/1.4042128

Khare, S., Dell'Amico, M., Knight, C., and McGarry, S. (2013). Selection of Materials for High Temperature Sensible Energy Storage. *Solar Energ. Mater. Solar Cell* 115, 114–122. doi:10.1016/j.solmat.2013.03.009

Ma, Z., Glatzmaier, G. C., and Mehos, M. (2014). Development of Solid Particle thermal Energy Storage for Concentrating Solar Power Plants that Use Fluidized Bed Technology. *Energ. Proced.* 49, 898–907. doi:10.1016/j.egypro.2014.03.097

Mastronardo, E., Qian, X., CoronadoHaile, J. M. S. M., and Haile, S. M. (2020). The Favourable Thermodynamic Properties of Fe-Doped CaMnO3 for Thermochemical Heat Storage. *J. Mater. Chem. A.* 8, 8503–8517. doi:10.1039/d0ta02031a

Matches Equipment Cost (2018). Available at: http://matche.com/equipcost/Exchanger.html (Accessed 06 22, 2018).

Mehos, M., Turchi, C., Vidal, J., Wagner, M., Ma, Z., Ho, C., et al. (2017). Concentrating Solar Power Gen3 Demonstration Roadmap. NREL/TP-5500-67464, 2017.

Miller, J. E., Ambrosini, A., Babiniec, S. M., Coker, E. N., Ho, C. K., Al-Ansary, H., et al. (2016). High Performance Reduction/oxidation Metal Oxides for Thermochemical Energy Storage (PROMOTES) 2016, Proceedings of the ASME 10th International Conference on Energy Sustainability ES2016, Charlotte, North Carolina, ES2016–59660. June 26–30, 2016. doi:10.1115/es2016-59660

Neises, M., Tescari, S., de Oliveira, L., Roeb, M., Sattler, C., and Wong, B. (2012). Solar-heated Rotary kiln for Thermochemical Energy Storage. *Solar Energy* 86, 3040–3048. doi:10.1016/j.solener.2012.07.012

Preisner, N. C., Block, T., Linder, M., and Leion, H. (2018). Stabilizing Particles of Manganese-Iron Oxide with Additives for Thermochemical Energy Storage. *Energy Technol.* 6 (11), 2154–2165. doi:10.1002/ente.201800211

Preisner, N. C., Bürger, I., Wokon, M., and Linder, M. (2020). Numerical Investigations of a Counter-current Moving Bed Reactor for Thermochemical Energy Storage at High Temperatures. *Energies* 13, 772. doi:10.3390/en13030772

Preisner, N. C., and Linder, M. (2020). A Moving Bed Reactor for Thermochemical Energy Storage Based on Metal Oxides. *Energies* 13, 1232. doi:10.3390/en13051232

Repole, K. K. D., and Jeter, S. M. (2016). Design and Analysis of a High Temperature Particulate Hoist for Proposed Particle Heating Concentrator Solar Power Systems. *ASME Energy Sustainability* 2016. doi:10.1115/ES2016-59619

Schöniger, F., Thonig, R., Resch, G., and Lilliestam, J. (2021). Making the Sun Shine at Night: Comparing the Cost of Dispatchable Concentrating Solar Power and Photovoltaics with Storage. *Energ. Sourc. B: Econ. Plann. Pol.* 16 (1), 55–74. doi:10.1080/15567249.2020.1843565

Schrader, A. J., Bush, H. E., Ranjan, D., and Loutzenhiser, P. G. (2020). Aluminum-doped Calcium Manganite Particles for Solar Thermochemical Energy Storage: Reactor Design, Particle Characterization, and Heat and Mass Transfer Modelling. *Int. J. Heat Mass Transfer* 152, 119461. doi:10.1016/j.ijheatmasstransfer.2020.119461

Schrader, A. J., Muroyama, A. P., and Loutzenhiser, P. G. (2015). Solar Electricity via an Air Brayton Cycle with an Integrated Two-step Thermochemical Cycle for Heat Storage Based on Co3O4/CoO Redox Reactions: Thermodynamic Analysis. *Solar Energy* 118, 485–495. doi:10.1016/j.solener.2015.05.045

Schwarzbözl, P., Pitz-Paal, R., and Schmitz, M. (2009). *Visual HFLCAL–A Software Tool for Layout and Optimisation of Heliostat Fields*. Berlin: Proceedings SolarPACES.

Siegel, N., Gross, M., Ho, C., Phan, T., and Yuan, J. (2014). Physical Properties of Solid Particle thermal Energy Storage media for Concentrating Solar Power Applications. *Energ. Proced.* 49, 1015–1023. doi:10.1016/j.egypro.2014.03.109

Siegel, N. P., Gross, M. D., and Coury, R. (2015). The Development of Direct Absorption and Storage media for Falling Particle Solar central Receivers. *J. Solar Energ. Eng.* 137, 041003. doi:10.1115/1.4030069

Tamme, R., Taut, U., Streuber, C., and Kalfa, H. (1991). Energy Storage Development for Solar thermal Processes. *Solar Energ. Mater.* 24, 386–396. doi:10.1016/0165-1633(91)90077-x

Tescari, S., Singh, A., Agrafiotis, C., de Oliveira, L., Breuer, S., Schlögl-Knothe, B., et al. (2017). Experimental Evaluation of a Pilot-Scale Thermochemical Storage System for a Concentrated Solar Power Plant. *Appl. Energ.* 189, 66–75. doi:10.1016/j.apenergy.2016.12.032

Tescari, S., Sundarraj, P., Moumin, G., Duarte, J. P. R., Agrafiotis, C., de Oliveira, L., et al. (2020). Solar Rotary kiln for Continuous Treatment of Particle Material: Chemical Experiments from Micro to Milli Meter Particle Size. *AIP Conf. Proc.* 2303, 140007. doi:10.1063/5.0029271

Weinrebe, G., von Reeken, F., Wöhrbach, M., Plaz, T., Göcke, V., and Balz, M. (2014). Towards Holistic Power Tower System Optimization. *Energ. Proced.* 49, 1573–1581. doi:10.1016/j.egypro.2014.03.166

Wokon, M., Block, T., Nicolai, S., Linder, M., and Schmücker, M. (2017b). Thermodynamic and Kinetic Investigation of a Technical Grade Manganese-Iron Binary Oxide for Thermochemical Energy Storage. *Solar Energy* 153, 471–485. doi:10.1016/j.solener.2017.05.045

Wokon, M., Kohzer, A., and Linder, M. (2017a). Investigations on Thermochemical Energy Storage Based on Technical Grade Manganese-Iron Oxide in a Lab-Scale Packed Bed Reactor. *Solar Energy* 153, 200–214. doi:10.1016/j.solener.2017.05.034

Wong, B. (2011). *Thermochemical Heat Storage for Concentrated Solar Power*. San Diego, CA: Final Report for the U.S. Department of EnergyU.S.A. Available at: http://www.osti.gov/scitech/biblio/1039304/(Accessed on 03 20, 2021).

Wu, W., Amsbeck, L., Buck, R., Uhlig, R., and Ritz-Paal, R. (2014). Proof of Concept Test of a Centrifugal Particle Receiver. *Energ. Proced.* 49, 560–568. doi:10.1016/j.egypro.2014.03.060

Yilmaz, D., Darwish, E., and Leion, H. (2021). Utilization of Promising Calcium Manganite Oxygen Carriers for Potential Thermochemical Energy Storage Application. *Ind. Eng. Chem. Res.* 60, 1250–1258. doi:10.1021/acs.iecr.0c05182

Zunft, S., Hänel, M., Krüger, M., and Dreißigacker, V. (2014). A Design Study for Regenerator-type Heat Storage in Solar Tower Plants-Results and Conclusions of the HOTSPOT Project. *Energ. Proced.* 49, 1088–1096. doi:10.1016/j.egypro.2014.03.118

Conflict of Interest: The authors declare that the research was conducted in the absence of any commercial or financial relationships that could be construed as a potential conflict of interest.

frontiers in Energy Research

ORIGINAL RESEARCH
published: 06 October 2021
doi: 10.3389/fenrg.2021.748665

Experimental Investigation of a Thermochemical Reactor for High-Temperature Heat Storage via Carbonation-Calcination Based Cycles

*Michael Wild, Lorenz Lüönd and Aldo Steinfeld**

Department of Mechanical and Process Engineering, ETH Zurich, Zurich, Switzerland

We report on the design of a modular, high-temperature thermochemical energy storage system based on endothermic-exothermic reversible gas-solid reactions for application in concentrated solar power and industrial thermal processes. It consists of an array of tubular reactors, each containing an annular packed bed subjected to radial flow, and integrated in series with a thermocline-based sensible thermal energy storage. The calcination-carbonation of limestone, $CaCO_3 \leftrightarrow CaO + CO_2$, is selected as the reversible thermochemical reaction for the experimental demonstration. Synthetized 4.2 mm-mean size agglomerates and 2 mm-mean size granules of CaO with 42 %wt sintering-inhibitor MgO support attained reaction extents of up to 84.0% for agglomerates and 31.9% for granules, and good cycling stability in pressure-swing and temperature-swing thermogravimetric runs. A lab-scale reactor prototype is fabricated and tested with both formulations for 80 consecutive carbonation-calcination cycles at ambient pressure using a temperature-swing mode between 830°C and 930°C. The reactor exhibited stable cyclic operation and low pressure drop, and yielded specific gravimetric and volumetric heat storage capacities of 866 kJ/kg and 322 MJ/m^3 for agglomerates, respectively, and 450 kJ/kg and 134 MJ/m^3 for granules, respectively.

Keywords: thermochemical storage, solar, process heat, calcium looping, reactor

OPEN ACCESS

Edited by:
Alicia Bayon,
Arizona State University, United States

Reviewed by:
Ernesto Mura,
Independent Researcher, Germany
Qiang Liu,
China University of Petroleum, China
Carlos Ortiz,
Loyola Andalusia University, Spain

****Correspondence:***
Aldo Steinfeld
aldo.steinfeld@ethz.ch

Specialty section:
This article was submitted to Process and Energy Systems Engineering, a section of the journal Frontiers in Energy Research

Received: *30 July 2021*
Accepted: *17 September 2021*
Published: *06 October 2021*

Citation:
Wild M, Lüönd L and Steinfeld A (2021) Experimental Investigation of a Thermochemical Reactor for High-Temperature Heat Storage via Carbonation-Calcination Based Cycles. Front. Energy Res. 9:748665. doi: 10.3389/fenrg.2021.748665

INTRODUCTION

Thermal Energy Storage (TES) enables the use of intermittent concentrated solar energy for supplying high-temperature heat round-the-clock to industrial processes and for solar thermal power generation (Glatzmaier, 2011; Henry et al., 2020). The main TES approaches are based on sensible, latent and thermochemical heat, and combinations thereof. Sensible heat storage has been mainly deployed as molten salt (Kuravi et al., 2013) and thermocline based systems (Mostafavi Tehrani et al., 2017; Zanganeh et al., 2012). The latter can be applied to store heat at temperatures

Abbreviations: χ, reaction extent [-]; FS, full-scale; HTF, heat transfer fluid; L, standard liters; MFM, mass flowmeters; MFC, mass flow controllers; SHS, sensible heat storage; TES, thermal energy storage; TCS, thermochemical heat storage; TGA, thermogravimetric analysis.

above 600°C using a packed-bed of rocks with a separate heat transfer fluid (HTF) (Hänchen et al., 2011; Zanganeh et al., 2012). However, thermocline-based concepts inherently suffer from a temperature profile degradation after multiple charging-discharging cycles, leading to an undesired drop in the HTF outflow temperature during discharge (Stekli et al., 2013). Several mitigation strategies have been explored, such as multi-tank arrangements (Roos and Haselbacher, 2021), flow flushing and extraction (Geissbühler et al., 2019), and combined sensible-latent heat storage systems (Zanganeh et al., 2015). In general, current technologies based on sensible and latent heat storage are limited in temperature by materials constraints and in energy storage density by their specific heat capacity and enthalpy of phase change.

Of special interest is the thermochemical heat storage, which makes use of reversible endothermic-exothermic reactions for storing high-temperature heat for long term and with superior energy storage density (Abedin and Rosen, 2011; André and Abanades, 2020; Carrillo et al., 2019; King et al., 2019; Mette et al., 2012; Peng et al., 2017; Yuan et al., 2018). Reactors for thermochemical heat storage using gas-solid reactions can be classified into directly and indirectly irradiated reactors. Directly irradiated reactor concepts use solids directly exposed to concentrated solar radiation, for example in granular flows (Schrader et al., 2020) and rotary kilns (Neises et al., 2012), providing efficient radiative heat transfer directly to the reaction site. In contrast, indirectly irradiated concepts use a separate HTF to transfer the heat into the solids, either by direct contact or via a heat exchanger. A widely applied example in this category are fixed bed reactors, which feature higher volumetric heat storage capacity than particle flows and avoid the complexity of moving particles at high temperatures (Cosquillo Mejia et al., 2020; Criado et al., 2017; Schaube et al., 2013; Schmidt et al., 2014), but at the expense of inferior heat transfer rates. On the other hand, if the reaction chamber is separated from the HTF, the reaction pressure can be controlled independently, enabling control of the reaction equilibrium temperature and, in turn, the reaction rate and the heat release/uptake, thereby allowing for stable outflow temperatures during discharging (Ströhle et al., 2017). This allows to form a simple control loop with the HTF outflow temperature and the reactor pressure. The combination of sensible and thermochemical heat storage also addresses the limited operating temperature range of the thermochemical storage alone (Agrafiotis et al., 2016).

In this study, we present the engineering design of a thermochemical reactor for the combined sensible-thermochemical TES system which features several intriguing advantages such as high specific heat storage capacity and low pressure drop, as well as modularity, scalability, and robustness. A lab-scale reactor prototype was fabricated and tested using the $CaO/CaCO_3$ calcination-carbonation reversible reaction at temperatures around 900°C. The synthesis and characterization of the solid material to avoid sintering and enable cyclic stability is presented. The experimental setup and the performance of the reactor prototype for multiple consecutive cycles are described in detail.

THERMOCHEMICAL REACTOR DESIGN

The combined sensible-thermochemical TES system is depicted in **Figure 1A**. It encompasses two units in series: 1) the sensible heat storage (SHS) unit, which consists of a thermocline-based packed bed of rocks or ceramics subjected to the HTF flow; and 2) the thermochemical heat storage (TCS) unit, which consists of a modular array of stacked tubular reactors arranged in a cross-flow heat exchanger configuration. The TCS unit is positioned downstream of the SHS unit and the HTF is common to both. As the SHS unit has already been extensively studied (Hänchen et al., 2011; Zanganeh et al., 2012), the present study focusses on the design and experimental investigation of the TCS unit–i.e., the thermochemical reactor—for performing a reversible endothermic/exothermic gas-solid dissociation reaction of the form A(s) ↔ B(s) + C(g). Examples are the reduction-oxidation of metal oxides and the calcination-carbonation of metal carbonates (André and Abanades, 2020). In the scope of this investigation, the calcination-carbonation of limestone:

$$CaCO_3 \leftrightarrow CaO + CO_2$$
$$\Delta H^{\circ}_{298K} = 178\ \text{kJ/mol}\ CO_2;\ \Delta G^{\circ} = 0\ \text{at}\ T = 1167\ K$$

was selected as a model reaction among the various screened metal oxides, hydroxides, sulfides, and carbonates (André et al., 2016), because of its safe handling, reasonably fast reaction rates in both directions, operating temperature in the range 800–1,000°C, and additionally because it is a well-known reaction from the cement manufacturing. **Figure 1B** shows the cross-section of a single reactor tube of the TCS unit. It consists of an outer cylindrical shell, an annular packed bed of solid reactants/products $CaO/CaCO_3$, and a concentric porous inner tube permeable to the gaseous reactant/product CO_2. This inner tube has a single gas connection on one side for the inlet/outlet of CO_2, which is transported across the porous tube walls to/from the packed bed. With this arrangement, fluid flow is uniform across the packed bed and the pressure drop is kept low. During heat charging, the reactor is partially evacuated to lower the equilibrium temperature, thereby favouring the endothermic calcination of $CaCO_3$ into CaO, while CO_2 evolved is stored outside the reactor. During discharging, CO_2 is pumped back under higher pressure to the packed bed to increase the equilibrium temperature, thereby favouring the exothermic carbonation of CaO into $CaCO_3$.

MATERIAL SYNTHESIS AND CHARACTERIZATION

Preliminary experimental runs have indicated poor stability of pure $CaCO_3$ during multiple carbonation-calcination cycles due to sintering. Thus, MgO obtained by calcination of magnesium oxalate dihydrate ($MgC_2O_4{\cdot}2H_2O$) precursor at 700°C was applied as sintering inhibitor (Li et al., 2009). Two synthesis methods with identical final composition were employed: a wet-mixed slurry that is dried to form agglomerates, and a drop granulation method to form granules (Gigantino et al., 2020).

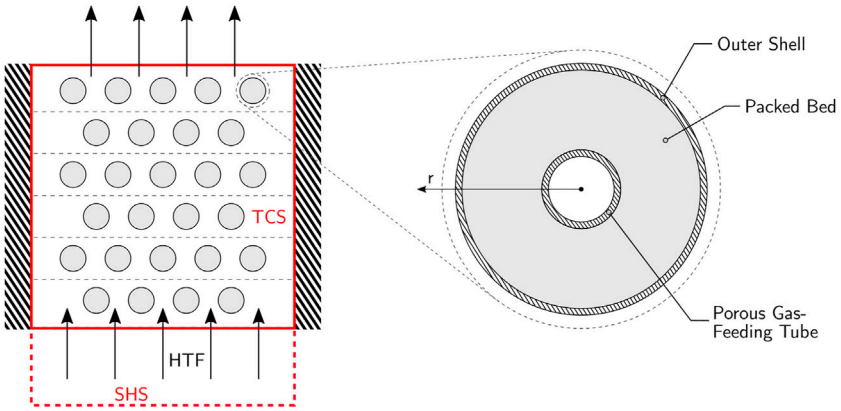

FIGURE 1 | ***Left***: Schematic cross-section of the TES system, comprising a layered thermochemical heat storage (TCS) unit on top of a sensible heat storage (SHS) unit. ***Right***: Schematic cross-section of a single reactor tube of the TCS unit.

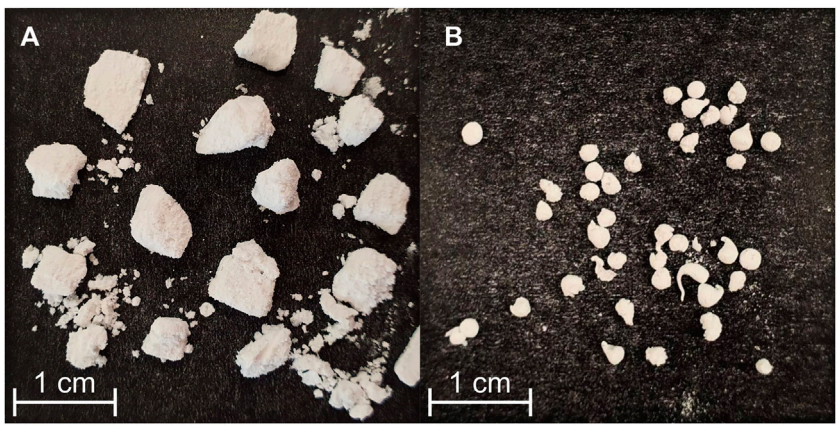

FIGURE 2 | (A) Agglomerates, **(B)** granules.

Agglomerates—Magnesium oxide was mixed with calcium acetate ($Ca(CH_3COO)_2{\cdot}H_2O$), adding 2-propanol and left in a roll-mill overnight to mix thoroughly. The slurry was then air-dried and broken into irregular pieces of 4.2 ± 2.3 mm equivalent diameter of a sphere with the same projected surface, as determined by optical granulometry. Calcination at 800°C for 2 h yielded the final material with a composition of CaO:MgO = 58:42%wt. The synthesized agglomerates have a bulk density of 231 $kg \cdot m^{-3}$ when loosely packed and calcined. Variations in sintering temperature (up to 930°C), precursor preparation, particle size, and mixing method were explored to find an optimally stable material formulation. **Figure 2A** shows a sample of the finished agglomerate.

Granules—Magnesium oxide was mixed with sieved (250 μm) calcium acetate at a ratio of MgO: $Ca(CH_3COO)_2{\cdot}H_2O$ = 1:4.34 by manual shaking. After adding 6.5%wt pore former (150 μm milled carbon fiber), a binder solution containing ethyl cellulose dissolved in *N*-Methyl-2-pyrrolidone was added to form a slurry. Using a syringe with needle diameter of 1.1 mm, the slurry was then manually dropped into a stirred beaker containing demineralized water and a surfactant (Tween 80), from a height of around 50 mm. The resulting granules were air-dried before being calcined under atmospheric gas conditions at 1,260°C for 1 h, allowing for the organic components to burn off. The sintered granules have a composition of CaO:MgO = 58:42%wt (same as agglomerates), a diameter of 1.74 ± 0.35 mm, and bulk density of 205 $kg \cdot m^{-3}$. Pore former contents in the range 0–8.5%wt and sintering temperatures in the range 1,250–1,300°C were also investigated, and the aforementioned values yielded the most stable granules. **Figure 2B** shows a sample of the finished granules.

Performance and cycling stability of both formulations were examined by thermogravimetric analysis (TGA, Netzsch STA 409 CD, flat plate crucible). All TGA experiments were executed with temperature swings between 830°C (carbonation) and 930°C (calcination) under 1 bar CO_2 atmosphere. Plateaus were held for 30 min each, with ramps of 15°C/min between them. **Figure 3** shows the carbonation extent for 30 consecutive carbonation-

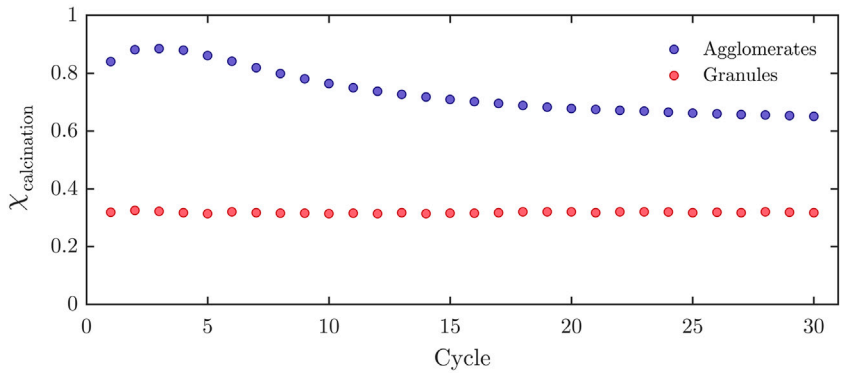

FIGURE 3 | Reaction extents for agglomerates and granules over 30 consecutive carbonation-calcination cycles, performed in the TGA using a temperature-swing between 830°C and 930°C with dwell times of 30 min.

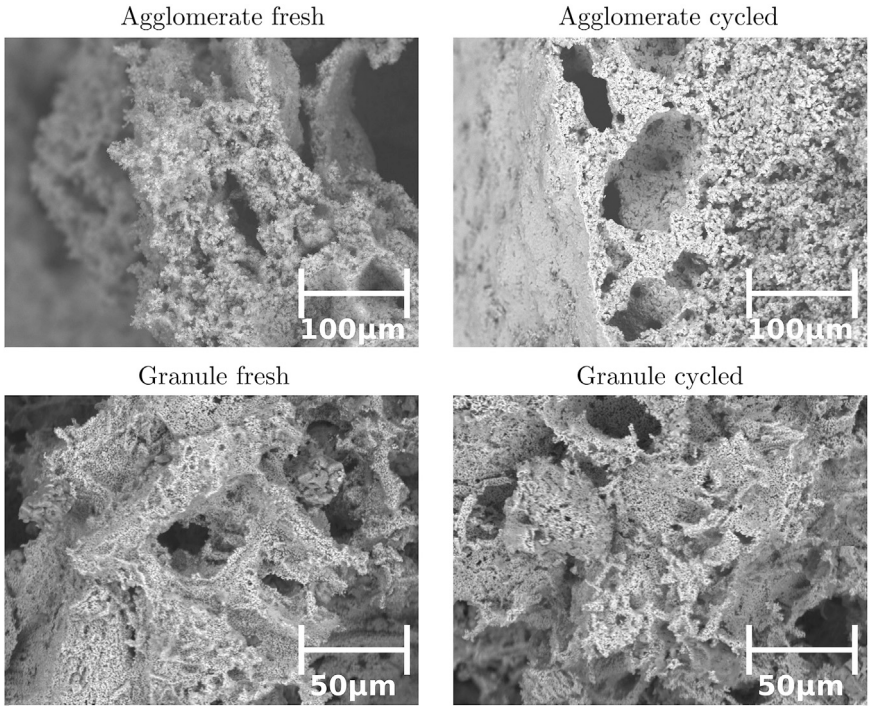

FIGURE 4 | SEM images of agglomerate before **(top left)** and after cycling (**top right**), and granules before **(bottom left)** and after cycling **(bottom right)**.

calcination cycles for both formulations. The reaction extent is defined for each direction as:

$$\chi_{carbonation} = \frac{n_{CaCO_3}}{n_{CaCO_3} + n_{CaO}}, \quad \chi_{calcination} = \frac{n_{CaO}}{n_{CaCO_3} + n_{CaO}} \tag{1}$$

For both formulations, the difference between $\chi_{calcination}$ and $\chi_{carbonation}$ for any given cycle was less than 1.25%, confirming reversibility. However, agglomerates exhibited an initial $\chi_{carbonation}$ = 84.02% which decreased by 22.5% over 30 consecutive cycles. In contrast, the granules exhibited a rather constant reaction extent, initially $\chi_{carbonation}$ = 31.9% which decreased by only 0.49% over 30 consecutive cycles. The degradation in performance of the agglomerates is presumably due to the lower calcination temperature during their synthesis as higher temperatures would break them, which ultimately led to the closing of pores due to sintering during the actual cycling. **Figure 4** shows the SEM images of the agglomerates and granules before and after cycling. It is observed that the boundary of the agglomerate becomes less porous after cycling, while the morphology of the granule remains relatively unchanged.

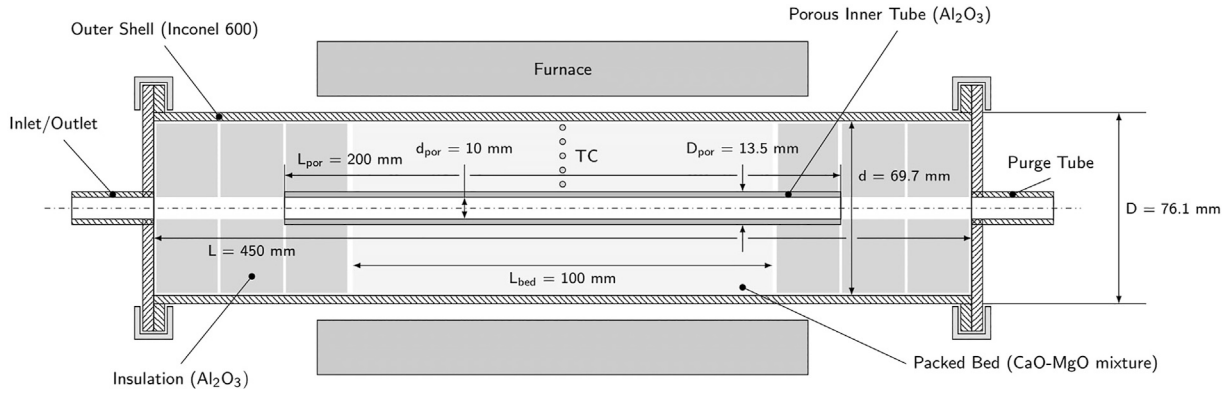

FIGURE 5 | Schematic cross-section of the experimental TCS reactor consisting of an Inconel shell, central porous gas-feeding tube, and annular packed-bed of solid reactants, enclosed by a tubular electric furnace.

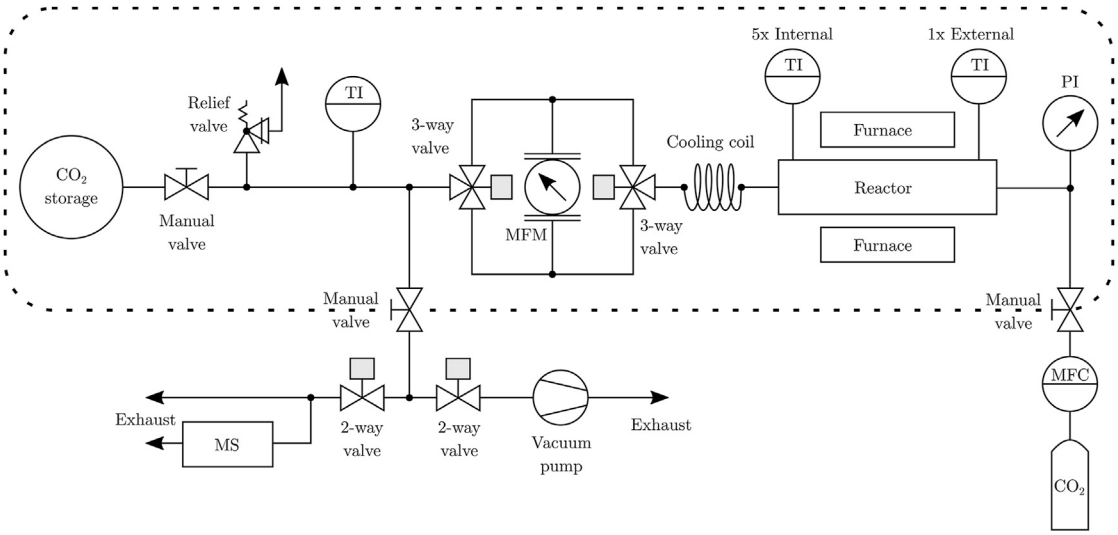

FIGURE 6 | Piping and instrumentation diagram of the experimental setup. The dashed box indicates the system configuration during normal operation.

TCS REACTOR PROTOTYPE AND EXPERIMENTAL SETUP

The lab-scale TCS reactor prototype is schematically shown in **Figure 5**. The main body consists of a 76.1 mm-outer diameter, 3.2 mm-thickness cylindrical shell made of Inconel 600 and a concentric 13.5 mm-outer diameter, 2 mm-thickness porous gas-feeding tube made of alumina (Rauschert Rapor P20). These concentric tubes contain the annular packed bed of reactants with an active volume of 364 cm^3, enclosed on both sides by Al_2O_3 insulation disks which also hold the central tube in place. Blind flanges fixed with clamps close off the reactor on both sides. Steel tubes are welded concentrically in both flanges, connecting the reactor to the rest of the setup. The reactor is placed in a tubular electric furnace (Carbolite HST 12/200) with a homogeneous heating zone of 200 mm. Five K-type thermocouples (DIN 60584-2, Cl. 1, ± 1.5°C) are inserted axially to measure the temperature distribution in the packed bed in the radial direction. They are positioned centrally in longitudinal direction and in a horizontal plane at radii of 10.8, 15.8, 20.8, 25.8 and 30.8 mm from the centerline. Two additional shielded thermocouples measure the reactor shell temperature and the outlet gas temperature.

The piping and instrumentation diagram of the complete experimental setup is shown in **Figure 6**. The experimental procedure starts with purging the reactor by vacuum pumping to 100 mbar followed by perfusing with CO_2 from a gas bottle (purity 99.995%). After reaching ambient pressure, the gas bag (Restek gas sampling bag RT-22968) begins to fill. The gas composition is monitored by mass spectrometery (Pfeiffer OmniStar GSD 320 O1). This purging cycle is to verify that

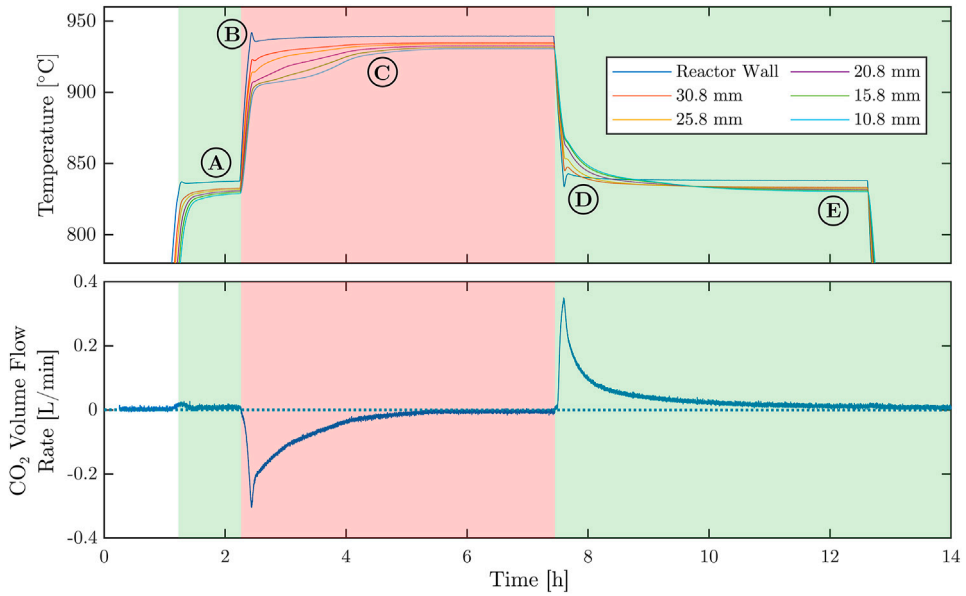

FIGURE 7 | Representative measurement of a single calcination-carbonation cycle for agglomerates, performed in the TCS reactor using a temperature-swing between 830°C and 930°C.

no impurities are left in the system. During normal operation, the manual valves connecting the system to the gas supply and the mass spectrometer/vacuum pump are closed. The furnace then drives the carbonation and calcination cycles. The unidirectional low pressure drop mass flowmeter (Bronkhorst F-201CV, ± 1% FS at 4 Ln/min) is embedded in a valve assembly that ensures that the flow is always in the same direction, independent of the current carbonation/calcination state. The LabView control system detects a state change automatically dependent on mass flow and temperature gradient changes, and switches the 3-way valves accordingly.

The TCS reactor is operated in a temperature-swing mode under ambient pressure CO_2. While the use of a gas bag ensures constant ambient pressure, the pressure in the reactor center is constantly monitored to verify that no significant pressure drop is occurring between the two. In this configuration, the only measured input variable is the prescribed temperature profile within the reactor and the only measured output is the CO_2 mass flow rate in/out of the reactor.

EXPERIMENTAL RESULTS WITH THE TCS REACTOR

Single Cycle—After an initial carbonation step held for 1 h, a single calcination/carbonation cycle was conducted with agglomerates using a temperature swing between 835°C and 935°C at a heating/cooling rate of 15°C/min and holding the temperature (plateaus) for 5 h at each reaction step. The duration of this single cycle was much longer than usual (~35 min) for the purpose of studying the temporal variation of temperatures within the packed bed and the corresponding reaction rates as the reaction extent approaches full completion. **Figure 7** shows the temperatures measured at the reactor wall and within the packed bed (top), and the CO_2 volumetric flow rate (bottom, standard liters per min L/min) as a function of time. Green and red backgrounds indicate the carbonation and calcination steps, respectively. Positive volume flows correspond to CO_2 flow into the reactor during the carbonation step; negative values correspond to the outflow during the calcination step. Five distinct regimes are observed (indicated A–E): A) low volume flow during the first carbonation step because the initial material was mostly already carbonated; B) slight temperature overshoot because of the set point controller of the tubular furnace; C) temperature profiles change because of the endothermic calcination step and approach steady-state as the calcination reaches completion; D) same effect as for regime C but for the subsequent exothermic carbonation; and E) noticeable temperature drop from the reactor wall to the packed bed at approximate steady-state conditions because of heat losses by conduction.

Reactor modelling indicates that the reaction extent is locally approaching chemical equilibrium, such that mass and heat transfer effects are dominating (Wild and Steinfeld, 2021). The relatively slow reaction rates observed are mainly attributed to the poor heat transfer rate of the packed bed, which is predominantly driven by conduction across the porous medium. This rate-controlling mechanism is strongly dependent on the effective thermal conductivity of the packed bed, which in turn depends on the morphology of the solid reactants, and can impose an upper size limitation on the radial thickness of the annular packed bed. As aforementioned, the upscaling foresees the use of an array of tubular reactors, each containing an annular packed bed with radial thickness of comparable magnitude as the one of the prototype reactor.

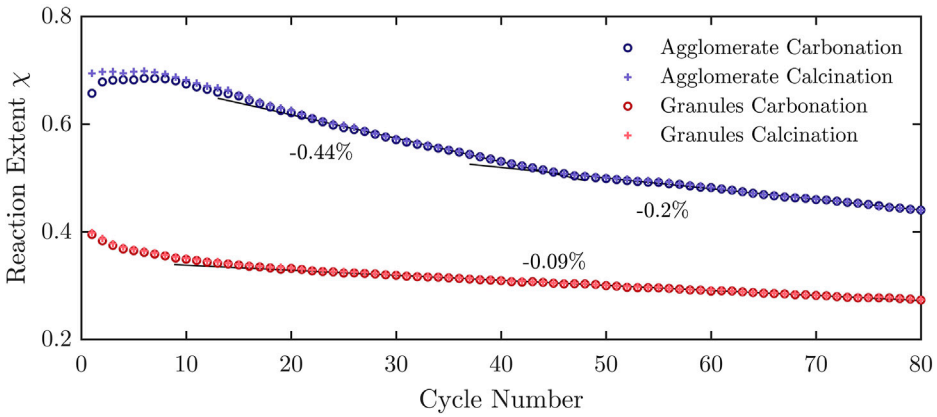

FIGURE 8 | Reaction extents for agglomerates and granules over 80 consecutive carbonation-calcination cycles, performed in the TCS reactor using a temperature-swing between 830°C and 930°C with dwell times of 93 min. Indicated is the linear degradation.

Multiple Cycles—Experimental runs with 80 consecutive carbonation/calcination cycles were conducted for both agglomerates and granules using a temperature swing between 830°C and 930°C with a duration of 93 min for each step. Since shrinking had been observed with the fresh synthetized material, the reactants were cycled for over 80 cycles beforehand. A mass of 133.17 g of agglomerate, and 102.72 g of granules were loaded into the reactor. The theoretical maximum CO_2 volume corresponds to 23.23 and 17.92 L (standard liters), respectively. Gas volumes were used to determine the reaction extent.

Figure 8 shows the measured carbonation and calcination reaction extents for both formulations. Similar to the TG runs, the mean difference between $\chi_{calcination}$ and $\chi_{carbonation}$ was 0.57% for agglomerates and 0.41% for granules, confirming reversibility. However, for the agglomerates, a linear degradation by about 0.44% per cycle is observed from cycle #15 to #45 and by 0.2% per cycle from cycle #45 to #80. The reaction extent decreased from a maximum $\chi_{calcination}$ = 68.5% for cycle #6, corresponding to a measured uptake/release CO_2 volume of 15.91 L, to a minimum $\chi_{calcination}$ = 44.1% for cycle #80, corresponding to 10.27 L CO_2. Clearly, the granules exhibited superior cyclic stability but still some degradation by about 0.09% per cycle, from the initial maximum $\chi_{calcination}$ = 39.5% for cycle #1, corresponding to 7.08 L CO_2, to $\chi_{calcination}$ = 27.4% for cycle #80, corresponding to 4.92 L CO_2. Thus, over 80 consecutive cycles, the degradation observed was 35.4% for agglomerates and 30.4% for granules.

Based on the maximal CO_2 volumes measured, the calculated specific gravimetric and volumetric heat storage capacities were 866 kJ/kg and 322 MJ/m^3 for agglomerates, respectively, and 450 kJ/kg and 134 MJ/m^3 for granules, respectively. The higher energy densities of the agglomerates (both volumetric and gravimetric) came at the cost of poor stability over consecutive cycles. The granules exhibited very good cycling stability over 30 consecutive cycles in the TGA, but degradation was observed over 80 consecutive cycles in the reactor. This is attributed primarily to heat and mass transfer effects in the packed bed reactor vis-a-vis a single layer of granules and shorter cycle duration in the TGA. These detrimental effects could be mitigated under pressure-swing isothermal operation.

An upper limit to the pressure drop in radial direction across the packed bed was calculated based on Darcy's law using values of permeability $\kappa = 4.086 \cdot 10^{-13}$ m^2 and $\kappa_I = 5.675 \cdot 10^{-8}$ kg $\cdot$ Pa$^{-1} \cdot$ s^{-2} determined in a separate experiment. Assuming radial velocity of 0.0017 m/s at the inner boundary of the packed bed (corresponding to the highest measured values of the mass flow rate at 0.42 L/min), the maximum pressure drop for agglomerates over the complete bed is 31 mbar, confirming the low pressure drop for this radial flow configuration of the TCS reactor.

SUMMARY AND CONCLUSION

We have designed a thermochemical reactor for the storage of high-temperature process heat using a reversible reaction of the form A(s) ↔ B(s) + C(g) which can be particularly applied to metal oxides, hydroxides, sulfides, and carbonates. The CaO carbonation - $CaCO_3$ calcination reaction was selected as model reaction. To prevent sintering CaO:MgO = 58:42%wt was synthetized in the form of agglomerates and granules. As proof-of-concept, we have fabricated a lab-scale single-tube reactor prototype and demonstrated its operation for 80 consecutive cycles in a 830–930°C temperature-swing mode. The cyclic stability for granules was clearly superior than that for agglomerates. The experimental data obtained has been used to validate a heat and mass transfer numerical model for design optimization (Wild and Steinfeld, 2021). The TCS reactor is modular and scalable in a cross-flow heat exchanger configuration, can be operated in both temperature-swing and pressure-swing cyclic modes, and can be combined in series with a thermocline-based sensible heat storage. When applied to store concentrated solar heat, it enables the decarbonization of several key energy-intensive industrial processes such as metallurgical processing and cement manufacturing, as well as the efficient thermal production of solar power and fuels.

DATA AVAILABILITY STATEMENT

The raw data supporting the conclusion of this article will be made available by the authors, without undue reservation.

AUTHOR CONTRIBUTIONS

MW and AS conceived the process and associated thermochemical reactor; MW and LL synthetized the materials, executed the experiments, and processed the experimental data; AS supervised the project; all authors contributed to the writing of the manuscript.

FUNDING

We gratefully acknowledge the financial support by the Swiss National Science Foundation (Project No. 173438).

ACKNOWLEDGMENTS

We thank Philipp Haueter, Marco Gigantino, Brendan Bulfin, Thomas Frei, Simon Meier, Paul Leudet de Vallée, and Julian Urech for the technical support with the material synthesis, experimental setup and experimental campaign.

REFERENCES

Abedin, A. H., and Rosen, M. A. (2011). A Critical Review of Thermochemical Energy Storage Systems. *Torej* 4, 42–46. doi:10.2174/1876387101004010042

Agrafiotis, C., Roeb, M., and Sattler, C. (2016). Exploitation of Thermochemical Cycles Based on Solid Oxide Redox Systems for Thermochemical Storage of Solar Heat. Part 4: Screening of Oxides for Use in Cascaded Thermochemical Storage Concepts. *Solar Energy* 139, 695–710. doi:10.1016/j.solener.2016.04.034

André, L., Abanades, S., and Flamant, G. (2016). Screening of Thermochemical Systems Based on Solid-Gas Reversible Reactions for High Temperature Solar thermal Energy Storage. *Renew. Sust. Energ. Rev.* 64, 703–715. doi:10.1016/j.rser.2016.06.043

André, L., and Abanades, S. (2020). Recent Advances in Thermochemical Energy Storage via Solid-Gas Reversible Reactions at High Temperature. *Energies* 13, 5859. doi:10.3390/en13225859

Carrillo, A. J., González-Aguilar, J., Romero, M., Coronado, J. M., Gonzaléz-Aguilar, J., Romero, M., et al. (2019). Solar Energy on Demand: A Review on High Temperature Thermochemical Heat Storage Systems and Materials. *Chem. Rev.* 119, 4777–4816. doi:10.1021/acs.chemrev.8b00315

Cosquillo Mejia, A., Afflerbach, S., Linder, M., and Schmidt, M. (2020). Experimental Analysis of Encapsulated CaO/Ca(OH)2 Granules as Thermochemical Storage in a Novel Moving Bed Reactor. *Appl. Therm. Eng.* 169, 114961. doi:10.1016/j.applthermaleng.2020.114961

Criado, Y. A., Huille, A., Rougé, S., and Abanades, J. C. (2017). Experimental Investigation and Model Validation of a CaO/Ca(OH)2 Fluidized Bed Reactor for Thermochemical Energy Storage Applications. *Chem. Eng. J.* 313, 1194–1205. doi:10.1016/j.cej.2016.11.010

Geissbühler, L., Mathur, A., Mularczyk, A., and Haselbacher, A. (2019). An Assessment of Thermocline-Control Methods for Packed-Bed thermal-energy Storage in CSP Plants, Part 1: Method Descriptions. *Solar Energy* 178, 341–350. doi:10.1016/j.solener.2018.12.015

Gigantino, M., Sas Brunser, S., and Steinfeld, A. (2020). High-Temperature Thermochemical Heat Storage via the CuO/Cu2O Redox Cycle: From Material Synthesis to Packed-Bed Reactor Engineering and Cyclic Operation. *Energy Fuels* 34, 16772–16782. doi:10.1021/acs.energyfuels.0c02572

Glatzmaier, G. (2011). *Summary Report for Concentrating Solar Power Thermal Storage Workshop: New Concepts and Materials for Thermal Energy Storage and Heat-Transfer Fluids*, 2011.

Hänchen, M., Brückner, S., and Steinfeld, A. (2011). High-temperature thermal Storage Using a Packed Bed of Rocks - Heat Transfer Analysis and Experimental Validation. *Appl. Therm. Eng.* 31, 1798–1806. doi:10.1016/j.applthermaleng.2010.10.034

Henry, A., Prasher, R., and Majumdar, A. (2020). Five thermal Energy Grand Challenges for Decarbonization. *Nat. Energ.* 5, 635–637. doi:10.1038/s41560-020-0675-9

King, K., Randhir, K., Petrasch, J., and Klausner, J. (2019). Enhancing Thermochemical Energy Storage Density of Magnesium-manganese Oxides. *Energy Storage* 1. doi:10.1002/est2.83

Kuravi, S., Trahan, J., Goswami, D. Y., Rahman, M. M., and Stefanakos, E. K. (2013). Thermal Energy Storage Technologies and Systems for Concentrating Solar Power Plants. *Prog. Energ. Combustion Sci.* 39, 285–319. doi:10.1016/j.pecs.2013.02.001

Li, L., King, D. L., Nie, Z., and Howard, C. (2009). Magnesia-Stabilized Calcium Oxide Absorbents with Improved Durability for High Temperature CO2 Capture. *Ind. Eng. Chem. Res.* 48, 10604–10613. doi:10.1021/ie901166b

Mette, B., Kerskes, H., and Drück, H. (2012). Concepts of Long-Term Thermochemical Energy Storage for Solar thermal Applications - Selected Examples. *Energ. Proced.* 30, 321–330. doi:10.1016/j.egypro.2012.11.038

Mostafavi Tehrani, S. S., Taylor, R. A., Nithyanandam, K., and Shafiei Ghazani, A. (2017). Annual Comparative Performance and Cost Analysis of High Temperature, Sensible thermal Energy Storage Systems Integrated with a Concentrated Solar Power Plant. *Solar Energy* 153, 153–172. doi:10.1016/j.solener.2017.05.044

Neises, M., Tescari, S., de Oliveira, L., Roeb, M., Sattler, C., and Wong, B. (2012). Solar-heated Rotary kiln for Thermochemical Energy Storage. *Solar Energy* 86, 3040–3048. doi:10.1016/j.solener.2012.07.012

Peng, X., Root, T. W., and Maravelias, C. T. (2017). Storing Solar Energy with Chemistry: the Role of Thermochemical Storage in Concentrating Solar Power. *Green. Chem.* 19, 2427–2438. doi:10.1039/c7gc00023e

Roos, P., and Haselbacher, A. (2021). Thermocline Control through Multi-Tank thermal-energy Storage Systems. *Appl. Energ.* 281, 115971. doi:10.1016/j.apenergy.2020.115971

Schaube, F., Kohzer, A., Schütz, J., Wörner, A., and Müller-Steinhagen, H. (2013). De- and Rehydration of Ca(OH)2 in a Reactor with Direct Heat Transfer for Thermo-Chemical Heat Storage. Part A: Experimental Results. *Chem. Eng. Res. Des.* 91, 856–864. doi:10.1016/j.cherd.2012.09.020

Schmidt, M., Szczukowski, C., Roßkopf, C., Linder, M., and Wörner, A. (2014). Experimental Results of a 10 kW High Temperature Thermochemical Storage Reactor Based on Calcium Hydroxide. *Appl. Therm. Eng.* 62, 553–559. doi:10.1016/j.applthermaleng.2013.09.020

Schrader, A. J., Schieber, G. L., Ambrosini, A., and Loutzenhiser, P. G. (2020). Experimental Demonstration of a 5 kWth Granular-Flow Reactor for Solar Thermochemical Energy Storage with Aluminum-Doped Calcium Manganite Particles. *Appl. Therm. Eng.* 173, 115257. doi:10.1016/j.applthermaleng.2020.115257

Stekli, J., Irwin, L., and Pitchumani, R. (2013). Technical Challenges and Opportunities for Concentrating Solar Power with Thermal Energy Storage. *Therm. Sci. Eng. Appl.* 5, 021011. doi:10.1115/1.4024143

Ströhle, S., Haselbacher, A., Jovanovic, Z. R., and Steinfeld, A. (2017). Upgrading Sensible-Heat Storage with a Thermochemical Storage Section Operated at Variable Pressure: An Effective Way toward Active Control of the Heat-Transfer Fluid Outflow Temperature. *Appl. Energ.* 196, 51–61. doi:10.1016/j.apenergy.2017.03.125

Wild, M., and Steinfeld, A. (2021). A Thermochemical Energy Storage Reactor Model - Code Formulation, Verification, and Experimental Validation. In Proceedings of the CHT-21 International Symposium on Advances in Computational Heat Transfer. Rio de Janeiro, Brazil, Aug, 15–19.

Yuan, Y., Li, Y., and Zhao, J. (2018). Development on Thermochemical Energy Storage Based on CaO-Based Materials: A Review. *Sustainability* 10, 2660. doi:10.3390/su10082660

Zanganeh, G., Khanna, R., Walser, C., Pedretti, A., Haselbacher, A., and Steinfeld, A. (2015). Experimental and Numerical Investigation of Combined Sensible-Latent Heat for thermal Energy Storage at 575°C and above. *Solar Energy* 114, 77–90. doi:10.1016/j.solener.2015.01.022

Zanganeh, G., Pedretti, A., Zavattoni, S., Barbato, M., and Steinfeld, A. (2012). Packed-bed thermal Storage for Concentrated Solar Power - Pilot-Scale Demonstration and Industrial-Scale Design. *Solar Energy* 86, 3084–3098. doi:10.1016/j.solener.2012.07.019

Conflict of Interest: The authors declare that the research was conducted in the absence of any commercial or financial relationships that could be construed as a potential conflict of interest.

Publisher's Note: All claims expressed in this article are solely those of the authors and do not necessarily represent those of their affiliated organizations, or those of the publisher, the editors and the reviewers. Any product that may be evaluated in this article, or claim that may be made by its manufacturer, is not guaranteed or endorsed by the publisher.

frontiers in Energy Research

BRIEF RESEARCH REPORT
published: 22 October 2021
doi: 10.3389/fenrg.2021.750600

Computationally Accelerated Discovery and Experimental Demonstration of $Gd_{0.5}La_{0.5}Co_{0.5}Fe_{0.5}O_3$ for Solar Thermochemical Hydrogen Production

OPEN ACCESS

Edited by:
Alicia Bayon,
Arizona State University, United States

Reviewed by:
Matteo Fasano,
Polytechnic University of Turin, Italy
Krishna Kamol Ghose,
University of New South Wales Canberra, Australia

***Correspondence:**
Eric N. Coker
encoker@sandia.gov

Specialty section:
This article was submitted to Solar Energy, a section of the journal Frontiers in Energy Research

Received: *30 July 2021*
Accepted: *05 October 2021*
Published: *22 October 2021*

Citation:
Park JE, Bare ZJL, Morelock RJ, Rodriguez MA, Ambrosini A, Musgrave CB, McDaniel AH and Coker EN (2021) Computationally Accelerated Discovery and Experimental Demonstration of $Gd_{0.5}La_{0.5}Co_{0.5}Fe_{0.5}O_3$ for Solar Thermochemical Hydrogen Production. Front. Energy Res. 9:750600. doi: 10.3389/fenrg.2021.750600

*James Eujin Park[1], Zachary J. L. Bare[2], Ryan J. Morelock[2], Mark A. Rodriguez[1], Andrea Ambrosini[1], Charles B. Musgrave[2,3,4], Anthony H. McDaniel[5] and Eric N. Coker[1]**

[1]Sandia National Laboratories, Albuquerque, NM, United States, [2]Department of Chemical and Biological Engineering, University of Colorado Boulder, Boulder, CO, United States, [3]Department of Chemistry, University of Colorado Boulder, Boulder, CO, United States, [4]Renewable and Sustainable Energy Institute, University of Colorado Boulder, Boulder, CO, United States, [5]Sandia National Laboratories, Livermore, CA, United States

Solar thermochemical hydrogen (STCH) production is a promising method to generate carbon neutral fuels by splitting water utilizing metal oxide materials and concentrated solar energy. The discovery of materials with enhanced water-splitting performance is critical for STCH to play a major role in the emerging renewable energy portfolio. While perovskite materials have been the focus of many recent efforts, materials screening can be time consuming due to the myriad chemical compositions possible. This can be greatly accelerated through computationally screening materials parameters including oxygen vacancy formation energy, phase stability, and electron effective mass. In this work, the perovskite $Gd_{0.5}La_{0.5}Co_{0.5}Fe_{0.5}O_3$ (GLCF), was computationally determined to be a potential water splitter, and its activity was experimentally demonstrated. During water splitting tests with a thermal reduction temperature of 1,350°C, hydrogen yields of 101 µmol/g and 141 µmol/g were obtained at re-oxidation temperatures of 850 and 1,000°C, respectively, with increasing production observed during subsequent cycles. This is a significant improvement from similar compounds studied before ($La_{0.6}Sr_{0.4}Co_{0.2}Fe_{0.8}O_3$ and $LaFe_{0.75}Co_{0.25}O_3$) that suffer from performance degradation with subsequent cycles. Confirmed with high temperature x-ray diffraction (HT-XRD) patterns under inert and oxidizing atmosphere, the GLCF mainly maintained its phase while some decomposition to $Gd_{2-x}La_xO_3$ was observed.

Keywords: concentrated solar energy, thermochemical water splitting, hydrogen, density functional theory, perovskite

INTRODUCTION

Solar thermochemical hydrogen (STCH) production has been studied as a potential path to produce alternative fuels (Miller et al., 2014). This reaction is generally a two-step process that generates hydrogen (H_2) gas by splitting water using metal oxide materials and concentrated solar energy (Steinfeld, 2005; Smestad and Steinfeld, 2012). In the first step of a typical STCH cycle, the metal oxide is thermally reduced under inert atmosphere at high temperature (>1,200°C, achieved using concentrated solar-thermal flux), creating oxygen vacancies in the metal oxide and releasing oxygen gas (Scheffe and Steinfeld, 2014). In the second re-oxidation step at a lower temperature under steam, the oxygen-deficient metal oxide splits water to produce H_2 gas while regenerating the metal oxide for consecutive water splitting cycles. While a combined photovoltaic/electrolytic system can be an alternative method for generating H_2 from water (Ivy, 2004), the efficiency of STCH systems were predicted to potentially exceed the efficiency of the combined system (Siegel et al., 2013).

Different classes of materials have been studied demonstrating STCH capabilities, including fluorites (CeO_2) (Gauckler et al., 1997; Abanades et al., 2010; Chueh et al., 2010; Scheffe and Steinfeld, 2014; Rao and Dey, 2017), iron oxides (Fe_3O_4) (Nakamura, 1977; Kodama et al., 2004; Coker et al., 2011; Scheffe and Steinfeld, 2014), and spinel ferrites (MFe_2O_4, M = Cu, Ni, Zn, etc.) (Tamaura et al., 1995; Allendorf et al., 2008; Miller et al., 2008; Fresno et al., 2009; Scheffe and Steinfeld, 2014). Additionally, perovskite oxides (ABO_3) have been investigated heavily with many perovskite materials demonstrated to possess water splitting capabilities (McDaniel et al., 2013; Yang et al., 2014; Rao and Dey, 2017; Barcellos et al., 2018; Nair and Abanades, 2018; Qian et al., 2020a; Qian et al., 2020b). A large chemical space of perovskite materials is available due to the flexibility in chemical compositions and crystal structures the formula can stabilize (Vasala and Karppinen, 2015). For this reason, perovskite oxides are fertile ground for discovering new STCH materials with high efficiencies.

With the vast composition space of inorganic materials, preliminary computational materials screening has become an important tool for accelerating materials discovery. Computational methods were previously applied to materials screening for the solid-state hydrogen storage reaction and chemical looping process (Clary et al., 2020; Singstock et al., 2020). For STCH, ternary (ABO_3) and quaternary ($AA'BO_3$) perovskites were explored to computationally evaluate their oxygen vacancy formation energies, electronic properties, and thermodynamic stabilities, with several promising candidate materials predicted based on these results (Emery et al., 2016; Sai Gautam et al., 2020). In this work, we report $Gd_{0.5}La_{0.5}Co_{0.5}Fe_{0.5}O_3$ (GLCF) as a new STCH material that was discovered using a computational screening approach and experimentally demonstrated as a STCH producing material.

METHODS

Computational Screening Framework

Potential STCH compounds from the $A_2BB'O_6$, $AA'B_2O_6$, and $AA'BB'O_6$ compositional spaces were first screened for stability as perovskites using the machine learned descriptor τ (Bartel et al., 2019). τ classifies potential perovskite compositions as perovskite or non-perovskite using the Shannon radii (rA, rB, rX) of the A, B, and X site ions and the formal oxidation state of the A site cation as inputs. This descriptor exhibits 92% accuracy for predicting theoretical perovskite synthesizability for ABX_3 compositions and 91% accuracy for $A_2BB'X_6$ compositions, where fractional weighting of the B site cation radii is used (Bartel et al., 2019). Of the compounds identified by τ as synthesizable as perovskites, the STCH relevant properties of >1,000 Gd-containing compositions were evaluated in a high-throughput optimization scheme (Bare et al., 2021a). The compositions La_2CoFeO_6, $GdLaCoFeO_6$, and Gd_2CoFeO_6 are predicted by τ to be stable as perovskites (with formal oxidation states of +3 used for Gd, La, Co, and Fe and -2 used for O) and are predicted by DFT to have favorable STCH properties (see Results and Discussion).

PySPuDS (Bare et al., 2021b), a custom high-throughput python wrapper for the bond valence method (BVM) based Structure Prediction and Diagnostic Software (SPuDS), was used to generate initial perovskite geometries for DFT optimization (Lufaso and Woodward, 2001). The BVM Global Instability Index (GII), which SPuDS minimizes to predict the phase and magnitude of perovskite octahedral tilting, is strongly correlated with DFT energy in perovskite oxides (Morelock et al., 2021). This enables SPuDS to accurately predict perovskite ground state polymorph structures consistent with DFT, thereby substantially reducing the computational expense associated with high-throughput DFT investigations (Bare et al., 2021b). Initial geometries for DFT optimizations of the La_2CoFeO_6, $GdLaCoFeO_6$, and Gd_2CoFeO_6 perovskites were generated in the a-b+a- Glazer mode, as this is the ground state tilting mode most frequently predicted by DFT for experimentally observed ABO_3 perovskite oxides (Bare et al., 2021b). Atomic configurations for cation alloying on the B site were generated using rock salt site ordering, while configurations for alloying on the A sites were generated that minimize the Ewald sum.

The specific pseudopotentials and Hubbard +U parameters used for GGA+U DFT optimizations are compatible with the Materials Project (MP) database (Jain et al., 2013), which tabulates the structures and energies of >130,000 inorganic materials. Calculations were performed using the Vienna Ab initio Simulation Program (VASP 5.4.1) (Kresse and Hafner, 1993; Kresse and Hafner, 1994; Kresse and Furthmüller, 1996a; Kresse and Furthmüller, 1996b) with periodic boundary conditions utilizing projector augmented wave (PAW) pseudopotentials (Kresse and Joubert, 1999) and the Perdew-Burke-Ernzerhof (PBE) exchange-correlation functional (Perdew et al., 1996). +U parameters of 3.32 and 5.3 were used for Co^{3+} and Fe^{3+}, respectively, consistent with pymatgen's MPRelaxSet (Jain et al., 2013). The electronic wave functions were expanded in a plane wave basis with an energy cutoff of 520 eV. The Brillouin

zones were sampled during geometry optimizations using an automatically generated Γ-centered Monkhorst-Pack k-point mesh with a grid density of at least 1,000/(atoms/unit cell). Oxide-specific corrections to DFT total energies were included to maintain compatibility with the MP (Jain et al., 2013).

We explicitly considered the effects of magnetism by first performing two consecutive spin-polarized relaxations initialized in a high-spin ferromagnetic configuration with species-specific initial magnetic moments dictated by the default MP spin parameters. Then, magnetic sampling of the computed structures was performed for up to 20 different magnetic symmetries using pymatgen's MagneticStructureEnumerator (Ong et al., 2013). Finally, the internal coordinates of the DFT structures–with lattice vectors and initial magnetic moments fixed from previous optimizations–were optimized such that total energies were converged to within 10^{-6} eV, and forces converged to within 0.01 eV/Å. The effects of spin configuration on the electronic density of states (DOS) were also explicitly described in this manner. Calculations to determine oxygen vacancy energies were performed using the aforementioned convergence criteria for all symmetrically unique vacancies at a defect concentration of $C_d = 0.0833$.

Materials

All chemicals and gases were purchased and used as-received: gadolinium (III) oxide (Gd_2O_3, Alfa Aesar, 99.999%), lanthanum (III) oxide (La_2O_3, Aldrich, 99.99%), cobalt (II, III) oxide (Co_3O_4, Alfa Aesar, 99.99%), and iron (III) oxide (Fe_2O_3, Acros Organics, 99.999%), argon gas (Matheson, UHP grade), and air (Matheson, ultra-zero grade).

Synthesis of $Gd_{0.5}La_{0.5}Co_{0.5}Fe_{0.5}O_3$

Synthesis was conducted via a solid state synthesis route. For a 2 g scale reaction, stoichiometric amounts of gadolinium (III) oxide (0.7151 g), lanthanum (III) oxide (0.6427 g), cobalt (II, III) oxide (0.3167 g), and iron (III) oxide (0.3150 g) were ground by hand in an agate mortar and pestle for ~10 min. The resulting powder mixture was calcined in air at 600°C (5°C/min, 12 h dwell), then sintered in air at 1,300°C (9°C/min, 12 h dwell) with intermediate grinding.

Characterization

Powder X-ray diffraction (XRD) was collected on Bruker D2 Phaser X-ray Diffractometer with Cu Kα radiation. Profile fitting of diffraction patterns were performed with GSAS-II (Toby and Von Dreele, 2013). Thermogravimetric analysis (TGA) was performed on a Netzsch STA 449 F1 Jupiter thermal analyzer.

Thermochemical cycling experiments were conducted under gas flow rates of 100 ml/min. For thermal reduction under Ar (100 ml/min), the sample (~50 mg) was first heated to 1,250°C (10°C/min), held isothermally for 30 min (thermal reduction), cooled to 400°C (25°C/min), then held isothermally for 30 min. For re-oxidation, the gas was switched to a mixture of air (80 ml/min) and Ar (20 ml/min), and the sample was heated to 1,100°C (10°C/min), isothermally held for 30 min, then cooled to 200°C (25°C/min). For repeated consecutive analyses, the sample was re-weighed between runs. TGA baseline correction was performed with an empty crucible. All thermograms shown here are corrected.

Water splitting experiments were conducted in a stagnation flow reactor (SFR) equipped with a laser-based sample heater and a mass spectrometer; the experimental details are described in previous papers (Scheffe et al., 2011; Arifin et al., 2012; Scheffe et al., 2013). In brief, the powder sample was placed in a tube furnace to maintain the oxidation temperature, and then irradiated by an IR laser through an optical access window to achieve the desired reduction temperature. The amount of oxygen gas evolved during reduction under Ar and hydrogen gas evolved during oxidation under 40 vol% steam were measured using a mass spectrometer.

High temperature XRD (HT-XRD) was performed on a Scintag PAD X-ray diffractometer, equipped with a Buehler hot-stage with Pt/Rh heating strip and surround heater. The hot stage resides within a sealed chamber with an X-ray-transparent beryllium window, and gas flow (either helium or air) was maintained at 200 ml/min. The data was analyzed using MDI Jade 8.2 software, and the plot was constructed with square root of intensity to easily observe low intensity peaks.

RESULTS AND DISCUSSION

To evaluate compound stability relative to decomposition, the DFT computed energies of the La_2CoFeO_6 (L2CF), $GdLaCoFeO_6$ (GLCF), and Gd_2CoFeO_6 (G2CF) perovskites optimized in the monoclinic, triclinic, and monoclinic space groups, respectively, (**Supplementary Figure S1**) were compared to the DFT computed energies of their potential decomposition products tabulated in the MP database. The energy of a material relative to the convex hull, E_{hull}, quantifies a material's stability relative to its decomposition products. Monoclinic L2CF, triclinic GLCF, and monoclinic G2CF exhibit E_{hull} of 0, 6.8, and 0 meV/atom, respectively, predicting that all three STCH candidates can be successfully synthesized as perovskites relative to their competing phases. The combination of the τ-predicted stabilities and E_{hull} values of L2CF, GLCF, and G2CF suggests that Gd-La-Co-Fe-O is a promising compositional space for experimentally synthesizable perovskite oxides. We thus selected L2CF, GLCF, and G2CF from our high-throughput screening and computed additional STCH-relevant properties for these compounds, including DOS and charge neutral oxygen vacancy formation enthalpies (ΔH_{Ovac}).

The distributions of ΔH_{Ovac} computed by DFT for the symmetrically unique sites of L2CF, GLCF, and G2CF are shown in **Figure 1A**. The ΔH_{Ovac} distribution of GLCF is bounded by the ΔH_{Ovac} distributions of L2CF (lower bound) and G2CF (upper bound). Herein, we use the DFT computed ΔH_{Ovac} of CeO_2 (3.95 eV/atom) (Abanades and Flamant, 2006; Chueh and Haile, 2010), the gold standard STCH redox mediator (Muhich et al., 2016), as the upper bound for the STCH active range and a liberal lower bound of 2 eV/atom to account for uncertainty in DFT energetics (Naghavi et al., 2020). Materials approaching the minimum ΔH_{Ovac} for STCH activity exhibit slow oxidation kinetics and/or degradation during redox cycling,

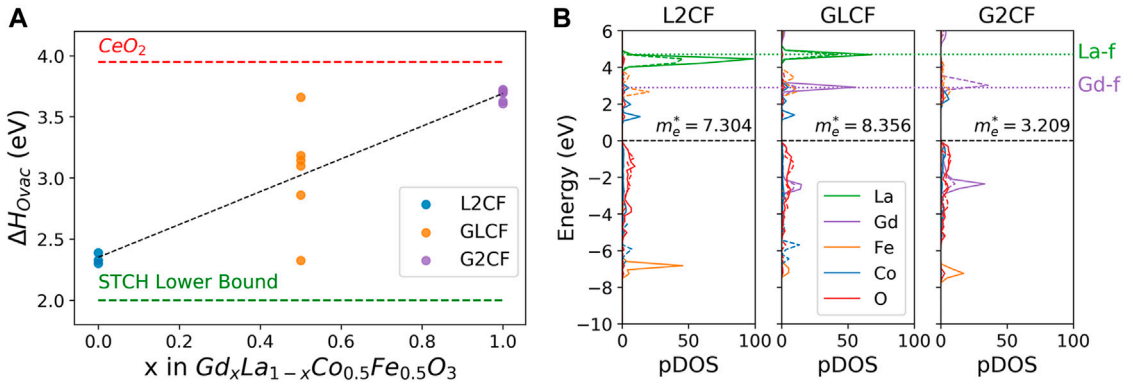

FIGURE 1 | (A) Computed ΔH_{Ovac} values vs Gd concentration (x) in $Gd_xLa_{1-x}Co_{0.5}Fe_{0.5}O_3$, showing that higher x increases ΔH_{Ovac}, thus the stability of oxygen. All three materials studied are within the estimated STCH active range (2.0 eV ≤ ΔH_{Ovac} ≤ 3.95 eV). The mean vacancy enthalpy ΔH_{Ovac} is described by the equation, ΔH_{Ovac} = 1.34x + 2.35 (R^2 = 0.999), where x is the fractional concentration of Gd on the A site. **(B)** DFT computed DOS for La_2CoFeO_6 (L2CF), $GdLaCoFeO_6$ (GLCF), and Gd_2CoFeO_6 (G2CF). For GLCF, a larger multiplicity of Gd-f orbitals closer to the conduction band minimum than La-f orbitals is shown, leading to the largest calculated DOS electron effective mass at 1000 K (m_e = 8.356).

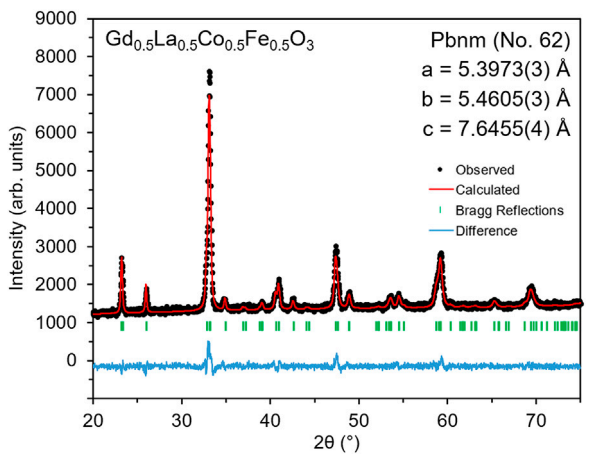

FIGURE 2 | Room temperature XRD pattern with LeBail profile fitting for $Gd_{0.5}La_{0.5}Co_{0.5}Fe_{0.5}O_3$, showing it to be isostructural to the orthorhombic perovskite, $LaFeO_3$ (Proskurnina et al., 2007).

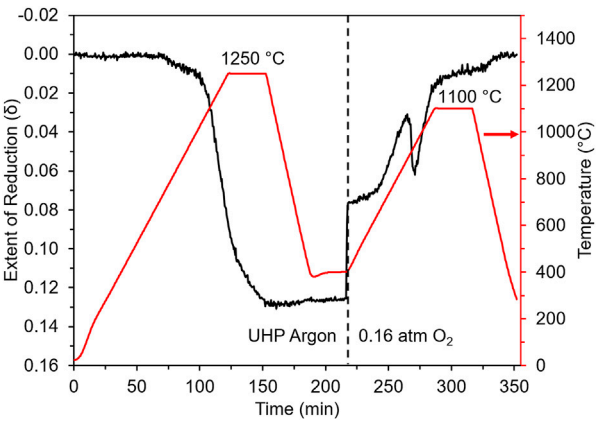

FIGURE 3 | TGA results of the second redox cycle showing redox behavior of GLCF. The red curve corresponds to the sample temperature, and the black line corresponds to the extent of reduction (δ in $Gd_{0.5}La_{0.5}Co_{0.5}Fe_{0.5}O_{3-\delta}$).

whereas materials approaching the maximum ΔH_{Ovac} for STCH activity suffer from reduced H_2 capacity (Muhich et al., 2016). GLCF exhibits both O vacancies with low and high ΔH_{Ovac}, where vacancies with low ΔH_{Ovac} participate in H_2 production and those with high ΔH_{Ovac} are less likely to form under STCH operating conditions and therefore enable preservation of the perovskite lattice during redox cycling. This ΔH_{Ovac} distribution predicts enhanced cyclability of GLCF relative to L2CF and increased H_2 production capacity relative to G2CF.

Additionally, GLCF exhibits a large DOS effective mass, m_e, that arises from its large concentration of accessible electronic states near the conduction band minimum (CBM). Lany showed that large m_e corresponds with large electronic contributions to the entropy of reduction S_{red} in STCH processes (Lany, 2018) that benefits STCH performance at high temperatures (Meredig and Wolverton, 2009). **Figure 1B** shows the DFT computed DOS for L2CF, GLCF, and G2CF. GLCF exhibits a larger DOS m_e at 1000 K (m_e = 8.356) than both L2CF (m_e = 7.304) and G2CF (m_e = 3.209). The introduction of Gd into the nominally La-occupied A site of L2CF results in unoccupied states that lie closer to the CBM than those of La alone, which increases m_e. However, complete substitution of Gd for La increases the splitting of the unoccupied Gd-f states that results in lowering m_e relative to GLCF. Due to its favorable ΔH_{Ovac} distribution and larger m_e relative to L2CF and G2CF, GLCF was recommended for experimental synthesis and characterization of STCH performance.

The room temperature XRD pattern of the synthesized GLCF is shown in **Figure 2**. The resulting material is isostructural to $LaFeO_3$, $GdFeO_3$, and $La_{1-x}Gd_xFeO_3$ (x = 0, 0.2, 0.5, 0.8, and 1), which are all orthorhombic perovskites (Proskurnina et al., 2007; Wiglusz et al., 2015; Orlov et al., 2016). LeBail profile fitting analysis was performed, confirming the GLCF crystalizes in the Pbnm space group (No. 62) with no additional secondary phases. The lattice parameters for GLCF (a = 5.3973(3) Å, b = 5.4605(3)

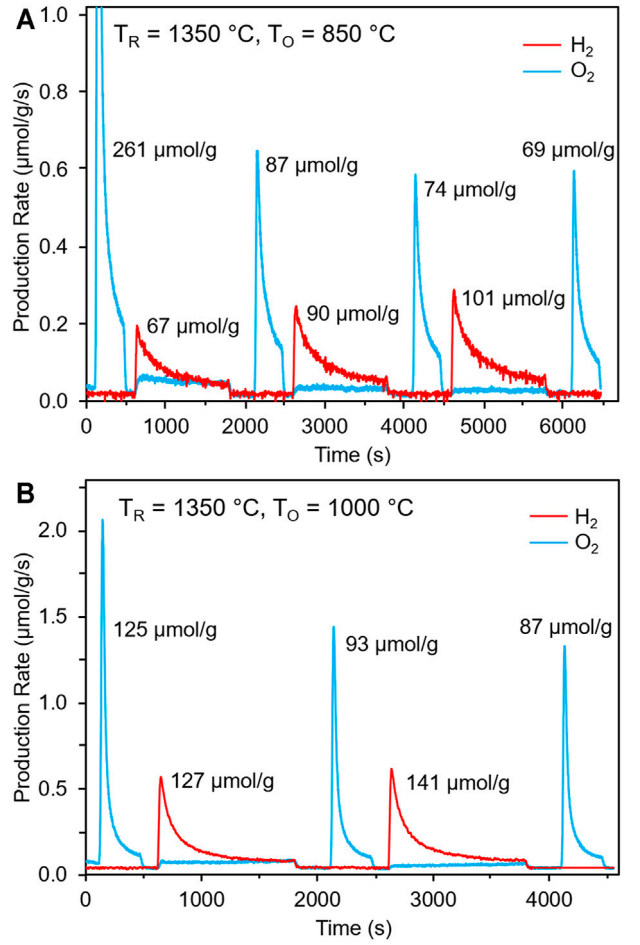

FIGURE 4 | Water splitting experiment on GLCF at T_R = 1,350°C (330 s) and **(A)** T_O = 850°C and **(B)** T_O = 1,000°C with 40 vol% H_2O (1,200 s).

Å, c = 7.6455(4) Å) are slightly smaller than $LaFeO_3$ (a = 5.5506(6) Å, b = 5.5608(5) Å, c = 7.8464(9) Å) (Proskurnina et al., 2007). This is likely due to the smaller atomic radii of Gd and Co compared to La and Fe, respectively (Shannon, 1976).

The redox behavior of GLCF was examined through thermogravimetric analysis (TGA), which monitors the mass change with respect to temperature and atmosphere (Ar or air). In the case of these materials, the mass change corresponds to gain/loss of oxygen. The mass change was converted to the extent of reduction (δ), assuming $Gd_{0.5}La_{0.5}Co_{0.5}Fe_{0.5}O_{3-\delta}$ during redox cycling. The as-prepared powder was subjected to redox cycles, comprising a reduction step at 1,250°C under Ar followed by a re-oxidation step at 1,100°C under air, corresponding to 0.16 atm O_2. The redox cycle was repeated twice with the two redox cycles showing similar behavior. The second redox cycle is shown in **Figure 3**. During thermal reduction, a shallow weight loss was observed at ~750°C, followed by a steeper weight loss onset at ~1,030°C. After the isotherm at 1,250°C, the extent of reduction (δ) was ~0.13. During re-oxidation, the mass sharply increased when the gas was switched from Ar to air at 400°C, followed by a more gradual increase as the temperature was raised. The dip in the extent of reduction seen between 900 and 1,100°C is attributed to a phase change in the material, that is, formation of a phase at around 900°C that ejects oxygen to achieve stability. This change in δ is reproducible between cycles. The sample mass returns to the starting mass after the re-oxidation step.

The water splitting capability of GLCF was verified using a stagnation flow reactor (SFR). **Figure 4** shows the water splitting results performed with a thermal reduction temperature (T_R) of 1,350°C for 330 s and re-oxidation temperatures (T_O) of 850 and 1,000°C for 1,200 s under 40 vol% H_2O. Water splitting was observed under both sets of conditions, with the amount of H_2 produced increasing with each cycle. For T_O = 850°C (**Figure 4A**), the amount of H_2 produced was 67, 90, and 101 μmol/g for each consecutive cycle. Moreover, significantly less O_2 was released in the second reduction cycle compared to the first cycle, likely due to the water splitting step being kinetically limited. This is also evident from the long tails of H_2 gas evolved during the re-oxidation steps. For T_O = 1,000°C (**Figure 4B**), the H_2 capacity increased (127 and 141 μmol/g), evident of an improvement in the rate of water splitting at higher temperature. Similar to the T_O = 850°C experiment, more H_2 was produced as cycle-number increased. In an ideal situation, once steady state has been achieved, the amount of H_2 should be twice of the amount of O_2 produced. From the SFR experiments with repeated cycles, GLCF is evolving and approaching this ideal steady state, though additional studies are needed to understand this behavior.

While $LaFeO_3$ was previously reported to have negligible solar thermochemical H_2O and CO_2 conversion behavior (Jiang et al., 2014; Chen et al., 2017), similar perovskites to GLCF, $La_{0.6}Sr_{0.4}Co_{0.2}Fe_{0.8}O_3$ and $LaFe_{0.75}Co_{0.25}O_3$, were shown to be active for solar thermochemical CO_2 conversion (STCH activity is unknown) (Nair and Abanades, 2018), indicating that the mixing of Co and Fe may have contributed to the solar thermochemical conversion activity. For $La_{0.6}Sr_{0.4}Co_{0.2}Fe_{0.8}O_3$ and $LaFe_{0.75}Co_{0.25}O_3$, however, CO production decreased substantially during subsequent cycles (Nair and Abanades, 2018). The substitution of Gd for La may have contributed to minimizing performance degradation as predicted by DFT calculations.

In terms of its water splitting ability, at T_R = 1,350°C and T_O = 850°C, GLCF produced more H_2 (101 μmol/g) than CeO_2 (50 μmol/g) (Barcellos et al., 2018). However, GLCF produced less H_2 compared to the previously studied perovskite materials $BaCe_{0.25}Mn_{0.75}O_3$ (BCM) and $Sr_{0.4}La_{0.6}Mn_{0.6}Al_{0.4}O_3$ (SLMA4664) (McDaniel et al., 2013; Barcellos et al., 2018). BCM and SLMA4664 produced 140 μmol/g (T_R = 1,350°C, T_O = 850°C) and 307 μmol/g (T_R = 1,350°C, T_O = 1,000°C) of H_2, respectively (McDaniel et al., 2013; Barcellos et al., 2018). However, direct comparisons of performance reported for different conditions (temperature, atmosphere, and time) for various materials that have different optimized conditions for STCH can lead to incorrect conclusions about the H_2 production capabilities of candidate materials. In the present case, the water splitting experimental conditions implemented for GLCF have not yet been optimized. Nevertheless, computational screening

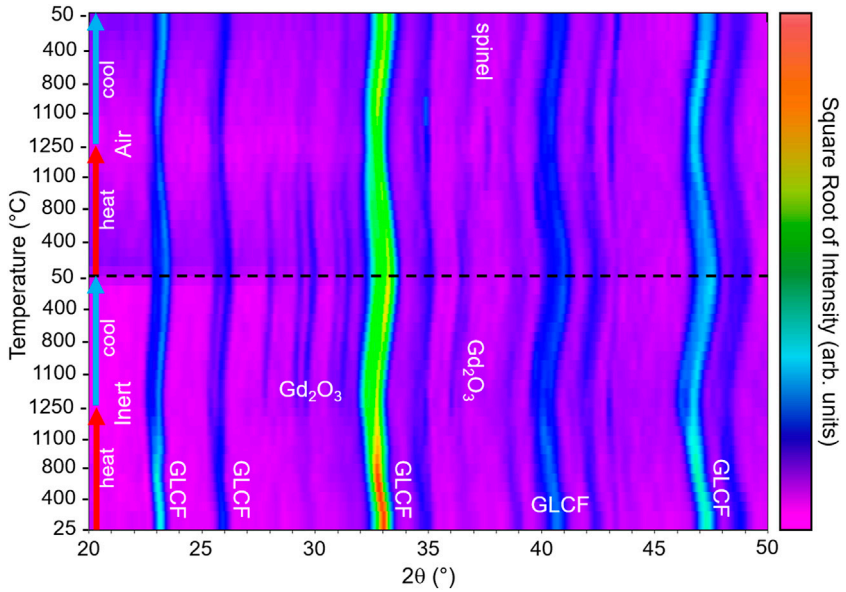

FIGURE 5 | HT-XRD pattern of GLCF, heating from room temperature to 1,250°C then cooling to 50°C under He flow, followed by the identical thermal profile under air. The experiment progresses from the bottom of the plot to the top.

greatly accelerated the discovery of GLCF as a water splitting material, which would otherwise have been experimentally time consuming due to the vast chemical space of perovskite materials.

To understand the phase stability in GLCF during redox cycling, HT-XRD patterns were collected first from room temperature to 1,250°C to 50°C under He for thermal reduction, then with an identical temperature profile under air for re-oxidation. The GLCF sample was redox-cycled (T_R = 1,250°C under Ar, T_O = 1,100°C under air) before collecting the HT-XRD patterns. The HT-XRD pattens are shown in **Figure 5**. During the HT-XRD experiment, GLCF appears to maintain its perovskite phase as the major phase, but the major peaks broaden and exhibit some peak splitting occurring during reduction. In addition to the changes in the major GLCF phase, during cool down at ~1,200°C under He, additional peaks appear corresponding to Gd_2O_3 phase. Due to the shift in peaks, it may have different chemistry (i.e. $Gd_{2-x}La_xO_3$). The additional Gd_2O_3 phase remains in the pattern until heated under air at ~700–800°C during re-oxidation. The disappearance of the Gd_2O_3 phase may correspond to the increase in the extent of reduction observed in the TG experiment at ~900°C during reoxidation. Moreover, a spinel phase appears during cool down under air. Overall, during the redox cycle, the perovskite phase persists, agreeing with the stable STCH activity observed in the SFR results and TGA cycling tests.

CONCLUSION

Solar thermochemical hydrogen production (STCH) significantly contributes to the renewable energy portfolio. However, materials discovery with high efficiency is needed, and computational screening can greatly accelerate this process. This was demonstrated with $Gd_{0.5}La_{0.5}Co_{0.5}Fe_{0.5}O_3$ (GLCF), a perovskite oxide, that was computationally determined first, then experimentally demonstrated. When compared to $LaCo_{0.5}Fe_{0.5}O_3$, it was predicted that GLCF would have higher phase stability due to the incorporation of Gd on the La site. The synthesis of a single phase GLCF sample was achieved. With redox activity confirmed through thermogravimetric analysis, stable water splitting behavior over multiple cycles was also observed. When compared to previously reported $La_{0.6}Sr_{0.4}Co_{0.2}Fe_{0.8}O_3$ and $LaFe_{0.75}Co_{0.25}O_3$, which suffered from performance degradation with subsequent cycles, the Gd substitution of La plays a significant role to maintain water splitting performance. Based on high temperature x-ray diffraction experiments, the GLCF perovskite phase persists which potentially contributes to the stable water splitting performance. This work demonstrates that computational materials screening can greatly accelerate the discovery of new water splitting materials. Through computational screening, potential water splitting materials were narrowed down to a promising STCH material from the vast chemical space of perovskite materials, and a unique strategy of incorporating a rare earth element that improved the stability was demonstrated.

DATA AVAILABILITY STATEMENT

The original contributions presented in the study are included in the article/**Supplementary Material**, further inquiries can be directed to the corresponding author.

AUTHOR CONTRIBUTIONS

JP conducted material synthesis and characterization and drafted the manuscript. ZB and RM conducted the DFT calculations and wrote sections of the manuscript. MR, AM, and EC conducted materials characterization. AA provided guidance on material synthesis. CM supervised the DFT calculations.

FUNDING

This work was supported by the U.S. Department of Energy (DOE), Office of Energy Efficiency and Renewable Energy (EERE), Hydrogen and Fuel Cell Technologies Office (HFTO), and specifically the HydroGEN Advanced Water Splitting Materials Consortium, established as part of the Energy Materials Network under this same office (award DE-EE0008088). CM, ZB and RM also acknowledge support from the National Science Foundation, awards NSF CHEM-1800592 and CBET-2016225. Sandia National Laboratories is a multi-mission laboratory managed and operated by National Technology and Engineering Solutions of Sandia, LLC., a wholly owned subsidiary of Honeywell International, Inc., for the U.S. Department of Energy's National Nuclear Security Administration under contract DE-NA0003525. The views expressed in this article do not necessarily represent the views of the U.S. Department of Energy or the United States Government.

SUPPLEMENTARY MATERIAL

The Supplementary Material for this article can be found online at: https://www.frontiersin.org/articles/10.3389/fenrg.2021.750600/full#supplementary-material

REFERENCES

Abanades, S., and Flamant, G. (2006). Thermochemical Hydrogen Production from a Two-step Solar-Driven Water-Splitting Cycle Based on Cerium Oxides. *Solar Energy* 80 (12), 1611–1623. doi:10.1016/j.solener.2005.12.005

Abanades, S., Legal, A., Cordier, A., Peraudeau, G., Flamant, G., and Julbe, A. (2010). Investigation of Reactive Cerium-Based Oxides for H2 Production by Thermochemical Two-step Water-Splitting. *J. Mater. Sci.* 45 (15), 4163–4173. doi:10.1007/s10853-010-4506-4

Allendorf, M. D., Diver, R. B., Siegel, N. P., and Miller, J. E. (2008). Two-Step Water Splitting Using Mixed-Metal Ferrites: Thermodynamic Analysis and Characterization of Synthesized Materials. *Energy Fuels* 22 (6), 4115–4124. doi:10.1021/ef8005004

Arifin, D., Aston, V. J., Liang, X., McDaniel, A. H., and Weimer, A. W. (2012). CoFe2O4 on a Porous Al2O3 Nanostructure for Solar Thermochemical CO2 Splitting. *Energy Environ. Sci.* 5 (11), 9438–9443. doi:10.1039/C2EE22090C

Bartel, C. J., Sutton, C., Goldsmith, B. R., Ouyang, R., Musgrave, C. B., Ghiringhelli, L. M., et al. (2019). New Tolerance Factor to Predict the Stability of Perovskite Oxides and Halides. *Sci. Adv.* 5 (2), eaav0693. doi:10.1126/sciadv.aav0693

Chen, Z., Jiang, Q., Tong, J., Yang, M., Jiang, Z., and Li, C. (2017). Enhancement Effects of Dopants and SiO2 Support on Mixed Metal Ferrites Based Two-step Thermochemical Water Splitting. *Solar Energy* 144, 643–659. doi:10.1016/j.solener.2017.01.049

Chueh, W. C., Falter, C., Abbott, M., Scipio, D., Furler, P., Haile, S. M., et al. (2010). High-Flux Solar-Driven Thermochemical Dissociation of CO2 and H2O Using Nonstoichiometric Ceria. *Science* 330 (6012), 1797–1801. doi:10.1126/science.1197834

Chueh, W. C., and Haile, S. M. (2010). A Thermochemical Study of Ceria: Exploiting an Old Material for New Modes of Energy Conversion and CO 2 Mitigation. *Phil. Trans. R. Soc. A.* 368 (1923), 3269–3294. doi:10.1098/rsta.2010.0114

Clary, J. M., Holder, A. M., and Musgrave, C. B. (2020). Computationally Predicted High-Throughput Free-Energy Phase Diagrams for the Discovery of Solid-State Hydrogen Storage Reactions. *ACS Appl. Mater. Inter.* 12 (43), 48553–48564. doi:10.1021/acsami.0c13298

Coker, E. N., Ambrosini, A., Ambrosini, A., Rodriguez, M. A., and Miller, J. E. (2011). Ferrite-YSZ Composites for Solar Thermochemical Production of Synthetic Fuels: in Operando Characterization of CO2 Reduction. *J. Mater. Chem.* 21 (29), 10767–10776. doi:10.1039/C1JM11053E

Emery, A. A., Saal, J. E., Kirklin, S., Hegde, V. I., and Wolverton, C. (2016). High-Throughput Computational Screening of Perovskites for Thermochemical Water Splitting Applications. *Chem. Mater.* 28 (16), 5621–5634. doi:10.1021/acs.chemmater.6b01182

Fresno, F., Fernández-Saavedra, R., Belén Gómez-Mancebo, M., Vidal, A., Sánchez, M., Isabel Rucandio, M., et al. (2009). Solar Hydrogen Production by Two-step Thermochemical Cycles: Evaluation of the Activity of Commercial Ferrites. *Int. J. Hydrogen Energ.* 34 (7), 2918–2924. doi:10.1016/j.ijhydene.2009.02.020

Gauckler, L. J., Go¨dickemeier, M., and Schneider, D. (1997). Nonstoichiometry and Defect Chemistry of Ceria Solid Solutions. *J. Electroceram.* 1 (2), 165–172. doi:10.1023/A:1009928817542

Ivy, J. (2004). "Summary of Electrolytic Hydrogen Production," NREL/MP-560-36734, Colorado: National Renewable Energy Laboratory.

Jain, A., Ong, S. P., Hautier, G., Chen, W., Richards, W. D., Dacek, S., et al. (2013). Commentary: The Materials Project: A Materials Genome Approach to Accelerating Materials Innovation. *APL Mater.* 1 (1), 011002. doi:10.1063/1.4812323

Jiang, Q., Tong, J., Zhou, G., Jiang, Z., Li, Z., and Li, C. (2014). Thermochemical CO2 Splitting Reaction with Supported LaxA1−xFeyB1−yO3 (A=Sr, Ce, B=Co, Mn; 0⩽x, Y⩽1) Perovskite Oxides. *Solar Energy* 103, 425–437. doi:10.1016/j.solener.2014.02.033

Kodama, T., Nakamuro, Y., and Mizuno, T. (2004). A Two-step Thermochemical Water Splitting by Iron-Oxide on Stabilized Zirconia. *J. Sol. Energ. Eng.* 128 (1), 3–7. doi:10.1115/1.1878852

Kresse, G., and Furthmüller, J. (1996a). Efficiency of Ab-Initio Total Energy Calculations for Metals and Semiconductors Using a Plane-Wave Basis Set. *Comput. Mater. Sci.* 6 (1), 15–50. doi:10.1016/0927-0256(96)00008-0

Kresse, G., and Furthmüller, J. (1996b). Efficient Iterative Schemes Forab Initiottotal-Energy Calculations Using a Plane-Wave Basis Set. *Phys. Rev. B* 54 (16), 11169–11186. doi:10.1103/PhysRevB.54.11169

Kresse, G., and Hafner, J. (1993). Ab Initiomolecular Dynamics for Liquid Metals. *Phys. Rev. B* 47 (1), 558–561. doi:10.1103/PhysRevB.47.558

Kresse, G., and Hafner, J. (1994). Ab Initiomolecular-Dynamics Simulation of the Liquid-Metal-Amorphous-Semiconductor Transition in Germanium. *Phys. Rev. B* 49 (20), 14251–14269. doi:10.1103/PhysRevB.49.14251

Kresse, G., and Joubert, D. (1999). From Ultrasoft Pseudopotentials to the Projector Augmented-Wave Method. *Phys. Rev. B* 59 (3), 1758–1775. doi:10.1103/PhysRevB.59.1758

Lany, S. (2018). Communication: The Electronic Entropy of Charged Defect Formation and its Impact on Thermochemical Redox Cycles. *J. Chem. Phys.* 148 (7), 071101. doi:10.1063/1.5022176

Lufaso, M. W., and Woodward, P. M. (2001). Prediction of the Crystal Structures of Perovskites Using the Software Program SPuDS. *Acta Crystallogr. Sect B* 57, 725–738. doi:10.1107/s0108768101015282

McDaniel, A. H., Miller, E. C., Arifin, D., Ambrosini, A., Coker, E. N., O'Hayre, R., et al. (2013). Sr- and Mn-Doped LaAlO3−δ for Solar Thermochemical H2 and CO Production. *Energ. Environ. Sci.* 6 (8), 2424–2428. doi:10.1039/C3EE41372A

Meredig, B., and Wolverton, C. (2009). First-principles Thermodynamic Framework for the Evaluation of thermochemicalH2O- orCO2-Splitting Materials. *Phys. Rev. B* 80 (24), 245119. doi:10.1103/PhysRevB.80.245119

Miller, J. E., Allendorf, M. D., Diver, R. B., Evans, L. R., Siegel, N. P., and Stuecker, J. N. (2008). Metal Oxide Composites and Structures for Ultra-high

Temperature Solar Thermochemical Cycles. *J. Mater. Sci.* 43 (14), 4714–4728. doi:10.1007/s10853-007-2354-7

Miller, J. E., McDaniel, A. H., and Allendorf, M. D. (2014). Considerations in the Design of Materials for Solar-Driven Fuel Production Using Metal-Oxide Thermochemical Cycles. *Adv. Energ. Mater.* 4 (2), 1300469. doi:10.1002/aenm.201300469

Morelock, R., Bare, Z. J. L., and Musgrave, C. B. (2021). Bond Valence Parameterization for the Accurate Description of DFT Energetics in ABO3 Perovskites. *under Rev.*

Muhich, C. L., Ehrhart, B. D., Al-Shankiti, I., Ward, B. J., Musgrave, C. B., and Weimer, A. W. (2016). A Review and Perspective of Efficient Hydrogen Generation via Solar Thermal Water Splitting. *Wires Energ. Environ* 5 (3), 261–287. doi:10.1002/wene.174

Naghavi, S. S., He, J., and Wolverton, C. (2020). CeTi2O6-A Promising Oxide for Solar Thermochemical Hydrogen Production. *ACS Appl. Mater. Inter.* 12 (19), 21521–21527. doi:10.1021/acsami.0c01083

Nair, M. M., and Abanades, S. (2018). Experimental Screening of Perovskite Oxides as Efficient Redox Materials for Solar Thermochemical CO2 Conversion. *Sustainable Energ. Fuels* 2 (4), 843–854. doi:10.1039/C7SE00516D

Nakamura, T. (1977). Hydrogen Production from Water Utilizing Solar Heat at High Temperatures. *Solar Energy* 19 (5), 467–475. doi:10.1016/0038-092X(77)90102-5

Ong, S. P., Richards, W. D., Jain, A., Hautier, G., Kocher, M., Cholia, S., et al. (2013). Python Materials Genomics (Pymatgen): A Robust, Open-Source Python Library for Materials Analysis. *Comput. Mater. Sci.* 68, 314–319. doi:10.1016/j.commatsci.2012.10.028

Orlov, Y. S., Dudnikov, V. A., Gorev, M. V., Vereshchagin, S. N., Solov'ev, L. A., and Ovchinnikov, S. G. (2016). Thermal Properties of Rare Earth Cobalt Oxides and of La1-X Gd X CoO3 Solid Solutions. *Jetp Lett.* 103 (9), 607–612. doi:10.1134/S0021364016090058

Perdew, J. P., Burke, K., and Ernzerhof, M. (1996). Generalized Gradient Approximation Made Simple. *Phys. Rev. Lett.* 77 (18), 3865–3868. doi:10.1103/PhysRevLett.77.3865

Proskurnina, N. V., Voronin, V. I., Cherepanov, V. A., and Kiselev, E. A. (2007). Phase Equilibria and crystal Structure of the Solid Solution LaFe1−xNixO3−δ (0≤x≤1). *Prog. Solid State. Chem.* 35 (2), 233–239. doi:10.1016/j.progsolidstchem.2007.01.022

Qian, X., He, J., Mastronardo, E., Baldassarri, B., Wolverton, C., and Haile, S. M. (2020a). Favorable Redox Thermodynamics of SrTi0.5Mn0.5O3−δ in Solar Thermochemical Water Splitting. *Chem. Mater.* 32, 9335–9346. doi:10.1021/acs.chemmater.0c03278

Qian, X., He, J., Mastronardo, E., Baldassarri, B., Yuan, W., Wolverton, C., et al. (2021b). Outstanding Properties and Performance of CaTi0.5Mn0.5O3-δ for Solar-Driven Thermochemical Hydrogen Production. *Matter* 4, 688–708. doi:10.1016/j.matt.2020.11.016

Rao, C. N. R., and Dey, S. (2017). Solar Thermochemical Splitting of Water to Generate Hydrogen. *Proc. Natl. Acad. Sci. U S A.* 114 (51), 13385–13393. doi:10.1073/pnas.1700104114

R. Barcellos, D., Sanders, M. D., Tong, J., McDanielA.Hand O'Hayre, R. P. (2018). BaCe0.25Mn0.75O3−δ-a Promising Perovskite-type Oxide for Solar Thermochemical Hydrogen Production. *Energ. Environ. Sci.* 11 (11), 3256–3265. doi:10.1039/C8EE01989D

Sai Gautam, G., Stechel, E. B., and Carter, E. A. (2020). Exploring Ca-Ce-M-O (M = 3d Transition Metal) Oxide Perovskites for Solar Thermochemical Applications. *Chem. Mater.* 32 (23), 9964–9982. doi:10.1021/acs.chemmater.0c02912

Scheffe, J. R., Allendorf, M. D., Coker, E. N., Jacobs, B. W., McDaniel, A. H., and Weimer, A. W. (2011). Hydrogen Production via Chemical Looping Redox Cycles Using Atomic Layer Deposition-Synthesized Iron Oxide and Cobalt Ferrites. *Chem. Mater.* 23 (8), 2030–2038. doi:10.1021/cm103622e

Scheffe, J. R., McDaniel, A. H., Allendorf, M. D., and Weimer, A. W. (2013). Kinetics and Mechanism of Solar-Thermochemical H2 Production by Oxidation of a Cobalt Ferrite-Zirconia Composite. *Energ. Environ. Sci.* 6 (3), 963–973. doi:10.1039/C3EE23568H

Scheffe, J. R., and Steinfeld, A. (2014). Oxygen Exchange Materials for Solar Thermochemical Splitting of H2O and CO2: A Review. *Mater. Today* 17 (7), 341–348. doi:10.1016/j.mattod.2014.04.025

Shannon, R. D. (1976). Revised Effective Ionic Radii and Systematic Studies of Interatomic Distances in Halides and Chalcogenides. *Acta Cryst. Sect A.* 32 (5), 751–767. doi:10.1107/S0567739476001551

Siegel, N. P., Miller, J. E., Ermanoski, I., Diver, R. B., and Stechel, E. B. (2013). Factors Affecting the Efficiency of Solar Driven Metal Oxide Thermochemical Cycles. *Ind. Eng. Chem. Res.* 52 (9), 3276–3286. doi:10.1021/ie400193q

Singstock, N. R., Bartel, C. J., Holder, A. M., and Musgrave, C. B. (2020). High-Throughput Analysis of Materials for Chemical Looping Processes. *Adv. Energ. Mater.* 10 (27), 2000685. doi:10.1002/aenm.202000685

Smestad, G. P., and Steinfeld, A. (2012). Review: Photochemical and Thermochemical Production of Solar Fuels from H2O and CO2 Using Metal Oxide Catalysts. *Ind. Eng. Chem. Res.* 51 (37), 11828–11840. doi:10.1021/ie3007962

Steinfeld, A. (2005). Solar Thermochemical Production of Hydrogen-Aa Review. *Solar Energy* 78 (5), 603–615. doi:10.1016/j.solener.2003.12.012

Tamaura, Y., Steinfeld, A., Kuhn, P., and Ehrensberger, K. (1995). Production of Solar Hydrogen by a Novel, 2-Step, Water-Splitting Thermochemical Cycle. *Energy* 20 (4), 325–330. doi:10.1016/0360-5442(94)00099-O

Toby, B. H., and Von Dreele, R. B. (2013). GSAS-II: The Genesis of a Modern Open-Source All Purpose Crystallography Software Package. *J. Appl. Cryst.* 46, 544–549. doi:10.1107/s0021889813003531

Vasala, S., and Karppinen, M. (2015). A2B′B″O6 Perovskites: A Review. *Prog. Solid State. Chem.* 43 (1), 1–36. doi:10.1016/j.progsolidstchem.2014.08.001

Wiglusz, R. J., Kordek, K., Małecka, M., Ciupa, A., Ptak, M., Pazik, R., et al. (2015). A New Approach in the Synthesis of La1−xGdxFeO3 Perovskite Nanoparticles - Structural and Magnetic Characterization. *Dalton Trans.* 44 (46), 20067–20074. doi:10.1039/C5DT03378K

Yang, C.-K., Yamazaki, Y., Aydin, A., and Haile, S. M. (2014). Thermodynamic and Kinetic Assessments of Strontium-Doped Lanthanum Manganite Perovskites for Two-step Thermochemical Water Splitting. *J. Mater. Chem. A.* 2 (33), 13612–13623. doi:10.1039/C4TA02694B

Conflict of Interest: The authors declare that the research was conducted in the absence of any commercial or financial relationships that could be construed as a potential conflict of interest.

Publisher's Note: All claims expressed in this article are solely those of the authors and do not necessarily represent those of their affiliated organizations, or those of the publisher, the editors and the reviewers. Any product that may be evaluated in this article, or claim that may be made by its manufacturer, is not guaranteed or endorsed by the publisher.

frontiers in Energy Research

ORIGINAL RESEARCH
published: 01 December 2021
doi: 10.3389/fenrg.2021.734288

Techno-Economic Analysis of a Concentrating Solar Power Plant Using Redox-Active Metal Oxides as Heat Transfer Fluid and Storage Media

*Brandon T. Gorman[1], Mariana Lanzarini-Lopes[1], Nathan G. Johnson[2], James E. Miller[3] and Ellen B. Stechel[3]**

[1]The School of Sustainable Engineering and the Built Environment, Arizona State University, Tempe, AZ, United States, [2]The Polytechnic School, Arizona State University, Mesa, AZ, United States, [3]ASU LightWorks, The School of Molecular Sciences, Arizona State University, Arizona State University, Tempe, AZ, United States

We present results for a one-dimensional quasi-steady-state thermodynamic model developed for a 111.7 MW_e concentrating solar power (CSP) system using a redox-active metal oxide as the heat storage media and heat transfer agent integrated with a combined cycle air Brayton power block. In the energy charging and discharging processes, the metal oxide $CaAl_{0.2}Mn_{0.8}O_{2.9-\delta}$ (CAM28) undergoes a reversible, high temperature redox cycle including an endothermic oxygen-releasing reaction and exothermic oxygen-incorporation reaction. Concentrated solar radiation heats the redox-active oxide particles under partial vacuum to drive the reduction extent deeper for increased energy density at a fixed temperature, thereby increasing storage capacity while limiting the required on sun temperature. Direct counter-current contact of the reduced particles with compressed air from the Brayton compressor releases stored chemical and sensible energy, heating the air to 1,200°C at the turbine inlet while cooling and reoxidizing the particles. The cool oxidized particles recirculate through the solar receiver subsystem for another cycle of heating and reduction (oxygen release). We applied the techno-economic model to 1) size components, 2) examine intraday operation with varying solar insolation, 3) estimate annual performance characteristics over a simulated year, 4) estimate the levelized cost of electricity (LCOE), and 5) perform sensitivity analyses to evaluate factors that affect performance and cost. Simulations use hourly solar radiation data from Barstow, California to assess the performance of a 111.7 MW_e system with solar multiples (SMs) varying from 1.2 to 2.4 and storage capacities of 6–14 h. The baseline system with 6 h storage and SM of 1.8 has a capacity factor of 54.2%, an increase from 32.3% capacity factor with no storage, and an average annual energy efficiency of 20.6%. Calculations show a system with an output of 710 GWh_e net electricity per year, 12 h storage, and SM of 2.4 to have an installed cost of $329 million, and an LCOE of 5.98 ¢/kWh_e. This value meets the U.S. Department of Energy's SunShot 2020 target of 6.0 ¢/kWh_e (U. S Department of Energy, 2012), but falls just shy of the 5.0 ¢/kWh_e 2030 CSP target for dispatchable electricity (U. S Department of Energy, 2017). The cost and performance results are minimally sensitive to most design parameters. However, a one-point change in the weighted annual cost of capital from 8 to

OPEN ACCESS

Edited by:
Alfonso J. Carrillo, Instituto de Tecnología Química (ITQ), Spain

Reviewed by:
Miguel Angel Reyes-Belmonte, Rey Juan Carlos University, Spain
Nick AuYeung, Oregon State University, United States

***Correspondence:**
Ellen B. Stechel
ellen.stechel@asu.edu

Specialty section:
This article was submitted to Solar Energy, a section of the journal Frontiers in Energy Research

Received: *30 June 2021*
Accepted: *26 August 2021*
Published: *01 December 2021*

Citation:
Gorman BT, Lanzarini-Lopes M, Johnson NG, Miller JE and Stechel EB (2021) Techno-Economic Analysis of a Concentrating Solar Power Plant Using Redox-Active Metal Oxides as Heat Transfer Fluid and Storage Media. Front. Energy Res. 9:734288. doi: 10.3389/fenrg.2021.734288

7% (better understood as a 12.5% change) translates directly to an 11% decrease (0.66 ¢/kWhe) in the LCOE.

Keywords: concentrating solar power, redox active metal oxide materials, thermochemical cycles, renewable energy, techno-economic analysis, thermochemical energy storage

INTRODUCTION

Global energy production from concentrating solar power (CSP) is expected to increase from 12 TWh in 2018 to an estimated 67–153 TWh in 2035, depending on the scenario (International Energy Agency, 2019). Total global installed capacity of CSP was 6.451 GW in 2019 (Helioscsp, 2020). IEA reports that as of the latter half of 2020 projects totaling almost 2 GW of additional capacity were under construction with 17 of the 18 projects incorporating some form of storage, e.g., molten salt (International Energy Agency, 2020). Empirical data from installed systems indicates that CSP technologies can achieve cost reductions, comparable to the reductions seen in solar photovoltaic (PV), from continued technology innovation, learning through deployment, and increased commercial competition (Lilliestam et al., 2017). CSP technologies with thermal energy storage (TES) and thermochemical energy storage (TCES) offer additional benefits in providing firm power, peak power support, and off-sun power for utility-scale generation in locations with abundant direct solar radiation (Mendelsohn et al., 2012; U.S. Department of Energy, 2014b).

CSP designs include power towers, parabolic troughs, linear Fresnel reflectors, and parabolic dishes. The higher operating temperatures of power towers, compared to parabolic trough and linear Fresnel designs, have a thermodynamic advantage that translates into cost reductions per unit energy produced (Behar et al., 2013). Basic power tower designs include five constituent systems: 1) a solar field for concentrating solar energy onto a receiver, 2) an elevated solar receiver to capture solar radiation reflected from the field, 3) heat transfer fluid(s) (HTF) to transport heat from the receiver to the power block, 4) heat exchanger(s) to transfer heat between HTF's in the system, and 5) a power block to convert thermal energy into electric power. Most deployments today use TES to increase plant productivity, mitigate solar resource intermittency, and shift or extend production to off-sun hours. Advanced designs could use TCES as concepts evolve from laboratory R&D to a commercial ready state. CSP systems with energy storage allow utilities to schedule electricity generation from solar power (Gil et al., 2010; Denholm and Hummon, 2012). The ability to dispatch solar power is helpful for utilities seeking to avoid "duck curve" events in system net load that occur when solar photovoltaic (PV) output peaks mid-day and then declines in the late afternoon as residential loads increase (Janko et al., 2016). Further, energy storage can extend operating hours of the power block and increase capacity factors from 27 to 80% (Renewable Energy Policy Network for the 21st Century (REN21), 2015), and thereby reduce the levelized cost of energy (LCOE) (Price and Kearney, 2003; Stoddard et al., 2006; Renewable Energy Policy Network for the 21st Century (REN21), 2015). Currently installed CSP systems reached 10.3 ¢/kWh in 2017 (Mehos et al., 2016) with lower LCOE reflected in many bids for new projects. These vary by region, with successful bids reported to be as low as 6.3 ¢/kWh in Australia (Shemer, 2018a), 7.1 ¢/kWh in Morocco, and 7.3 ¢/kWh in Dubai (CSP Focus, 2019). An unsuccessful bid for a project in Chile was reported to be less than 5.0 ¢/kWh (Shemer, 2018a). Recent technical advancements in HTFs and materials are helping increase system performance and decrease cost (Liu et al., 2016).

This study develops and applies a techno-economic model of a 111.7 MW_e CSP system with a redox-active metal oxide (MO) acting as both the HTF and TCES media. The techno-economic model provides a means to 1) size components, 2) examine intraday operation with varying solar insolation, 3) calculate annual performance over a simulated year, 4) estimate the LCOE, and 5) perform sensitivity analyses to evaluate factors that affect performance and cost. Application of the model to the modern Ivanpah solar generating facility operating in California, USA provided validation. The validated model indicates that an LCOE less than 6.0 ¢/kWh_e is achievable given the cost assumptions for operation and maintenance and solar field (with site preparation) of 40 \$/kW_e-yr and 85 \$/m^2, respectively, for a 111.7 MW_e CSP system installed with 12 h storage and SM of 2.4.

BACKGROUND

It is well known that higher temperatures (higher exergy) permit increased thermodynamic efficiency in power generation. However, current CSP plants operate at relatively low temperatures due to limitations in plant design (e.g., solar receiver geometry), physical and chemical properties of CSP materials, and thermal limitations of HTFs. The use of multiple fluids in a single CSP system such as oil in the solar receiver, molten salt in thermal energy storage, and steam in the power block (Glatzmaier, 2011) can be partly mitigate these challenges. However, for systems utilizing only sensible energy, the fluid with the lowest upper temperature boundary still limits the maximum possible temperature in the power block.

Molten salt and synthetic oils are HTFs commonly used in solar applications. Parabolic trough and linear Fresnel systems typically use synthetic oils, while power tower systems often utilize molten salts (Solar Power and Chemical Energy Systems (SolarPACES), 2020). Molten nitrate salts are preferable to oils for sensible heat storage due to their improved thermal stability, high thermal conductivity, low vapor pressure and viscosity, and relatively high energy density (Gil et al., 2010; Glatzmaier, 2011; Tian and Zhao, 2013; Vignarooban et al., 2015). However, the nitrate molten

salt operating temperature range is 220°C–565°C (bounded by fusion and decomposition temperatures, respectively). These relatively low temperatures necessarily result in low (Carnot limited) power block efficiencies. Phase-changing materials are alternatives that capitalize on large latent heats for fusion and vaporization to increase stored energy density and raise operating temperatures (Zalba et al., 2003; Farid ewhich offer several advantagest al., 2004; Gil et al., 2010; Kuravi et al., 2013). Materials that undergo solid-liquid transitions have lower volumetric expansion when compared to liquid-gas transitions (Kuravi et al., 2013), yet solid-phase materials have lower thermal conductivity and are more difficult to transport than fluids (Regin et al., 2008). Solid phase-changing materials presently have limited applications within dish-Stirling engine systems wherein heat transfer occurs isothermally (Shabgard et al., 2013; Sharifi et al., 2015).

Materials that undergo a thermochemical reaction also have the potential to improve energy density, increase operating temperatures, and in some cases can act as the both HTF and storage media (Gil et al., 2010). Particle-based systems of this type build on the foundation of inert particle sensible energy systems being developed, e.g., for application to super-critical CO_2 (sCO_2) power cycles (Albrecht et al., 2020; González-Portillo et al., 2021). Ongoing research is evaluating the use of redox-active MO particles as a means of capturing and storing solar energy as a combination of sensible and chemical energy (General Atomics Project Staff, 2011; Neises et al., 2012; Pardo et al., 2014; Babiniec et al., 2015a; Miller et al., 2016). For these materials, solar energy heats particles above the temperature at which an endothermic reduction reaction liberates oxygen. The energetically charged MO can be stored or used immediately to heat compressed air from the compressor of an air Brayton power block, as studied herein. Both the sensible heat and heat from the reoxidation reaction are exchanged when reduced particles come into direct contact with the compressed air. Oxygen content is restored in the particles as oxygen molecules are removed from the gas phase. While binary metal oxides such as cobalt oxide, which cycles between Co_3O_4 and CoO, are considered to be options for this purpose (Ho and Iverson, 2014; Muroyama et al., 2015; Bush et al., 2017; Schrader et al., 2017), this study focuses on a specific group of MOs known as mixed ionic-electronic conductors (MIECs) which offer several advantages:

- Highly tunable—Thermodynamic properties manipulated through compositional variations.
- Cost reduction—Expensive constituent elements avoided through compositional variations.
- Swift utilization of bulk particles—Fast oxygen ion transport facilitates rapid and complete utilization of the capacity for reaction, i.e., mass transfer limitations do not confine the reactions to near surface regions.
- High operating temperatures—MOs remain stable at much higher temperatures than oil and molten nitrate salts, offering the opportunity to improve system efficiency.
- High energy density—Both sensible and chemical energy are stored.
- Stability over a large number of cycles—Minimal performance loss from potential chemical degradation

In the current work, we assume the use of a calcium-, aluminum-, and manganese-containing perovskite as it offers a reasonable reduction enthalpy at low material cost, fast kinetics, and superior mass specific heat capacity (Babiniec et al., 2015a; Miller et al., 2016). Related materials were reported for indirectly providing lower temperature heat to sCO_2 power cycles (Imponenti et al., 2018; Albrecht et al., 2018). The material remains in the solid state up to at least 1,250°C (Babiniec et al., 2015a) and does not undergo major crystalline phase transitions, even while undergoing compositional changes (loss and uptake of oxygen). **Eq. 1** shows the general form of a reversible perovskite reduction/reoxidation reaction where the reduction extent depends on temperature and partial pressure of oxygen (Babiniec et al., 2015a; Babiniec et al., 2015b; Miller et al., 2016):

$$\frac{1}{\delta}ABO_{3-x} \leftrightarrow \frac{1}{\delta}ABO_{3-x-\delta} + \frac{1}{2}O_2(g) \tag{1}$$

The specific perovskite composition considered herein is $CaAl_{0.2}Mn_{0.8}O_{2.9-\delta}$ (CAM28), where the A-site cation is Ca, and the B-site is shared by Al and Mn. Reduction extents as large as $\delta = 0.322$ have been measured for this material, and are reported alongside reaction enthalpies, which vary a function of reduction extent (Babiniec et al., 2015a).

THERMODYNAMIC MODEL DEVELOPMENT

The one-dimensional thermodynamic model consists of nine system components including five power tower components (solar receiver, hot storage, reoxidation reactor, cold storage, and heat exchanger), two auxiliary components (vacuum pump, particle lift), the solar field, and power block. The **Supplementary Material** presents the full set of 154 thermodynamic equations for these components; we summarize them herein. We developed computational procedures in Python with fluid thermodynamic properties taken from CoolProp (Bell et al., 2014). We developed a separate model of the power block in Engineering Equation Solver (EES) to validate results against available manufacturer values and theoretical limits.

System Overview

Figure 1A provides a conceptual illustration of the process in which the solar field reflects and concentrates direct normal irradiance (DNI) into the solar receiver reduction reactor (SR3). Gravity feeds oxidized particles through the SR3 where they are heated and endothermically reduced. A pump expels evolved oxygen and maintains a partial vacuum, and hence low oxygen partial pressure, in the SR3. Reduced particles exiting the SR3 can be stored in an insulated hot storage bin. Gravity feeds reduced particles from the hot storage bin into the reoxidation reactor (ROx) to come into direct contact with pressurized air

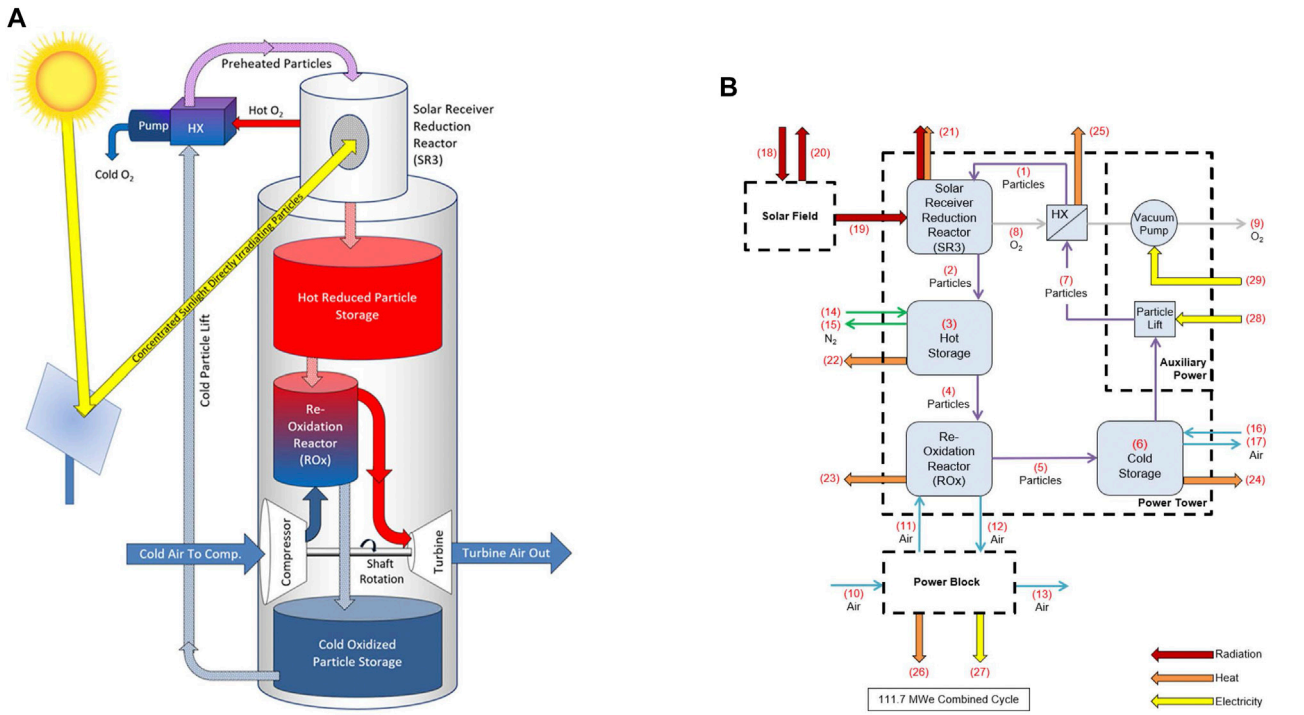

FIGURE 1 | (A) Conceptual diagram of the CSP/TCES system (Miller and Gill, 2020), and **(B)** accompanying schematic indicating mass and energy flows for the four major subsystems: solar field, power tower, power block, and auxiliary power.

TABLE 1 | CAM28 particle characteristics.

Variable	Value	Units	Description
M_p	135.82	g/mol	Molar mass
ρ_p	3,942	kg/m^3	Particle density[a]
$C_{P,p}$	125.91	J/mol-K	Specific heat[b]
ΔH_{rxn}	320,000	J/mol-O_2	Reduction enthalpy[a]
D_p	0.00013	M	Diameter
C_d	0.50	—	Drag coefficient (sphere)[c]
δ	0.2367	—	Reduction extent

[a]*Babiniec et al., 2015a.*
[b]*Coker et al., 2016.*
[c]*The Engineering Toolbox, 2004.*

(*via* the gas turbine compressor) flowing counter-current to the particles (**Supplementary Figure S2**). The resulting heat transfer and exothermic reoxidation reaction effectively increases the air to a temperature approaching 1,200°C. Heated air exiting the ROx flows to a combined cycle power block for electricity generation. Reoxidized particles can be stored in cold storage or sent back to the SR3 using a particle lift to repeat the thermodynamic cycle. A recuperating heat exchanger between high-temperature oxygen exiting the SR3 and low-temperature reduced particles entering the SR3 is included as to improve system efficiency and partially cool the O_2.

A quasi-steady state thermodynamic model has been developed for the process. **Figure 1B** depicts the associated block diagram of components and mass and energy flows. Each component has input and output states that are solved directly or through iterative computation (e.g., the oxygen and particle streams between the SR3 and heat exchanger components are interdependent). High-temperature particle receivers for PROMOTES and other applications remain in developmental, pre-commercial stages (Muroyama et al., 2015; Ho, 2017). However, for demonstration purposes, a reactor was developed wherein particles were directly irradiated as they flowed down an inclined plane (see, for example, Schrader et al., 2020).

Therefore, the SR3 model is simplified to a concentric cylindrical geometry with adequate size for an inclined plane (**Supplementary Figure S3**). There is interior cavity for particle flow, cavity insulation, evacuated space, and then exterior shell for maintaining structural integrity, along with a quartz window. The ROx model is a set of cylindrical pipes in which falling particles and rising air come into direct contact to undergo simultaneous chemical and sensible heat exchange.

Thermodynamic Input Data

Table 1 provides the characteristics for the CAM28 particles. Molar mass (M_p) was determined from the molecular formula and specific heat was taken from experimental measurements (Coker et al., 2016). Particle diameter (D_p) was chosen as 130 microns, which is between the 100 and 150 microns suggested by a corresponding computational fluid dynamics (CFD) model of the ROx reactor (Babiniec, S.M., personal communication, 2018). Particle reduction was assumed to occur at 1,125°C and 200 Pa,

TABLE 2 | Fixed temperatures (°C).

Variable	Value	Description
T_2	1,125	Particles from SR3 to hot storage
T_5	393 (T_{11})	Particles from ROx to cold storage
T_8	1,125 (T_2)	Oxygen from SR3 to heat exchanger
T_{10}	25	Ambient air into Brayton engine compressor
T_{11}	393	Air from Brayton engine compressor into ROx
T_{12}	1,200	Air from ROx into Brayton engine turbine
T_{13}	574	Exhaust air from Brayton engine turbine
T_{14}	25	Nitrogen into hot storage
T_{16}	25	Air into cold storage

resulting in a reduction extent (δ) of 0.2367 (interpolated from experimental measurements).

Nine of the mass flow streams shown in **Figure 1B** have fixed temperatures (given in **Table 2**), while other state point temperatures varied during calculations. The corresponding CFD model of the ROx indicated that particle outlet (T_2) and oxygen outlet (T_8) temperatures from the SR3 should be set to 1,125°C for the ROx to achieve 1,200°C for air turbine inlet temperature (T_{12}). ROx particle outlet temperature (T_5) is set equal to ROx air inlet temperature (T_{11}) as a simplifying approximation. Compressor air inlet temperature (T_{10}) is set to ambient. Turbine air exhaust temperature (T_{13}) is set using manufacturer specifications of the gas turbine of the Ansaldo Energia AE64.3A combined cycle engine (Ansaldo Energia, 2013). Air inlet (T_{11}) and air outlet (T_{12}) temperatures about the ROx correspond to AE64.3A compressor outlet and turbine inlet temperatures, respectively, as evaluated using the EES model described in **Supplementary Material**. Nitrogen (T_{14}) and air (T_{16}) are assumed to enter hot storage and cold storage, respectively, at ambient temperature to maintain atmospheric pressure and isolating the reduced particles from air and premature reactive discharge.

Table 3 provides input values for the ROx, SR3, heat exchanger, particle lift, vacuum pump, hot storage, and cold storage components. Air pressure (P_{comp}^{ROx}) and molar flow rate ($\dot{n}_{air}^{ROx}$) through the ROx are set equal to parameters given from the AE64.3A gas turbine specifications (Ansaldo Energia, 2013). Total particle residence time (t_r^{ROx}) within the ROx is approximated as the sum of residence time for particle reoxidation (t_{ox}^{ROx}) and residence time for sensible energy exchange (t_{ex}^{ROx}) to reach ROx boundary states. A lumped-capacitance model of a falling particle in the ROx provide an approximate residence time for sensible energy exchange. This results in a total particle residence time of 4 s, comparable to the 3.6 s of the corresponding CFD model of the ROx.

Thermal loss calculations for the ROx, SR3, hot storage, and cold storage use the conduction, convection, and radiation parameters given in **Table 3**. The ROx (k_{ins}^{ROx}, t_{ins}^{ROx}) and SR3 (k_{ins}^{SR3}, t_{ins}^{SR3}) insulation material is 1.5 inches of Zircar's RSLE-57 (ZIRCAR Refractory Composites, Inc., 2005), a reinforced silica matrix composite used in similar high-temperature receivers for its durability at high temperatures (Christian and Ho, 2016). The SR3 main body (k_{body}^{SR3}, t_{body}^{SR3}) is 1.0 inch of 304 stainless steel (Aerospace Specification Metals, Inc. AISI Type 304 Stainless Steel) rather than HD board reported elsewhere (Christian and Ho, 2016) as additional structural support was assumed necessary. The SR3 ratio of the cavity's interior surface area to aperture area (γ_{lr}) is taken as a design choice and evaluated further in sensitivity analysis.

The solar field efficiency (η_{sf}) uses the midpoint of reported annual average values of 52 and 64% (Ehrhart and Gill, 2013; Eddhibi et al., 2015). The SR3 has a minimum operating DNI (DNI_{co}) of 350 W/m^2 as a conservative estimation, whereas 300 W/m^2 was used elsewhere (Zhang et al., 2010). The solar flux at the receiver aperture (F_{avg}) assumes a concentration ratio of 2,000 suns (Zhang et al., 2013); i.e., 2 MW/m^2 at the design point DNI (DNI_{dp}). Calculations assume a conservative 1 m diameter for the SR3 quartz window (D_{win}); values up to 1.7 m diameter have been reported in designs for some high-pressure receivers (Karni et al., 1998; Saung and Miller, 2014). The electric-to-mechanical efficiency of the particle lift (η_{lift}) is assumed similar to mine hoists (de la Vergne, 2003), and the electrical efficiency of the vacuum pump (η_{pump}) is set to 40% (see **Supplementary Material Section 7**).

Hot (k_{ins}^{HS}, t_{ins}^{HS}) and cold (k_{ins}^{CS}, t_{ins}^{CS}) storage insulation includes a combination of firebrick, perlite concrete, and reinforced concrete (El-Leathy et al., 2014; Ho et al., 2014) that have thermal conductivities of 0.21–0.57 W/m-K, 0.078–0.35 W/m-K, and 0.99–1.10 W/m-K, respectively, at high temperatures (Christy Refractories, 2004; Kanbur et al., 2013; Perlite Institute, Inc., 2014). **Table 4** provides layer thicknesses alongside costs. Overall, thermal conductivity for storage insulation was approximated as 0.5 W/m-K, a conservative estimate relative to 0.31 W/m-K calculated for the firebrick, perlite concrete, and reinforced concrete layers in series.

Thermodynamic Performance Metrics

Performance was evaluated using annual system efficiency and capacity factor averages of time series simulations. Simulations of system operation are indexed into discrete time increments (minutes, 15-minutes, hours, etc.) using i with 1 and ζ corresponding to the first and last indices, respectively, of the simulated year (e.g., ζ = 8760 when using hours). If the simulated time step resolution is finer than the DNI data set's resolution, the simulated time indices use repeated DNI values (instead of interpolated) that correspond to their time period in the DNI data set (e.g., all simulated time indices in hour 1 use the DNI value corresponding to hour 1). High resolution time stepping simulates a more continuous dispatch schedule that avoids the problem of discarding an entire hour if storage or dispatch limits would be exceeded within that hour increment; i.e. it reduces spillage. Annual generation increases by up to 11% when using 5-min time steps and up to 10% when using 10-minute time steps at small storage sizes (e.g., 2 hours) relative to hourly time steps. Computational cost increases significantly when increasing time step resolution from 10-minute to 5-min time steps but yields negligible thermal performance increase for storage sizes larger than 4 hours. Therefore, performance simulations reported here employ 10-minute time steps.

TABLE 3 | Component specifications.

Component	Variable	Value	Units	Description
ROx	P_{comp}^{ROx}	1,692,127.50	Pa	Air pressure inside the ROx
	$\dot{n}_{air}^{ROx}$	7,344.83	mol/s	Air molar flow rate through the ROx
	t_{ins}^{ROx}	0.0381	M	Thickness of ROx insulation
	k_{ins}^{ROx}	0.750	W/m-K	Thermal conductivity of ROx pipe insulation
	t_{ox}^{ROx}	1	S	Residence time for chemical energy exchange in the ROx[a]
	t_{ex}^{ROx}	3	S	Residence time for sensible energy exchange in the ROx
	t_{r}^{ROx}	4	S	Total particle residence time in the ROx
Power block	η_{pb}	53.5	%	Combined cycle efficiency[b]
	P_{pb}	111.7	MW_e	Combined cycle rated power output[b]
SR3 and solar field	$P_{O_2}^{SR3}$	200.00	Pa	Partial pressure of oxygen inside the SR3[c]
	DNI_{dp}	900	W/m^2	DNI used in design point system sizing
	DNI_{co}	350	W/m^2	DNI cutoff below which CSP is not operated
	η_{sf}	58	%	Solar field efficiency
	ε_{ap}	1.00	—	Emissivity for SR3 radiation losses (blackbody)
	ε_{ins}	0.80	—	Emissivity of SR3 insulation (silica RSLE-57)[d]
	ε_{body}	0.70	—	Emissivity of SR3 main body (304 stainless steel)[e]
	D_{win}	1.00	M	Diameter of each SR3 receiver window
	F_{avg}	2,000,000	W/m^2	Average solar flux density at receiver aperture
	γ_{cav}	33	—	Ratio of SR3 cavity interior surface to aperture areas
	γ_{lr}	2	—	Ratio of SR3 cavity length to cavity radius[c]
	t_{ins}^{SR3}	0.0381	M	Thickness of SR3 insulation
	t_{body}^{SR3}	0.0254	M	Thickness of SR3 main body
	k_{ins}^{SR3}	0.75	W/m-K	Thermal conductivity of SR3 insulation
	k_{body}^{SR3}	16.00	W/m-K	Thermal conductivity of SR3 main body
Heat exchanger, particle lift, and vacuum pump	U^{HX}	12	W/m^2-K	Heat transfer coefficient for oxygen-to-air heat exchanger[f]
	ϵ^{HX}	85	%	Heat exchanger effectiveness at design point
	H_{lift}	135	M	Height of particle lift[g]
	η_{lift}	80	%	Efficiency of particle lift
	η_{pump}	40	%	Efficiency of vacuum pump
	ML_{min}	20	%	Minimum motor loading[h]
Hot storage and cold storage	u	10	%	Ullage space for particle storage
	ϱ_p	65	%	Particle packing density in storage (spheres)[i]
	HD^{HS}	1.5	—	Ratio of storage bin height to diameter
	t_{ins}^{HS}	0.715	M	Hot storage insulation thickness
	k_{ins}^{HS}	0.5	W/m-K	Hot storage insulation thermal conductivity
	t_{ins}^{CS}	0.715	M	Cold storage insulation thickness
	k_{ins}^{CS}	0.5	W/m-K	Cold storage insulation thermal conductivity

[a]*Imponenti et al., 2016.*
[b]*Ansaldo Energia, 2013.*
[c]*Schrader et al., 2017.*
[d]*Schrader et al., 2015.*
[e]*Mikron Instrument Company, Inc 2014.*
[f]*The Engineering Toolbox, 2003.*
[g]*Collado and Guallar, 2013.*
[h]*U.S. Department of Energy, 2014a.*
[i]*Jaeger and Nagel, 1992.*

TABLE 4 | Parameter values for economic evaluations.

Component	Variable	Description	Value	Units	Notes
ROx/SR3	$C_{m,r}$	Material cost	1,160	$/m^2	Unpublished data for work described in[a]
	$F_{m,r}$	Material factor	2	—	Estimate to account for material fabrication
Power block	$F_{t,p}$	Turbine prefactor	4,768	$/kW	[b]Turbine factors based on a power law fit from existing turbines of various rated powers and costs. 10% reduction in cost of the power block assumed to account for replacing the power block combustor with the ROx
	$F_{t,s}$	Scale factor	–0.260	—	
	$F_{t,i}$	Installation factor	2	—	
	F_{rc}	ROx deduction	10	%	
	$F_{t,c}$	Complexity factor	1.35	—	
Solar field	C_{sf}	Cost of field	85	$/m^2	[c]Costs of the solar field based on DOE SunShot targets, i.e., improvements on current commercial technology incorporated into these values
Heat exchanger, particle lift, and vacuum pump	$C_{hx,b}$	HX base cost	13,832	$	The vacuum pump (VP) and heat exchanger (HX) costs were scaled based on published costs estimations from[d,e] respectively. Both were adjusted to 2015 costs with CEPCI values
	$C_{hx,a}$	Cost per area	185	$/m^2	
	Vp_0	VP base cost	4,041	$	
	Vp_1	VP scaling cost	1,600	$/kWh	
	F_{se}	Elevator scaling	2,600	$	Scaled based on[a] and adjusted to 2015 prices
Hot storage and cold storage	C_{ng}	N_2 generator cost	300,000	$	Capital cost of purchasing a nitrogen generator[f]
	$c_{ins,0}$	Insulating layers 0–4 costs	110,000	$/m^3	Volume of insulation scales with storage size at fixed thicknesses of 0.005, 0.115, 0.37, 0.025, 0.2 m for layers 0: compatibility layer 1: insulating firebrick, 2: perlite concrete, 3: expansion board, 4: reinforced concrete respectively. Values where obtained from[g]
	$c_{ins,1}$		11,000	$/m^3	
	$c_{ins,2}$		4,700	$/m^3	
	$c_{ins,3}$		5,200	$/m^3	
	$c_{ins,4}$		1,050	$/m^3	
	$F_{c,misc}$	Miscellaneous	5	%	
	A_{hs}		A_{hs}	A_{hs}	A_{hs}
	F_V	Upper hopper to lower hopper volume ratio	18	%	lower hopper and upper hopper to collect output from lift
	CF_{uh}	Complexity Factor	3	—	Upper hopper complexity relative to lower hopper
Particles	C_{pa}	Particle cost	1	$/kg	[h]Cost of production of the specific composition of the material
	M_{pa}	Particle Multiplier	2	—	Estimate to account for the capital equipment and utilities in the synthesis of the particles
Tower	F_{ps}	Prescaling factor	26,582	$	[i]Based on a fit from existing installed CSP tower costs, where the cost varies with the receiver rating adjusted to 2015
	F_s	Scaling factor	0.95	—	
Cost multipliers	P_s	Setting percent	20	%	Values from[j]
	M_e	Electrical multiplier	8.4	%	
	Mu_p	Piping multiplier	6.0	%	
Other financial metrics	C_{con}	Contingency	25	%	[k,l]These values represent conservative choices from an array of published options. Validation of these choices included the reproducibility of Ivanpah solar power plant (see **Supplementary Material**.). C_{omi} is a SunShot target. Particle replacement is inferred from[m], see **Supplementary Material**.
	F_{own}	Owners fraction	17	%	
	$WACC$	Weighted avg. cost of capital	8	%/year	
	C_{omi}	Yearly operating costs	40	$/kW$_e$-yr	
	F_{rep}	Particle replacement	10	%/year	

[a]*Ho et al., 2014.*
[b]*Nye Thermodynamics Corp 2016. Gas Turbine Prices - $ per kW.*
[c]*Laird, 2011.*
[d]*US Vacuum Pumps 2017.*
[e]*Loh et al., 2002.*
[f]*Proprietary vendor quote.*
[g]*El-Leathy et al., 2014.*
[h]*InfoMine Inc 2016.*
[i]*Sargent & Lundy LLC Consulting Group, 2003.*
[j]*Peters and Timmerhaus, 2003.*
[k]*US Energy Information Administration, 2014.*
[l]*US Energy Information Administration, 2015.*
[m]*Ryden et al., 2014.*

TABLE 5 | Scaling equations for equipment costs.

Component	Cost equation
Particles	$C_{pa} = m_{pa} \cdot M_{pa} \cdot C_{pa,i}$
SR3	$C_{SR3} = C_{m,r} \cdot F_{m,r} \cdot A_{SR3} \cdot N_{rec} \cdot (1 + P_s)$
Hot storage	$C_{sH} = (\sum_{i=0}^{4} c_i) \cdot (1 + F_{c,misc}) + C_{ng}$
Lower hopper	$C_{sLH} = A_{hs} \cdot C_{m,r} \cdot F_{m,r} \cdot (1 + P_s) \cdot F_{SV}^{2/3}$
Upper hopper	$C_{UH} = CF_{uh} \cdot A_{hs} \cdot C_{m,r} \cdot F_{m,r} \cdot (1 + P_s) \cdot F_V^{2/3}$
ROx	$C_{ROx} = A_{ROX} \cdot C_{m,r} \cdot F_{m,r} \cdot (1 + P_s)$
Heat exchanger	$C_{HX} = C_{hx,b} + C_{hx,a} \cdot A_{hx}$
Vacuum pump	$C_{vp} = (Vp_0 + Vp_1 \cdot (\dot{E}_{29}/N^{SR3})) \cdot (1 + P_s + M_e + Mu_p) \cdot N^{SR3}$
Power block	$C_{pb} = (1 - F_{rc}) \cdot F_{t,i} \cdot F_{t,c} \cdot P_R \cdot F_{t,p} \cdot (P_R^{F_{t,s}}(1 + P_s + M_e + Mu_p))$
Solar field	$C_{sf} = A_{sf} \cdot (C_{sf})$
Tower	$C_{tower} = (1 + P_s + M_e) \cdot F_{ps} \cdot R_{rating}^{F_s}$
Elevator	$C_{elevator} = F_{se} \cdot R_{rating}$

Annual average system efficiency ($\overline{\eta_{sys}}$) is calculated using **Eq. 2** as the product of the annual average efficiencies of four subsystems as given in **Eqs 3–6**. Annual average solar field efficiency ($\overline{\eta_{sf}}$) from **Eq. 3** is less than rated efficiency (η_{sf}) due to the lower bound DNI cutoff value and losses due to spillage. Annual average power tower efficiency ($\overline{\eta_{pt}}$) is calculated using **Eq. 4** as the net thermal energy input to the air Brayton turbine divided by the net thermal energy input to the SR3. This quantity also accounts for changes (from losses) in energy storage of the hot and cold storage bins from the initial hour of operation to the last hour of operation. Annual average power block efficiency ($\overline{\eta_{pb}}$) is calculated using **Eq. 5** as the ratio of the annual net electric generation to the thermal energy input to the air Brayton turbine. Annual average auxiliary subsystem efficiency ($\overline{\eta_{aux}}$) is calculated using **Eq. 6** as 100% minus the ratio of annual electricity used for work (particle lift and vacuum pump) to the annual net turbine electric generation. System capacity factor (CF_{sys}) is calculated using **Eq. 7** as the summation of the actual net electricity generation for the year divided by the maximum electricity generation at full capacity for a year.

$$\overline{\eta_{sys}} = \overline{\eta_{sf}} \cdot \overline{\eta_{pt}} \cdot \overline{\eta_{pb}} \cdot \overline{\eta_{aux}} \tag{2}$$

$$\overline{\eta_{sf}} = \frac{\sum_{i=1}^{\zeta} (E_{19}^i)}{\sum_{i=1}^{\zeta} (E_{18}^i)} \tag{3}$$

$$\overline{\eta_{pt}} = \frac{\sum_{i=1}^{\zeta} (E_{12}^i - E_{11}^i) + E_{HS}^{\zeta} + E_{CS}^{\zeta}}{\sum_{i=1}^{\zeta} (E_{19}^i) + E_{HS}^1 + E_{CS}^1} \tag{4}$$

$$\overline{\eta_{pb}} = \frac{\sum_{i=1}^{\zeta} (E_{27}^i)}{\sum_{i=1}^{\zeta} (E_{12}^i - E_{11}^i)} \tag{5}$$

$$\overline{\eta_{aux}} = 1 - \frac{\sum_{i=1}^{\zeta} (E_{28}^i + E_{29}^i)}{\sum_{i=1}^{\zeta} (E_{27}^i)} \tag{6}$$

$$CF_{sys} = \frac{\sum_{i=1}^{\zeta} (E_{27}^i)}{\zeta \cdot P_{pb}} \tag{7}$$

ECONOMIC MODEL DEVELOPMENT

A validated cost model populated with component sizes from the thermodynamic model gives estimates for the initial capital costs, operating and maintenance costs, and LCOE of the full-scale CSP system. Applying the model to the Ivanpah CSP power plant provided the validation. (See **Supplementary Material Section 3.4**).

Economic Input Data

Table 4 summarizes parameters applied to estimate the total installed project cost and LCOE of the CSP system described herein. The values in the table are from manufacturer data, historical cost data for installed CSP plants, and engineering estimates when necessary. We performed sensitivity analysis to assess the relative impact of different assumptions on total capital cost and delivered energy cost.

Economic Performance Metrics

Component costs are estimated beginning with an independent variable (e.g., component size), then applying the cost parameters in **Table 4** as well as scaling functions (e.g., linear relation or power law), and cost multipliers (e.g., setting, piping, electrical, owner's cost, and contingency) (**Table 5**). Multipliers account for added services or parts such as electrical, piping, fabrication, and setting.

The installed costs of most components (C_{com}), with exception of the power block and tower, scale linearly (although not necessarily proportionally) as a function of scale parameter (C_{sp}), fit constants (A_{sp}, B_{sp}), and total cost multipliers ($C_M = 1 + multipliers$) shown in **Eq. 8**.

$$C_{com} = \left(A_{sp} + B_{sp} \cdot C_{sp}\right) \cdot C_M \tag{8}$$

The cost of hot storage include five insulation layers that are costed independently as illustrated in **Eq. 9**, where $V_0 = V_{hs}$.

$$c_i = (V_i - V_{i-1}) \cdot C_{ins,i} \tag{9}$$

Costs of the tower and power block scale with a power law as shown in **Eq. 10**.

$$C_{com} = A_{pf} \cdot B_{parameter}^{C_f} \cdot C_M \tag{10}$$

The balance of plant is estimated based on the power rating (P_R), the balance of plant for steam (B_{ps}), the percent of power generated from the steam engine (P_{st}), and the balance of plant scale factor (B_{psf}) as shown in **Eq. 11**.

$$C_{bp} = P_R \cdot B_{ps} \cdot \left(P_{st}^{B_{psf}}\right) \tag{11}$$

The total capital cost (C_{tca}) is a function of the cost of components (C_{com}), the balance of plant (C_{bp}), the cost of controls ($C_{control} = F_{control} \cdot \sum (C_{com})$), owners' cost ($C_{own}$), and contingency ($C_{con}$) (**Eq. 12**). In this context, controls refer to the electronics needed to control and operate the entire plant.

$$C_{tca} = \sum\left(C_{com} + C_{control} + C_{bp}\right) \cdot (1 + C_{own} + C_{con}) \tag{12}$$

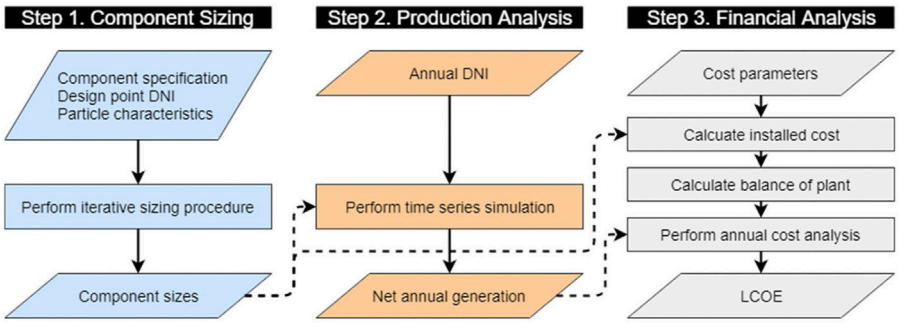

FIGURE 2 | High-level procedural summary for technoeconomic analyses.

TABLE 6 | Mass and energy flows, and temperatures at the design state for fluid streams (see **Figure 1B** for stream numbers).

Stream	Molar flow (mol/s)	Energy flow (MW)	Temperature (°C)	Material
1	2,788.00	134.93	409	Particle
2	2,788.00	491.71	1,125	Particle
3	N/A	N/A	1,120 (T4)	Particle
4	1,548.87	272.19	1,120	Particle
5	1,548.87	71.77	393	Particle
6	N/A	N/A	388 (T7)	Particle
7	2,788.00	127.43	388	Particle
8	329.90	13.17	1,125	Oxygen
9	329.90	5.67	499	Oxygen
10	7,352.43	0.00	298	Air
11	7,352.43	90.51	393	Air
12	7,352.43	289.00	1,200	Air
13	7,352.43	86.79	405	Air
14	0.00	0.00	298	Nitrogen
15	0.58	0.02	1,120	Nitrogen
16	1.21	0.00	298	Air
17	0.00	0.00	388	Air

TABLE 7 | Radiation, heat, and electricity flows at the design point (see **Figure 1B**).

Stream	Energy flow (MW)	Energy
18	773.07	Radiation
19	448.38	Radiation
20	324.69	Radiation
21	78.43	Radiation & Heat
22	0.47	Heat
23	1.94	Heat
24	0.19	Heat
25	0.00	Heat
26	0.00	Heat
27	111.70	Electricity
28	0.63	Electricity
29	12.73	Electricity

The LCOE in ¢/kWh$_e$ is calculated using **Eq. 13** as a function of total annual cost of operation and maintenance ($C_{O\&M}$), C_{tca}, weighted average cost of capital ($WACC$), cost of material replacement per year ($C_{rep} = F_{rep} \cdot C_{pa}$) estimated to be a fraction of the particle inventory replaced per year, and electrical production (E_p) in kWh$_e$/year of the model accounting for parasitic losses.

$$LCOE = \frac{C_{O\&M} + C_{tca} \cdot WACC + C_{rep}}{E_p} \tag{13}$$

SIMULATION PROCEDURES

A high-level illustration of the three-step technoeconomic analysis is provided in **Figure 2** with detailed procedural summaries and equation sets given in Supplementary Information. Step one sizes each component using the DNI_{dp}, component specifications, and characteristics of CAM28 particles. State values for the 29 stream are also calculated at the DNI_{dp}. Step two simulates plant production over a one-year period using DNI typical meteorological day (tmy3) data from Barstow (Daggett), California, USA (National Renewable Energy Laboratory, 2008). Power dispatch occurs based on solar availability and particle availability in the hot or cold storage bins. Step 3 is a financial analysis that calculates the balance of

TABLE 8 | Component sizing results.

Variable	Value	Units	Description
A^{HX}	1,930	m^2	Contact surface area in the heat exchanger
$P_{lift,min}$	125,538	W	Minimum power consumption of particle lift
$P_{pump,min}$	2,546,549	W	Minimum power consumption of vacuum pump
ϱ_p^{ROx}	0.03	%	Volume fraction of particles in ROx pipes
N_{pipe}	23	—	Number of pipes in the ROx
$D_{h,ins}^{ROx}$	2.80	M	Diameter of interior surface of ROx pipe insulation
L_{pipe}	5.12	M	Length of a ROx pipe
N_p	33,456,000	mol	Moles of CAM28 in the system (m_{pa} = 4.52 × 10^6 kg)
V^{HS}	1,953	m^3	Volume of hot storage bin
V^{CS}	1,953	m^3	Volume of cold storage bin
$A_{1.0}^{sf}$	477,203	m^2	Area of the solar field array for solar multiple of 1.0
N^{SR3}	285	—	Number of SR3 units (3 per tower)
$r_{h,ins}^{SR3}$	1.17	m	Radius of hot surface of SR3 insulation
$r_{c,body}^{SR3}$	1.37	m	Radius of cold surface of SR3 main body
L^{SR3}	2.35	m	Length of SR3 cavity

plant costs and total annual cost using design-independent assumptions, chemical engineering cost estimations, and SunShot targets for the solar field and O&M (Laird, 2011). While optimistic, well-documented roadmaps for achieving SunShot targets (U. S Department of Energy, 2012; U. S Department of Energy, 2017) have been developed. The System Advisor Model Version 2017, (SAM 2017.9.5) validated the results. Further details are included in **supplementary Material**. Lastly, independent parameters in each step are varied to assess the sensitivity on thermodyanic performance and cost.

RESULTS

Component Sizes

Tables 6, **7** provide simulated state information for DNI_{dp} of 900 W/m^2, *SM* of 1.8, and with the hot storage and cold storage bins initialized at half-capacity of particles. Particles displace a small amount of nitrogen from the hot storage bin while filling. Similarly, a small amount of air backfills the cold storage bin when removing particles. **Table 8** provides component sizes calculated for the input values from **Tables 1**, **2**, **3** with the energy balance and sizing equation sets detailed in **Supplementary Material**. The corresponding ROx CFD model (Babiniec, S.M., personal communication, 2016) provides four operational constraints that include the ROx pipe diameter ($D_{h,ins}^{ROx}$) between 2 and 4 m, ROx pipe length (L_{pipe}) between 4 and 8 m, ROx particle outlet velocity exceeding 1 m/s, and total ROx surface area between 1,000 and 2,000 m^2. These constraints are satisfied using 23 pipes (N_{pipe}), each of diameter 2.80 m and length 5.12 m, and an average volume fraction (ϱ_p^{ROx}) of 0.03%. This ROx configuration supplies enough heated air to the power block to operate at rated power for 1 hour using 5,576,000 moles of particles. This amount scales to 33,456,000 moles of CAM28 particles (N_p) and storage bins with an internal volume (V^{HS}, V^{CS}) of 1,953 m^3 to provide 6 h energy storage. Solar field area at SM 1.0 ($A_{1.0}^{sf}$) is 477,203 m^2. That, in turn, implies 858,965 m^2 for a *SM* of 1.8. SR3 sizing results in 285 receiver units ($A_{1.0}^{sf}$) each with a 1 m diameter window at 2,000 suns concentration, i.e., 2 MW/m^2 and 1.57 MW_{th} through each window at design point.

Intraday Operational Behavior

Figure 3 shows example intraday operational behavior during three seasonally representative days taken from the tmy3 dataset (National Renewable Energy Laboratory, 2008). A detailed description of the data set is provided in the user manual (Wilcox and Marion, 2008). Representative days were chosen as those from each season whose DNI most closely matched the seasonal (astronomical) average calculated from the data set. This illustration shows the particle molar flow rate through the SR3 and ROx (left vertical axis) and the amounts of particles stored in the hot and cold bins (right vertical axis). Results are shown for the baseline system with 6 hours of energy storage and a *SM* of 1.8. Power was dispatched when there were sufficient particles in

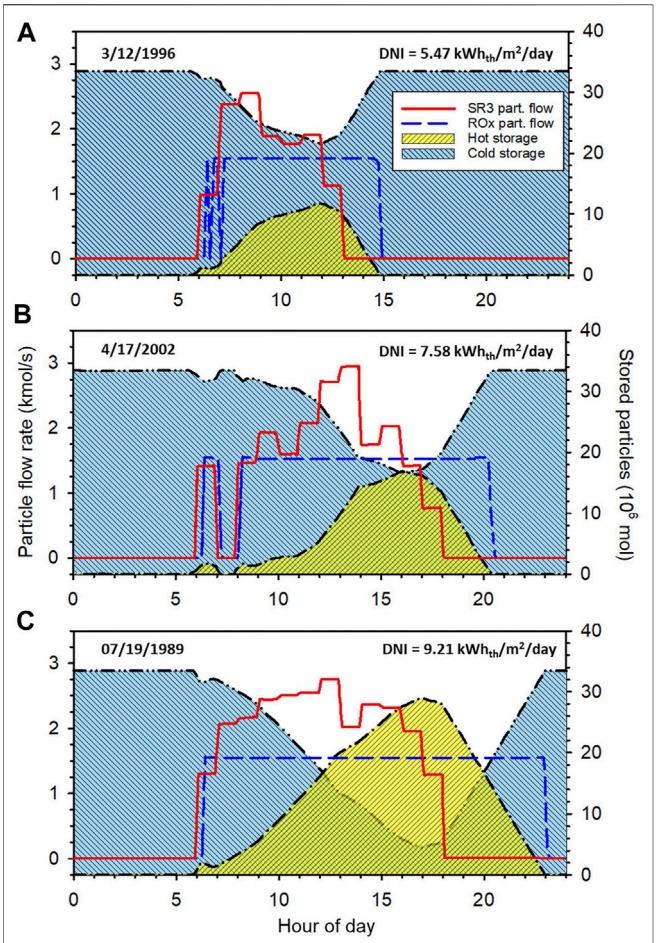

FIGURE 3 | Intraday dispatch schedule using seasonally representative DNI data from tmy3. **(A)**, winter **(B)**, spring and fall, and **(C)** summer.

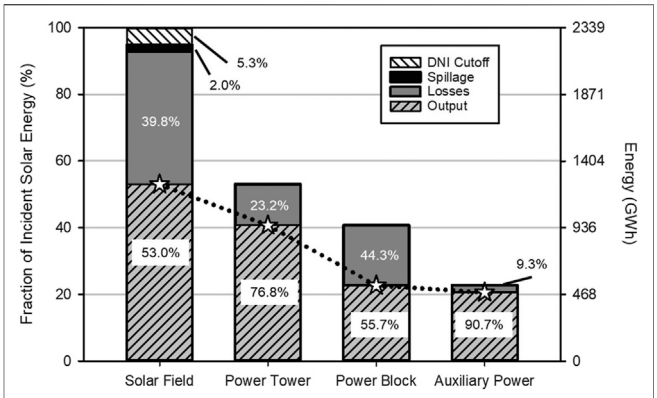

FIGURE 4 | Annual average energy efficiency from incident solar to electricity applying tmy3 data.

hot storage (prior to charging from the SR3) to supply the power block for the time step. The system generated the rated power output of 111.7 MW_e for 13.1 h on April 17 (1.46 GWh_e), 16.7 h on June 14 (1.86 GWh_e), and 8.2 h on March 12 (0.91 GWh_e). The specified days in April and June utilized about 0.5 kWh_{th} less irradiance than the values shown in **Figure 3** due to the DNI cutoff, while the day in March utilized about 1.0 kWh_{th} less for the same reason.

Annual Performance

Figure 4 documents the efficiency losses along the path from the incident solar energy to the electrical output for the baseline system. Examining the major components, the solar field receives 2,339.4 GWh_{th} of incident solar radiation in the simulated year and experiences losses of 123.5 GWh_{th} from the DNI cutoff, 930.6 GWh_{th} from collection losses, and 45.8 GWh_{th} from spillage losses. Thermal losses occurring in the SR3, hot storage, cold storage, and heat exchanger consume 288.0 GWh_{th} of the 1,239.3 GWh_{th} energy entering the power tower. The power block efficiency of 55.7% yields 530.2 GWh_e of electric generation, with power for the particle lift and vacuum pump consuming a total of 49.4 GWh_e to give 480.8 GWh_e of exportable energy annually. Replacing the combustor with the ROx accounts for the higher-than-rated power block efficiency. Taken as a whole, this baseline system has an annual capacity factor of 54.2% and average system efficiency of 20.6%. Note that solar collection losses and power block conversion losses account for the greatest part of the total by far at 930.6 and 421.0 GWh_{th}, respectively. The remaining losses (thermal equivalent) in decreasing order are SR3 heat and radiation losses (268.7 GWh_{th}), DNI cutoff (123.5 GWh_{th}), vacuum pump (84.5 GWh_{th}, 47.1 GWh_e), spillage (45.8 GWh_{th}), oxygen exhaust (14.1 GWh_{th}), storage losses (5.2 GWh_{th}), and particle lift (4.1 GWh_{th}, 2.3 GWh_e).

System Sizing and Energy Cost

Figure 5 illustrates the combined impacts of particle storage capacity (2–14 h in 2-hour increments) and size of the solar field (*SM* from 1.2 to 2.6 in 0.2 increments) on the annualized capacity factor, system efficiency, total capital cost, and LCOE. Further increases in storage capacity, e.g., to 16 h, increase capital costs with little change in capacity factor or system efficiency and thus increase LCOE relative to 14 hrs, and are therefore not shown for clarity in the figure. **Figure 5.A** shows that the annual electricity generation (capacity factor) has a maximum value for each value of *SM*. That is, for each value of *SM*, there is a limit corresponding to a specific storage capacity, after which, further increases in storage have no impact. The capacity factor assumes a single value of 369 GWh_e (37.8%) for all storage values at a *SM* of 1.2. This limit then increases by up to 60 GWh_e (6.0%) every 0.2 increment in *SM* with increasing amounts of storage required to reach the new limit. At the upper limits, 14 h storage and a *SM* of 2.6, we calculate an annual generation (capacity factor) of 755 GWh_e (77.2%).

System efficiency slightly increases for all storage sizes as *SM* increases but then sharply decreases at higher *SM*s (**Figure 5.B**). The exception is the 2-hour storage case, which exhibits only the decrease. The initial increase with *SM* is attributable to increases in component utilization exceeding the associated losses. That is,

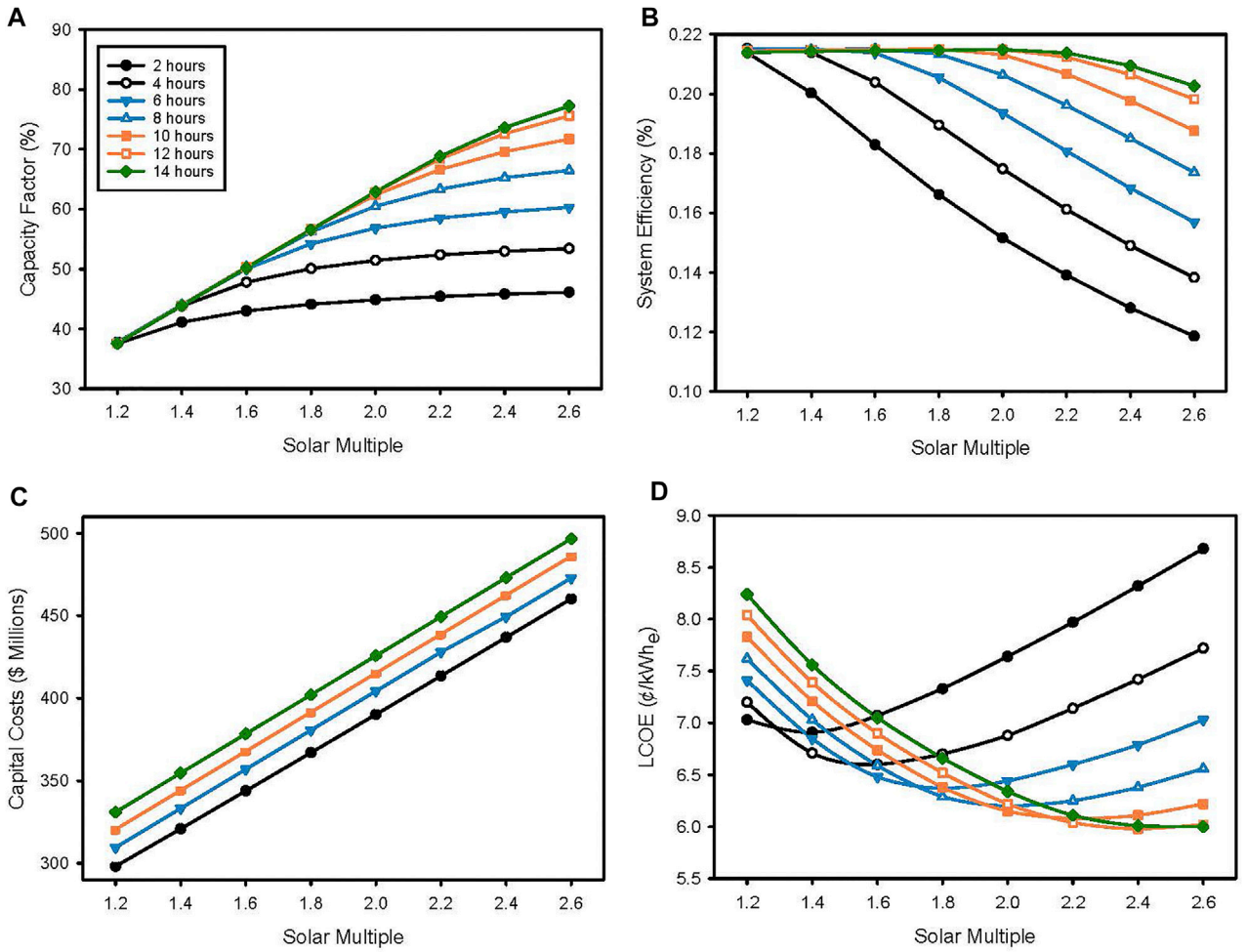

FIGURE 5 | Effect of storage capacity and solar multiple on **(A)** capacity factor, **(B)** system efficiency, **(C)** total capital cost, and **(D)** LCOE.

for a given storage capacity, component efficiency initially increases with scale. The subsequent decreases at higher *SM*s are attributable to increased spillage and SR3 thermal losses. In other words, as the *SM* is increased, the system eventually becomes storage limited. Hence, from an efficiency point of view, there is an optimal *SM* for each fixed storage capacity, and vice versa. The maximum system efficiency of 21.6% was realized with both 12 and 14 h storage at a *SM* of 2.0.

Total plant capital cost scaled about $6.5 million for every additional 2 hours of storage and approximately $23 million for every 0.2 increment in *SM* (**Figure 5.C**). Each value of storage capacity yields a minimum value of LCOE at a different *SM* (**Figure 5.D**). The specific minimum values of LCOE are 6.91 ¢/kWh$_e$ (2 hrs, *SM* 1.4), 6.60 ¢/kWh$_e$ (4 hrs, 1.6), 6.37 ¢/kWh$_e$ (6 hrs, 1.8), 6.20 ¢/kWh$_e$ (8 hrs, 2.0), 6.08 ¢/kWh$_e$ (10 hrs, 2.2), 5.98 ¢/kWh$_e$ (12 hrs, 2.4), and 6.00 ¢/kWh$_e$ (14 hrs, 2.6). The overall lowest simulated LCOE of 5.98 ¢/kWh$_e$ is found for the 12 h storage system and has a corresponding capacity factor of 72.6%, system efficiency of 20.8% ($\overline{\eta_{sf}}$ = 53.2%, $\overline{\eta_{pt}}$ = 76.8%, $\overline{\eta_{pb}}$ = 55.7%, $\overline{\eta_{aux}}$ = 91.4%), and a total capital cost of $467.8 million.

Figure 6 compares the cost breakdown for the baseline system (A) to the lower LCOE alternative with increased storage capacity of 12 h and a *SM* of 2.4 (B). The lower LCOE alternative requires a larger total capital cost due to increase in component sizes and replacement costs. An increase in productivity from 530,519 MWh$_e$/yr to 710,170 MWh$_e$/yr offsets these expenditures, which results in a 0.39 ¢/kWh$_e$ decrease in LCOE.

SENSITIVITY

We performed sensitivity analyses for major design and economic parameters to assess impact on system performance and LCOE, respectively. We evaluated ten thermodynamic parameters and five economic parameters. The results highlight components of particular importance to the design and point to opportunities to decrease LCOE.

Influence of Design Parameters

Table 9 (upper portion) illustrates the impact of six different design parameters on capacity factor: system efficiency, total

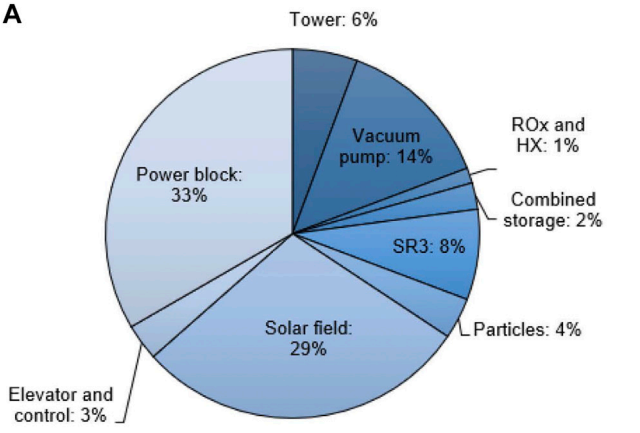

Total installed cost	$	268,299,373
Total capital cost	$	380,985,124
Total capital cost per year	$	30,478,809
Particle replacement	$	910,003
Operation and maintenance	$	2,422,492
Generation capacity	MWh/yr	530,519
LCOE	¢/kWhe	6.37

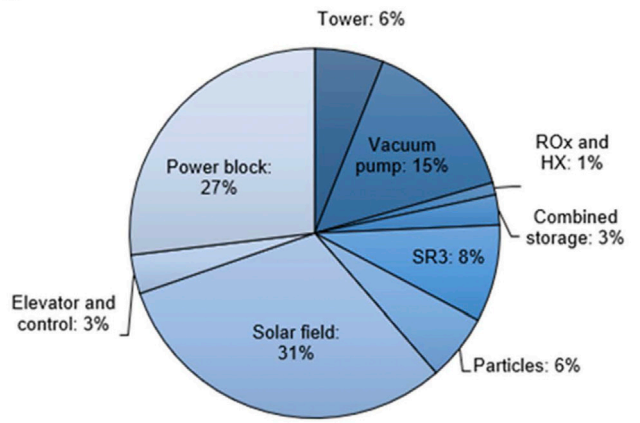

Total installed cost	$	329,470,117
Total capital cost	$	467,847,566
Total capital cost per year	$	37,427,805
Particle replacement	$	1,820,006
Operation and maintenance	$	3,242,825
Generation capacity	MWh/yr	710,170
LCOE	¢/kWhe	5.98

FIGURE 6 | (A) Cost breakdown and LCOE for baseline system with 6 h of storage and SM = 1.8, and **(B)** lower LCOE case with 12 h of storage and SM = 2.4.

capital cost, and LCOE relative to the best case (12 h storage, *SM* = 2.4, capacity factor = 72.6%, system efficiency = 20.8%, total project cost = $467.8 million, and LCOE of 5.98 ¢/kWh$_e$). Not shown in the table are results for an additional four parameters: thicknesses of SR3 stainless steel body (t_{body}^{SR3}), ROx insulation (t_{ins}^{ROx}), hot storage insulation (t_{ins}^{HS}), and cold storage insulation (t_{ins}^{CS}). Changes in these parameters of −/+ 50% of base values yielded less than 0.1% change in system efficiency and less than 0.01 ¢/kWh$_e$ change in LCOE.

Of the six parameters in the table, reducing the ratio of the SR3 cavity interior surface area to aperture area, γ_{cav}, by 50% gives the largest increase in system efficiency (0.6%), a 2.0% increase in capacity factor, and a decrease in LCOE of 0.35 ¢/kWh$_e$. While lowering this variable reduces thermal losses about the SR3 due to less surface area of the SR3 interior, insufficient surface area can inhibit adsorption in the receiver, not considered in this analysis. More detailed calculations to optimize receiver efficiency relative to size is outside the scope of this effort. Reducing the particle outlet temperature, T_2, by 50°C (thus also changing $\delta = 0.2161$, $A^{HX} = 2,523$, $A_{1.0}^{sf} = 467,150$, $N_p = 72,253,200$, $V^{HS} = 4,218$, $V^{CS} = 4,218$, $L_{pipe} = 5.15$, $D_{h,ins}^{ROx} = 2.90$) is the second most impactful change for efficiency we evaluated, increasing system efficiency by 0.6% and capacity factor by 0.4% while decreasing LCOE by only 0.04 ¢/kWh$_e$. This change reduces thermal losses from the SR3, but low particle temperature increases the challenge in reaching the 1,200°C turbine air inlet temperature. Increasing the solar flux density, F_{avg}, by 12.5%, i.e. increasing the energy entering the SR3, gives the third largest increase in system efficiency, 0.4%, with an accompanying increase in capacity factor of 1.3% and decrease in LCOE of 0.14 ¢/kWh$_e$. Flux density is limited in practice by the optical precision and mirror quality of the solar field, and/or use of secondary concentrators, both of which carry cost implications not included in these evaluations. Reducing γ_{lr} by 50% achieves the fourth largest increase in system efficiency, 0.3%, with an increase in capacity factor of 1.2% and decrease in LCOE by 0.07 ¢/kWh$_e$. This change decreases thermal losses from the SR3, but carries the same tradeoffs as changes to γ_{cav}. Increasing t_{ins}^{SR3} by 50% increased system efficiency by 0.2% and capacity factor by 0.6%, and decreased LCOE by 0.04 ¢/kWh$_e$. Changes in A^{HX} by 50% has negligible impact.

Influence of Cost Parameters

Varying cost parameters results in changes in LCOE, but not the CSP plant's generation capacity. We analyzed five cost parameters, each of which have a positive correlation with the LCOE, and present the results in **Table 9** (lower portion). The base case is the same as that for design parameters.

Weighted Average Cost of Capital

As expected, the WACC has by far the greatest impact of all the parameters on the LCOE. A ±1.0% change in the WACC scales to ±11% (0.66 ¢/kWh$_e$) in the LCOE. A WACC of 7.5% (8% is used for the base case) is reasonable for countries with low interest rates and stable banking systems such as countries of the Organisation for Economic Co-operation and Development (OECD) and China. However, WACC is as high as 10% or even 11% in other parts of the world (International Renewable Energy Agency, 2015). The WACC assumes that the plant has both debt and equity. Lowering perceived risk of renewables in policy and regulation can effectively reduce WACC and therefore LCOE.

SR3 Multiplier

The SR3 accounts for ~8% of the installed costs and as such provides a significant opportunity for total cost reduction. The multiplication

TABLE 9 | Effect of selected design and economic parameters on various performance metrics and LCOE. T_2 = SR3 particle outlet temperature, A^{HX} = contact surface area in the heat exchanger, γ_{cav} = ratio of SR3 cavity interior surface area to aperture area, γ_{lr} = SR3 ratio of cavity length to cavity radius, F_{avg} = Average flux density of the receiver aperture, t_{ins}^{SR3} = thickness of the SR3 insulation.

Engineering parameters							
Variable (nominal value)			**Annual generation (GWh)**	**Capacity factor (%)**	**System efficiency (%)**	**Capital cost ($ millions)**	**LCOE (¢/kWh)**
	Best case result		**710.2**	**72.6**	**20.8**	**467.8**	**5.98**
	min/max	**change**					
T_2 (1,125°C)	1,075	±50°C	4	0.38	0.64	–3.0	–0.04
	1,175		–4	–0.41	–0.61	3.6	0.05
A^{HX}(2,572 m^2)	1,286	±50%	–2	–0.22	–06	–0.73	0.01
	3,858		1.0	0.06	0.02	0.53	0.00
γ_{cav}(32)	16	±50%	20	2.04	0.60	–17.8	–0.35
	48		–23	–2.39	–0.70	17.8	0.40
γ_{lr}(2)	1	±50%	11	1.16	0.34	1.1	–0.07
	3		-6	–0.66	–0.19	0.59	0.04
F_{avg}(2 MW/m^2)	1.75	±12.5%	–19	–1.89	–0.55	4.8	0.20
	2.25		13	1.13	0.38	–3.8	–0.14
t_{ins}^{SR3}(0.0254 m)	0.0127	±50%	–7	–0.74	–0.22	–0.66	0.05
	0.0381		5	0.55	0.16	0.51	–0.04
Economic Parameters							
WACC (8%)	7	±12.5%					±0.66
	9						
SR3 Multiplier (2.0)	1.5	±25%					±0.14
	2.5						
Contingency (25%)	20	±20%					±0.19
	30						
Particle Multiplier (2.0)	1.5	±25%					±0.14
	2.5						
Setting Percent (20%)	15	±25%					±0.13
	25						

factor in the SR3 cost equation accounts for the uncertainties associated with this novel reactor (**Table 5**). A 25% change in the multiplication factor changes the LCOE by 2.3% (0.14 ¢/kWh$_e$).

Contingency

The contingency parameter accounts for any unpredicted cost. We opted for a conservative design value of 25% in the base simulations. Installing the plant in a predictable area with low risk of natural disasters or political would justify a decrease in this value. A 5% change (to 20%) on this parameter decreases LCOE by an estimated 3.1%.

Particle Multiplier

Although well characterized, the metal oxide is not a commercial product and therefore cost and performance uncertainties remain. In the base case, the particles account for 4% of the LCOE. The particle multiplier embodies the added cost of fabricating particles from raw materials. As illustrated, a 25% change in the particle multiplier results in a 2.4% change in LCOE.

Setting Percent

The setting percent is a cost for installing components of the CSP plant. A 5% absolute decrease on setting multiplier reduces the LCOE by an estimated 2.2%.

CONCLUSION

We developed a one-dimensional quasi-dynamic thermodynamic model of a 111.7 MW$_e$ combined cycle air Brayton CSP system that uses a redox-active metal oxide as the heat transfer fluid and TCES media and an accompanying economic model of the system. Energy is stored as both sensible heat and chemical potential. We applied the two models to size components, simulate intraday operational behavior with varying solar insolation, evaluate annual energy efficiency and capacity factor, and calculate system costs and electrical energy production and cost.

A baseline system with 6 h storage and SM of 1.8 has a capacity factor of 54.2%, annual average system efficiency of 20.6%, and an

LCOE of 6.37 ¢/kWh$_e$ over a simulated year using solar insolation data for Barstow, California, USA. The subsystem energy efficiencies for the solar field, power tower, power block, and auxiliary power are 53.0, 76.8, 55.7, and 90.7%, respectively. Solar field optical losses, power block conversion losses, and SR3 losses account for 930.6, 421.0, 268.7 GWh$_{th}$, respectively, of the 2,339.4 GWh incident radiation. Increasing the storage capacity to 12 h and *SM* to 2.4 increases the capacity factor and system efficiency to 72.6 and 20.8%, respectively, and reduces the LCOE to 5.98 ¢/kWh$_e$. These high capacity factors far exceed those of contemporary solar thermal 21.8%, solar PV 25.7%, and wind 34.6% plants, and compare favorably to capacity factors reported for the year 2017 in the U.S. for combined cycle natural gas 51.3%, coal 53.7%, geothermal 74.0%, and nuclear 92.2% power (US Energy Information Administration, 2018).

Our results suggest that metal oxide based thermochemical energy storage could substantially decrease the unsubsidized cost of CSP technologies; the results for the 12 h, *SM* 2.4 simulations are 42% less than the recently published value of ~10.3 ¢/kWh$_e$ (Mehos et al., 2016). Examining the operation and purchase cost assumptions to identify opportunities for improvement, we note that the potential to decrease the DNI cutoff from 350 W/m^2 to 200 W/m^2. However, for the 12 h, *SM* 2.4 case the additional generation only provides additional cost reduction from 5.98 ¢/kWh$_e$ to 5.88 ¢/kWh$_e$ (a 1.7% improvement). A detailed analysis, e.g., with higher fidelity to examine transients on start-up, is necessary to provide more confidence that this change is reasonable. Combined cycle power blocks that operate at higher temperatures and hence higher efficiencies, may offer improvements. However, higher temperatures will result in greater thermal losses elsewhere in the system and/or require additional expenditures to minimize these and other issues that arise. That aside, turbomachinery is subject to ongoing improvements that may provide additional efficiency and cost benefits. Other components offering potential cost reductions include the vacuum pump, the SR3, and the ROx. Deploying a new thermochemical sorption pumping technology to provide the vacuum is a clear opportunity (Brendelberger et al., 2018). In any case, as the development and deployment of CSP technology continues to expand, total capital cost per kW$_e$ (capex) should continue to drop. Cost estimates as low as $ 3,000/kW$_e$ by 2050 are reported (Shemer, 2018b), far below the $4,188/kW$_e$ calculated in this study.

More rigorous sensitivity analyses show that variations in most design parameters have relatively minimal impact on cost and performance metrics including LCOE, with the exception of a 50% reduction in SR3 cavity interior surface area that improves LCOE by 0.35 ¢/kWh$_e$. However, this result should be strongly caveated. Changing the SR3 cavity interior surface area has secondary impacts, for example on particle residence time and reactor radiative efficiency, that would likely alter the results but were outside the scope of this study. Increasing the flux density at the SR3 aperture by 12.5% decreased the LCOE by 0.14 ¢/kWh$_e$, but again the result may not be feasible without incurring additional, unaccounted-for costs. No variation examined for any of the 10 parameters design parameters evaluated results in a change in system efficiency that exceeds 0.6%. Variations in cost parameters have a more direct impact on LCOE. The WACC, which applies to the system as a whole, is particularly important. A one-point change in the WACC from 8 to 7% (better understood as a 12.5% change) translates directly to an 11% decrease (0.66 ¢/kWhe) in the LCOE. Changes in other cost parameters scale more proportionally to their contribution to the overall cost.

DATA AVAILABILITY STATEMENT

The original contributions presented in the study are included in the article/**Supplementary Material**, further inquiries can be directed to the corresponding author.

AUTHOR CONTRIBUTIONS

BTG: thermodynamic/process modeling, heat and material balances, equipment sizing, writing and reviewing drafts. ML-L: economic modeling, writing and reviewing drafts. NGJ: supervision, writing and editing drafts. JEM: project conception and management, writing, reviewing and editing drafts. Writing and preparing final versions. EBS: supervision, systems and technoeconomic models and verification, writing, reviewing and editing drafts and final versions.

FUNDING

The U.S. Department of Energy (DOE) SunShot Initiative provided funding for the project entitled High Performance Reduction/Oxidation Metal Oxides for Thermochemical Energy Storage (PROMOTES) under award number DE-FOA-0000805-1541 as part of the CSP:ELEMENTS program. The NSF IGERT-SUN (1144616) program at Arizona State University work also provided partial funding. The PROMOTES project portion of the funding at Arizona State University was provided via a subcontract from Sandia National Laboratories. Sandia National Laboratories is a multi-mission laboratory managed and operated by National Technology and Engineering Solutions of Sandia LLC, a wholly owned subsidiary of Honeywell International Inc. for the U.S. Department of Energy's National Nuclear Security Administration under contract DE-NA0003525.

ACKNOWLEDGMENTS

The authors would like to thank all the members of the PROMOTES team for useful conversations and insights, including Dr. Andrea Ambrosini, Prof. Hany Al Ansari, Dr. Sean Babiniec, Dr. Eric Coker, Dr. Cliff Ho, Prof. Sheldon Jeter, Prof. Peter Loutzenheiser, and Andrew Schrader.

SUPPLEMENTARY MATERIAL

The Supplementary Material for this article can be found online at: https://www.frontiersin.org/articles/10.3389/fenrg.2021.734288/full#supplementary-material

REFERENCES

Aerospace Specification Metals, Inc. AISI Type 304 Stainless Steel (). Aerospace Specification Metals, Inc. Data from: AISI Type 304 Stainless Steel. Available at: http://asm.matweb.com/search/SpecificMaterial.asp? bassnum=MQ304A (Accessed December 22, 2020).

Albrecht, K. J., Carlson, M. D., Laubscher, H. F., Crandell, R., DeLovato, N., and Ho, C. K. (2020). Testing and Model Validation of a Prototype Moving Packed-Bed Particle-To-sCO_2 Heat Exchanger. *AIP Conf. Proc.* 2303, 030002. doi:10.1063/5.0031483

Albrecht, K. J., Jackson, G. S., and Braun, R. J. (2018). Evaluating Thermodynamic Performance Limits of Thermochemical Energy Storage Subsystems Using Reactive Perovskite Oxide Particles for Concentrating Solar Power. *Solar Energy* 167, 179–193. doi:10.1016/j.solener.2018.03.078

Ansaldo Energia (2013). AE64.3A Gas Turbine (Data Sheet). Available at: http://ansaldoenergia.it/easyUp/file/gas_turbine_ae64_3a_june2013.pdf.

Babiniec, S. M., Coker, E. N., Miller, J. E., and Ambrosini, A. (2015a). Doped Calcium Manganites for Advanced High-Temperature Thermochemical Energy Storage. *Int. J. Energ. Res.* 40, 280–284. doi:10.1002/er.3467

Babiniec, S. M., Coker, E. N., Miller, J. E., and Ambrosini, A. (2015b). Investigation of La_x $Sr_{1-x}Co_y$ $M_{1-y}O_{3-\delta}$ (M = Mn, Fe) Perovskite Materials as Thermochemical Energy Storage media. *Sol. Energy* 118, 451–459. doi:10.1016/j.solener.2015.05.040

Behar, O., Khellaf, A., and Mohammedi, K. (2013). A Review of Studies on central Receiver Solar thermal Power Plants. *Renew. Sustain. Energ. Rev.* 23, 12–39. doi:10.1016/j.rser.2013.02.017

Bell, I. H., Wronski, J., Quoilin, S., and Lemort, V. (2014). Pure and Pseudo-pure Fluid Thermophysical Property Evaluation and the Open-Source Thermophysical Property Library CoolProp. *Ind. Eng. Chem. Res.* 53, 2498–2508. doi:10.1021/ie4033999

Brendelberger, S., Vieten, J., Vidyasagar, M. J., Roeb, M., and Sattler, C. (2018). Demonstration of Thermochemical Oxygen Pumping for Atmosphere Control in Reduction Reactions. *Solar Energy* 170, 273–279. doi:10.1016/j.solener.2018.05.063

Christian, J., and Ho, C. (2016). Design Requirements, Challenges, and Solutions for High-Temperature Falling Particle Receivers. *AIP Conf. Proc.* 1734, 030008. doi:10.1063/1.4949060

Christy Refractories (2004). Data From: Insulating Firebrick. Available at: http://www.christyco.com/pdf/crc/Insulating_Firebrick_Data_Sheet.pdf.

Coker, E., Babiniec, S., Ambrosini, A., and Miller, J. (2016). "Metal Oxides With Ionic-Electronic Conductivity for Thermochemical Energy Storage," in *ECI Symposium Series: CO_2 Summit II: Technologies and Opportunities (preprint/presentation)*. Document available at https://www.osti.gov/servlets/purl/1365103. Abstract available at http://dc.engconfintl.org/co2_summit2/38 (Accessed September 13, 2021).

Collado, F. J., and Guallar, J. (2013). A Review of Optimized Design Layouts for Solar Power tower Plants with campo Code. *Renew. Sustain. Energ. Rev.* 20, 142–154. doi:10.1016/j.rser.2012.11.076

CSP Focus (2019). Chile CSP Developer Predicts World's Lowest price in June (November 28, 2019). Available at: http://www.cspfocus.cn/en/market/detail_2406.htm (Accessed December 11, 2020).

de la Vergne, J. (2003). *Hard Rock Miner's Handbook*. third ed. Tempe, AZ: McIntosh Engineering Limited.

Denholm, P., and Hummon, M. (2012). Simulating the Value of Concentrating Solar Power with Thermal Energy Storage in a Production Cost Model. *Natl. Renew. Energ. Lab. Tech. Rep. NREL/TP-6A20-56731*. doi:10.2172/1059140

Eddhibi, F., Amara, M. B., Balghouthi, M., and Guizani, A. (2015). Optical Study of Solar tower Power Plants. *J. Phys. Conf. Ser.* 596, 012018. doi:10.1088/1742-6596/596/1/012018

Ehrhart, B., and Gill, D. (2014). Evaluation of Annual Efficiencies of High Temperature central Receiver Concentrated Solar Power Plants with thermal Energy Storage. *Energ. Proced.* 49, 752–761. doi:10.1016/j.egypro.2014.03.081

El-Leathy, A., Jeter, S., Al-Ansary, H., Abdel-Khalik, S., Roop, J., Golob, M., et al. (2014). Thermal Performance Evaluation of Two thermal Energy Storage Tank Design Concepts for Use with a Solid Particle Receiver-Based Solar Power tower. *Energies* 7, 8201–8216. doi:10.3390/en7128201

Evan Bush, H., Schlichting, K.-P., Gill, R. J., Jeter, S. M., and Loutzenhiser, P. G. (2017). Design and Characterization of a Novel Upward Flow Reactor for the Study of High-Temperature Thermal Reduction for Solar-Driven Processes. *Energy Eng.* 139 (5), 051004, 2017 . Sol. doi:10.1115/1.4037191

Farid, M. M., Khudhair, A. M., Razack, S. A. K., and Al-Hallaj, S. (2004). A Review on Phase Change Energy Storage: Materials and Applications. *Energ. Convers. Manage.* 45, 1597–1615. doi:10.1016/j.enconman.2003.09.015

General Atomics Project Staff (2011). *Thermochemical Heat Storage for Concentrated Solar Power, GA–C27137* (Technical report). San Diego, CA: Prepared General Atomics for the U.S. Department of Energy under DE-FG36-08GO18145. doi:10.2172/1039304

Gil, A., Medrano, M., Martorell, I., Lázaro, A., Dolado, P., Zalba, B., et al. (2010). State of the Art on High Temperature thermal Energy Storage for Power Generation. Part 1-Concepts, Materials and Modellization. *Renew. Sustain. Energ. Rev.* 14, 31–55. doi:10.1016/j.rser.2009.07.035

Glatzmaier, G. (2011). Summary Report for Concentrating Solar Power Thermal Storage Workshop: New Concepts and Materials for Thermal Energy Storage and Heat-Transfer Fluids, NREL/TP- 5500-52134. (Technical report). Golden, CO: National Renewable Energy Laboratory. doi:10.2172/1022291

González-Portillo, L. F., Albrecht, K., and Ho, C. K. (2021). Techno-Economic Optimization of CSP Plants with Free-Falling Particle Receivers. *Entropy* 23, 76. doi:10.3390/e23010076

Helioscsp (2020). Concentrated Solar Power Had a Global Total Installed Capacity of 6,451 MW in 2019. Available at: http://helioscsp.com/concentrated-solar-power-had-a-global-total-installed-capacity-of-6451-mw-in-2019/ (Accessed December 11, 2020).

Ho, C., Christian, J., Gill, D., Moya, A., Jeter, S., Abdel-Khalik, S., et al. (2014). Technology Advancements for Next Generation Falling Particle Receivers. *Energ. Proced.* 49, 398–407. doi:10.1016/j.egypro.2014.03.043

Ho, C. K. (2017). Advances in central Receivers for Concentrating Solar Applications. *Solar Energy* 152, 38–56. doi:10.1016/j.solener.2017.03.048

Ho, C. K., and Iverson, B. D. (2014). Review of High-Temperature central Receiver Designs for Concentrating Solar Power. *Renew. Sustain. Energ. Rev.* 29, 835–846. doi:10.1016/j.rser.2013.08.099

Imponenti, L., Albrecht, K. J., Braun, R. J., and Jackson, G. S. (2016). Measuring Thermochemical Energy Storage Capacity with Redox Cycles of Doped-CaMnO3. *ECS Trans.* 72, 11–22. doi:10.1149/07207.0011ecst

Imponenti, L., Albrecht, K. J., Kharait, R., Sanders, M. D., and Jackson, G. S. (2018). Redox Cycles with Doped Calcium Manganites for Thermochemical Energy Storage to 1000 °C. *Appl. Energ.* 230, 1–18. doi:10.1016/j.apenergy.2018.08.044

InfoMine Inc. (2016). Data from: Commodity and Metal Prices. Currently Available at https://www.mining.com/markets/.

International Energy Agency (2020). *Renewables 2020 – Analysis and Forecast to 2025*. Paris: IEA.

International Energy Agency (2019). *World Energy Outlook 2019*. Paris: IEA. ISBN 978-92-64-97300-8.

International Renewable Energy Agency (2015). *Renewable Power Generation Costs in 2014*. Abu Dhabi: IRENA. Available at: https://irena.org/-/media/Files/IRENA/Agency/Publication/2015/IRENA_RE_Power_Costs_2014_report.pdf.

Jaeger, H. M., and Nagel, S. R. (1992). Physics of the Granular State. *Science* 255, 1523–1531. doi:10.1126/science.255.5051.1523

Janko, S. A., Arnold, M. R., and Johnson, N. G. (2016). Implications of High-Penetration Renewables for Ratepayers and Utilities in the Residential Solar Photovoltaic (PV) Market. *Appl. Energ.* 180, 37–51. doi:10.1016/j.apenergy.2016.07.041

Kanbur, B. B., Atayilmaz, S. O., Demir, H., Koca, A., and Gemici, Z. (2013). Investigating the thermal Conductivity of Different concrete and Reinforced concrete Models with Numerical and Experimental Methods. Recent Adv. *Mech. Eng. Appl. Recent Adv.* 8, 95–101.

Karni, J., Kribus, A., Ostraich, B., and Kochavi, E. (1998). A High-Pressure Window for Volumetric Solar Receivers. *J. Sol. Energ. Eng.* 120, 101–107. doi:10.1115/1.2888051

Kuravi, S., Trahan, J., Goswami, D. Y., Rahman, M. M., and Stefanakos, E. K. (2013). Thermal Energy Storage Technologies and Systems for Concentrating Solar Power Plants. *Prog. Energ. Combustion Sci.* 39, 285–319. doi:10.1016/j.pecs.2013.02.001

Laird, J. (2011). The Biggest challenge. *Renew. Energ. Focus* 12, 72–77. doi:10.1016/s1755-0084(11)70106-5

Lilliestam, J., Labordena, M., Patt, A., and Pfenninger, S. (2017). Empirically Observed Learning Rates for Concentrating Solar Power and Their Responses to Regime Change. *Nat. Energ.* 2, 17094. doi:10.1038/nenergy.2017.94

Liu, M., Steven Tay, N. H., Belusko, M., Jacob, R., Will, G., et al. (2016). Review on Concentrating Solar Power Plants and New Developments in High Temperature thermal Energy Storage Technologies. *Renew. Sustain. Energ. Rev.* 53, 1411–1432. doi:10.1016/j.rser.2015.09.026

Loh, H. P., Lyons, J., Lyons, J., and White, C. W. 2002). Process Equipment Cost Estimation, Final Report. doi:10.2172/797810

Mehos, M., Turchi, C., Jorgenson, J., Denholm, P., Ho, C., and Armijo, K. (2016). On the Path to SunShot: Advancing Concentrating Solar Power Technology, Performance, and Dispatchability. NNREL/TP-5500-65688 and SAND2016-2237R. (Technical report). Golden, CO and Albuquerque, NM: National Renewable Energy Laboratory and Sandia National Laboratories. http://www.nrel.gov/docs/fy16osti/65688.pdf

Mendelsohn, M., Lowder, T., and Canavan, B. (2012). Utility-Scale Concentrating Solar Power and Photovoltaic Projects: A Technology and Market Overview. *Natl. Renew. Energ. Lab. Tech. Rep. NREL/TP-6A20-51137*. doi:10.2172/1039803

Mikron Instrument Company, Inc (2014). Data from: Table of Emissivity of Various Surfaces. Available at: http://www-eng.lbl.gov/~dw/projects/DW4229_LHC_detector_analysis/calculations/emissivity2.pdf

Miller, J. E., Ambrosini, A., Babiniec, S. M., Coker, E. N., Ho, C. K., Al-Ansary, H., et al. (2016). High Performance Reduction/Oxidation Metal Oxides for Thermochemical Energy Storage (PROMOTES), Paper No. ES2016–59660. V001T04A024. doi:10.1115/ES2016-59660

Miller, J., and Gill, D. (2014). SunShot Initiative: Awardee Technical Summary. High Performance Reduction/Oxidation Metal Oxides for Thermochemical Energy Storage (PROMOTES). Available at: https://energy.gov/eere/sunshot/project-profile-high-performance-reductionoxidation-metal-oxides-thermochemical-energy (Accessed December 20, 2020).

Muroyama, A. P., Schrader, A. J., and Loutzenhiser, P. G. (2015). Solar Electricity via an Air Brayton Cycle with an Integrated Two-step Thermochemical Cycle for Heat Storage Based on Co_3O_4/CoO Redox Reactions II: Kinetic Analyses. *Solar Energy* 122, 409–418. doi:10.1016/j.solener.2015.08.038

National Renewable Energy Laboratory (2008). Data From: National Solar Radiation Data Base. Available at: http://rredc.nrel.gov/solar/old_data/nsrdb/1991-2005/tmy3/by_state_and_city.htmlhttps://nsrdb.nrel.gov/data-sets/archives.html.

Neises, M., Tescari, S., de Oliveira, L., Roeb, M., Sattler, C., and Wong, B. (2012). Solar-heated Rotary kiln for Thermochemical Energy Storage. *Solar Energy* 86, 3040–3048. doi:10.1016/j.solener.2012.07.012

Nye Thermodynamics Corp (2016). Gas Turbine Prices. Data from: Gas Turbine Prices $ per kW. Available at: http://nyethermodynamics.com/trader/kwprice.htm.

Pardo, P., Deydier, A., Anxionnaz-Minvielle, Z., Rougé, S., Cabassud, M., and Cognet, P. (2014). A Review on High Temperature Thermochemical Heat Energy Storage. *Renew. Sustain. Energ. Rev.* 32, 591–610. doi:10.1016/j.rser.2013.12.014

Perlite Institute, Inc (2014). Data From: Overview of Perlite Concrete). Available at: https://www.perlite.org/library-perlite-info/construction-perlite/Perlite-Concrete.pdf.

Peters, M. S., and Timmerhaus, K. D. (2003). *Plant Design and Economics for Chemical Engineers*. 5th ed. New York: McGraw-Hill.

Price, H., and Kearney, D. (2003). Reducing the Cost of Energy from Parabolic Trough Solar Power Plants. *Solar Energy* 591, ISEC2003–44069. doi:10.1115/isec2003-44069

Regin, A. F., Solanki, S. C., and Saini, J. S. (2008). Heat Transfer Characteristics of thermal Energy Storage System Using PCM Capsules: A Review. *Renew. Sustain. Energ. Rev.* 12 (9), 2438–2458. doi:10.1016/j.rser.2007.06.009

Renewable Energy Policy Network for the 21st Century (REN21) (2015). *Renewables 2015 Global Status Report*. Paris, France: GSR2015_Full-Report_English.pdf (ren21.net) (Accessed December 22, 2020).

Rydén, M., Moldenhauer, P., Lindqvist, S., Mattisson, T., and Lyngfelt, A. (2014). Measuring Attrition Resistance of Oxygen Carrier Particles for Chemical Looping Combustion with a Customized Jet Cup. *Powder Technol.* 256, 75–86. doi:10.1016/j.powtec.2014.01.085

Sargent & Lundy LLC Consulting Group. (2003). Assessment of Parabolic Trough and Power Tower Solar Technology Cost and Performance Forecasts. NREL/SR-550-34440. (Technical Report). Golden, CO: National Renewable Energy Laboratory. doi:10.2172/15005520

Saung, E., and Miller, F. J. (2014). Dome Window and Mount Design for a 5 MWth Solar Receiver. *Energ. Proced.* 49, 514–523. doi:10.1016/j.egypro.2014.03.055

Schrader, A. J., De Dominicis, G., Schieber, G. L., and Loutzenhiser, P. G. (2017). Solar Electricity via an Air Brayton Cycle with an Integrated Two-step Thermochemical Cycle for Heat Storage Based on Co_3O_4/CoO Redox Reactions III: Solar Thermochemical Reactor Design and Modeling. *Solar Energy* 150, 584–595. doi:10.1016/j.solener.2017.05.003

Schrader, A. J., Muroyama, A. P., and Loutzenhiser, P. G. (2015). Solar Electricity via an Air Brayton Cycle with an Integrated Two-step Thermochemical Cycle for Heat Storage Based on Co_3O_4/CoO Redox Reactions: Thermodynamic Analysis. *Solar Energy* 118, 485–495. doi:10.1016/j.solener.2015.05.045

Schrader, A. J., Schieber, G. L., Ambrosini, A., and Loutzenhiser, P. G. (2020). Experimental Demonstration of a 5 kWth Granular-Flow Reactor for Solar Thermochemical Energy Storage with Aluminum-Doped Calcium Manganite Particles. *Appl. Therm. Eng.* 173, 115257. doi:10.1016/j.applthermaleng.2020.115257

Shabgard, H., Faghri, A., Bergman, T. L., and Andraka, C. E. (2013). Numerical Simulation of Heat Pipe-Assisted Latent Heat Thermal Energy Storage Unit for Dish-Stirling Systems. *J. Sol. Energy Eng.*, 136, 021025. doi:10.1115/1.4025973

Sharifi, N., Faghri, A., Bergman, T. L., and Andraka, C. E. (2015). Simulation of Heat Pipe-Assisted Latent Heat thermal Energy Storage with Simultaneous Charging and Discharging. *Int. J. Heat Mass Transfer* 80, 170–179. doi:10.1016/j.ijheatmasstransfer.2014.09.013

Shemer, N. (2018b). New Energy Update. CSP Capex Costs Fall by Almost Half as Developers Shift towards China and Middle East. Available at: http://analysis.newenergyupdate.com/csp-today/csp-capex-costs-fall-almost-half-developers-shift-towards-china-and-middle-easthttps://www.reutersevents.com/renewables/csp-today/csp-capex-costs-fall-almost-half-developers-shift-towards-china-and-middle-east (now available at April 16, 2018).

Shemer, N. (2018a). Reuters Events: Renewables. As CSP Bids Fall to Record Lows, Prices Diverge between Regions. Available at: https://www.reutersevents.com/renewables/csp-today/csp-bids-fall-record-lows-prices-diverge-between-regions (Accessed FebruaryDecember 2011, 20182020).

Solar Power and Chemical Energy Systems (SolarPACES) worldwide database of CSP projects (2020). Maintained by National Renewable Energy Laboratory. Available at: www.nrel.gov/csp/data-tools.htmlhttps://solarpaces.nrel.gov/ (Accessed December 22, 2020).

Stoddard, L., Abiecunas, J., and O'Connell, R. (2006). Economic, Energy, and Environmental Benefits of Concentrating Solar Power in California. NREL/SR-550-39291. (Technical report). Golden, CO: National Renewable Energy Laboratory. doi:10.2172/881924

System Advisor Model Version 2017.9.5 (2017). National Renewable Energy Laboratory. Golden. Available at: https://sam.nrel.gov/content/downloads (Accessed October 31, 2016).

The Engineering Toolbox (2004). Data From: Drag Coefficient. Available at: http://www.engineeringtoolbox.com/drag-coefficient-d_627.html

The Engineering Toolbox (2003). Data From: Heat Exchanger Heat Transfer Coefficients. Available at: http://www.engineeringtoolbox.com/heat-transfer-coefficients-exchangers-d_450.html

Tian, Y., and Zhao, C. Y. (2013). A Review of Solar Collectors and thermal Energy Storage in Solar thermal Applications. *Appl. Energ.* 104, 538–553. doi:10.1016/j.apenergy.2012.11.051

U.S Department of Energy. (2012). SunShot Vision Study: February 2012, DOE/GO-102012-3037. (Technical report). Washington, D.C.: USDOEdoi:10.2172/1039075

US Vacuum Pumps. (2017). Available at: www.usvacuumpumps.com (Accessed August, 2017).

U.S Department of Energy (2014b). Determining Electric Motor Load and Efficiency. Available at: https://www.energy.gov/sites/prod/files/2014/04/f15/10097517.pdf.

U.S Department of Energy (2014a). MAP: Concentrating Solar Power across the United States. Available at: https://energy.gov/articles/map-concentrating-solar-power-across-united-states (Accessed December 22, 2020).

U.S Department of Energy (2017). The SunShot 2030 Goals: 3¢ Per Kilowatt Hour for PV and 5¢ Per Kilowatt Hour for Dispatchable CSP. Report DOE/EE-1501. Available at: https://www.energy.gov/sites/prod/files/2020/09/f79/SunShot%202030%20White%20Paper.pdf.

U.S. Energy Information Administration (2015). *Annual Energy Outlook 2015 with Projections to 2040*. DOE/EIA0383(2015). Washington, DC: US Department of Energy. Available at: https://www.eia.gov/outlooks/aeo/pdf/0383(2015).pdf.

U.S. Energy Information Administration (2018). Electric Power Monthly with Data for October 2018, December 2018. *USIEA Tech. Rep.* Available at: https://www.eia.gov/electricity/monthly.

U.S. Energy Information Administration (2014). Washington, DC: US Department of Energy. Available at: https://www.eia.gov/outlooks/aeo/nems/documentation/international/pdf/m071(2014).pdf.International Energy Module of the National Energy Modeling System: Model Documentation 2014.

Vignarooban, K., Xu, X., Arvay, A., Hsu, K., and Kannan, A. M. (2015). Heat Transfer Fluids for Concentrating Solar Power Systems - A Review. *Appl. Energ.* 146, 383–396. doi:10.1016/j.apenergy.2015.01.125

Wilcox, S., and Marion, W. (2008). Users Manual for TMY3 Data Sets. NREL/TP-581-43156. (Technical report). Golden, CO: National Renewable Energy Laboratory. doi:10.2172/928611

Zalba, B., Marı´n, J. M., Cabeza, L. F., and Mehling, H. (2003). Review on thermal Energy Storage with Phase Change: Materials, Heat Transfer Analysis and Applications. *Appl. Therm. Eng.* 23, 251–283. doi:10.1016/s1359-4311(02)00192-8

Zhang, H. L., Baeyens, J., Degrève, J., and Cacères, G. (2013). Concentrated Solar Power Plants: Review and Design Methodology. *Renew. Sustain. Energ. Rev.* 22, 466–481. doi:10.1016/j.rser.2013.01.032

Zhang, Y., Smith, S. J., Kyle, G. P., and Stackhouse, P. W. (2010). Modeling the Potential for thermal Concentrating Solar Power Technologies. *Energy Policy* 38, 7884–7897. doi:10.1016/j.enpol.2010.09.008

ZIRCAR Refractory Composites, Inc. (2005). Silica Composite Materials (Data Sheet). Available at: http://www.zrci.com/wdpr/wp-content/uploads/2016/05/zrci201.pdf\.

Conflict of Interest: The authors declare that the research was conducted in the absence of any commercial or financial relationships that could be construed as a potential conflict of interest.

Publisher's Note: All claims expressed in this article are solely those of the authors and do not necessarily represent those of their affiliated organizations, or those of the publisher, the editors and the reviewers. Any product that may be evaluated in this article, or claim that may be made by its manufacturer, is not guaranteed or endorsed by the publisher.

frontiers | Frontiers in Energy Research

ORIGINAL RESEARCH
published: 14 April 2022
doi: 10.3389/fenrg.2022.774099

Modified Calcium Manganites for Thermochemical Energy Storage Applications

James E. Miller[1], Sean M. Babiniec[2], Eric N. Coker[3], Peter G. Loutzenhiser[4], Ellen B. Stechel[5] and Andrea Ambrosini[6]*

[1]Arizona State University LightWorks® and the School of Sustainability (former address: Sandia National Laboratories, Albuquerque, New Mexico, USA), Tempe, AZ, United States, [2]Sandia National Laboratories, Thermal Sciences and Engineering Department, Albuquerque, NM, United States, [3]Sandia National Laboratories, Advanced Materials Laboratory, Albuquerque, NM, United States, [4]The George W. Woodruff School of Mechanical Engineering, Georgia Institute of Technology, Atlanta, GA, United States, [5]Arizona State University LightWorks® and the School of Molecular Sciences, Tempe, AZ, United States, [6]Sandia National Laboratories, Concentrating Solar Technologies, Albuquerque, NM, United States

$CaAl_{0.2}Mn_{0.8}O_{3-\delta}$ (CAM28) and $CaTi_{0.2}Mn_{0.8}O_{3-\delta}$ (CTM28) are perovskite metal oxides developed for high-temperature thermochemical energy storage (TCES) applications, e.g., in support of air Brayton power generation. Previous reports for these compounds focus on the equilibrium non-stoichiometry (δ) as a function of temperature and oxygen partial pressure (pO_2) and the endotherm (or exotherm) accompanying changes in δ resulting from thermal reduction (or re-oxidation). Herein, we report results for elemental substitution and doping (Al, Co, Fe, La, Sr, Ti, Y, Zn, and Zr) of calcium manganites (CM) that establish the preference for CAM28 and CTM28. Techniques employed include conventional (screening and equilibrium) and ballistically heated multi-cycle thermogravimetric analysis (TGA), conventional and high temperature (*in-situ*) X-ray diffraction (XRD), and differential scanning calorimetry (DSC). Forward-looking results for A-site Y-doped materials, e.g., $Ca_{0.9}Y_{0.1}MnO_{3-\delta}$ (CYM910), establish a route to increasing the reduction enthalpy relative to CAM28 and CTM28, albeit at the expense of increased reduction temperatures and raw materials costs. A thermodynamic model presented for CAM28, but extendable to related materials, provides values for the reaction enthalpy and extent of reduction as a function of temperature and oxygen partial pressure for use in design efforts. Taken as a whole, the results support the choice of Al-doped $CaMnO_{3-\delta}$ as a low-cost material for TCES in a high temperature air Brayton application, but point the way to achieving higher stored energy densities that could lead to overall cost savings.

Keywords: thermochemical energy storage, metal oxides, mixed ionic electronic conductor, MIEC, calcium manganite $CaMnO_3$, concentrating solar power (CSP), compound energy formalism

OPEN ACCESS

Edited by:
Emanuela Mastronardo, University of Messina, Italy

Reviewed by:
Xin Qian, Georgia Institute of Technology, United States
Juan M. Coronado, Spanish National Research Council (CSIC), Spain

****Correspondence:***
James E. Miller
Jim.E.Miller@asu.edu

Specialty section:
This article was submitted to Solar Energy, a section of the journal Frontiers in Energy Research

Received: *10 September 2021*
Accepted: *09 February 2022*
Published: *14 April 2022*

Citation:
Miller JE, Babiniec SM, Coker EN, Loutzenhiser PG, Stechel EB and Ambrosini A (2022) Modified Calcium Manganites for Thermochemical Energy Storage Applications. Front. Energy Res. 10:774099. doi: 10.3389/fenrg.2022.774099

INTRODUCTION

It is widely understood that reliable and cost effective hourly, daily, and seasonal energy storage solutions are absolutely critical to achieving deep penetration of renewable technologies into the energy ecosystem. Thermal energy storage (TES) is the approach generally applied to concentrating solar power (CSP) technology, as it is highly efficient, readily scalable, and provides power on demand while "right sizing" the power generating subsystem to cost-saving high capacity factors. Sensible heat storage in molten salts is the state of the art technology for

CSP and provides an energy density of approximately ~410 kJ/kg (Wu et al., 2011; Stekli et al., 2013). However, better solutions are actively sought after due to several shortcomings. These include upper temperature limits that preclude higher efficiency power cycles and the relatively low energy densities that increase system volumes and hence associated costs. Furthermore, molten salts present significant materials and operational challenges, as they tend to be corrosive and are subject to solidification if temperatures are allowed to fall too low. Indeed, problems with the salt storage system are often cited in discussions of the disappointing performance and financial failures of the Crescent Dunes CSP plant in Nevada, USA (Chamberlain, 2020; Mehos et al., 2020).

Thermochemical energy storage (TCES) is an alternative approach in which at least a fraction of the energy storage is achieved through the use of selective and reversible chemical reactions; the remaining fraction is stored as sensible heat. Interest in this approach is motivated by the potential to store and deliver heat at higher temperatures for more efficient power generation, the potential for more cost-effective, higher energy density storage, and of course the possibility to avoid the materials compatibility and handling issues of molten salts. Furthermore, at least some TCES approaches appear to be cost competitive with molten salt (Bayon et al., 2018). These factors have helped fuel a recent boom in interest in solar TCES; a Scopus search produces over 250 publications for the search terms "solar" AND "thermochemical energy storage" for the 5 years spanning 2015–2020, and only 52 for the preceding 5 years. Additionally, general reviews for TCES were published in each of the previous 3 years (Chen et al., 2018; Prasad et al., 2019; Laurie and Abanades, 2020), along with reviews targeting specific chemistries (*see* below) and implementations (Almendros-Ibáñez et al., 2019).

Briefly, though details vary, TCES technologies are commonly sorted into categories based on the reaction chemistry or substrate, or in some cases phases involved in the reaction (gas, gas-solid, gas-liquid). Examples include hydrides, oxides, and gas phase reactions. Oxides are further categorized into carbonate formation/decomposition, hydration/dehydration, and oxidation/reduction systems. Gas phase reactions include ammonia synthesis/decomposition (sometimes considered as a hydride system), sulfur based chemistries, reforming, and dehydrogenation/hydrogenation chemistries. Oxide systems account for much of the recent work. In particular, calcium oxide looping, which also has applications beyond TCES, has been the subject of intense interest, with both options (CO_2 and H_2O) under development as discussed in several recent reviews (Yuan et al., 2018; Ortiz et al., 2019; Yan et al., 2020). Redox systems are also the subject of many efforts and can further be divided into those which undergo a stoichiometric reduction to a new crystal phase, and mixed-ionic/electronic conducting (MIEC) materials that are capable of supporting a large number of oxygen vacancies without undergoing a crystallographic phase change. Manganese, cobalt and to some extent copper oxides account for much of the effort on the stoichiometric approach, with work typically directed towards one or more of the following topics: characterization, tuning performance and operating conditions, enhancing reversibility, measuring and improving reaction kinetics and stability (e.g., sinter resistance), and developing systems for implementation of TCES at scale with these materials. The reader is directed to recent reviews for additional information (Dizaji and Hosseini, 2018; Wu et al., 2018). Note that these stoichiometric redox reactions are discrete. That is, thermodynamically, the reduction can proceed to completion at a single transition temperature for a specific oxygen partial pressure (pO_2). For example, Co_3O_4 reduces to CoO (releasing O_2) endothermically (ΔH_{red} = 844 kJ/kg Co_3O_4 (Carillo et al., 2014)) at ~885°C in air (Hutchings et al., 2006), while reoxidation in air will take place at any temperature below that. Of course, increasing or decreasing the pO_2 shifts the temperature separating the oxidizing region from the reducing region up or down, respectively. Detailed kinetic studies of reduction and oxidation as function temperature and pO_2 have been reported (Muroyama et al., 2015). Generally, oxidation kinetics are sluggish at temperatures <700°C (Agrafiotis et al., 2014).

In contrast to stoichiometric oxides, the redox-active MIEC materials of interest, often of the perovskite structural family, transition through a continuum of redox states (oxygen stoichiometries) without undergoing major structural rearrangements. This is accomplished through the creation and destruction of oxygen vacancies in the crystal lattice with the thermodynamic equilibrium composition of the solid being a function of both the temperature and pO_2 of the surrounding gas phase. As there is no fundamental change in structure, the reaction is represented by the parameter δ, denoting the deviation in oxygen stoichiometry from the fully oxidized state. For a perovskite, this can be represented as

$$\frac{1}{\delta}ABO_3 \leftrightarrow \frac{1}{\delta}ABO_{3-\delta} + \frac{1}{2}O_2(g) \quad (1)$$

As suggested by the AB notation, there is an almost endless array of compositions that can be produced *via* cation variation and substitution (of a metal with the same oxidation state) or doping (introducing a metal with a different oxidation state) on both the A and B sites (Pena and Fierro, 2001). In other words, the materials and their thermodynamics (i.e., δ as a function of T and pO_2), are highly tunable. The principle limitation of this class of materials is that the redox capacity, embodied by δ, tends to be small in comparison to the stoichiometric oxides. However, the combination of high ionic and electronic conductivities in an MIEC facilitate reaction and oxygen transport throughout the bulk of the material thereby promoting reaction kinetics and complete utilization of the available redox capacity. This makes them more competitive with the stoichiometric reactions which do not have similar beneficial properties. Additionally, MIECs tend to be very stable at high temperatures. In total, this combination of properties makes them attractive materials candidates across a broad application space beyond TCES including water and carbon

dioxide splitting (Miller, et al., 2014; Bayon et al., 2020), separating or removing O_2 from air (Ezbiri et al., 2015; Vieten et al., 2016; Bush et al., 2019) and pumping oxygen from reactive systems (Brendelberger et al., 2017, 2018, 2019). Each application has a unique set of priorities and hence materials and thermodynamic requirements or targets. As a result, compositions of interest for different applications tend to vary significantly.

Our materials development efforts in the TCES space have primarily been directed towards the specific application of producing a heated pressurized air stream for power generation *via* an air Brayton turbine. Conceptually, the combustion section in the system is replaced by a gas-solid heat exchanger wherein compressed air is heated from 300–400°C to >1000°C (preferably 1200°C) (Miller et al., 2016; Gorman et al., 2021) by direct and counter-current contact with hot, reduced MIEC particles (Babiniec, et al., 2016a). The heat is drawn from both the oxidation exotherm and the sensible heat of the oxide particle. In some cases, e.g., if a large oxidation exotherm occurs at a high enough temperature range, the air outlet temperature can exceed the particle storage temperature (Babiniec, et al., 2016a). We began our efforts with $ABO_{3-\delta}$ (A = La, Ba, Sr, K; B = Co, Mn, Fe) perovskites (Babiniec, et al., 2015; Babiniec, et al., 2016b). Gokon et al. have reported on similar materials targeting temperatures >600°C (Gokon et al., 2019). We then transitioned to calcium manganites ($CaB_xMn_{1-x}O_3$, B = Al, Ti) with improved storage capacity and cost profiles (Babiniec, et al., 2016c). Sr-subsituted calcium manganites targeting similar applications with slightly different targets and implementations have been reported (Imponenti, et al., 2018; Albrecht et al., 2018; Vieten et al., 2016). Cr-doped calcium manganites synthesized by ball-milling have also be examined (Lucio et al., 2019), as have La-doped calcium manganites (Mastronardo et al., 2021). Herein, we present results for elemental substitution and doping that helped establish the preference for aluminum doping and titanium substitution in the calcium manganites, along with forward-looking results focused on A-site Y-doped materials. These latter compounds establish a route to higher reduction enthalpy, albeit at the expense of increased reduction temperatures and raw materials costs. We also present a thermodynamic model for calcium manganites, and related materials, that provide values for the reaction enthalpy and extent of reduction as a function of temperature and pO_2, appropriate for use in analysis and design efforts.

MATERIALS AND METHODS

All perovskite oxides were synthesized using the previously described modification of Pechini's method, as reported in (Babiniec et al., 2015). All constituent elements (Ca, Al, Co, Fe, Mn, Zn, Zr, Sr, and La) with the exception of Ti, were sourced from nitrates and dissolved in DI water in the desired stoichiometric cation ratios, along with excess citric acid as a chelating agent. The solution was dried, the recovered material combusted, and then calcined in a furnace with an air environment. For compositions containing Ti, an analogous procedure was followed, however the Ti was sourced as an isopropoxide and ethylene glycol was used in place of DI water to circumvent hydrolysis of the precursor. In either case, the resulting powder was recovered and pressed into a pellet and calcined at high temperature (1000–1250°C) to produce a dense solid which was subsequently ground in a mortar and pestle to a fine power. Sieves were used to recover particles falling in a specific size range for evaluation. As previously reported, optimal particle sizes for heat recovery in a counter-flow direct-contact gas-solid heat exchanger concept are 100–200 μm (Babiniec et al., 2016a). For convenience, a shorthand notation indicative of the constituent elements and their relative stoichiometries is adopted. For example, $CaAl_{0.2}Mn_{0.8}O_{3-\delta}$ is CAM28 and $Ca_{0.8}La_{0.2}Ti_{0.2}Mn_{0.8}O_{3-\delta}$ is CLTM8228. Refer to **Tables 1**, **2** for a complete listing.

Room temperature crystallographic data were typically recorded using PANalytical X'Pert and Bruker AXS D8 Advance X-ray diffractometers (XRDs) with CuKα radiation. Crystal structure and phase composition were determined by analyzing XRD patterns using Jade software (Materials Data Inc. Jade+, Livermore, CA, United States). Materials with a calculated impurity of <5% were categorized as single-phase. *In-situ* XRD experiments were performed using a previously-described Scintag PAD X diffractometer (Thermo Electron Inc., Waltham, MA, United States) using a similar method (Coker et al., 2012). Scans were collected at 100°C increments while heating from ambient to 1200°C (e.g., 25, 200, 300, 400, . . ., 1100, 1200) and then back (1200, 1100, . . ., 50) under controlled environment (air or 500 ppm O_2 in N_2).

Three previously developed and reported thermogravimetric (TGA) methods were applied in this study. The first is a relatively simple screening procedure performed using a TA Instruments Q600 TG/DSC (Babiniec et al., 2015). In short, an initial break-in cycle to ensure a common starting point for all materials was performed by ramping the material at 20°C/min to 1250°C in air and holding for 30 min, then cooling back to 200°C and holding for 30 min. This is immediately followed an evaluation cycle consisting of an identical ramp in air to 1250°C with a 10 min hold in air, then a 20 min hold in Ar, 20 more minutes hold in air, and then cooling to 200°C in air (the final temperature typically deviates by 25–50°C above the 200°C target as there is no active cooling and no hold). Four different descriptive metrics are extracted from this evaluation for comparison: the temperature at which reduction is initially observed during the ramp, and the change in oxygen stoichiometry ($\Delta\delta$) occurring during each stage of the process ($\Delta\delta_1$ reduction in air, $\Delta\delta_2$ further reduction in argon, and $\Delta\delta_3$ reoxidation in air while cooling). A tangent line method was used when the data was amenable (presented reasonably linear slopes) to determine the initial temperatures. In each case the $\Delta\delta$ values are calculated as

$$\left|\Delta\delta\right| = \left(\left|\Delta m\right| / m_{init}\right)\left(MW_{ABO_3} / MW_O\right) \quad (2)$$

Where Δm is the mass change measured by TGA, m_{init} is the initial mass set as that after the break in cycle, MW_{ABO3} is the molecular weight of the perovskite assuming that the initial state of the material is stoichiometric ABO_3 ($\delta = 0$), and MW_O is the molecular weight of monatomic oxygen.

TABLE 1 | Thermogravimetric screening results for $CaAMnBO_3$ compositions.

Material	Single phase?[a]	T_{red} (°C)[b]	$\Delta\delta_1$	$\Delta\delta_2$	$\Delta\delta_3$
Baseline					
$La_{0.3}Sr_{0.7}Co_{0.9}Mn_{0.1}O_{3-\delta}$ (LSCM3791)	No	343	0.31	0.12	0.39
Sample Set 1					
$CaMnO_{3-\delta}$ (CM)	Yes	875	0.20	0.10	0.27
$CaAl_{0.2}Mn_{0.8}O_{3-\delta}$ (CAM28)	Yes	759	0.20	0.10	0.27
$CaCo_{0.2}Mn_{0.8}O_{3-\delta}$ (CCM28)	Yes	730	0.19	0.12	0.27
$CaFe_{0.2}Mn_{0.8}O_{3-\delta}$ (CFM28)	Yes	418	0.19	0.12	0.28
$CaFe_{0.4}Mn_{0.6}O_{3-\delta}$ (CFM46)	Yes	427	0.16	0.10	0.24
$CaTi_{0.2}Mn_{0.8}O_{3-\delta}$ (CTM28)	Yes	901	0.15	0.11	0.21
Sample Set 2					
$CaY_{0.2}Mn_{0.8}O_3$ (CYM28)	No	1022	0.03	0.07	0.07
$CaZn_{0.2}Mn_{0.8}O_3$ (CZnM28)	No	872	0.13	0.10	0.20
$CaZr_{0.2}Mn_{0.8}O_3$ (CZrM28)	No	867	0.17	0.10	0.24
Sample Set 3					
$CaTi_{0.05}Mn_{0.95}O_3$ (CTM0595)	Yes	843	0.21	0.13	0.29
$CaTi_{0.4}Mn_{0.6}O_{3-\delta}$ (CTM46)	Yes	992	0.09	0.09	0.13
$CaTi_{0.6}Mn_{0.4}O_3$ (CTM64)	Yes	951	0.06	0.08	0.10
$Ca_{0.8}La_{0.2}Ti_{0.2}Mn_{0.8}O_{3-\delta}$ (CLTM8228)	Yes	1020	0.05	0.10	0.09
$Ca_{0.5}La_{0.5}Ti_{0.5}Mn_{0.5}O_3$ (CLTM5555)	Yes	970	0.02	0.04	0.03
$Ca_{0.8}Sr_{0.2}Ti_{0.2}Mn_{0.8}O_{3-\delta}$ (CSTM8228)	Yes	827	0.16	0.11	0.24

Results for LSCM 3791 are provided as a baseline for comparison. Green shading denotes "parent" composition. Blue shading denotes materials selected for further analysis based on a combination of reduction temperatures (higher temperatures preferred) and large redox capacity (reoxidation $\Delta\delta_3 > 0.2$).
[a]*Determined by XRD.*
[b]*Initial reduction temperature.*

TABLE 2 | Thermogravimetric screening results for A-site Y-doped $CaMnO_3$.

Material	Single phase?[a]	T_{red} (°C)[b]	$\Delta\delta_1$	$\Delta\delta_2$	$\Delta\delta_3$
Benchmarks for comparison					
$CaMnO_3$	Yes	875	0.22	0.13	0.32
$CaY_{0.2}Mn_{0.8}O_{3-\delta}$ (CYM28)	No	1022	0.03	0.07	0.07
$CaAl_{0.2}Mn_{0.8}O_{3-\delta}$ (CAM28)	Yes	759	0.20	0.10	0.27
A-site Y-doped					
$Ca_{0.9}Y_{0.1}MnO_{3-\delta}$ (CYM910)	Yes	966	0.16	0.12	0.25
$Ca_{0.8}Y_{0.2}MnO_{3-\delta}$ (CYM820)	Yes	1158	0.11	0.072	0.18
$Ca_{0.7}Y_{0.3}MnO_{3-\delta}$ (CYM730)	Yes	1162	0.0056	0.015	0.074
$Ca_{0.6}Y_{0.4}MnO_{3-\delta}$ (CYM640)	Yes	NA[c]	NA[c]	NA[c]	NA[c]
$Ca_{0.5}Y_{0.5}MnO_{3-\delta}$ (CYM550)	Yes	NA[c]	NA[c]	NA[c]	NA[c]
A-site and B-sited doped					
$Ca_{0.9}Y_{0.1}Al_{0.2}Mn_{0.8}O_{3-\delta}$ (CYAM9128)	Yes	827	0.20	0.10	0.29
$Ca_{0.8}Y_{0.2}Al_{0.2}Mn_{0.8}O_{3-\delta}$ (CYAM8228)	Yes	981	—	—	—

Results for parent composition, B-site Y-doped sample, and CAM28 provided for comparison (green shading). Blue shading denotes materials selected for further analysis based on a combination of reduction temperatures (higher temperatures preferred) and large redox capacity (reoxidation $\Delta\delta_3 > 0.2$). —, Data not available.
[a]*Determined by XRD.*
[b]*Initial reduction temperature.*
[c]*T_{red} exceeds limits of TGA experiment (1250°C), therefore no appreciable reduction is measured.*

In the second method, a Netzsch STA 449 F3 Jupiter TGA was used to obtain equilibrium measurements of mass over a range of temperatures and O_2 partial pressures (Babiniec et al., 2015; 2016b; 2016c). Following a single break-in cycle and an initial mass measurement at a low temperature (e.g., 200°C) and pO_2 of 0.9 atm to establish an assumed $\delta = 0$ condition, samples were given adequate time to equilibrate at temperatures of 950, 1025, 1100, 1175, and 1250°C, with O_2 partial pressures of 0.9, 0.1, 0.01, and 0.001 atm at each temperature. (Note this is different set of temperatures than the referenced work; this set is skewed more towards higher temperatures.) The complete set of measurements was completed three times on individual samples and the results averaged. The resulting data sets were subjected to van't Hoff analysis to extract an enthalpy and entropy for each oxygen content (δ). These enthalpies were subsequently integrated from zero up to the δ of interest to determine the energy storage profile for the continuous reaction (Mizusaki et al., 1991; Babiniec et al., 2015, 2016b, 2016c).

This instrument was also used in DSC mode with simultaneous TGA to characterize apparent phase transitions for several materials. Powder samples weighing ca. 45 mg were ramped from ambient temperature to 1250°C and back down to 200°C at 25°C/min in an environment of 90% O_2 in an Ar balance to limit interference from the endothermic reduction reaction. Similar analyses were conducted in gaseous environments of 20% O_2 and 500 ppm O_2 with ramp rates of 50°C/min. These latter tests were repeated at least three times to confirm the results reported herein are typical.

The third thermogravimetric method was used to assess multi-cycle and cycle-to-cycle stability and repeatability and employed a TA Instruments Discovery TGA with ballistic heating capabilities. Approximately 100 mg samples of perovskite powders, sieved to 75–150 μm particle size, were subjected to a break-in cycle and then cycled up to 100 times between 400 and 1050°C (the upper limit of the furnace), with 5 min dwell times. The heating and cooling rates were 400 and 200 K/min, respectively. The high temperature (reductive) dwell was carried out under flowing Ar, or a 10/90 (v/v) air/Ar mixture. Oxidation (low temperature dwell) was carried out under flowing air. The method deviates slightly from that previously reported through the use of shorter dwell times and different gaseous environments for oxidation and reduction rather than a constant air flow throughout (Babiniec et al., 2016b).

Heat capacities were measured by DSC in a Netzsch STA 409CD with a highly stable and thermally-uniform PtRh furnace and additional isothermal jacketing (30°C) to improve the precision of the measurement. In these experiments, the material was pre-reduced at 1000°C and then cooled in argon. The heat capacity experiment was then carried out in argon by ramping from 200 to 1000°C. The pre-reduction is critical so that no reaction occurs that would contribute to the heat signal and render the heat capacity determination difficult and unreliable. However, the resulting compromise is that there are fewer chemical bonds to store energy, and thus the measured heat capacity measured likely yields a lower-bound result.

Thermodynamic models were developed in Wolfram Mathematica using a two-parameter compound energy formalism, i.e., with no δ or temperature dependence in the enthalpy or entropy of formation. Parameterization was accomplished using a least squares fit. The derivation was validated against the well-known Zinkevich model (Zinkevich et al., 2006) for ceria. For further validation, we developed a method to map the results from the compound energy formalism to the correlation developed by Bulfin and co-workers (Bulfin, et al., 2013).

RESULTS

Materials Screening

In an earlier publication, we reported two doped calcium manganites with promise for high-temperature TCES, $CaAl_{0.2}Mn_{0.8}O_{3-\delta}$ (CAM28), and $CaTi_{0.2}Mn_{0.8}O_{3-\delta}$ (CTM28) (Babiniec, et al., 2016c). The baseline material for comparison was $La_{0.3}Sr_{0.7}Co_{0.9}Mn_{0.1}O_{3-\delta}$ (LSCM3791), which had been identified in an earlier study (Babiniec, et al., 2015; 2016b). These two formulations were identified as alternatives for development through a design and screening process described here. The principal metric is storage capacity (i.e., thermodynamics). Other concerns include applicable temperature range, stability (thermal, physical, chemical), reaction kinetics, and cost. The energy contribution of the thermal reduction depends on two parameters: the reduction extent in each cycle, $\Delta\delta$, and the associated reduction enthalpy in that δ range. (For simplicity, in our calculations we generally assume $\delta = 0$ for the material in the fully oxidized state and adjust the MW and stoichiometry to account for vacancies arising from doping, i.e., $\Delta\delta = \delta$ unless otherwise indicated.)

The approach to maximize δ was to increase the average B-site oxidation state by using non-labile, low oxidation state cations on the A-sites. The approach to maximize the enthalpy was to manipulate the B-site (primarily) and A-site (secondarily) composition to drive the reduction to the high end of the temperature range of interest. Materials that require higher temperatures (or lower pO_2) to drive reaction typically have larger reaction enthalpies. This follows from a basic conceptualization and reports that the entropy change varies over a fairly small range and is largely attributable to O_2 gas formation (Meredig and Wolverton, 2009), recent advances in manipulating the entropy for thermochemical applications *via* configurational contributions from the solid notwithstanding (Zhai et al., 2018; Gautam et al., 2020). In any case, a balance must be achieved, because too large an increase in the enthalpy can compromise the reaction extent under conditions of interest. In search of this balance we combined elements known to form stronger and weaker metal oxygen bonds into single compounds.

Regarding the sensible heat component of the energy storage, heat capacities scale with the number of atoms. Thus, the molar and volumetric sensible heat can reasonably be expected to vary little from one perovskite to another. That is, this property is not subject to significant manipulation. However, the mass-normalized energy storage densities (sensible and thermochemical) scale proportionally to molecular weight. To the degree that stored mass impacts system design, cost, and efficiencies, molecular weight can be a consideration. In practice, we focused on and applied TGA to screen for materials with the goal of identifying materials with as high an initial reduction temperature as possible with reasonable extents of reduction ($\Delta\delta_3 > 0.2$), giving preference to low-cost, earth abundant elements with lower molecular weights.

Calcium manganite ($CaMnO_3$, CM) perovskites were selected as the basis for materials studies aimed at improved performance relative to LSCM3791 due to their adherence to the criteria. Calcium is a +2 cation, requiring the B-site cation to be at the maximum oxidation state of +4 in the stoichiometric material. Calcium is a relatively low molecular weight, low cost, abundant element, as is manganese. Additionally, previous studies showed that $CaMnO_{3-\delta}$ materials reduced at high temperatures (~800°C in air, Bakken et al., 2005a) and were amenable to substitution, e.g., with non-labile metals such as Al and Ti. However the parent CM has also been reported to have limited thermal stability (Bakken et al., 2005b; Leonidova et al., 2011). Therefore, in addition to manipulating the redox thermodynamics, an additional goal of substituting other elements into the manganites was to improve the thermal stability.

The pre-screen data for CM and for each doped $CaMnO_3$ perovskite are found in **Table 1**, along with LSCM3791 data for comparison. Note that the procedure should not be understood as providing equilibrium values of δ, but rather as an efficient method for identifying promising candidates for further study. The data provide an indication of the relative reduction enthalpy (higher reaction onset is an indication of larger enthalpy), redox capacity ($\Delta\delta_1$ and $\Delta\delta_2$) and reversibility ($\Delta\delta_3$), and reasonable kinetics (the values are obtained after limited hold times, or in the case of $\Delta\delta_3$, at the end of the ramp cycle time). The first set of samples evaluated included CM and similarly B-site substituted/doped materials containing one of two relatively labile cations (Fe, Co), each with a range of known oxidation states in metal oxides (+4, +3, and +2), or one of two non-labile cations, Al and Ti, expected to be present in the 3+ and 4+ oxidation states, respectively. Note that replacing Mn^{4+} with Al^{3+} requires either the oxidation of Mn^{4+} to Mn^{5+} (possibly facilitating reduction), the formation of oxygen vacancies to maintain electric neutrality (possibly inhibiting reduction), or some balance of the two. The 20% doping/substitution level was selected as being large enough to discern an impact, but likely small enough to preserve the $ABO_{3-\delta}$ single phase stoichiometry of the product.

Each material in this set was single phase by XRD and crystallized in an orthorhombic space group (Supplementary Material, **Supplementary Figure S1**). In this case, the a and b lattice parameters are very similar, closely relating the observed structures to tetragonal. As anticipated, each member of this initial set of materials displayed reduction onset temperatures higher than LSCM3791, while retaining significant redox capacity ($\Delta\delta_3 > 0.2$). However, the ferrite compositions CFM28 and CFM46 had significantly lower reduction onset temperatures than the other formulations and the parent material, an indication that the Fe was initially present in a highly reducible Fe^{4+} state. CFM formulations were dropped from further consideration based on this result.

Each of the remaining materials, CM, CTM28, CCM28, and CAM28, was annealed in flowing Ar for 5 h at 1000°C to evaluate the possible effects of deep reduction (**Supplementary Figure S2**). XRD was conducted on the annealed material to determine any phase changes due to the reduction process. CM and CCM28 were found to have decomposed (**Supplementary Figures S2A,B**), consistent with previous reports for CM, and excluded from further study. CTM28 and CAM28 did not decompose, but rather converted from the orthorhombic structure to the tetragonal (distorted cubic) perovskite phase with a corresponding increase in lattice parameters (**Supplementary Figures S2C,D**). CTM28 and CAM28 were advanced forward for further study.

Based on the results for CTM28 and CAM28, second and third sets of compounds were synthesized for evaluation (**Table 1**). The goals and metrics remained the same–further increases in reduction temperature without excessive loss of reaction extent. The second set of compounds expanded the selection of non-labile compounds to include Zn, Y, and Zr, which were anticipated to assume the +2, +3, and +4 oxidation states, respectively. The materials from the second set of compounds did not form single phases by XRD. The Y-doped material, CYM28, segregated into at least two phases that index to an A-site doped orthorhombic perovskite and A-site doped tetragonal Ca_2MnO_4 phase (**Supplementary Figure S3A**). The reduction temperature of CYM28 increased significantly above that of CM, but the redox capacity was very limited. In CZnM28 samples, ZnO precipitated out, at least in part, leaving a presumably-redox-active tetragonal calcium manganite phase (**Supplementary Figure S3B**). CZrM28 also phase segregated, in this case into two orthorhombic ABO_3 perovskites ($CaMnO_3$, $CaZrO_3$) (**Supplementary Figure S3C**). CZnM28 and CZrM28 each have initial reduction temperatures similar to CM and satisfy the reaction extent criteria. Of the two, CZrM28 was chosen for further study, despite crystallizing in two phases, because it displayed the most promising redox capacity as well as rapid kinetics, and circumvented the possibility of volatility issues often encountered with Zn compounds at high temperature.

The third set of samples expanded the range of Ti substitution and combined Ti substitution with La or Sr A-site doping/substitution. Each of the synthesized materials are single-phase and adopt the same orthorhombic perovskite structure as the parent CTM28 compound. CTM46 and CTM64 exhibit increased reduction onset temperatures over CTM28, but the redox capacity of the materials declined significantly and were eliminated from further study. On the other hand, the initial reduction temperature of CTM0595 decreased compared to CTM28, but its redox capacity improved. As the net enthalpic trade-off between those two properties was not known, CTM0595 was selected for additional analysis. However, the material was found to decompose at high temperature and low pO_2, similar to the parent CM, indicating that doping at the 5% level is inadequate to provide the required stabilization. As a result the material was eliminated from further evaluation. Regarding the A- and B-site modified materials, CSTM8228 exhibited redox properties very similar to CTM28, suggesting there would be little or no benefit for the added expense. Nonetheless this material was selected for further evaluation as it met the screening criteria. On the other hand, La, likely substituting as a 3+ cation, significantly increased the reduction temperature albeit at the expense of a collapse in the redox capacity. As a result, the two La-doped materials were eliminated from further consideration.

Since the completion of this work, a detailed study of CTM55 in the context of water splitting has been published. An enthalpy

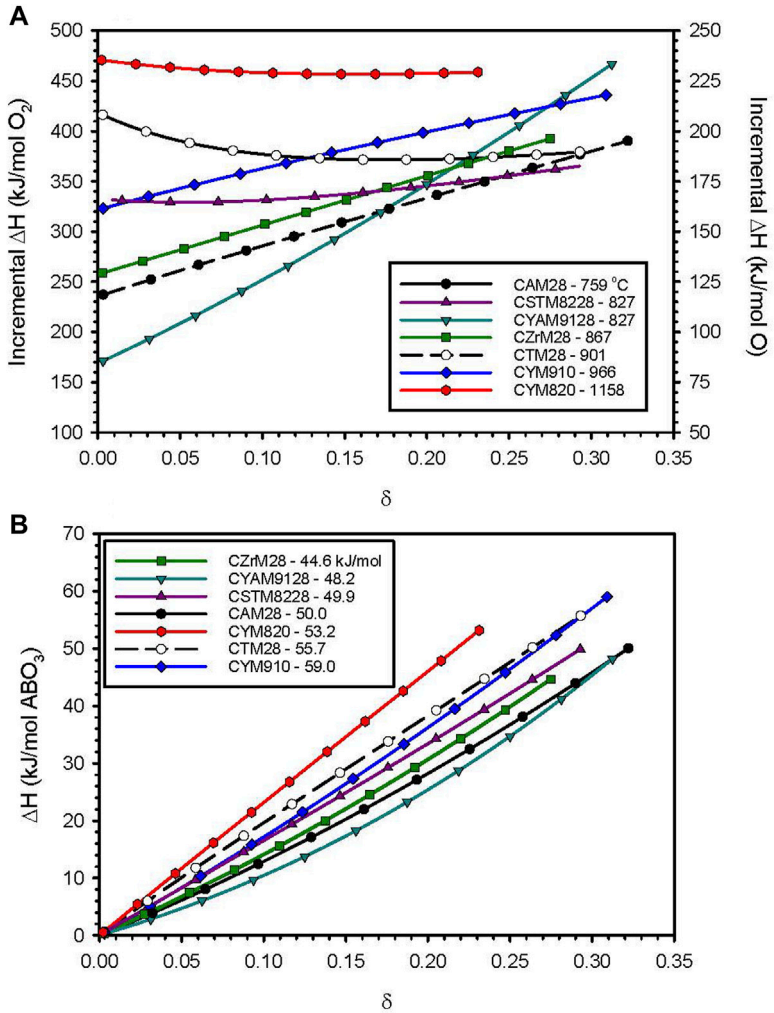

FIGURE 1 | Results from van't Hoff analysis of TGA data for selected perovskite formulations. **(A)** Incremental reduction enthalpy as a function of δ. Captions list the initial reduction temperature observed by TGA (°C). **(B)** Cumulative reduction enthalpy data from **Figure 1A** integrated from 0 to δ. Captions indicate the measured value at the largest realized value of δ. **Supplementary Figure S5** provides these same results on a mass basis and includes data points taken from the literature for other calcium manganites.

of 400–560 kJ/mol O_2 and a maximum δ of 0.225 were reported, e.g., at T = 1500°C and pO_2 = 0.00082 atm (Qian, et al., 2021). This is consistent with our observations regarding CTM46 and CTM64.

Screening of A-Site Y-Doping

In the screening studies described above, only Y-doping and La A-site doping resulted in reduction temperatures above that achievable with Ti alone. It was also observed that Y appeared to prefer to reside on the A-site of the calcium manganites. These observations prompted screening studies of intentional Y A-site doping. The results are presented in **Table 2** alongside data for CM, CAM28, and CYM28 for ease of comparison. Each of the A-site doped materials crystallized as a single phase by XRD rather than the multiphase composition that comprised CYM28. The CYM patterns exhibit peak splitting that becomes more pronounced as the concentration of Y increases (**Supplementary Figure S4**). In pure CM, similar splitting has been attributed to oxygen vacancy ordering as oxygen is removed from the lattice (Chiang and Poeppelmeier, 1991). However, the inclusion of Y^{3+} cations on the A-site does not require vacancy formation to achieve charge neutrality for these materials, though it cannot be ruled out. (Mn can assume the +3 oxidation state to balance the Y.) Thus, we suggest the splitting is possibly the result of distortion in the crystal lattice arising from the presence of the slightly smaller Y cation. The doubly-doped materials CYAM9128 and CYAM8228 do not exhibit similar splitting, suggesting the presence of Al on the B-site balances or stabilizes the lattice against distortion.

The data in **Table 2** further illustrate the success of this approach. Each of the A-site Y-doped materials exhibits a higher initial reduction temperature than its parent (CM for CYM samples and CAM for CYAM samples). Additionally the reduction temperature adheres to a clear pattern of increasing

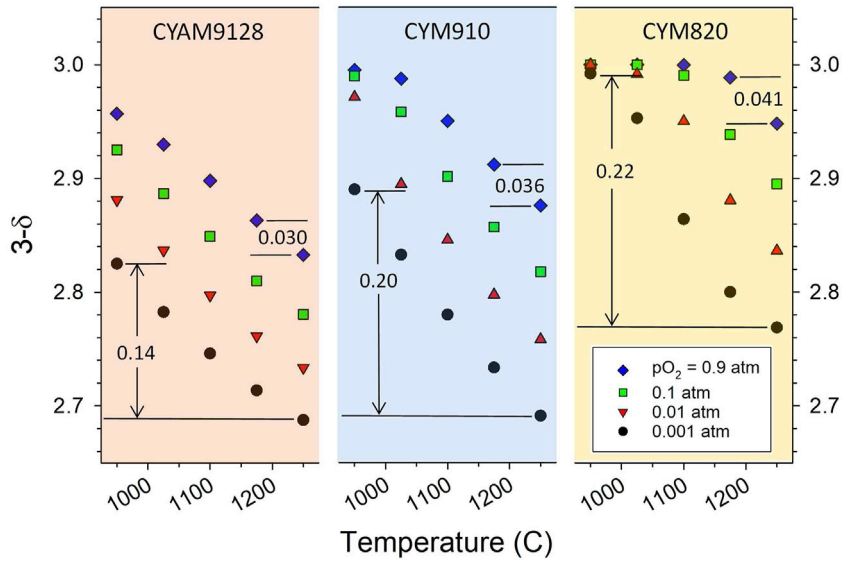

FIGURE 2 | Measured oxygen stoichiometry (3-δ) of CYAM9128, CYM910 and CYM820 as a function of temperature and pO_2 (assumes δ = 0 in fully oxidized state). Numbers in the graphs indicate Δδ values for the associated temperature interval and illustrate that for a given pO_2, the dependence of δ with T (the slope) increases in the order CYAM9128 < CYM910 < CYM820, the opposite of the trend for ΔH with δ (**Figure 1A**). *See* also **Supplementary Figure S6**.

with yttrium concentration. (CYM550 is a possible exception as the reduction temperature of both CYM640 and CYM550 exceed the upper limit of the screening, 1250°C.) As expected, the redox capacity shows a trend of decreasing with increasing initial reduction temperature. However, as the highest of these temperatures are so near the temperature limit of the experiment, it is possible, perhaps even likely, that these materials have significant reduction capacity which is not sampled by this screen. In any case, CYM910 and CYAM9128 fully meet the screening criteria and were further evaluated. CYM820 was also selected for further study as it exhibited significant redox capacity even though reduction began within <100°C from the upper temperature limit.

Reduction Enthalpies by TGA

The δ-dependent enthalpies extracted *via* van't Hoff analysis are plotted in **Figure 1A**, while the cumulative molar reduction enthalpies (i.e., integrated from 0 to δ) are plotted in **Figure 1B** for CZrM28, CSTM8228, CYM910, CYAM9128, and CYM820. Previously reported values for CTM28 and CAM28 are included for comparison (Babiniec et al., 2016c). Results normalized on a mass basis are provided in **Supplementary Figure S5** and **Supplementary Table S1** alongside literature values for related CM materials. The data in each plot extends to the δ value corresponding to the most extreme experimental condition: 1250°C, and pO_2 = 0.001 atm. The data in **Figure 1B** reflect differences in volumetric storage capacities since each material should have very similar molar volumes and molar sensible heat capacities. That said, the relative results on a mass basis are quite similar given that the molecular weights for this group of materials varies by only 12.5% from least (CAM28) to greatest (CYM820).

The initial reduction temperature (provided in the figure legend) and the low-δ enthalpies do not show a 1:1 correlation in **Figure 1A**. This is likely reflective of the fact that a somewhat subjective method of determination (particularly in cases where the data exhibited significant curvature and baseline drift) of the initial temperature was applied to data collected during a rapid temperature ramp where small differences in kinetics may have a significant impact. Differences in entropy terms for the materials may also play a role. Nonetheless, **Figures 1A,B** show that the initial reduction temperature is a fairly coarse, but effective, screen for identifying materials of interest. The highest cumulative enthalpies correspond to the three materials with the highest initial reduction temperatures. And, with the exception of one, the materials show higher enthalpic potential than the previously identified CAM28 across the range of δ, and two also show improvements over CTM28. The highest total enthalpy is observed for CYM910, however, CYM820 shows potential to eclipse that if δ is increased, e.g., through higher reduction temperatures. This trend highlights the ability to influence reduction thermodynamics *via* A-site doping, with implications for the design of future materials.

Note that the thermodynamic data in **Figure 1A** are informative of the reduction behavior beyond the reduction onset temperatures. A large variation in ΔH over the range of δ values, i.e., a material that seemingly becomes increasingly difficult to reduce with increases in δ (*see* discussion in *Thermodynamic Modeling* section regarding δ and T dependence), is an indication that for a given pO_2 the material reduces incrementally over a larger temperature range than one with a more uniform (small slope with δ) enthalpy. That is, a relatively constant ΔH indicates that a large portion of the reduction, i.e., change in δ, will take place over a relatively

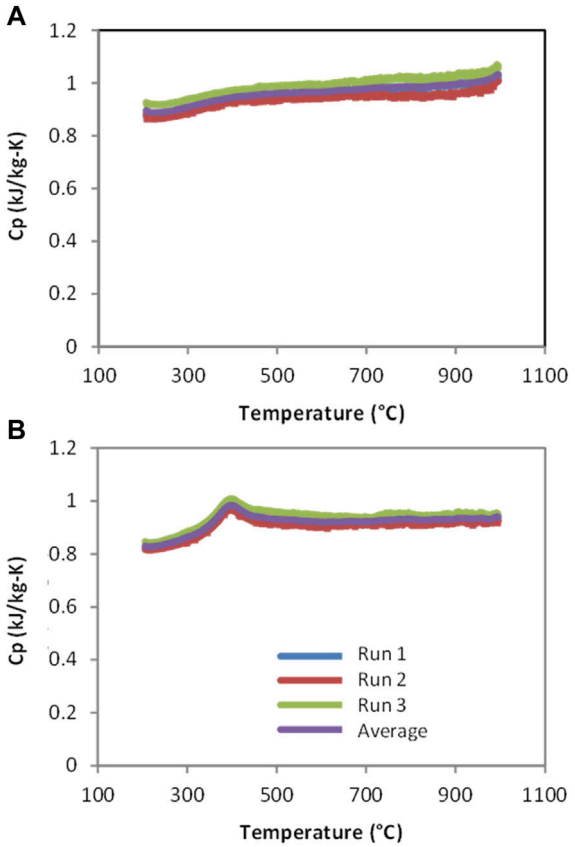

FIGURE 3 | Triplicate DSC measurements of heat capacity for **(A)** CAM28, and **(B)** CTM28.

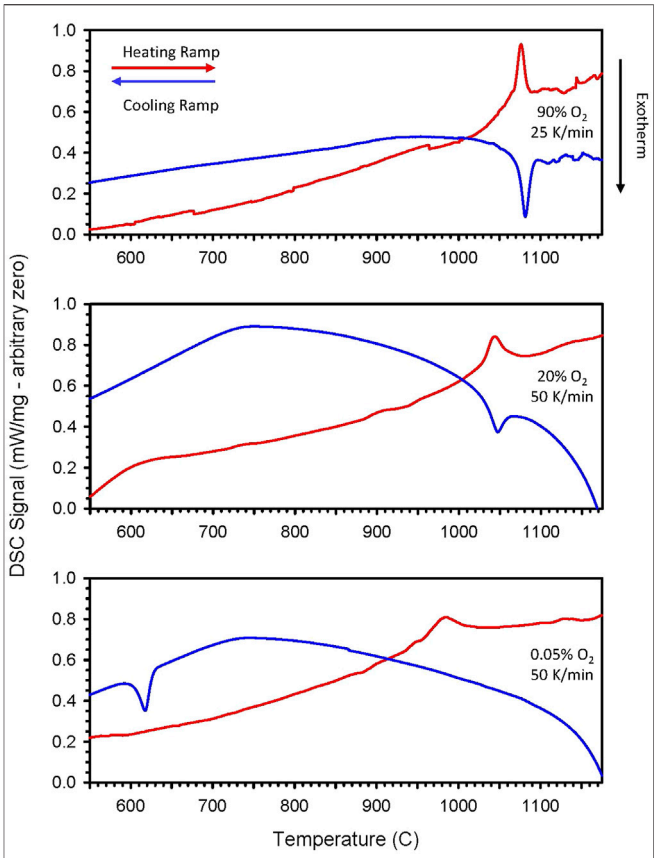

FIGURE 4 | Individual DSC traces of CYM910 show small endothermic and corresponding exothermic peaks during ramp up and ramp down of temperature, respectively. Peak positions vary as a function of ramp rate and gaseous environment (pO_2). (Top: 90% O_2, 25°C/min; middle: 20% O_2, 50°C/min, bottom: 500 ppm O_2, 50°C/min). Peak positions and corresponding δ values elucidated *via* concurrent TGA are given in **Supplementary Table S2**. These peaks are likely indicators of phase changes that take place as a function of temperature and reduction state of the oxide. The depicted behavior is reproducible over several cycles. Similar behavior is observed for CZrM28 (**Supplementary Figure S7** and **Supplementary Table S2**).

small, but specific, range of ΔT for a given pO_2. This is illustrated in **Figure 2** and **Supplementary Figure S6** wherein the experimental 3-δ values (assuming no native vacancies) for CYM820, CYM910, CYAM9128 are plotted as a function of T and various pO_2 values. For a given pO_2, the dependence of δ with T (the slope) is seen to increase in the order CYAM9128 < CYM910 < CYM820. These three samples are seen in **Figure 1A** to have enthalpy values that have large, intermediate, and little dependence on δ, respectively, thereby illustrating the point.

DSC Analysis

In an earlier publication we reported that preliminary results for CAM28 and CTM28 suggested that the heat capacities are consistent with theoretical values (Miller et al., 2016). The theoretical Dulong-Petit limit of 3NR or 15R for perovskites is 125 J/mol-K. After accounting for the molecular weights, this works out to 0.89 and 0.91 kJ/kg-K, for CAM28 and CTM28, respectively. The specific heats of thermally reduced CAM28 and CTM28 determined by differential scanning calorimetry (DSC) over the range of 200–1000°C and shown in **Figure 3** confirm our earlier report. Note the measurements were highly reproducible, with a maximum deviation between runs of ~0.035 kJ/kg-K for CAM28 and ~0.019 kJ/kg-K for CTM28. The heat capacities depicted in **Figure 3** likely represent a lower-bound result, as the reduction necessary to accomplish the measurement decreases the number of atoms in the material. The curve for CAM28 is well-behaved (**Figure 3A**), with a small inflection observed near the beginning and a more prominent one approaching the ending at each curve, i.e., at 200°C and approaching 1000°C. The former may result from the establishment of temperature equilibrium while the latter may represent the onset of a transition (*see* below). The possibility of reaction onset is unlikely due to the pretreatment and the absence of a similar observation for CTM28, which would be expected if residual O_2 in the argon allowed for partial reoxidation of the samples after pretreatment. In contrast to CAM28, CTM28 has a clear and reproducible peak at ~375°C (**Figure 3B**). The area under the peak accounts for an endotherm of approximately 5 J/g. This behavior is suggestive of the material undergoing reversible phase transition or ordering. The low temperature for this transition relative to those reported immediately below and in

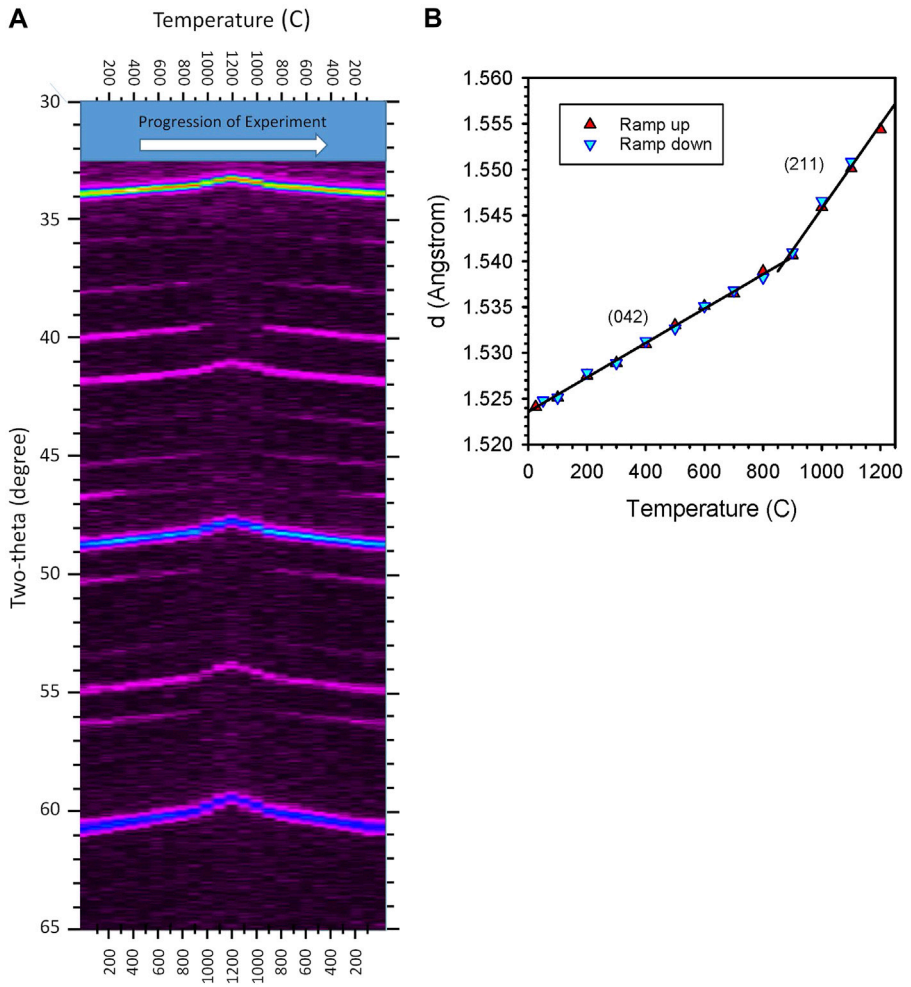

FIGURE 5 | Results for *in-situ* XRD of CYM910 under flowing N_2 with 500 ppm O_2. Aside from end points, scans were done in 100°C increments (25, 100, 200 . . . 1100, 1200, 1100 . . . 200, 100, 50°C). **(A)** XRD intensity plot. Reversible peak shifts are attributable to a combination of thermal expansion across the temperature range and a phase (symmetry) change at the highest temperatures. The disappearance and reappearance of peaks are attributable to symmetry (phase) changes. Elapsed time increases from left to right. **(B)**: Variation in d-spacing calculated for the intense peak appearing between 59 and 61° two-theta for the experiment shown in **(A)**. With the lines provided to guide the eye, and taking **(A)** into account, it is clear that a transition from an orthorhombic to tetragonal phase occurs at a temperature near 900°C. The peak index changes accordingly, as shown. *See* **Supplementary Figure S8** for an alternate visualization of the data.

the *In-Situ XRD* section may be attributable to the pre-reduction and presence of vacancies.

During TGA/DSC prescreening of CZrM28 and CYM910, small peaks not corresponding to reduction phenomena were noted in the DSC signals. In each case, an endothermic peak was observed during the ramps to high temperature, and corresponding exothermic peaks were observed during cooling. Careful DSC measurements were made to better characterize these observations. Initially, high pO_2 conditions were employed to prevent or minimize interference from the reduction reaction. For CYM910, endothermic and exothermic peaks were observed at 1076 and 1081°C, respectively (**Figure 4** and **Supplementary Table S2**), and for CZrM28 at 950 and 958°C (**Supplementary Figure S7** and **Supplementary Table S2**). Careful peak integration with background subtraction gave values of 8.3 J/g for CZrM28 and 9.3 J/g for CYM910, similar in magnitude to the peak observed for CTM28, suggesting a similar origin, likely a phase transition (*vide infra*) The potential contribution to the total storage capacity from these transitions is very small, less than 5% of the reduction endotherm. The apparent features found at higher temperature, e.g., in the 90% O_2 traces, are believed to be artifacts as they are not reproduced under other conditions and not readily correlated with other observations. However, we cannot entirely rule out the possibility that these features are the result of a low energy transition such as vacancy ordering, lattice distortion, or very minor impurity.

Additional DSC data was collected for these materials under 20% and 500 ppm O_2 at a ramp rate of 50°C/min. Representative traces for these conditions are also shown in **Figure 4** and **Supplementary Figure S7**, and summarized in

Supplementary Table S2. Under 20% O_2, the peaks shift to a lower temperature but remain relatively closely spaced. Even larger shifts towards lower temperatures are observed under 500 ppm O_2, and the peak positions during the heating and cooling ramps vary significantly from one another. In fact, a peak is not observed during the cooling ramp for CZrM28 under 500 ppm O_2. These trends are indicative that the events responsible for the peaks are not only a function of the temperature, but of the reduction state of the material as well. As is readily seen in **Supplementary Table S2**, a deeper reduction state (larger δ) correlates with lower temperature DSC features. The divergence of the peaks under 500 ppm O_2 results in part from the fact that the materials begin in a highly oxidized state and are reduced during the heating ramp, but do not return or even approach that state during reoxidation (cooling) at low pO_2. Complicating this is the fact that the temperature ramps are rapid so that the material composition is not at thermodynamic equilibrium with the gas phase at all points during the ramps. The temperature increase outpaces the move towards equilibrium *via* reduction, and the decrease likewise outpaces the oxidation, particularly in the lower temperature regions. That is, in the case of 500 ppm O_2, δ is quite asymmetric and not at equilibrium as a function of temperature for heating and cooling, resulting in the divergence in the DSC from one another. In contrast, for 90 and 20% O_2, where oxidation and reduction are only expected at the highest temperatures, δ is fairly consistent (symmetric) as a function of T during the heating and cooling ramps.

In-Situ XRD

In-situ XRD characterization was done for samples of CAM28, CYM910, CYAM9128 and CZrM28. CAM28, CYM910, and CYAM9128 were heated and cooled in flowing gas containing 500 ppm O_2. CYM910 was also heated and cooled under air. The biphasic CZrM28 material was heated and cooled under both low pO_2 and in air, the latter to avoid possible decomposition of the CM phase. A representative example is shown for CYM910 in **Figure 5** and **Supplementary Figures S8, S9**. In each case, samples were observed to convert from an orthorhombic perovskite phase to a tetragonal (slightly-distorted-cubic) phase in high temperature scans. These transitions were observed to occur in the ranges $800 \leq T \leq 900$°C for CAM28; $1000 \leq T \leq 1100$°C for CYM910 in air and $800 \leq T \leq 900$°C in 500 ppm O_2; $900 \leq T \leq 1000$°C for CYAM9128; and $800 \leq T \leq 900$°C for CZrM28 in 500 ppm O_2 and $900 \leq T \leq 1000$°C in air. In the particular case of CZrM28, both of the constituent perovskites were maintained as distinct materials throughout the entire temperature scan with only the CM phase undergoing a phase change (**Supplementary Figures S10, S11**). The center of these temperature ranges are within 17–123°C of the observed initial reduction temperatures (**Tables 1**, **2**). More significantly, the peaks observed in DSC for CZrM28 and CYM910 in 20% O_2 (**Supplementary Table S2**) fall within the respective ranges observed by *in-situ* XRD in air. For the 500 ppm O_2 evaluations, the regions overlap in both cases. These results provide strong evidence that the "additional" energetic events observed in DSC are associated with phase transformations of the various perovskites.

Multi-Cycle TGA

We previously reported the results from ballistically heated, multi-cycle TGA evaluations of CAM28 and CTM28 (50 and 100 cycles, respectively, between 400 and 1050°C in air) (Miller et al., 2016). These results demonstrate the substantial stability of these materials, and the qualitatively rapid redox kinetics. The observed changes in Δδ were +0.0004, for CTM28 over 100 cycles, and −0.002 in 50 cycles for CAM28. CTM28 reoxidized fully during cool-down in less than 5 min. Furthermore, the particles exhibit no changes in structure (by XRD) nor particle morphology (by SEM) after cycling (the particles begin and end in a "fully oxidized" state) (Babiniec et al., 2016b). Stability was further verified over 10 cycles in a rapidly heated up-flow reactor (UFR) (Bush et al., 2017) for CAM28, CTM28, and LSCM3791 (**Supplementary Figure S12**). Reduction kinetics were observed to be so rapid that they could be modeled assuming a heat-transfer limited reaction under some conditions (Schrader et al., 2020). Additionally, sintering was characterized *via* dilatometry. Sintering temperatures were determined by the tangent line method to be 1197 and 1211°C for CAM28 and CTM28, respectively. The sintering results likely represent a worst case as the measurements were conducted with a particle packing density orders of magnitude higher than what is expected in particle storage (Miller et al., 2016). Taken as a whole, these results verify that the transition events seen in XRD and DSC for CAM28 do not present a barrier to repeated cycling; the transitions are complete and reversible over the cycle. Furthermore they are suggestive that similar observations for other materials are not necessarily indications of stability issues.

Similar multi-cycle TGA studies were completed for CYAM9128, CYM910, and CZrM28. An example illustrating the procedure and demonstrating cycle-to-cycle repeatability for CYAM9128, reduced in Ar and oxidized in air, is provided as **Figure 6**. In the case of CYM910, reduced in 90:10 Ar:air and oxidized in air, an increase in mass was observed over the course of the experiment. As post-reaction XRD showed no phase changes, it is presumed this is the result of an inadequate break-in time (the sample was not quite in an equilibrium "fully oxidized" state after break-in), or a baseline shift, or most likely a combination of both. This latter possibility is supported by two observations. First, Δδ is observed to increase primarily over the first 20 cycles or so with weight gain being larger than weight loss (**Supplementary Figure S13**). The divergence between gain and loss diminishes with increasing cycles. That is, the sample was slowing moving towards a more fully oxidized state in the earlier cycles. The process required multiple cycles as the oxidation temperature was low and the hold times short. It is reasonable to assume Δδ will eventually reach a steady state plateau constrained by equilibrium and kinetic considerations. Second, while the Δδ curve flattens after the early cycles, the reported mass for the oxidized state increases steadily over the latter half of the experiment (**Figure 6**). This is consistent with a slight baseline shift taking place over the second day of the lengthy evaluation. In any case,

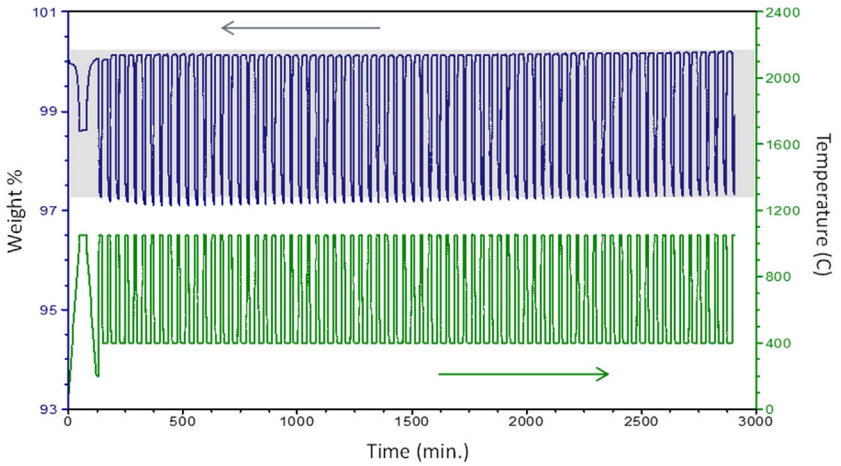

FIGURE 6 | Multi-cycle TGA of CYAM9128 illustrating stability over 74 cycles (reduction in Ar, oxidation in air). First cycle is a break-in to bring sample to a known condition and not counted. Shading is provided as an aid to the eye due to slight baseline shifts.

the experiment demonstrates cycling is reversible, rapid, and resists degradation.

The results for CZrM28, reduced in Ar and oxidized in air, stand in sharp contrast to the others. **Supplementary Figure S14** shows that the measured Δδ increases over the first 15 cycles and then exhibits a decline that becomes severe by cycle 20. The rate of decline has significantly slowed by the final (100th) cycle. However, the Δδ capacity has been reduced to <30% of its peak value. Recalling that this sample is composed of a mixture of $CaZrO_3$ and $CaMnO_3$ phases, and assuming, as above, that $CaZrO_3$ is irreducible under these conditions, the result is consistent with the decomposition of $CaMnO_3$ under high temperature reducing conditions (**Supplementary Figure S2A**), though this could not be confirmed by XRD due to insufficient sample recovery. This result illustrates the importance of evaluating the stability of candidate materials over a large number of cycles at the extremes of the conditions they might be subjected to (e.g., temperatures, reducing atmospheres, and rapid transients).

Thermodynamic Modeling

The simplified van't Hoff relationship is a convenient and simple method for fitting TGA data and extracting thermodynamic parameters from sets of TGA data. It lacks utility for design and analysis work, however, as it does not provide an equation set predicting δ as a function of T and pO_2, for example. Nonetheless, it is theory-based in that the linearized van't Hoff relationship is derived from the equilibrium expression for the reduction reaction, assuming that the gas phase is ideal, the activities of the oxidized and reduced phases are nearly identical, and the thermodynamic parameters are functions of only δ and not temperature. That is, the temperature dependence is convoluted into the δ dependence.

The van't Hoff analysis requires T and pO_2 data pairs at constant δ. Unfortunately, TGA does not lend itself well to collecting constant δ data. Rather, as described in **Materials and Methods**, δ is measured across the T and pO_2 ranges of interest. Lines of constant δ are then numerically generated by interpolation from the typically sparse data set (e.g., 20 points spanning >600°C, and nearly four orders of magnitude for pO_2). In our case, this analysis is done by fitting a line to each constant pO_2 data set (δ = mT+b), and then applying these fits to generate constant δ data sets in $\ln(pO_2)$, 1/T format. Performing linear regression on these generated data sets yields the van't Hoff parameters; ΔH and ΔS are extracted from the slope and intercept, respectively. While we find linear fits to constant pO_2 data (in our case five points) are generally quite good, there is nothing physical supporting this choice. Any reasonable numerical approach to describing the pO_2, T, δ surface could be adapted, and non-linear approaches may be needed, especially for cases where larger data sets are available.

Given the significant assumptions and limitations inherent to the van't Hoff approach, we sought to develop an alternate, potentially more rigorous, method of analyzing TGA data sets, giving preference to one tied to predictive computational methods. We began with the widely known compound energy formalism (CEF) (Hillert, 2001). The CEF is a method for computing the thermodynamic properties for solid solution phases, i.e., those with two or more sublattices with possible variations in composition, including variations in reduction state. The CEF offers a theory-backed basis to derive an improved general functional relationship for fitting TGA data that supports the derivation of thermodynamic parameters with their δ- and T-dependence. The resulting models are functional for systems and analysis efforts.

As a solution based approach, the CEF combines weighted contributions from simple end members, accounts for configurational entropy (mixing), and corrects from these simple linear combinations (regular solution) with "excess terms."

$$G_{ABO_3} = y_i^A y_j^B y_k^X G^0_{A_iB_jX_k} + RT\left(S_A + S_B + 3^*S_X\right) + G_{excess} \quad (3)$$

To elaborate, the set of end members in the CEF consists of all possible combinations with a single constituent species on each

sublattice; constituent species include all the elements and possible charge states in the composition of interest and lattice vacancies. For the ABO_3 perovskites, there are three sublattices, A, B and X, represented as $A_iB_jX_k$ where i, j, and k reflect the possible species, on the A, B, and X sub-lattices, respectively. For CAM28, the 12-fold coordinated A sub-lattice consists of only Ca^{2+}. On the six-fold coordinated B sub-lattice, there are three possible species: Al^{3+}, Mn^{4+}, and Mn^{3+} (excluding the possibility of either Mn^{5+} or Mn^{2+}). For the X sublattice, the possible species are O^{2-} and vacancies (v). The weighted fractions are represented as y_α^γ where α is each possible species on a given sublattice γ = A, B, X, and $\sum y_\alpha^\gamma = 1$, summed on α for each sub-lattice. The end member contribution is thus:

$$y_i^A y_j^B y_k^X G^0_{A_iB_jX_k} \tag{4}$$

For CAM28, the weighting terms are:

$$y^A_{Ca} = 1, \tag{5}$$

$$y^{B3+}_{Al} = x = 0.2,\ y^{B4+}_{Mn} = 1 - x - 2\delta = 0.8 - 2\delta,\ y^{B3+}_{Mn} = 2\delta \tag{6}$$

$$y^X_{O2-} = 1 - \delta/3,\ y^X_V = \delta/3 \tag{7}$$

An Important Simplification Is

$$G^0_{A_iB_jX_v} = G^0_{A_iB_jX_{O2-}} - {}^3\!/_2 G^0_{O_2}. \tag{8}$$

The configurational entropy contribution to the CEF is constructed around the assumption of ideal random mixing on each sublattice, i.e., a random solution model, which is:

$$TS_{conf} = RT\,(S_A + S_B + 3\ S_X^*) = -RT \sum\nolimits_{\alpha,\gamma} n^\gamma y_\alpha^\gamma\, ln\left(y_\alpha^\gamma\right) \tag{9}$$

Where n^γ is the stoichiometric coefficient of sublattice γ. The excess term accounts for interactions between species and are often accounted for using Redlich-Kister polynomial expressions (Redlich and Kister, 1948).

With this background, we return to the goal of deriving a useful expression from the CEF that relates the equilibrium composition of the solid (δ) to the externally imposed or constrained pO_2 of the gas phase and temperature (T). Phase equilibria requires that the oxygen chemical potential (OCP) or a related state function be equivalent in the solid and gas phases. Here we opt for a unitless state function that we refer to as $\tilde{g}$

$$\tilde{g} \equiv -\frac{G}{RT} = \frac{S}{R} - \frac{H}{RT} \tag{10}$$

Where G, S, and H, are the Gibbs free energy, entropy, and enthalpy, respectively. The OCP in the gas phase is $\frac{1}{2}G_{O2}$; in the solid the OCP is $\frac{dG_{solid}}{dz} = -\frac{dG_{solid}}{d\delta}$ where z is the oxygen concentration and δ is the off-stoichiometry. For convenience, we apply two simple transforms to T and pO_2.

$$\tilde{\beta} = \frac{T_{ref}}{T}\ \ and\ \ u = \frac{1}{2} ln\left(\frac{p_{ref}}{p_{O_2}}\right) \tag{11}$$

We choose reference values of significance to the TGA campaign and compounds of interest, $T_{ref} = 1073.15\,Kelvin$ and $p_{ref} = 0.20946\,Atm$ (pO_2 in air at ambient). These transforms provide unitless variables or coordinates, and hence avoid potential confusion related to units. The phase equilibrium can thus be stated as

$$\frac{d\tilde{g}_{solid}(T,\delta)}{d\delta} = -\frac{1}{2}\tilde{g}_{O_2}(T, p_{O2}),\ or \tag{12}$$

$$\frac{d\tilde{g}_{solid}\left(\tilde{\beta},\delta\right)}{d\delta} = -\frac{1}{2}\tilde{g}_{O_2}\left(\tilde{\beta}; p_{ref}\right) - u \tag{13}$$

For any metal oxide, we derived the following form, truncated to three temperature terms, for the solid phase:

$$\frac{d\tilde{g}_{solid}\left(\tilde{\beta},\delta\right)}{d\delta} = p_0(\delta) - \tilde{\beta}\, p_1(\delta) - \ln\left(\tilde{\beta}\right) p_2(\delta) + \sigma(\delta) \tag{14}$$

Given the limited range in $\tilde{\beta}$, three temperature terms are generally sufficient. The three polynomials $p_0(\delta),\ p_1(\delta)\ and\ p_2(\delta)$ are typically no more than quadratic functions of δ originating from the excess terms, and $\sigma(\delta)$ is the derivative of the configurational entropy with respect to δ determined only by structure and valence.

$$p_j(\delta) = a_{0j} + a_{1j}\,\delta + a_{2j}\,\delta^2 \tag{15}$$

$$\sigma(\delta) = \frac{d\,S^{config}/R}{d\delta} \tag{16}$$

The reduction enthalpy and entropy of the solid then rigorously follow from the variational principle and Gibbs relationship, respectively as:

$$\frac{dH_{solid}}{d\delta} = -\frac{d^2\tilde{g}_{solid}}{d\delta d\beta} = p_1(\delta) + \frac{p_2(\delta)}{\tilde{\beta}} \tag{17}$$

$$\frac{d\Delta H}{d\delta} = \frac{dH_{solid}}{d\delta} + \frac{1}{2}H_{O_2} = p_1(\delta) + \frac{p_2(\delta)}{\tilde{\beta}} + \frac{1}{2}H_{O_2} \tag{18}$$

$$\frac{dS_{solid}}{d\delta} = \frac{d\tilde{g}_{solid}}{d\delta} + \tilde{\beta}\,\frac{dH_{solid}}{d\delta} \tag{19}$$

$$\frac{d\Delta S}{d\delta} = \frac{dS_{solid}}{d\delta} + \frac{1}{2}S_{O_2} = p_0(\delta) + \left(1 - \ln\left(\tilde{\beta}\right)\right)p_2(\delta) + \sigma(\delta) + \frac{1}{2}S_{O_2} \tag{20}$$

For the gas phase, we use an analytic fit to tabulated data for temperature ($\tilde{\beta}$) dependence at pO_2 = 1 bar (HSC, 2021), and transform to the reference pressure

$$\tilde{g}_{O_2}\left(\tilde{\beta},p_{ref}\right) = 26.2977 + 0.7843\,\tilde{\beta} - 2.6316\,\ln\left[\tilde{\beta}\right] + \frac{1.5084}{\tilde{\beta}} - \frac{0.307}{\tilde{\beta}^2} + \frac{0.0347}{\tilde{\beta}^3} + 0.007\tilde{\beta}^2 \tag{21}$$

Or alternately in a linear approximation,

$$\tilde{g}_{O_2}\left(\tilde{\beta},p_{ref}\right) = 30.5410 - 1.6387\,\tilde{\beta} \tag{22}$$

With both sides of the phase equilibrium equation defined, the tools are in place to derive parameters from TGA or similar data to apply to modeling and development efforts. Note that the CEF-derived model physically limits the fitting parameters and functional form and enables semi-empirical and/or computational parameterization (Gautam et al., 2020). First,

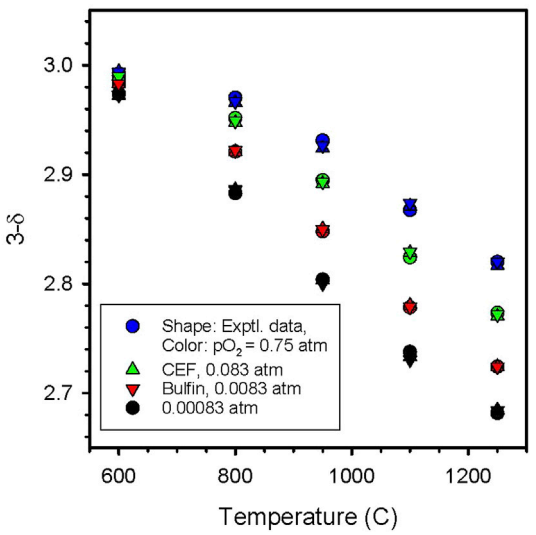

FIGURE 7 | Comparison of CEF and Bulfin fits to CAM28 data. The shape of the data point indicates the data set (experimental - circle, CEP–up triangle, Bulfin–down triangle) while the color indicates the pO_2 (blue – 0.75 atm, green – 0.083 atm, red – 0.0083 atm, black – 0.00083 atm). Both approaches fit the data well. No distinction between approaches can be discerned, given the currently available data.

by way of validation, we have confirmed (*see* "Model Validation" in supporting material) that we are able to invert the data and infer the parameters for ceria from the well-known Zinkevich model (Zinkevich et al., 2006). Returning to CAM28, we find that, despite the possibility of using nine parameters, we achieve a good fit to the previously published data with just two fitting parameters in a linear least squares fit and could not get statistically significant additional terms,

$$p_0(\delta) = a_{00} = -5.49 \tag{23}$$

$$p_1(\delta) = a_{01} = 15.85 \tag{24}$$

Where (recalling x = 0.2 for CAM28)

$$\sigma(CAM;\delta) = 6ArcTanh\left(\frac{1}{3}(3-2\delta-x)\right) + 2\,ln(1-2\delta-x) - 2Ln(2\delta) \tag{25}$$

Note that $p_1(\delta)$ is ~141 kJ/mol O and thus ΔH is 154 kJ/mol (308 kJ/mol O_2) at T_{ref}, independent of δ. (A variation in reduction enthalpy with temperature results from changes in the gas phase enthalpy with temperature.) This value is comparable to the value obtained from van't Hoff analysis, 311 kJ/mol O_2, when averaged over δ = 0.0–0.3221. Experience with a number of different compounds suggests that good fits with this method will often require only a subset of the parameters, i.e., that the extracted enthalpy values will be constant over the full range of δ. Changing our assumptions, e.g., allowing Mn to be present as Mn^{5+}, did not improve the fit; others make the fit become unphysical.

An alternative to our approach is to derive an analytic expression for $\delta(T, pO_2)$ by formulating rate equations for re-oxidation and reduction reactions and setting them equal to one another as the equilibrium condition. With this approach, Bulfin et al. arrive at the following equation (Bulfin et al., 2013).

$$\left(\frac{\delta}{\delta_m-\delta}\right) = \left(\frac{A_{red}}{A_{ox}}\right)\left(\frac{p_{O2}}{p_{ref}}\right)^{-n} e^{-\frac{E_a}{RT}} \tag{26}$$

Where δ_m is the maximum possible value of δ (physically limited by stability), A_{red} and A_{ox} are pre-exponential factors for Arrhenius expressions, n is the reaction order in gas phase O, and E_a is the net activation energy (E_{red}–E_{ox}). We mapped this formulation into our equation form to provide a comparison.

Then, the mapping yields the following expressions in place of our polynomials.

$$p_0(\delta) = \frac{1}{2n} ln\left(\frac{A_{red}}{A_{ox}}\right) - \frac{30.5278}{2} \tag{27}$$

$$p_1(\delta) = \frac{1}{2n}\frac{E_a}{RT_{ref}} - \frac{1.6387}{2} \tag{28}$$

$$\sigma(\delta) = \frac{1}{2n} ln\left(\frac{\delta_m-\delta}{\delta}\right) \tag{29}$$

Where,

$$\left(\frac{A_{red}}{A_{ox}}\right) = 190.522 \tag{30}$$

$$E_a = 65.9664\frac{kJ}{mol} \tag{31}$$

$$n = 0.216 \tag{32}$$

$$\delta_m = 0.408 \tag{33}$$

Figure 7 shows both the quality of the fit as well as the comparison between the two fits. For practical purposes, the results are indistinguishable; the derived reduction enthalpy and entropy are the same in each case. However, the CEF fit requires only two parameters while the Bulfin approach uses four: n, (A_{red}/A_{ox}), E_a, and δ_m.

To summarize, the CEF approach yields thermodynamic equations that are grounded in theory and that are not only useful for materials comparisons, but directly applicable to systems studies. If the data support it, the approach will accommodate both δ- and T-dependence for the thermodynamic parameters. The Bulfin approach also has a physical basis. We postulate that the CEF approach should be more robust than Bulfin as it offers the possibility of more parameters. However, if true, this potential advantage will only become evident over time as more data sets are evaluated. In the current instance, the primary difference is that the CEF model provides a two parameter fit that is indistinguishable from the four parameter Bulfin model. For a similar quality fit, it is reasonable to conclude fewer parameters is an improvement. A note of caution: as formulated, both the CEF and Bulfin approaches assume no phase transitions occur, such as those we have observed and reported herein. That is, both approaches essentially average through the transition.

DISCUSSION AND SUMMARY

Calcium manganites were studied as alternatives to the previously identified LSCM379 for TCES with the primary goal of increasing the thermal storage capacity. This family of perovskites was selected as the basis based on several properties: *1*) a reducible B-site element (Mn) in the +4 oxidation state supports large redox capacity, *2*) reports of high reduction temperatures suggest large reduction endotherms, and *3*) elemental constituents that are relatively low molecular weight, low cost, and abundant support cost and mass energy density metrics. Compositions wherein 20% of the B-site element Mn were replaced Al, Co, Fe, Ti, Zn, Zr, and Y were synthesized and evaluated with the goal of maximizing the storage capacity and stabilizing the perovskite in high-temperature reducing conditions. A 40% Fe sample was also examined. Of these, only the Al, Co, Fe and Ti yielded single-phase materials at room temperature. The parent CM was also single phase in the as-prepared form. The presence of Fe (CFM28 and CFM46) decreased the reduction temperatures relative to CM, an indication of a decrease in reduction enthalpy. This is also suggestive of the presence of a highly reducible Fe^{4+} or Mn^{5+} species in the as-prepared material. CM and CCM28 decompose when exposed to reducing conditions, i.e., Co does not adequately stabilize CM for this application. Based on these results CM, CCM, and CFM compositions were excluded from further investigation.

CYM28 not only consisted of multiple phases but was largely irreducible when screened at 1250°C under flowing Ar. Therefore, B-site doped CYM compositions were also eliminated from further consideration. However, the results also suggested that Y prefers to occupy an A-site, prompting further investigation. Multiple phases in the as-prepared material, lack of clear advantage over CM in screening, and potential for Zn volatilization also discouraged further evaluations of CZnM formulations. As the most promising of the three multi-phase samples, CZrM28 was advanced for further evaluation, but found to deactivate during multicycle studies. This is consistent with CM being the active phase. Additionally it serves as an excellent illustration of the importance of evaluating samples over larger numbers of cycles and at the extremes of anticipated conditions.

In preliminary results, not presented here, decreasing the Ti content from 20 to 10% (CTM19) produced a sample with behavior very similar to CTM28. Further decreasing the Ti to 5% (CTM0595) produced a material that met screening criteria, but was found to be unstable under further examination. Increasing Ti content from 20 to 40 and 60% greatly decreased the redox capacity in the temperature range of interest. The introduction of La onto the A-site with Ti on the B-site (CLTM8228 and CLTM5555) likewise led to collapse of the redox capacity, at least in the temperature range of interest. These negative results are likely linked to the irreducibility of the Ti and La cations and the replacement of a portion of the Ca^{2+} cation with La^{3+} which requires partial reduction of the Mn to the 3+ state to maintain charge balance. The substitution of Sr^{2+} onto the A-site (CSTM8228) had little impact.

TABLE 3 | Recent prices (in US dollars per mole) reported for the metals comprising the evaluated MIECs.

Element	$/mol	Chemical form	Reference
Ca	<0.01	quicklime, CaO	a
Mn	0.11	99.7% Mn flake	b
Al	0.03	Al_2O_3	a
	0.06	Al ingot	
Ti	0.09	95% RutileTiO_2 sponge metal	a
	0.44		
Y	0.34	99.999% Y_2O_3	a

a) U.S. Geological Survey (2020). Mineral commodity summaries 2020. https://doi.org/10.3133/mcs2020. b) U.S. Geological Survey (2021), Mineral Industry Surveys: Manganese in October 2020. Mineral Industry Surveys (usgs.gov).

A-site Y-doped CM samples (CYM) are single phase by XRD. XRD peak splitting, which increased with Y content, was observed for these samples, presumably due to distortion of the crystal lattice. Y-doping pushed the reduction temperatures higher without catastrophic loss of redox capacity. Seemingly, the reduction temperature increases in a regular fashion with Y-content, although further verification is required as the reduction temperatures were pushed above the upper range of the experiments for the higher doping levels. For this reason, only CYM910 and CYM820 were studied further. However, the materials with higher Y content remain of potential interest for higher temperature applications. Doubly doping, with Y on the A-site, and Al on the B-site (CYAM9128, CYAM8228) results in initial reduction temperatures situated between those of the respective singly-doped compounds (CYM910, CYM82, and CAM28). It also eliminates peak splitting in XRD. This presents something of a contrast to somewhat analogous CLTM materials. Further inquiry is required to fully elucidate the differences, but note that the Y^{3+} can be charge balanced by Al^{3+} in the CYAM materials rather than the manganese alone. CYAM9128 was selected for further study.

Figure 1 depicts the reduction endotherms for each of the remaining materials, along with CZrM28 which had not yet been identified as unstable. The highest thermal capacity attributable to the redox reaction, 59 kJ/mol for CYM91, is 34% higher than that of LSCM3791 (44.1 kJ/mol) (Babiniec et al., 2015). **Figure 1B** shows that the cumulative reduction enthalpy over the range of interest are grouped in a narrow range across the set. Putting aside CZrM28, the smallest value (for CYAM9128) is 82% of the largest (for CYM910). The top four candidates from this evaluation, CYM910, CTM28, CYM820, and CAM28, are all singly modified with the best exhibiting a capacity that is only 18% larger than the worst performing of the group (or the worst 15% smaller than the best). However, as this difference can impact design parameters such as vessel sizes and flow rates throughout a solar power facility, it should not be dismissed as insignificant. On the other hand, though higher storage capacity decreases the required amount of material and potentially component sizes, the cost of the constituent elements should not be overlooked (**Table 3**). As can be seen, Y is the most costly element and it replaces the least costly, Ca. Aluminum, on the other hand, replaces a more expensive element, Mn. Ti may also

decrease the cost of elemental constituents, depending on the source. Materials cost therefore favors CAM28 and CTM28 over the CYM options.

Given these complexities, the most economical choice for a given application therefore can best be determined by evaluating the apparent tradeoffs within a system model. A basic thermodynamic model relating T, pO_2, δ, and ΔH of the perovskites is an essential tool for this exercise. Using CAM28 as an example, we have demonstrated that the CEF provides a good framework for developing these models from TGA. In the case of CAM28, the model provides good fits with only two parameters, though more can be applied as necessary. Heat capacities are also needed for this process. In this regard, CAM28 and CTM28 were demonstrated to conform to theoretical expectations. Similar materials will likely do so as well. Other important considerations for cost and operability include the long term stability and compatibility with materials of construction. Regarding the latter, previously reported studies with CAM and CTM materials indicate reaction can occur with commonly used insulating materials, necessitating the use of a zirconia-based liner, e.g., in hot storage bins (Miller et al., 2016).

There are many aspects to stability. Stable cycle-to-cycle performance is of course paramount. Our multicycle results help to establish the redox stability of CAM28, CTM28, CYM910, and CYAM9128. But given the experience with CZrM28, and the observation that small changes are still detectable after 100 cycles for example for CYM910, they also illustrate the importance of extended testing and/or understanding the changes occurring in the materials over time at a fundamental level. Our results illustrate the utility of *in-situ*, high-temperature XRD and DSC analyses in detecting and probing bulk changes (and verifying reversibility) in the perovskites occurring during the redox reaction that might not be apparent, for example, in a limited number of TGA cycles.

High-temperature deactivation/instability is often raised as a concern. However, many of the mechanisms by which active materials, such as catalysts, deactivate are not relevant here. For example, there are no highly-dispersed, high-surface area active materials to sinter or volatilize. Nor is there porosity that must be protected from thermally-driven collapse. Rather, the high temperatures promote rapid reaction, even with low surface area materials, and the inherent oxygen conductivity of this class of materials renders the entire particle accessible without porosity. As such, redox performance is relatively free from small changes in particle size. That said, bulk sintering or agglomeration which could impact flows, and attrition, which imposes a replacement cost and may require the installation of filters and other equipment, are significant concerns for operability and cost. Agglomeration has not been observed for any material in this study, and sintering onset temperatures for CAM28 and CTM28 are 1197 and 1211°C, respectively. As the test samples were highly dense and produced under high compressive loads, these results are very encouraging.

Techniques for evaluating and comparing attrition resistance are numerous but can be difficult to interpret without direct experience for some of the materials in the application environment to anchor the results. Fortunately, the attrition resistance of substituted calcium manganites has been evaluated in the context of fluidized chemical looping combustion and found to be very favorable (Rydén et al., 2014). For example, $CaMg_{0.1}Mn_{0.9}O_{(3-\delta)}$ was tested in a 10 kWth reactor with a generation of fines between 0.02 and 0.002%/h and was considered likely suitable for commercial use in this challenging environment.

In summary, substituted/doped calcium manganites, particularly CYM910, CTM28, CYM820, and CAM28, remain excellent candidates for high-temperature TCES (≤1250°C). CYM910 exhibits the highest chemical storage capacity of the group: 59 kJ/mol *via* reduction at 1250°C and pO_2 = 0.001 atm. CYM820, and potentially other A-site Y-doped compositions (e.g., CYM730), appear poised to eclipse this value if higher temperatures are used. While the materials may undergo minor structural changes during cycling, these appear to be fully reversible and more of an interest to science than barrier to application. While CAM28 is likely the least costly material, only an analysis with the full system context can determine the overall most economical choice.

Looking forward, and setting aside the need to eventually demonstrate materials and operations at the pilot scale we recommend several additional studies that could further lower barriers to implementation. First, characterization of the sensitivity of the results to the synthesis method and the batch-to-batch or lab-to-lab variability for a given method would further validate the results, as well as provide useful information for scaling-up the production. Careful XRD studies including Rietveld analysis would benefit this effort. Further, adding more data points to the T, pO_2, δ map for materials of greatest interest would also be recommended. Second, the robustness of the various materials should be evaluated. That is, operational limits for combinations of temperature, pO_2 and time, maximum achievable δ values before decomposition, etc., can be established by testing the material to failure. Options for recovery or regeneration can also be evaluated. This information has implications for full system design and operations, e.g., establishing how tightly different unit operations must be controlled, and identifying potential areas of concern when operations are upset or out of spec. Finally, validated kinetic expressions for reduction and oxidation across a broad range of temperatures and pO_2 values would be invaluable for system design and analysis. Given the difficulties associated with characterizing an extremely rapid batch reaction in a transient thermal and gaseous environment, this will require the application of specialized techniques and equipment, accounting for the paucity of this type of information.

DATA AVAILABILITY STATEMENT

The original contributions presented in the study are included in the article/**Supplementary Material**, further inquiries can be directed to the corresponding author.

AUTHOR CONTRIBUTIONS

JM: project conception, management, and direction; analysis; principle author. SB: materials conception, synthesis, characterization, and analysis. EC: Materials characterization and analysis. PL: project conception, supervision ES: project conception, thermodynamic modeling. AA: project conception, management, and direction; supervision; materials synthesis, characterization, and analysis.

FUNDING

The U.S. Department of Energy (DOE) SunShot Initiative provided funding for the project entitled High Performance Reduction/Oxidation Metal Oxides for Thermochemical Energy Storage (PROMOTES) under award number DE-FOA-0000805-1541 as part of the CSP:ELEMENTS program. Sandia National Laboratories is a multi-mission laboratory managed and operated by National Technology and Engineering Solutions of Sandia LLC, a wholly owned subsidiary of Honeywell International Inc. for the U.S. Department of Energy's National Nuclear Security Administration under contract DE-NA0003525.

ACKNOWLEDGMENTS

The authors would like to thank all the members of the PROMOTES team for useful conversations and insights.

SUPPLEMENTARY MATERIAL

The Supplementary Material for this article can be found online at: https://www.frontiersin.org/articles/10.3389/fenrg.2022.774099/full#supplementary-material

REFERENCES

Agrafiotis, C., Roeb, M., Schmücker, M., and Sattler, C. (2014). Exploitation of Thermochemical Cycles Based on Solid Oxide Redox Systems for Thermochemical Storage of Solar Heat. Part 1: Testing of Cobalt Oxide-Based Powders. *Solar Energy* 102, 189–211. doi:10.1016/j.solener.2013.12.032

Albrecht, K. J., Jackson, G. S., and Braun, R. J. (2018). Evaluating Thermodynamic Performance Limits of Thermochemical Energy Storage Subsystems Using Reactive Perovskite Oxide Particles for Concentrating Solar Power. *Solar Energy* 167, 179–193. doi:10.1016/j.solener.2018.03.078

Almendros-Ibáñez, J. A., Fernández-Torrijos, M., Díaz-Heras, M., Belmonte, J. F., and Sobrino, C. (2019). A Review of Solar thermal Energy Storage in Beds of Particles: Packed and Fluidized Beds. *Solar Energy* 192, 193–237. doi:10.1016/j.solener.2018.05.047

Babiniec, S. M., Coker, E. N., Ambrosini, A., and Miller, J. E. (2016b). ABO_3 (A = La, Ba, Sr, K; B = Co, Mn, Fe) Perovskites for Thermochemical Energy Storage. *AIP Conf. Proc.* 1734, 050006. doi:10.1063/1.4949104

Babiniec, S. M., Coker, E. N., Miller, J. E., and Ambrosini, A. (2016c). Doped Calcium Manganites for Advanced High-Temperature Thermochemical Energy Storage. *Int. J. Energ. Res.* 40, 280–284. doi:10.1002/er.3467

Babiniec, S. M., Coker, E. N., Miller, J. E., and Ambrosini, A. (2015). Investigation of La Sr1−Co M1−O3− (M = Mn, Fe) Perovskite Materials as Thermochemical Energy Storage media. *Solar Energy* 118, 451–459. doi:10.1016/j.solener.2015.05.040

Babiniec, S. M., Miller, J. E., Ambrosini, A., Stechel, E., Coker, E. N., Loutzenhiser, P. G., et al. (2016a). "Considerations for the Design of a High-Temperature Particle Reoxidation Reactor for Extraction of Heat in Thermochemical Energy Storage Systems," in *Proceedings of ASME International Conference on Energy Sustainability* (Charlotte, NC, USA). doi:10.1115/ES2016-59646

Bakken, E., Boeriogoates, J., Grande, T., Hovde, B., Norby, T., Rormark, L., et al. (2005a). Entropy of Oxidation and Redox Energetics of CaMnO. *Solid State Ionics* 176, 2261–2267. doi:10.1016/j.ssi.2005.06.009

Bakken, E., Norby, T., and Stolen, S. (2005b). Nonstoichiometry and Reductive Decomposition of CaMnO. *Solid State Ionics* 176, 217–223. doi:10.1016/j.ssi.2004.07.001

Bayon, A., Bader, R., Jafarian, M., Fedunik-Hofman, L., Sun, Y., Hinkley, J., et al. (2018). Techno-economic Assessment of Solid-Gas Thermochemical Energy Storage Systems for Solar thermal Power Application. *Energy* 149, 473e484. doi:10.1016/j.energy.2017.11.084

Bayon, A., de la Calle, A., Ghose, K. K., Page, A., and McNaughton, R. (2020). Experimental, Computational and Thermodynamic Studies in Perovskites Metal Oxides for Thermochemical Fuel Production: A Review. *Int. J. Hydrogen Energ.* 45, 12653–12679. doi:10.1016/j.ijhydene.2020.02.126

Brendelberger, S., Vieten, J., Roeb, M., and Sattler, C. (2019). Thermochemical Oxygen Pumping for Improved Hydrogen Production in Solar Redox Cycles. *Int. J. Hydrogen Energ.* 44, 9802–9810. doi:10.1016/j.ijhydene.2018.12.135

Brendelberger, S., Vieten, J., Vidyasagar, M. J., Roeb, M., and Sattler, C. (2018). Demonstration of Thermochemical Oxygen Pumping for Atmosphere Control in Reduction Reactions. *Solar Energy* 170, 273–279. doi:10.1016/j.solener.2018.05.063

Brendelberger, S., von Storch, H., Bulfin, B., and Sattler, C. (2017). Vacuum Pumping Options for Application in Solar Thermochemical Redox Cycles - Assessment of Mechanical-, Jet- and Thermochemical Pumping Systems. *Solar Energy* 141, 91–102. doi:10.1016/j.solener.2016.11.023

Bulfin, B., Lowe, A. J., Keogh, K. A., Murphy, B. E., Lübben, O., Krasnikov, S. A., et al. (2013). Analytical Model of CeO2 Oxidation and Reduction. *J. Phys. Chem. C* 117, 24129–24137. doi:10.1021/jp406578z

Bush, H. E., Datta, R., and Loutzenhiser, P. G. (2019). Aluminum-doped Strontium Ferrites for a Two-step Solar Thermochemical Air Separation Cycle: Thermodynamic Characterization and Cycle Analysis. *Solar Energy* 188, 775–786. doi:10.1016/j.solener.2019.06.059

Bush, H. E., Schlichting, K.-P., Gill, R. J., Jeter, S. M., and Loutzenhiser, P. G. (2017). Design and Characterization of a Novel Upward Flow Reactor for the Study of High-Temperature thermal Reduction for Solar-Driven Processes. *ASME. J. Sol. Energ. Eng.* 139, 051004. doi:10.1115/1.4037191

Carrillo, A. J., Moya, J., Bayón, A., Jana, P., de la Peña O'Shea, V. A., Romero, M., et al. (2014). Thermochemical Energy Storage at High Temperature via Redox Cycles of Mn and Co Oxides: Pure Oxides versus Mixed Ones. *Solar Energ. Mater. Solar Cell* 123, 47–57. doi:10.1016/j.solmat.2013.12.018

Chamberlain, K. (2020). *HeliosCSP "New Concentrated Solar Power Report Offers Learnings from Crescent Dunes Flop*. Available at: https://helioscsp.com/new-concentrated-solar-power-report-offers-learnings-from-crescent-dunes-flop/ (Accessed November 10, 2021).

Chen, X., Zhang, Z., Qi, C., Ling, X., and Peng, H. (2018). State of the Art on the High-Temperature Thermochemical Energy Storage Systems. *Energ. Convers. Manag.* 177, 792–815. doi:10.1016/j.enconman.2018.10.011

Chiang, C. C. K., and Poeppelmeier, K. R. (1991). Structural Investigation of Oxygen-Deficient Perovskite CaMnO2.75. *Mater. Lett.* 12, 102–108. doi:10.1016/0167-577X(91)90066-F

Coker, E. N., Rodriguez, M. A., Ambrosini, A., Miller, J. E., and Stechel, E. B. (2012). Using In-Situ Techniques to Probe High-Temperature Reactions: Thermochemical Cycles for the Production of Synthetic Fuels from CO2 and Water. *Powder Diffr.* 27, 117–125. doi:10.1017/S0885715612000255

Dizaji, H. B., and Hosseini, H. (2018). A Review of Material Screening in Pure and Mixed-Metal Oxide Thermochemical Energy Storage (TCES) Systems for Concentrated Solar Power (CSP) Applications. *Renew. Sust. Energ. Rev.* 98, 9–26. doi:10.1016/j.rser.2018.09.004

Ezbiri, M., Allen, K. M., Gàlvez, M. E., Michalsky, R., and Steinfeld, A. (2015). Design Principles of Perovskites for Thermochemical Oxygen Separation. *ChemSusChem* 8, 1966–1971. doi:10.1002/cssc.201500239

Gokon, N., Yawata, T., Bellan, S., Kodama, T., and Cho, H.-S. (2019). Thermochemical Behavior of Perovskite Oxides Based on LaxSr1-x(Mn, Fe, Co)O3-δ and BaySr1-yCoO3-δ Redox System for Thermochemical Energy Storage at High Temperatures. *Energy* 171, 971–980. doi:10.1016/j.energy.2019.01.081

Gorman, B. T., Lanzarini-Lopes, M., Johnson, N. G., Miller, J. E., and Stechel, E. B. (2021). Techno-economic Analysis of a Concentrating Solar Power Plant Using Redox-Active Metal Oxides as Heat Transfer Fluid and Storage media. *Front. Energy Res.* 9, 734288. doi:10.3389/fenrg.2021.734288

Hillert, M. (2001). The Compound Energy Formalism. *J. Alloys Comp.* 320, 161–176. doi:10.1016/S0925-8388(00)01481-X

HSC (2021). *HSC Chemistry 9*. Finland: Outotec.

Hutchings, K., Wilson, M., Larsen, P., and Cutler, R. (2006). Kinetic and Thermodynamic Considerations for Oxygen Absorption/desorption Using Cobalt Oxide. *Solid State Ionics* 177, 45–51. doi:10.1016/j.ssi.2005.10.005

Imponenti, L., Albrecht, K. J., Kharait, R., Sanders, M. D., and Jackson, G. S. (2018). Redox Cycles with Doped Calcium Manganites for Thermochemical Energy Storage to 1000 °C. *Appl. Energ.* 230, 1–18. doi:10.1016/j.apenergy.2018.08.044

Laurie, A., and Abanades, S. (2020). Recent Advances in Thermochemical Energy Storage via Solid–Gas Reversible Reactions at High Temperature. *Energies* 13, 5859. doi:10.3390/en13225859

Leonidova, E. I., Leonidov, I. A., Patrakeev, M. V., and Kozhevnikov, V. L. (2011). Oxygen Non-stoichiometry, High-Temperature Properties, and Phase Diagram of CaMnO3-δ. *J. Solid State. Electrochem.* 15, 1071–1075. doi:10.1007/s10008-010-1288-1

Lucio, B., Romero, M., and González-Aguilar, J. (2019). Analysis of Solid-State Reaction in the Performance of Doped Calcium Manganites for thermal Storage. *Solid State Ionics* 338, 47–57. doi:10.1016/j.ssi.2019.05.007

Mastronardo, E., Qian, X., Coronado, J. M., and Haile, S. M. (2021). Impact of La Doping on the Thermochemical Heat Storage Properties of CaMnO3-δ. *J. Energ. Storage* 40, 102793. doi:10.1016/j.est.2021.102793

Mehos, M., Price, H., Cable, R., Kearney, D., Kelly, B., Kolb, G., et al. (2020). *Concentrating Solar Power Best Practices Study*. Golden, CO: National Renewable Energy Laboratory. NREL/TP-5500-75763. Available at: www.nrel.gov/docs/fy20osti/75763.pdf.

Meredig, B., and Wolverton, C. (2009). First-principles Thermodynamic Framework for the Evaluation of thermochemicalH2O- orCO2-Splitting Materials. *Phys. Rev. B* 80, 245119-1–245119-8. doi:10.1103/PhysRevB.80.245119

Miller, J. E., Ambrosini, A., Coker, E. N., Ho, C. K., Al-Ansary, H., Jeter, S. M., et al. (2016). "High Performance Reduction/Oxidation Metal Oxides for Thermochemical Energy Storage (PROMOTES)," in Proceedings of ASME International Conference on Energy Sustainability (Charlotte, NC, USA). doi:10.1115/ES2016-59660

Miller, J. E., McDaniel, A. H., and Allendorf, M. D. (2014). Considerations in the Design of Materials for Solar-Driven Fuel Production Using Metal-Oxide Thermochemical Cycles. *Adv. Energ. Mater.* 4, 1300469. doi:10.1002/aenm.201300469

Mizusaki, J., Tagawa, H., Naraya, K., and Sasamoto, T. (1991). Nonstoichiometry and Thermochemical Stability of the Perovskite-type La1−xSrxMnO3−δ. *Solid State Ionics* 49, 111–118. doi:10.1016/0167-2738(91)90076-N

Muroyama, A. P., Schrader, A. J., and Loutzenhiser, P. G. (2015). Solar Electricity via an Air Brayton Cycle with an Integrated Two-step Thermochemical Cycle for Heat Storage Based on Co3O4/CoO Redox Reactions II: Kinetic Analyses. *Solar Energy* 122, 409–418. doi:10.1016/j.solener.2015.08.038

Ortiz, C., Valverde, J. M., Chacartegui, R., Perez-Maqueda, L. A., and Giménez, P. (2019). The Calcium-Looping (CaCO3/CaO) Process for Thermochemical Energy Storage in Concentrating Solar Power Plants. *Renew. Sust. Energ. Rev.* 113, 109252. doi:10.1016/j.rser.2019.109252

Peña, M. A., and Fierro, J. L. G. (2001). Chemical Structures and Performance of Perovskite Oxides. *Chem. Rev.* 101, 1981–2018. doi:10.1021/cr980129f

Qian, X., He, J., Mastronardo, E., Baldassarri, B., Yuan, W., Wolverton, C., et al. (2021). Outstanding Properties and Performance of CaTi0.5Mn0.5O3-δ for Solar-Driven Thermochemical Hydrogen Production. *Matter* 4, 688–708. doi:10.1016/j.matt.2020.11.016

Redlich, O., and Kister, A. T. (1948). Algebraic Representation of Thermodynamic Properties and the Classification of Solutions. *Ind. Eng. Chem.* 40, 345–348. doi:10.1021/ie50458a036

Rydén, M., Moldenhauer, P., Lindqvist, S., Mattisson, T., and Lyngfelt, A. (2014). Measuring Attrition Resistance of Oxygen Carrier Particles for Chemical Looping Combustion with a Customized Jet Cup. *Powder Tech.* 256, 75–86. doi:10.1016/j.powtec.2014.01.085

Sai Gautam, G., Stechel, E. B., and Carter, E. A. (2020). Exploring Ca-Ce-M-O (M = 3d Transition Metal) Oxide Perovskites for Solar Thermochemical Applications. *Chem. Mater.* 32, 9964–9982. doi:10.1021/acs.chemmater.0c02912

Schrader, A., Bush, H. E., Ranjan, D., and Loutzenhiser, P. G. (2020). Aluminum-doped Calcium Manganite Particles for Solar Thermochemical Energy Storage: Reactor Design, Particle Characterization, and Heat and Mass Transfer Modeling. *Int. J. Heat Mass Transfer* 152, 119461. doi:10.1016/j.ijheatmasstransfer.2020.119461

Stekli, J., Irwin, L., and Pitchumani, R. (2013). Technical Challenges and Opportunities for Concentrating Solar Power with thermal Energy Storage. *J. Therm. Sci. Eng. Appl.* 5, 021011. doi:10.1115/1.4024143

Sunku Prasad, J., Muthukumar, P., Desai, F., Basu, D. N., and Rahman, M. M. (2019). A Critical Review of High-Temperature Reversible Thermochemical Energy Storage Systems. *Appl. Energ.* 254, 113733. doi:10.1016/j.apenergy.2019.113733

Vieten, J., Bulfin, B., Call, F., Lange, M., Schmücker, M., Francke, A., et al. (2016). Perovskite Oxides for Application in Thermochemical Air Separation and Oxygen Storage. *J. Mater. Chem. A.* 4, 13652–13659. doi:10.1039/c6ta04867f

Wu, S., Zhou, C., Doroodchi, E., Nellore, R., and Moghtaderi, B. (2018). A Review on High-Temperature Thermochemical Energy Storage Based on Metal Oxides Redox Cycle. *Energ. Convers. Manag.* 168, 421–453. doi:10.1016/j.enconman.2018.05.017

Wu, Y.-t., Ren, N., Wang, T., and Ma, C.-f. (2011). Experimental Study on Optimized Composition of Mixed Carbonate Salt for Sensible Heat Storage in Solar thermal Power Plant. *Solar Energy* 85, 1957–1966. doi:10.1016/j.solener.2011.05.004

Yan, Y., Wang, K., Clough, P. T., and Anthony, E. J. (2020). Developments in Calcium/chemical Looping and Metal Oxide Redox Cycles for High-Temperature Thermochemical Energy Storage: A Review. *Fuel Process. Tech.* 199, 106280. doi:10.1016/j.fuproc.2019.106280

Yuan, Y., Li, Y., and Zhao, J. (2018). Development on Thermochemical Energy Storage Based on CaO-Based Materials: A Review. *Sustainability* 10, 2660. doi:10.3390/su10082660

Zhai, S., Rojas, J., Ahlborg, N., Lim, K., Toney, M. F., Jin, H., et al. (2018). The Use of Poly-Cation Oxides to Lower the Temperature of Two-step Thermochemical Water Splitting. *Energy Environ. Sci.* 11, 2172–2178. doi:10.1039/C8EE00050F

Zinkevich, M., Djurovic, D., and Aldinger, F. (2006). Thermodynamic Modelling of the Cerium-Oxygen System☆. *Solid State Ionics* 177, 989–1001. doi:10.1016/j.ssi.2006.02.044

Conflict of Interest: The authors declare that the research was conducted in the absence of any commercial or financial relationships that could be construed as a potential conflict of interest.

Publisher's Note: All claims expressed in this article are solely those of the authors and do not necessarily represent those of their affiliated organizations, or those of the publisher, the editors and the reviewers. Any product that may be evaluated in this article, or claim that may be made by its manufacturer, is not guaranteed or endorsed by the publisher.

Advantages of publishing in Frontiers

OPEN ACCESS
Articles are free to read for greatest visibility and readership

FAST PUBLICATION
Around 90 days from submission to decision

HIGH QUALITY PEER-REVIEW
Rigorous, collaborative, and constructive peer-review

TRANSPARENT PEER-REVIEW
Editors and reviewers acknowledged by name on published articles

Frontiers
Avenue du Tribunal-Fédéral 34
1005 Lausanne | Switzerland

Visit us: www.frontiersin.org
Contact us: frontiersin.org/about/contact

REPRODUCIBILITY OF RESEARCH
Support open data and methods to enhance research reproducibility

DIGITAL PUBLISHING
Articles designed for optimal readership across devices

FOLLOW US
@frontiersin

IMPACT METRICS
Advanced article metrics track visibility across digital media

EXTENSIVE PROMOTION
Marketing and promotion of impactful research

LOOP RESEARCH NETWORK
Our network increases your article's readership